



HAL
open science

Determination of Operating Margins Related to Multipactor Phenomena for Radio-Frequency Components of Magnetically Confined Controlled Nuclear Fusion Applications

Eva Al Hajj Sleiman

► **To cite this version:**

Eva Al Hajj Sleiman. Determination of Operating Margins Related to Multipactor Phenomena for Radio-Frequency Components of Magnetically Confined Controlled Nuclear Fusion Applications. Physics [physics]. Université Aix-Marseille (AMU), 2023. English. NNT : 2023AIXM0329 . tel-04290885

HAL Id: tel-04290885

<https://cea.hal.science/tel-04290885v1>

Submitted on 17 Nov 2023

HAL is a multi-disciplinary open access archive for the deposit and dissemination of scientific research documents, whether they are published or not. The documents may come from teaching and research institutions in France or abroad, or from public or private research centers.

L'archive ouverte pluridisciplinaire **HAL**, est destinée au dépôt et à la diffusion de documents scientifiques de niveau recherche, publiés ou non, émanant des établissements d'enseignement et de recherche français ou étrangers, des laboratoires publics ou privés.

THÈSE DE DOCTORAT

Soutenue à l'Université Aix-Marseille

le 19 octobre 2023 par

Eva Al Hajj Sleiman

Détermination des marges opérationnelles relatives au phénomène
multipactor des composants radiofréquences pour la fusion nucléaire
contrôlée par confinement magnétique

Discipline

Physique et Sciences de la Matière

Spécialité

Énergie, Rayonnement et Plasma

École doctorale

ED 352 — Physique et Sciences de la Matière

Laboratoire/Partenaires de recherche

CEA/IRFM, Cadarache
ONERA/DPHY, Toulouse

Composition du jury

Benito Gimeno-Martínez Professeur à l'Université de Valencia	Rapporteur
Éric Rius Professeur à l'Université de Bretagne	Rapporteur
Yves Elskens Professeur à l'Université Aix-Marseille	Président du jury
Yolanda Gómez Martínez Ingénieure Chercheuse, LPSC/IN2P3	Examinatrice
Thibault Hamelin Ingénieur Chercheur, CEA/IRFU	Examineur
Walid Helou Ingénieur Chercheur, ITER	Examineur
Julien Hillairet Directeur de Recherche, CEA/IRFM	Directeur de thèse
Mohamed Belhaj Directeur de Recherche, ONERA/DPHY	Encadrant
Nicolas Fil Ingénieur Chercheur, CNES	Membre Invité

Ph.D. Dissertation

**Determination of Operating Margins
Related to Multipactor Phenomena for
Radio-Frequency Components of
Magnetically Confined Controlled
Nuclear Fusion Applications**

Eva Al Hajj Sleiman

The 19th of October 2023

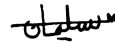
To the long-awaited, promising, & ambitious dream of mankind...

Affidavit

I, undersigned, Eva Al Hajj Sleiman, hereby declare that the work presented in this manuscript is my own work, carried out under the scientific supervision of Julien Hillairet and Mohamed Belhaj, in accordance with the principles of honesty, integrity and responsibility inherent to the research mission. The research work and the writing of this manuscript have been carried out in compliance with both the french national charter for Research Integrity and the Aix-Marseille University charter on the fight against plagiarism.

This work has not been submitted previously either in this country or in another country in the same or in a similar version to any other examination body.

Saint Paul Les Durance, 8th of June 2023.



List of Publications and Conference Participation

List of publications completed within the scope of the thesis project:

1. E. Al Hajj Sleiman, J. Hillairet, M. Belhaj, and S. Dadouch, "Evaluation of multipactor thresholds for coaxial lines subject to surface conditioning for the WEST ion cyclotron antenna," *Fusion Engineering and Design*, vol. 185, p. 113325, Oct. 2022. doi: 10.1016/j.fusengdes.2022.113325.
2. E. Al Hajj Sleiman, J. Hillairet, and M. Belhaj, "Multipactor-Triggering Powers' Modelling of a WEST ICRH Antenna During RF Conditioning," *IEEE Transactions on Plasma Science*, vol. 51, no. 5, pp. 1247-1255, Jan. 2023. doi: 10.1109/TPS.2023.3268293.
3. E. Al Hajj Sleiman, J. Hillairet, and M. Belhaj, "Multipactor Thresholds Prediction for Geometries Subject to Standing Waves," *IEEE Transactions on Plasma Science*, (submitted).
4. E. Al Hajj Sleiman, J. Hillairet, M. Belhaj, S. Dadouch, and V. Maquet, "Multipactor Predictions for Ion Cyclotron Resonance Heating Antennas of the tokamak WEST," *Nuclear Fusion*, vol. 63, no. 12, pp. 126054, Nov. 2023. doi: 10.1088/1741-4326/ad0509.

Participation in conferences and summer schools during the thesis period:

Conferences

1. Poster at the 24th Edition of the Topical Conference on Radio-Frequency Power in Plasmas (TCRFPP), from the 26th to 28th of September, 2022, Annapolis, United States.
2. Oral Presentation at the International Conference on Multipactor, Corona and Passive Intermodulation (MULCOPIM), from the 19th to 21th of October, 2022, Valencia, Spain.
3. Poster at the 49th Edition of the European Plasma Physics Conference (EPS), from the 3rd to 7th of July, 2023, Bordeaux, France.

Summer schools

1. « 14th Carolus Magnus Summer School on Plasma and Fusion Energy Physics », *Research Centre of Forschungszentrum Jülich*, from the 20th of September to 1st of October, 2021 [online].
2. « 1ère Edition, Ecole Fusion Pour Tous », *CEA, IRFM*, from the 20th to 24th of June, 2022 [Cadarache].

Résumé

Les ondes radiofréquences (RF) de haute puissance sont couramment utilisées dans des environnements sous vide pour la recherche sur la fusion nucléaire par confinement magnétique, notamment dans des dispositifs expérimentaux tels que les tokamaks. La capacité de transmission de puissance des antennes peut être limitée par le phénomène de multipactor, qui correspond à une augmentation exponentielle du nombre d'électrons. Ce phénomène survient, généralement, lorsque l'énergie des électrons entrant en collision avec les surfaces des composants est suffisamment élevée pour libérer des électrons supplémentaires et lorsque le mouvement des électrons est synchronisé avec le changement de phase du signal RF. Dans de telles conditions, un phénomène d'avalanche électronique se produit, pouvant générer des perturbations RF, une augmentation de la température locale des composants, entraînant une augmentation subséquente de la pression due à la désorption de particules de surface. Si ce phénomène n'est pas arrêté, il peut éventuellement déclencher une décharge corona ou un arc électrique dans le gaz résiduel à basse pression, ce qui peut entraîner la destruction partielle voire totale du composant.

L'initiation du multipactor dépend de l'amplitude et de la fréquence du champ électrique RF au sein du dispositif RF, ainsi que des propriétés d'émission d'électrons secondaires des matériaux utilisés, telles que leur composition de surface, leur morphologie, leur historique et de la présence d'un champ magnétique. La prédiction du multipactor est relativement bien comprise pour les géométries métalliques simples, mais reste incertaine pour les structures complexes avec des champs électriques multi-matériaux, telles que les fenêtres d'étanchéité RF composés de matériaux diélectriques et de conducteurs.

Sur le tokamak WEST situé au CEA-Cadarache en France, des systèmes RF sont utilisés pour le chauffage du plasma. En particulier, le phénomène suivant a été observé lors des campagnes expérimentales sur les trois antennes de chauffage par résonance cyclotronique ionique (ICRH) : lorsque seule une antenne est alimentée, la pression augmente dans les antennes qui ne le sont pas. Le problème est que dès que la pression dans l'une des antennes dépasse un seuil prédéfini, le système de sécurité interdit l'application de la puissance RF afin d'éviter la génération d'un plasma induit à l'intérieur de l'antenne, ce qui affecte l'opération du système ICRH. Le phénomène de multipactor est une possible explication de cette augmentation de pression et cette hypothèse est étudiée dans ce travail.

L'objectif de ces travaux est de modéliser le phénomène de multipactor pour des composants RF réalistes soumis à des ondes stationnaires, tels que les antennes ICRH de WEST. L'étude des mécanismes physiques à l'origine de ces augmentations de pression dans les

antennes vise à déterminer si le multipactor est responsable de ces niveaux de pression mesurés et s'il permet d'en donner une explication.

Summary

High-power radio-frequency (RF) waves are commonly used in a vacuum environment in magnetically confined nuclear fusion research in experimental devices such as tokamak. The power transmission capability of the antennas can be limited by the multipactor phenomenon — an exponential increase in the number of electrons. The multipactor effect generally occurs when the energy of the electrons colliding with the surfaces of the component is high enough to release additional electrons and when the electrons' motion is synchronised with the phase change of the RF signal. Under these conditions, an electron avalanche phenomenon is created, which can generate RF perturbations, rise in the local temperature of the components, leading to a subsequent increase in the pressure due to surface particle desorption, and, if not stopped, eventually trigger a corona discharge or an electric arc in the low-pressure residual gas that can lead to a component partial or total destruction.

The multipactor initiation depends on the RF electric field's magnitude and frequency within the RF device and the secondary electron emission properties of the materials used, *i.e.*, its surface composition, morphology, and history, and the presence of a magnetic field. The prediction of the multipactor is relatively well understood for simple metal geometries but remains uncertain for complex structures with multi-material and complex electric fields, such as RF feed-through composed of dielectric and conductive materials.

RF systems are used for plasma heating on the tokamak WEST, located at CEA-Cadarache in France. In particular, the following phenomenon was observed during experimental campaigns on the three Ion Cyclotron Resonance Heating (ICRH) antennas: when only one antenna is powered, the pressure increases in the antennas which are not powered. The problem is that once the pressure in one antenna exceeds a predefined threshold, the security system prohibits the application of RF power to avoid the generation of RF-induced plasma inside the antenna. The latter affects the operation of the ICRH system. The multipactor phenomenon is a possible cause explaining this pressure rise, and this hypothesis is investigated in this work.

The objective of this work is to model the multipactor phenomenon for realistic RF components subject to standing waves, such as the ICRH antennas of WEST. The study of the physical mechanisms underlying these pressure increases in the antennas aims to determine whether the multipactor is responsible for these measured pressure levels and if it provides an explanation for them.

Acknowledgement

I don't know where to start; in fact, the only thing I know is that I know nothing. Thereby, I will write what I felt must be within this section.

I will begin by thanking Who deserves all of the gratitude, thanking Who cannot be figured out, through that whose existence relies on Him. I thank Who is not lacking any kind of manifestation held by anything other than Him for it to act as an appearance for Him. I will begin by thanking who accepts my gratitude and thankfulness with His compassion, as my hope for Him does not cease. Who has never been absent, so that He may need something to point to Him. And Who has never been far-off, so that traces may lead to Him. Through Him and to Him, the three years have passed. He has always been present and has never left me alone or forgotten me.

But how can I ever show my gratitude? And the ability to show gratitude itself demands gratitude. When I say, "I am grateful to You." I have to say, "I am grateful that I am grateful to You." Ought to all of this, thank You, my forever supportive companion and haven when the wide courses fail to carry me.

Then, a longing towards the people of "al-Daher" fills me with gratitude and thankfulness for the blessed tree with its firm roots and branches in the heavens. They are the kind words within me and the source of guidance and enlightenment.

From the heavens to the beloved South, the Homeland, and the shining land of Jabal 'Amel. . . Thank you, my esteemed land. I owe you the gratitude of belonging to the spot of the fragrant roses and the olive trees with its ancient historical face. And where does this gratitude lead me, except where blackness becomes a symbol of firmness and strength with insightful vision, thus strengthening its roots? Then, being softened with a radiant white, which is the symbol of hearts imbued with the love of truth? These are the hearts attached and adorned with the love of the green — the essence of the ancient olive tree, the luminous olive that shines like the sun in the darkness of the path. Thus, red signifies nothing but the presence of the exquisite blossoms of Anemone, whose fragrance has spread, revealing their hidden beauty to the Earth. It is the beautiful dream every lover aspires to, especially since tomorrow is near for those patiently awaiting.

I extend my deepest gratitude to my PhD director, Julien, for his unwavering support, invaluable guidance, and mentorship throughout my PhD journey. His expertise and commitment to meaningful work have played a crucial role in shaping this research. I consider myself truly fortunate to have had Julien as a mentor, for whom I am grateful for the countless hours and infinite patience he invested in providing constructive feedback and fostering an agreeable environment — in all aspects.

Especially during challenging times, Julien consistently demonstrated his unwavering presence and openness to listen and discuss with clear insights. This achievement would not have been possible without his dedication. Thank you for being a source of inspiration and sharing your passion for RF engineering. I am profoundly grateful for the opportunity to learn and grow under your guidance.

I aspire to one day reflect to future students what I have learned from you, saying, "Indeed, I had the chance to be supervised by a kind soul and a remarkable human being — qualities I wholeheartedly recommend seeking when looking for PhD opportunities. I hope to be as effective as he is in teaching and mentoring."

I am sincerely grateful to my co-supervisor, Mohamed Belhaj, for the ease with which we communicated — even though I was rarely present at ONERA. His approachability and open communication made the research process more enriching and enjoyable. Thank you for your valuable support.

I am incredibly grateful for the privilege of meeting outstanding individuals at CEA and ONERA. The warmth, expertise, and respectful interactions made my PhD smooth and enriching. Each interaction has been a source of inspiration, and the spirit within the GSCP group has been invaluable. Thank you to everyone for contributing to an environment where great minds converge to share a journey of discovery with exceptional people. Special thanks are to Sarah Dadouch for her guidance and assistance during the long experiments day, ensuring smooth and productive working days in Toulouse.

I extend heartfelt thanks to my wonderful office mates, Lara and Sana, with whom I share not just meals but also countless beautiful moments. The laughter, conversations, and shared experiences have made the workplace enjoyable and supportive. Thank you for being more than colleagues.

Lara is a vibrant and positive force in our workplace. Her boundless energy, infectious positivity, and love for life have not only brightened our shared spaces but also uplifted the overall atmosphere. I have learned from you that nothing is impossible; all we need is consistency and belief!

Sana, whose calm demeanour and lovely presence have made a profound impact on our shared workspace. Sana is not only a wonderful listener but also a mysteriously beautiful soul, adding a unique and invaluable dimension to our shared experiences. Thank you, Sana, for your quiet strength and the beauty you bring to our daily routine.

I am also thankful to my friend, Ali, for being a consistent source of support and understanding. His clear mind, exceptional listening skills and insightful perspectives have been invaluable in navigating life's challenges. I am grateful for the enriching impact you have had on my life, pillar of strength!

Last but certainly not least, I would like to express my deepest gratitude to my family, Hassan, Rose, Ali, Sarah and Mohammad, my unwavering support system and the

bedrock of my journey. Their belief in me has been a guiding light, illuminating the path to my academic pursuits. Even when self-doubt crept in, their unshakeable faith fueled my determination. Their encouragement, understanding, and sacrifices have been the cornerstone of my achievements. Thank you for being my constant source of strength and believing in me more than I sometimes do. Your love and support have been my assets throughout my life.

I am beyond grateful to my parents, Hassan and Rose, who dedicated their lives to ensuring our well-being and providing us with the opportunity for a good life and a quality education. Their sacrifices, hard work, and unconditional support have been the foundation upon which I have built my achievements. Thank you for your enduring love, guidance, and the countless sacrifices you have made to help me reach where I am today. I love you.

Ali, the consistently silent but impactful support system and an unwavering advocate for my capabilities. His steadfast encouragement and belief in my potential have been a driving force throughout my life. Ali, your presence has been a motivation and reassurance source, going beyond words.

Sarah, my sister, best friend, and the most extraordinary soul I have ever known. Her perpetual smile, even in the face of difficulties, has been a constant inspiration. She is the one who believes in me unwaveringly, offering support and encouragement at every turn. Thank you, my dearest sister, for being my confidante, cheerleader and guiding light. Your presence has been a source of immeasurable strength throughout my life... Fadi, you are not forgotten, and your place in my heart is as special as Sarah's. Thank you for being a beautiful part of my journey.

I hold a special place in my heart for Mohammad, my beautiful little brother, whom I miss dearly. Thank you for being present as a source of great love and pride in my life!

8th of November, 2023

Résumé détaillé

Observation problématique d'une augmentation de pression dans les antennes ICRH de WEST

Au cours des campagnes expérimentales sur WEST, l'observation suivante a été faite sur les trois antennes *Ion Cyclotron Resonance Heating* (ICRH) : si une antenne ICRH est alimentée alors que les autres antennes sont éteintes, une augmentation de pression est observée dans les antennes non alimentées. Si la pression dépasse le seuil de sécurité prédéfini $p_{th} = 4,5 \times 10^{-3}$ Pa (Bernard et al. [1]), un dispositif de sécurité interdit l'application (ou la réapplication) de la puissance radio-fréquence (RF) afin d'éviter la génération et le maintien d'un plasma induit à l'intérieur des antennes, ce qui affecte le fonctionnement du système ICRH. Par conséquent, ce phénomène peut compliquer ou même arrêter le fonctionnement nominal des antennes. Un exemple d'augmentation de pression est présenté à la Figure 1, où une seule antenne ICRH est en fonctionnement (Q_1), tandis que les deux autres sont éteintes (Q_2 et Q_4). Lorsque l'antenne Q_1 couple sa puissance au plasma, la pression augmente à l'intérieur des deux antennes éteintes (Q_2 et Q_4). Cette pression est suffisante pour interdire l'utilisation de Q_2 et Q_4 , car elle dépasse le seuil de sécurité prédéfini p_{th} .

Une cause possible expliquant ces observations pourrait être le phénomène *multipactor*, une décharge RF résonante dans le vide (Vaughan [2]). Bien que les trois antennes ICRH de WEST fonctionnent à des fréquences légèrement différentes, les interférences entre les antennes pourraient être suffisantes pour induire du multipactor. Une conséquence possible dans le pire des cas est la métallisation des céramiques des capacités ou de la fenêtre RF si un plasma induit par multipactor est maintenu à proximité. L'objectif de ce travail est de déterminer si le multipactor est une explication plausible de l'augmentation de pression observée.

Définition du multipactor

Le multipactor est une décharge sous vide observée dans des structures radio-fréquences (RF) à des pressions suffisamment basses pour que le libre parcours moyen des électrons soit supérieur à la distance de séparation des électrodes, de sorte que les électrons se déplacent entre les électrodes sans subir de collisions avec les molécules de gaz. Le mécanisme du multipactor se maintient par l'émission d'électrons secondaires résultant

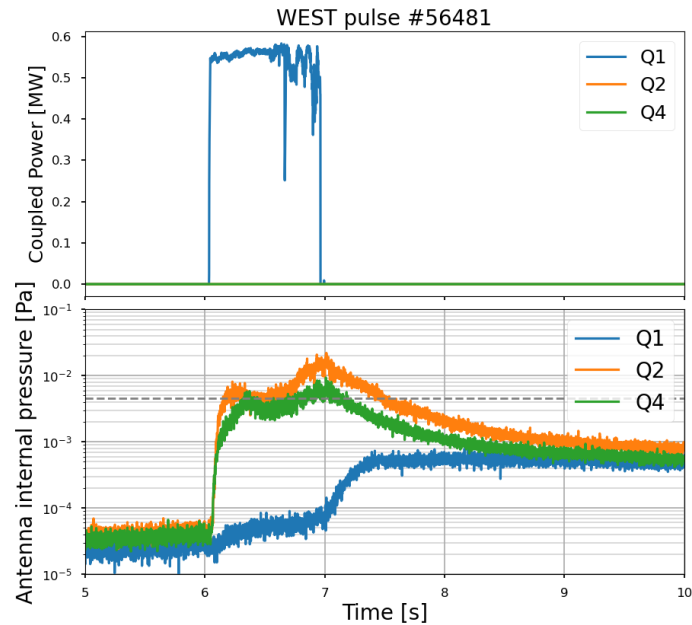


Figure 1: Un exemple démontrant l'augmentation de pression sur les antennes non alimentées (Q_2 et Q_4) sur le plasma lorsqu'une seule antenne est activée (Q_1 , fonctionnant avec 0.55 MW). Sur la figure supérieure, les puissances couplées des antennes sont tracées en fonction du temps. Sur la figure inférieure, la pression interne des antennes est tracée en fonction du temps, et la ligne pointillée grise représente la limite d'augmentation de pression (p_{th}) au-delà de laquelle l'application (ou la réapplication) de la puissance RF est interdite pour des raisons de sécurité.

de l'impact des électrons sur les surfaces du dispositif RF avec une énergie cinétique suffisante pour libérer, en moyenne, plus d'électrons secondaires que le nombre d'électrons incidents — de sorte que plus d'électrons sont générés que retirés. L'émission d'électrons secondaires peut provenir d'une surface métallique ou diélectrique.

Dans ce mécanisme, certains électrons primaires sont accélérés par le champ électrique RF, puis impactent une surface avec suffisamment d'énergie pour libérer des électrons secondaires supplémentaires. Le champ électrique peut à son tour accélérer les électrons libérés jusqu'à ce qu'une collision de surface se produise, suivie d'une nouvelle libération d'électrons secondaires, et le processus se poursuit. On observe alors une augmentation exponentielle de la population d'électrons lorsque ce phénomène se déclenche jusqu'à ce qu'un mécanisme de saturation limite la densité électronique ou qu'une décharge se produise.

Le multipactor peut être déclenché dans diverses géométries et sur une large gamme de fréquences, de la gamme des mégahertz à plusieurs dizaines de gigahertz. Le multipactor peut être observé dans des applications RF à basse pression/vide telles que les satellites

RF (De Lara et al. [3]), les cyclotrons (Woo and Ishimaru [4]), les cavités d'accélération (Shemelin and Belomestnykh [5]), les composants RF expérimentaux de tokamaks (Graves et al. [6] and Goniche et al. [7]) : antennes, lignes de transmission et fenêtres RF (Preist and Talcott [8], Hillairet et al. [9], and Jang et al. [10]); tubes à vide micro-ondes tels que les klystrons (Preist and Talcott [8] and Sounas [11]) ou les structures d'accélérateurs de particules (Petit et al. [12]).

Conséquences du multipactor

Dans certaines applications, les décharges initiées par le multipactor posent problème et ont des effets néfastes sur le fonctionnement nominal des dispositifs et peuvent : absorber et dissiper une partie de l'énergie électromagnétique, charger des cavités RF avec un nuage d'électrons (Udiljak et al. [13] and Sorolla [14]), conduire à l'apparition de discontinuités abruptes dans la transmission RF (Vaughan [2]), augmenter le niveau de bruit du système ou à une dégradation du signal (Semenov et al. [15]).

En dissipant la puissance électromagnétique, les décharges multipactor peuvent provoquer un échauffement et un dégazage (Sorolla [14]). Cette augmentation de la température locale du dispositif peut endommager les composants internes (Vaughan [2], Woode and Petit [16], and Ang et al. [17]), éroder des structures métalliques, perforer des parois sous vide (Kishek et al. [18]) et générer des harmoniques indésirables (Vaughan [2] and Udiljak et al. [19]).

Pour les dispositifs de fusion nucléaire, le multipactor affecte ou limite les performances des antennes de chauffage, réduit la fiabilité des systèmes de chauffage et de génération du courant par radiofréquence et limite la puissance maximale couplée au plasma (Graves et al. [6] and Goniche et al. [7]). Le multipactor peut induire des claquages à des pressions de gaz inférieures à celles prévues par la loi de *RF Paschen* en particulier en présence de champs magnétiques continus élevés (Graves [20] and Becerra [21]).

Enfin, le nuage d'électrons créé par le multipactor peut induire une réflexion de la puissance vers les générateurs, qui peut endommager les sources RF (klystrons ou tétrodes). Si la puissance RF n'est pas arrêtée, l'augmentation de la température et l'augmentation de la pression due à la désorption des particules peut conduire à un endommagement ou la destruction de composants. En effet, la pulvérisation de particules métalliques sur les matériaux diélectriques comme les céramiques va métalliser ces surfaces. Par effet Joule, les courants RF vont alors chauffer ces céramiques et les dilatations thermiques vont provoquer une rupture entraînant la perte de l'étanchéité du composant (Kim, Verboncoeur, and Lau [22]). D'autre part, un événement multipactor soutenu peut déclencher une décharge *corona*, une ionisation locale du gaz, conduisant à la destruction partielle voire totale des composants (Sorolla [14], Höhn et al. [23], and Yu [24]).

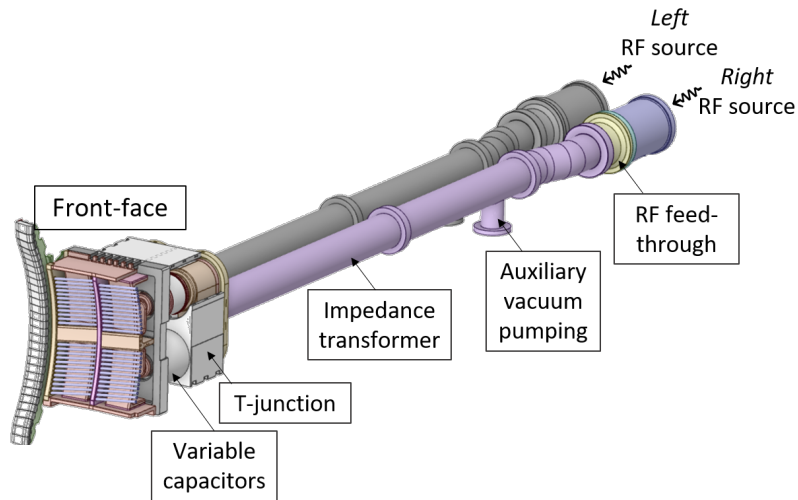


Figure 2: Une illustration des différents composants d'une antenne ICRH utilisée sur le tokamak WEST. Chaque côté possède son propre générateur haute puissance.

Dans ce travail, nous nous intéressons aux applications où les effets du multipactor sont néfastes, en particulier au système de chauffage par résonance cyclotronique ionique (ICRH) du tokamak expérimental de fusion WEST.

Description de l'antenne ICRH de WEST

Chaque antenne ICRH de WEST est composée de deux côtés : côté gauche et côté droit. Chaque côté est constitué de deux capacités variables, d'une jonction-T (un composant RF à trois ports), d'un transformateur d'impédance pour adapter l'impédance de la ligne coaxiale de transmission provenant du générateur ($30\ \Omega$) à la faible impédance de la jonction-T, et d'une fenêtre RF réalisée en alumine assurant l'étanchéité entre la partie sous vide et la partie pressurisé en azote des lignes de transmission du côté du générateur. Les deux capacités de chaque côté de l'antenne peuvent être réglées pour que l'antenne soit résonante à une fréquence donnée. Une illustration des différents composants d'une antenne ICRH est donnée dans la Figure 2.

Méthodologie

Afin d'expliquer les mécanismes physiques produisant l'augmentation de pression dans les antennes ICRH qui ne sont pas utilisées quand une seule antenne du système est

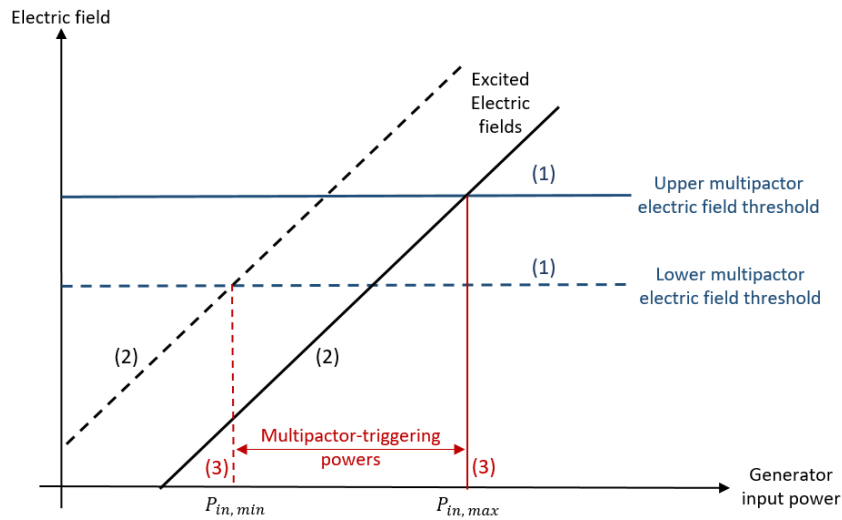


Figure 3: Illustration des trois principales étapes utilisées pour résoudre le problème pour une fréquence donnée. Les lignes bleues correspondent aux seuils de champ électrique du multipactor, les lignes noires correspondent aux champs électriques excités, et les lignes rouges correspondent aux puissances directes des générateurs résultants déclenchant le multipactor à l'intérieur de la géométrie.

alimentée, et de valider ou non l'hypothèse proposée que le multipactor est à l'origine de cette montée de pression mesurée, il est indispensable de modéliser le phénomène multipactor dans les antennes ICRH de WEST et d'étudier l'effet des couplages RF entre les deux côtés d'une même antenne et entre antennes.

La détermination des seuils multipactor dans les différents composants d'une antenne ICRH est un problème difficile, puisqu'il s'agit de composants RF 3D complexes sujets à des ondes stationnaires dues à la géométrie des antennes ainsi qu'aux conditions du plasma, contrairement au domaine du spatial où les composants sont adaptés à la charge, et donc sujets aux ondes progressives — sans réflexion d'ondes.

Pendant le fonctionnement des antennes WEST ICRH, l'opérateur doit prendre les décisions suivantes :

- ▶ Choisir le nombre d'antennes actives.
- ▶ Choisir la fréquence à laquelle chaque antenne en fonctionnement est accordée, c'est-à-dire à laquelle les capacités seront réglées pour que le circuit RF soit résonant.
- ▶ Régler les capacités de l'antenne (ou de chaque côté de l'antenne) à sa (leurs) fréquence(s) d'intérêt. Deux situations principales sont rencontrées : *i*) les capacités sont réglées pour que l'antenne résonne (ou à un côté de l'antenne) et sont appelées *capacités réglées*. *ii*) La capacité réglée à 120 pF (la valeur de capacité la plus élevée) et on parle de *capacités dérégées*, car l'antenne (ou le côté de l'antenne) n'est plus

résonante.

Avant d'opérer les antennes sur plasma, les antennes sont "conditionnées" par un étuvage jusqu'à 200 °C en début de campagne expérimentale puis par une phase de "conditionnement RF", consistant à augmenter progressivement le champ électrique RF dans les antennes pendant de courtes impulsions. Lors de cette phase, les opérateurs ICRH contrôlent la puissance incidente par côté et le décalage de phase entre les côtés d'une antenne, généralement en mode dipôle avec 180°.

En opération sur plasma, la puissance et la phase sont contrôlées en temps réel par le système de contrôle du plasma. Lorsqu'une antenne est alimentée, les deux côtés sont alimentés et les quatre capacités de l'antenne sont réglées pour la rendre résonante à la fréquence d'intérêt.

Dans cette section, notre objectif est de *i)* déterminer les puissances incidentes des générateurs et les états des capacités qui peuvent déclencher le multipactor à l'intérieur des différents côtés et composants des antennes à chaque fréquence d'intérêt. *ii)* En déduire les meilleures stratégies pour réduire ou éviter le multipactor dans différents scénarios opérationnels. Dans ce cas, l'opérateur pourrait choisir les paramètres de configuration — puissances incidentes des générateurs et état des capacités — pour réduire les problèmes opérationnels causés par le multipactor.

Pour atteindre nos objectifs, nous avons divisé l'analyse du problème en trois parties principales, illustrées schématiquement dans la Figure 3 pour une fréquence donnée :

1. Détermination des champs électriques responsables du déclenchement du multipactor à l'intérieur des différents composants de l'antenne (lignes bleues dans la Figure 3). Les champs électriques du multipactor sont déterminés selon notre méthodologie, détaillée dans le Chapitre 4. Nous l'avons appliquée sur les principaux composants des antennes WEST ICRH : la jonction-T, le transformateur d'impédance, et la fenêtre RF dans la plage de fréquence [46 – 65] MHz. Ces seuils sont appelés les *seuils de champ électrique du multipactor* et sont déterminés en tenant compte des propriétés de l'émission secondaire des matériaux opérationnels mesurées et pertinentes pour l'ICRH.
2. Résolution du champ électrique dans les sections de l'antenne en utilisant un solveur électromagnétique et un solveur de circuit (ANSYS Electronics). Ce dernier tient compte de manière auto-consistante des puissances des générateurs, de l'état des capacités et du couplage entre les deux côtés (ou entre antennes) pour des conditions de vide ou de plasma. Ainsi, cette étape permet de déterminer les *champs électriques excités* dans tous les composants de l'antenne (lignes noires dans la Figure 3).
3. Comparaison des *seuils de champ électrique du multipactor* aux *champs électriques excités*. Cela permet de déterminer les puissances incidentes des générateurs — seuils

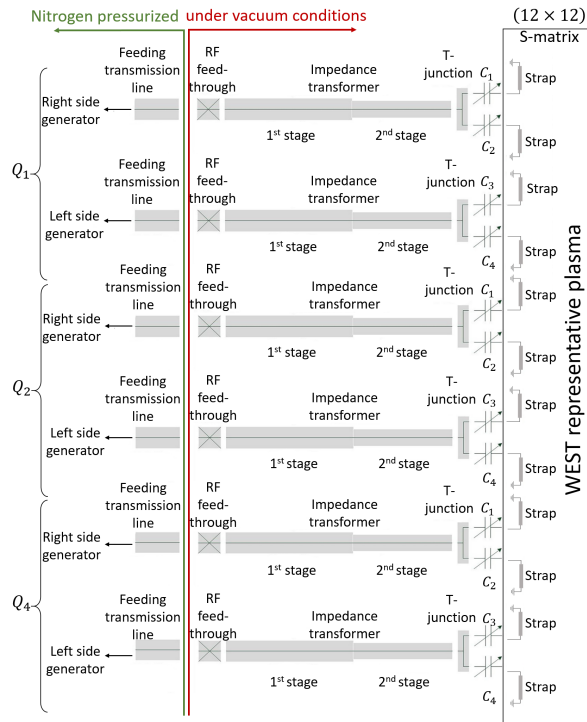


Figure 4: Modèle de circuit des trois antennes ICRH de WEST face au plasma, où les deux côtés de chaque antenne sont modélisés. Le scénario plasma représentatif de WEST est représenté par une matrice S de dimension (12×12) pour prendre en compte le couplage RF entre les antennes ICRH.

inférieurs et supérieurs — déclenchant le multipactor à l'intérieur des différents composants de l'antenne (points rouges dans la Figure 3).

Multipactor lors des scénarios de plasma

Nous souhaitons étudier la responsabilité du multipactor dans l'augmentation de pression mesurée dans les antennes ICRH non alimentées lorsqu'une seule antenne est alimentée.

Dans de tels scénarios, une fraction importante de la puissance des générateurs est couplée au plasma. La puissance incidente des générateurs lors des scénarios plasma se situe dans la plage [100 kW – 1.5 MW] par côté d'antenne, et est appliquée pendant plusieurs secondes. Dans ce fonctionnement, lorsqu'une antenne ICRH est alimentée, les deux côtés sont alimentés — avec la même puissance incidente — en configuration dipôle (180° entre les deux côtés).

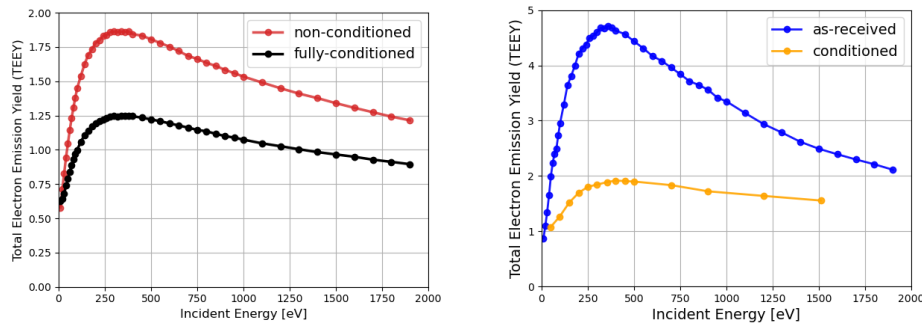


Figure 5: Gauche — Mesures de TEEY pour un échantillon représentatif revêtu d’argent d’une antenne ICRH de WEST, maintenu à 70 °C. En rouge, les données TEEY sont mesurées avant tout traitement de conditionnement ; et en noir, les données TEEY sont mesurées après un traitement de conditionnement complet de la surface (avec une dose électronique cumulative de $2338 \mu\text{C mm}^{-2}$). Droite — En bleu, les données TEEY pour un échantillon d’alumine tel qu’il est reçu. En orange, les données TEEY pour un échantillon d’alumine conditionné (Bira [25]).

Pendant le fonctionnement plasma, les opérateurs du système ICRH contrôlent la fréquence des générateurs et les quatre capacités variables internes de chacune des trois antennes ICRH. Nous avons étudié les deux cas opérationnels suivants :

- Case 1:** Une antenne ICRH est alimentée — les générateurs des deux côtés sont alimentés — et les quatre capacités sont *réglées* à 55 MHz. L’antenne opère en configuration dipôle, avec une différence de phase de 180° entre les deux côtés. Les deux autres antennes sont éteintes, et leurs capacités sont *réglées* à 55 MHz.
- Case 2:** Une antenne ICRH est alimentée — les générateurs des deux côtés sont alimentés — et les quatre capacités sont *réglées* à 55 MHz. L’antenne opère en configuration dipôle, avec une différence de phase de 180° entre les deux côtés. Les deux autres antennes sont éteintes, et leurs capacités sont *dérégées*.

Détermination des champs électriques des antennes

Le modèle de circuit des trois antennes ICRH représentant l’opération sur plasma est représenté dans la Figure 4. Les composants de chaque côté de l’antenne sont modélisés. Une matrice S représentative d’un scénario plasma de WEST est obtenue par un modèle numérique du plasma de WEST contenant les éléments rayonnants des trois antennes ICRH. Cette matrice est de dimension (12×12) car chaque face avant de l’antenne est décrite par un composant passif à quatre ports.

Pour une fréquence d’intérêt, le modèle permet de définir *i)* les puissances incidentes de tous les générateurs — la même puissance est appliquée aux générateurs du côté *gauche* et *droit* d’une même antenne ; *ii)* les capacités des quatre capacités de chaque antenne

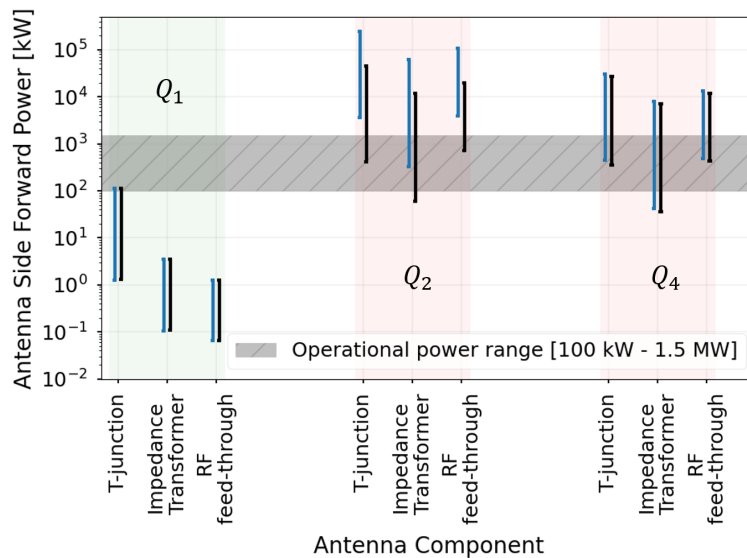


Figure 6: Les puissances incidentes d'un générateur déclenchant le multipactor dans la jonction-T, le transformateur d'impédance et la fenêtre RF de chaque antenne Q_1 , Q_2 et Q_4 . Les lignes verticales bleues (respectivement noires) correspondent aux puissances incidentes déclenchant le multipactor dans les composants du côté *gauche* (respectivement *droit*) de chaque antenne. La région grise hachurée correspond à la plage nominale de puissance opérationnelle d'un générateur alimenté.

ICRH ; *iii*) les conditions de couplage entre antennes (vide ou plasma). En résolvant de manière auto-consistante le modèle, on détermine les tensions et courants puis les *champs électriques excités* dans tous les composants des antennes ICRH.

Puissances incidentes des générateurs déclenchant le multipactor

Dans cette section, nous déterminons, pour chaque composant de chaque côté d'antenne, les puissances incidentes inférieures et supérieures des générateurs d'un seul côté déclenchant le multipactor à la fréquence de 55 MHz.

Résultats — Cas 1

Dans ce premier cas, les deux générateurs de l'antenne Q_1 sont alimentés avec la même puissance incidente, et les quatre capacités sont *réglées* pour que l'antenne résonne à 55 MHz. Q_2 et Q_4 ne sont pas alimentés et leurs capacités sont *réglées* à 55 MHz.

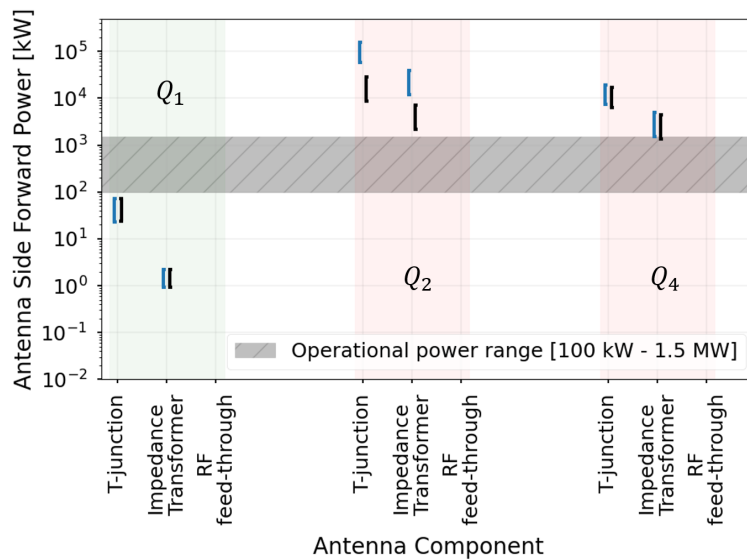


Figure 7: Même légende que pour la Figure 6.

Tout d'abord, nous avons pris en compte la courbe de données TEEY *non conditionnée* (courbe rouge de la Figure 5) des composants revêtus d'argent, ainsi que la courbe de données TEEY telle qu'elle est reçue pour la céramique d'alumine (courbe bleue de la Figure 5). Les résultats sont illustrés dans la Figure 6, où nous avons représenté la plage des puissances incidentes du générateur qui déclenche le multipactor dans chaque composant des antennes — la jonction-T, le transformateur d'impédance et la fenêtre RF. Les lignes verticales bleues (respectivement noires) correspondent aux puissances incidentes déclenchant le multipactor dans les composants du côté *gauche* (respectivement *droit*) de chaque antenne. La région grise hachurée correspond à la plage nominale de puissance opérationnelle d'un générateur alimenté [100 kW – 1.5 MW].

On constate que dans la plage opérationnelle d'un générateur des antennes ICRH de WEST, le multipactor est déclenché dans tous les composants des antennes non alimentées (Q₂ et Q₄), à l'exception de la jonction-T et de la fenêtre RF du côté *gauche* de l'antenne Q₂, car le champ électrique calculé dans la plage de puissance [100 kW – 1.5 MW] n'est pas suffisant pour déclencher le multipactor dans ces composants. La non-symétrie des résultats est expliquée par l'anisotropie du plasma simulé.

Ensuite, nous avons pris en compte la courbe de données TEEY *entièrement conditionnée* (courbe noire de la Figure 5) des composants revêtus d'argent et la courbe de données TEEY conditionnée de la céramique d'alumine (courbe orange de la Figure 5). Les résultats

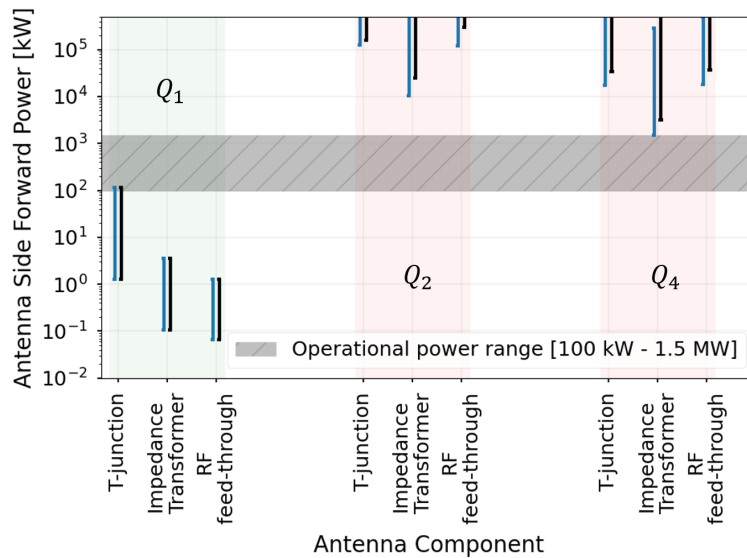


Figure 8: Même légende que pour la Figure 6.

sont illustrés dans la Figure 7. Il n'y a aucune plage de puissance incidente pour laquelle le multipactor est déclenché dans la fenêtre RF, car il n'y a pas de multipactor dans ce composant pour les données TEEY conditionnées.

Ainsi, la Figure 7 montre que le conditionnement réduit la plage de multipactor dans les différents composants des antennes. Dans la plage de puissance incidente [100 kW – 1.5 MW], il n'y a presque aucun déclenchement du multipactor dans les antennes non alimentées par rapport aux résultats de la Figure 6, à l'exception du transformateur d'impédance de Q_4 lorsque la puissance incidente est d'environ 1.5 MW.

Résultats — Cas 2

Dans ce deuxième cas, les deux générateurs de l'antenne Q_1 sont alimentés avec la même puissance incidente, et les quatre capacités sont réglées pour que l'antenne résonne à 55 MHz. Q_2 et Q_4 ne sont pas alimentés et leurs capacités sont *dérégées*. Les résultats correspondant aux courbes de données TEEY non conditionnées sont représentés dans la Figure 8. Cette dernière montre que, en raison du désaccord des capacités, il n'y a presque aucun déclenchement du multipactor dans les antennes non alimentées contrairement aux résultats de la Figure 6, à l'exception du transformateur d'impédance du côté *gauche*

de Q_4 lorsque la puissance incidente est d'environ 1.5 MW. Le multipactor n'est pas déclenché lorsque les données TEEY conditionnées sont utilisées.

Conclusion

Les résultats indiquent que lorsqu'une seule antenne ICRH de WEST est alimentée, tandis que les deux autres sont éteintes, le multipactor est déclenché dans les différents composants — jonction-T, transformateur d'impédance et fenêtre RF — des antennes non alimentées en raison du couplage entre les antennes. Le déclenchement du multipactor pourrait donc être la cause de l'augmentation de la pression interne, qui a été observée expérimentalement dans les antennes non alimentées. De plus, les résultats montrent que la plage de déclenchement du multipactor est réduite lorsque les surfaces sont conditionnées et que les capacités des antennes en mode désactivé sont dérégées. Cette dernière constatation a été observée lors de la phase de conditionnement RF et pendant le fonctionnement en présence du plasma.

En plus, les résultats de la formulation du problème d'augmentation de la pression à l'intérieur de l'antenne ont montré que l'augmentation de la pression causée par le multipactor est de l'ordre de 10^{-3} Pa. Cette dernière est en bonne correspondance avec les valeurs d'augmentation de pression observées expérimentalement (de 10^{-3} Pa à 10^{-2} Pa).

Contents

Contents	xxvi
List of Acronyms	xxix
General Introduction	xxx
1 Ion Cyclotron Resonance Heating Systems	1
1.1 Nuclear Fusion	1
1.2 Magnetically Confined Plasma Devices	4
1.2.1 Ohmic Heating: An Inductive Current-Drive Plasma Heating	5
1.2.2 Non-Inductive Current-Drive Plasma Heating	5
1.2.3 Additional Heating and Current Drive Systems	5
1.3 Ion Cyclotron Resonance Heating (ICRH) Systems	6
1.3.1 High-Power RF Generators	7
1.3.2 Transmission Lines	7
1.3.3 Matching Systems	8
1.3.4 Antennas	9
1.4 Overview of the Tokamak WEST	9
1.4.1 WEST ICRH Antennas' Description	10
1.4.2 WEST ICRH Main Diagnostic Systems	13
1.4.3 WEST ICRH Operational Conditions	14
1.5 Pressure Rise Problematic Observation on WEST ICRH Antennas	15
1.6 Chapter Summary	16
2 Material Electron Emission Characterisation	17
2.1 Electron Emission	17
2.1.1 Energy Distribution of Emitted Electrons	18
2.1.1.1 <i>Chung and Everhart's</i> energy distribution	19
2.1.1.2 <i>Maxwell-Boltzmann's</i> energy distribution	19
2.1.2 Angle Distribution of Emitted Electrons	20
2.1.2.1 Angle distribution of secondary electrons	20
2.1.2.2 Angle distribution of back-scattered electrons	20
2.2 Electron Emission Yield	20
2.2.1 Definition	20
2.2.2 TEEY Incident Angle Dependence	22
2.2.3 TEEY Measurements Techniques	22
2.2.4 <i>Vaughan's</i> Empirical TEEY Expressions	23
2.3 X-ray-induced Photoelectron Spectroscopy (XPS)	24
2.4 Surface Characterisation Means	27
2.4.1 Experimental Setup Description	27
2.4.2 Experimental Approach	28
2.4.3 Results and Discussions	29
2.5 Chapter Summary and Perspectives	32
3 Multipactor Phenomenon	33
3.1 Multipactor Definition	33
3.2 Historical Background on Multipactor	34
3.3 Multipactor Conditions	38

3.4	Multipactor Consequences	38
3.5	Multipactor Saturation Mechanisms	39
3.6	Multipactor Detection Methods	41
3.7	Multipactor Mitigation Techniques	42
3.8	Coaxial Transmission Lines	44
3.8.1	Geometry's Main RF Properties	44
3.8.2	Geometry's Main Multipactor Properties	45
3.8.3	Multipactor Analysis' State of the Art	46
3.8.3.1	Travelling wave case	46
3.8.3.2	Mixed and standing wave cases	49
3.8.3.3	Other interesting findings	51
3.9	Chapter Summary and Perspectives	53
4	Multipactor Thresholds Modelling	55
4.1	Numerical Multipactor Software Details	55
4.1.1	Spark-3D from Dassault Systems	58
4.1.2	Ansys-HFSS Multipaction	60
4.2	Multipactor Decision Algorithm	61
4.3	Multipactor Thresholds under Standing Waves	64
4.3.1	Methodology	64
4.3.2	Implementation	67
4.4	Coaxial Transmission Line's Results	68
4.4.1	Comparison with Experimental Data	68
4.4.2	Scaling Laws' Validation	69
4.4.3	Conditioning Effect on Multipactor Thresholds	71
4.4.4	MW and SW Results	73
4.5	Chapter Summary and Perspectives	76
5	Multipactor in Complex Geometries	77
5.1	Methodology Description	77
5.2	Multipactor Electric Fields Thresholds' Determination	79
5.2.1	T-junction and Impedance Transformer	79
5.2.2	RF feed-through	82
5.3	Multipactor during WEST ICRH RF Conditioning	84
5.3.1	Determination of the Antenna Electric Fields	85
5.3.2	Multipactor-Triggering Generators' Forward Powers	86
5.3.2.1	Results — Case 1	87
5.3.2.2	Results — Case 2	88
5.3.2.3	Results — Case 3	91
5.3.3	Conclusion on the Results	92
5.4	Multipactor during WEST ICRH Plasma Scenarios	92
5.4.1	Determination of the Antennas Electric Fields	93
5.4.2	Multipactor-Triggering Generators' Forward Powers	94
5.4.2.1	Results — Case 1	94
5.4.2.2	Results — Case 2	95
5.4.3	Conclusion on the Results	96
5.5	Multipactor on TITAN's Resonator	96
5.5.1	TITAN's Resonator Description	97
5.5.2	Multipactor Resonator Results	98
5.6	Chapter Summary and Perspectives	102

6	Multipactor Pressure Rise Estimation	103
6.1	Problem Formulation	103
6.1.1	Formulation 1 — Steady State Assumption	103
6.1.1.1	Pump-impinging molecular flux evaluation ϕ	104
6.1.1.2	Surfaces' molecular desorbed rate R	104
6.1.2	Formulation 2 — Transient State Assumption	106
6.2	Multipactor Pressure Rise Estimation	106
6.3	Experimental Pressure Rise	108
6.4	Discussion	109
7	General Conclusion and Perspectives	111
7.1	Conclusions	111
7.2	Perspectives and Future Works	113
	APPENDICES	115
A	Appendix A	117
B	Appendix B	121
	Bibliography	123

List of Acronyms

3D Three Dimensional.

AES Auger Electron Spectroscopy.

ALCHIMIE AnaLyse CHImique et mesure de l'éMIssion Électronique.

CEA Commissariat à l'Énergie Atomique et aux énergies alternatives.

CPS Counts Per Second.

CST-PS Computer Simulation Technology Particle Studio.

CW Continuous Wave.

DPHY Département PHYSique, instrumentation, environnement, espace.

EBEs Elastic Back-scattered Electrons.

ECRH Electron Cyclotron Resonance Heating.

ELMs Edge Localized Modes.

EM Electromagnetic.

EMT Electron Multiplier Tube.

FWHM Full Width at Half Maximum.

GM Global Method.

HFSS High-Frequency Structure Simulator.

IBEs Inelastic Back-scattered Electrons.

ICRH Ion Cyclotron Resonance Heating.

IRFM Institute for Magnetic Fusion Research.

ITER International Thermonuclear Experimental Reactor.

LHCD Lower Hybrid Current-Drive.

LM Local Method.

MCP Micro-Channel Plate.

MW Mixed Wave.

NBI Neutral Beam Injection.

ONERA Office National d'Études et de Recherches Aérospatiales.

PEs Primary Electrons.

PIC Particle In Cell.

PID Proportional-Integral-Derivative.

PMT Photo-Multiplier Tube.

RF Radio-Frequency.

RPAs Retarding Potential Analyzers.

SEs Secondary Electrons.

SEY Secondary Emission Yield.

SHAD Sub-Harmonic Arc Detection.

SW Standing Wave.

SWR Standing Wave Ratio.

TEEY Total Electron Emission Yield.

TEM Transverse Electro-Magnetic.

TW Travelling Wave.

UHV Ultra High Vacuum.

UV Ultra Violet.

VSWR Voltage Standing Wave Ratio.

WEST Tungsten (W) Environment in Steady-state Tokamak.

XPS X-ray-induced Photoelectron Spectroscopy.

General Introduction

The multipactor is an electron avalanche sustained by secondary electron emission from the surfaces of a vacuum radio-frequency (RF) device. It depends on the propagating RF electric field, frequency of operation, presence (or not) of a DC magnetic field, dimensions of the geometry, and the material's electron emission properties.

Although this phenomenon could be beneficial for some signal amplification applications, it is not the case for the RF heating systems of nuclear fusion devices. In particular, a performance-limiting phenomenon has been observed in the ion cyclotron resonance heating (ICRH) system of the tokamak WEST — located at the IRFM Laboratory of CEA in Cadarache, France. Indeed, if one of the three antennas composing the system is activated while the remaining two are off, a pressure rise is observed on the non-powered antennas. The latter is sufficient for prohibiting the (re)-application of the RF power.

A possible hypothesis for the pressure increase is the multipactor induced by the cross-talk between the antennas. Therefore, our objective is to validate or not this hypothesis.

Relating the pressure rise increase observed on the RF heating systems of the ICRH antennas to the multipactor phenomenon is not straightforward since the diagnostics deployed on the plasma heating systems are not directly specialised for multipactor detection. Therefore, we have proceeded systematically, starting by analysing the existence of the multipactor in such antennas, then determining the generators' forward powers triggering the electrons' multiplication in the various components while accounting for the RF coupling between the antennas of the ICRH system, ending with the estimation of the pressure rise caused by multipactor and comparing it to the experimental observations.

We summarise herein the contents of the chapters of this manuscript and link them together in the framework of the observed experimental problem. The original contributions are also included in their corresponding chapters.

We briefly introduce the magnetically confined nuclear fusion and describe the generic system of ICRH antennas, as well as the ICRH antenna system employed on the tokamak WEST in Chapter 1.

As the material emission properties are critical for accurate multipactor modelling, we dedicate Chapter 2 to analyse the emission properties of the representative material of the WEST ICRH antennas within relevant operational conditions. We measure the total electron emission yield (TEEY) of stainless steel silver-coated samples representative of the antennas' materials under operational baking and conditioning surface treatments. In addition, we monitor the chemical surface modifications of the sample *in-situ* using X-ray photoelectron spectroscopy (XPS).

We describe the multipactor phenomenon and its properties in Chapter 3. We present the current state of the art on the various RF applications suffering from the destructive effects of electron multiplication caused by the multipactor.

In Chapter 4, we rely on the "electron-time"'s evolution calculated with Spark-3D and Ansys-HFSS to develop a multipactor decision-making algorithm. The latter is based on the growth rate of electrons to determine, for any RF component, the thresholds for which multipactor appears — lowest threshold — and eventually disappears — highest threshold. We reproduced the literature scaling laws for a $50\ \Omega$ circular coaxial

transmission line subject to a travelling wave and compared them against measurements to verify the developed algorithm. Moreover, we analyse the surface conditioning effect on the lowest and highest voltage multipactor thresholds for $30\ \Omega$ and $50\ \Omega$ silver-coated circular coaxial transmission lines. Our findings reveal that surface conditioning leads to an increase (respectively decrease) in the lowest (respectively highest) multipactor thresholds.

Furthermore, as the ICRH antennas are subject to time-varying and various power ports' excitation, it was crucial to study the effect of the electric patterns resulting from the superposition of incident and reflected waves on the multipactor thresholds. As expressing the multipactor thresholds in terms of RF powers, is non-relevant in standing wave patterns, we develop multipactor criteria for the frequency range of interest regardless of the voltage standing wave ratio's variability (VSWR). We apply the developed methodology on a simple geometry of a $50\ \Omega$ cylindrical coaxial transmission line subject to travelling wave (TW), mixed wave (MW), and standing wave (SW) patterns to show the validity of the methodology in the ICRH frequency range.

We devote Chapter 5 to multipactor analysis in complex structured RF geometries. In particular, we verify the developed methodologies for various complex RF structures, such as the impedance transformer, T-junction, and RF feed-through used in the ICRH antennas, as well as the RF resonator test bed used to test high-power RF components. Moreover, we analyse the multipactor in one ICRH antenna during its conditioning phase for different possible scenarios, as one ICRH antenna is constituted of two generators powering two symmetrical sides connected through a front face facing the tokamak's vacuum vessel. Each antenna side is composed of an RF feed-through window, an impedance transformer, a T-junction, and two tuneable matching capacitors. Three different cases were studied: *i*) both sides are powered with tuned capacitors to match the antenna, *ii*) one side is powered while the capacitors of both sides are tuned, and *iii*) one side is powered with tuned capacitors, while the other is non-powered and its capacitors are detuned. For each studied case, we determine the generator(s) input power triggering multipactor in the various antenna sections within the frequency range of the ICRH antenna. The latter provides the best practices for operating the ICRH antennas during conditioning. Finally, we extend this analysis to the case of three antennas operating on plasma to determine the conditions for which multipactor could be triggered in the antennas.

In Chapter 6, we formulate the pressure rise problem by establishing a balance equation between the molecular desorption rate caused by the multipactor and the pumping rate. The latter is done to evaluate the pressure rise caused by the multipactor and compare it to the experimentally observed values.

Chapter 7 concludes the work and details several axes for future work.

All the developed methodologies could be applied to any multi-port RF component, whether this component is used in nuclear fusion, space applications, or any other application where multipactor is a concern.



1 Ion Cyclotron Resonance Heating Systems

You think that you are an infinitesimal being, though you encompass the entire universe.

Ali Ibn Abi Taleb

In this chapter, we introduce the nuclear fusion principle (Section 1.1) and describe the magnetically confined plasma devices (Section 1.2). In its second part, we illustrate the various components of a generic ion cyclotron resonance heating (ICRH) antenna (Section 1.3). Then we give more details about the ones employed on the device of the IRFM¹ laboratory in CEA Cadarache, France (Section 1.4). The last part is dedicated to the problem that we are interested in understanding and characterising its origin in this manuscript (Section 1.5).

1: IRFM stands for "Institute for Magnetic Fusion Research."

1.1 Nuclear Fusion

Fusion is a nuclear reaction that powers the core of the Sun, along with all the stars of the Universe. It is the process by which two light atomic nuclei combine to form a heavier atom while releasing tremendous amounts of energy.

In the core of the Sun, where the temperature reaches fifteen million kelvin, nuclei come within a very close range of each other and collide at high energies provided by the core's temperature. This high-energy collision is sufficient to overcome the electrostatic mutual Coulomb's repulsion force between the positively charged nuclei by the attractive nuclear force and to fuse the colliding atoms. The Coulomb's potential barrier is proportional to the product of the nuclei's charge numbers, making a fusion of nuclei with low charge numbers "easier."

The resulting heavier element's mass is not exactly the sum of the initial fused nuclei masses due to a fractional-mass defect, which is, in its turn, responsible for the enormous amount of released kinetic energy, as governed by Einstein's energy-mass equivalence formula $E = mc^2$.

For the fusion reaction to happen, atoms must be confined within a small space so that the collisions' probability increases. In the core of the Sun,

the gravitational forces ensure the confinement of the positively charged hydrogen nuclei for the fusion process to take place.

Since the 1920s, dating the first explanation of the fusion process, researchers have been on a quest to develop ways to harness energy from fusion reactions on Earth. Although further research and development are needed, nuclear fusion is a promising candidate for the increasing demand of substituting fossil fuels-based energy production with reliable and environment-friendly alternatives. Therefore, once controlled in a reactor at an industrial scale, nuclear fusion could become an ideal energy source to meet the world's demand.

Crossing the electrostatic Coulomb's barrier can be quantified in a probabilistic manner with the *reaction rate* r [reaction/(m³ s)], defined as the probability of reaction per time-unit and volume-unit. The reaction rate between mono-energetic ions of density n_1 [m⁻³] striking ions of density n_2 [m⁻³], is proportional to the species' density product and can be expressed by the following

$$r_{12} = n_1 n_2 \sigma_{12} v_{12}$$

where σ_{12} [m²], is the effective cross-section area and v_{12} is the velocity difference between the two species.

The product term $\sigma_{12} v_{12}$ is called the *reactivity* ([m³/s]) and is dependent on the colliding species' kinetic energies. Dropping the mono-energetic assumption and assuming the ions have Maxwellian velocity distribution, the average reactivity $\langle \sigma v \rangle_{12}$ can be derived from the velocities' distribution functions as follows

$$\langle \sigma v \rangle_{12} = \int_{-\infty}^{+\infty} \int_{-\infty}^{+\infty} \sigma(v_{12}) v_{12} f_1(v_1) f_2(v_2) dv_1 dv_2.$$

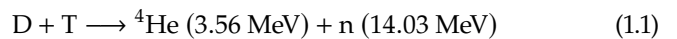
Therefore, the average reaction rate $\langle r_{12} \rangle$ is expressed by

$$\langle r_{12} \rangle = n_1 n_2 \langle \sigma v \rangle_{12}.$$

The average reactivity $\langle \sigma v \rangle_{12}$ has a temperature dependence that can be plotted for different fusion reactions as shown in Figure 1.1.

[27] Ball (2019)

The reaction of interest for controlled nuclear fusion [27] is the deuterium (D) - tritium (T) reaction (Equation 1.1), as it has the highest reaction rate reaching its maximum at a temperature of 64 keV. Deuterium and tritium are both hydrogen isotopes with respectively one neutron and two neutrons. The deuterium is abundant in seawater, and the tritium — a radioactive isotope of about 12 years of half-lifetime, which is relatively rare in nature — can be generated *in-situ* within the reactor².



2: The neutrons produced from the D-T reaction can be used to produce the tritium *in-situ* when reacting with lithium (Li) in a tritium breeding blanket:
 ${}^6\text{Li} + \text{n} \longrightarrow \text{T} + {}^4\text{He} + 4.8 \text{ MeV}.$

The D-T reaction releases a total energy of $E_{DT} = 17.59 \text{ MeV}$ per fusion reaction, with almost 80% of the energy carried out by neutrons. Under the assumption of equal density for deuterium and tritium, $n_D = n_T = \frac{n}{2}$, with n the electron density, the thermonuclear power density is

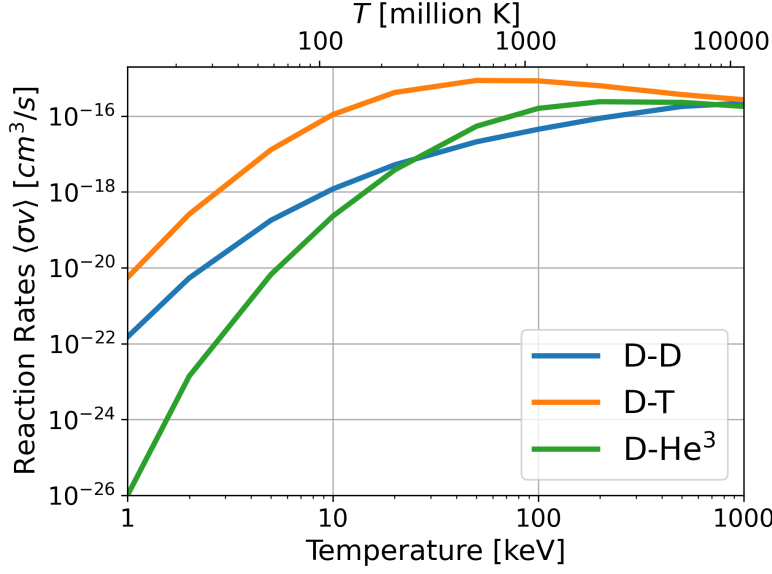


Figure 1.1: Fusion reactivity versus temperature for a few couples of fusion reactions: (deuterium-deuterium), (deuterium-tritium), and (deuterium-helium). Data are extracted from (Richardson (2019)).

proportional to the average reactivity and is expressed as

$$p_{\text{DT}} = \frac{n^2}{4} \langle\sigma v\rangle_{\text{DT}} E_{\text{DT}}. \quad (1.2)$$

Therefore, the total fusion power $P_{\text{fus}} = \int p_{\text{DT}} dV$ is released from both alpha particles (${}^4\text{He}$) and neutrons, and is expressed as follows

$$P_{\text{fus}} = P_{\alpha} + P_n. \quad (1.3)$$

The alpha particles' energy could be used to sustain fusion reactions, whereas neutrons, not confined by magnetic fields, heat the surrounding blanket, resulting in thermal energy that could be converted into electrical energy.

Although the D-T reaction produces high fusion power, a self-sustained fusion reaction requires heating the deuterium and tritium over 150 million kelvin temperatures. These temperatures are needed to achieve high enough particle density for the fusion reaction to take place. For such high temperatures, fusion fuels become in the *plasma* state of matter: a charged gas made of positive ions and free-moving electrons.

Fusion reactors are intrinsically safe as fusion reactions are self-limiting processes occurring under strict operational conditions, outside of which the plasma loses its energy and extinguishes. Moreover, while fusion reactor vessels' components will be nuclear wastes, they are not expected to be high-level long-lived wastes. The fusion reaction does not emit carbon dioxide or greenhouse gases into the atmosphere. Therefore, as a reactor could be started when needed, it could be a dispatchable low-carbon energy source.

The confinement by gravitational fields occurring in the core of the Sun is not doable on Earth. Therefore, sustaining a high plasma temperature in a steady-state regime requires a plasma confinement method. Several approaches for fusion confinement are possible: magnetic confinement, inertial confinement, and hybrid confinement approaches. In

3: The Lorentz force reads:

$$\vec{F} = q(\vec{E} + \vec{v} \times \vec{B})$$

where q is the particle's charge, \vec{v} the particle's velocity, \vec{E} and \vec{B} respectively the electric and magnetic fields.

4: The toroidal magnetic field is stronger than the poloidal magnetic field.

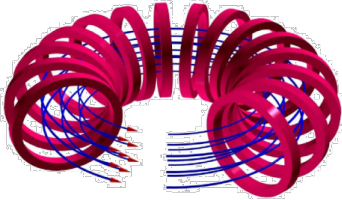


Figure 1.2: Toroidal magnetic field lines produced by toroidal coils.

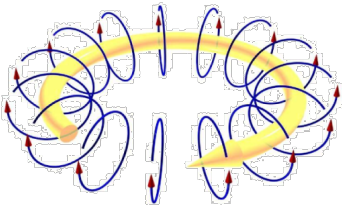


Figure 1.3: Poloidal magnetic field lines produced by the plasma current.

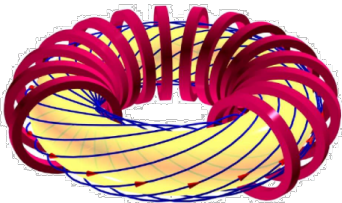


Figure 1.4: Helical magnetic field lines produced as a resultant of the toroidal and poloidal fields.

5: In operation device. The name is derived from "tungsten (W) Environment in Steady-state Tokamak."

6: Under construction device. The name is the acronym for "International Thermonuclear Experimental Reactor."

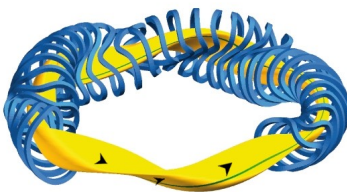


Figure 1.5: Helical magnetic field lines produced by helical coils in a stellarator.

this manuscript, only magnetic confinement techniques, presented in the following section, are of interest.

1.2 Magnetically Confined Plasma Devices

This confinement approach is known as *magnetic thermonuclear fusion*, where the plasma is trapped with a strong magnetic field. Owing to the Lorentz force³, the cross product of the particle's — electron or ion — velocity with the magnetic field will cause the particle to gyrate in a circular motion around the magnetic field lines. The magnetic field-based guidance of the charged particles is the basic principle for magnetically confined plasma devices.

Among other available systems using this principle, we are interested in the toroidal systems. These machines are mainly of two types, the *tokamak*-type and the *stellarator*-type.

The *tokamak*, derived from the acronym of a Russian expression translating to "toroidal chamber with axial magnetic coils," was developed in the Soviet Union in 1959 and is a magnetic device for high-temperature plasma confinement in the shape of an axially symmetric torus. In this device type, the plasma is confined in the vacuum vessel by the superposition of two magnetic fields: the toroidal and poloidal magnetic fields⁴.

The toroidal magnetic field is created by the toroidally placed magnetic field coils in the toroidal (horizontal) direction as shown in Figure 1.2. In addition to the toroidal magnetic field coils' set, the poloidal magnetic field coils' set consisting of a central solenoid and additional coils used for plasma positioning, shaping, and instability control purposes are concentric to the vacuum vessel of a tokamak.

Ramping a current in the central solenoid, which is the primary winding of a transformer-like system, induces an electrical field in the secondary winding, which is the plasma itself, in our case. This electric field is responsible for an induced current in the plasma, which, in its turn, creates a magnetic field in the poloidal (vertical) direction as shown in Figure 1.3.

The superposition of both toroidal and poloidal magnetic fields forms the helical twisted magnetic field, confining the plasma in the vacuum vessel. Figure 1.4 illustrates the tokamak's helical-shape magnetic field lines.

Nowadays, the tokamak is the leading magnetic configuration for fusion reactors, and there is, therefore, a large number of experimental tokamak devices currently in operation or under construction, among which, WEST⁵ (previously Tore-Supra), located at IRFM laboratory in CEA, Cadarache, France; and the project ITER⁶, in Cadarache, France.

The *stellarator* concept, invented at Princeton University in 1951, avoids the plasma current's generation need by changing the shape of the plasma to an asymmetrical torus via toroidal and external magnetic field coils of complex three-dimensional geometries to generate twisted magnetic field lines, which control the plasma confinement. An illustration of the

helical magnetic field lines and the helical toroidal coils are shown in Figure 1.5⁷.

As discussed in Section 1.1, the plasma temperature should reach tens of keV to achieve an optimal reaction rate — a temperature equal to ten times the Sun’s core temperature. The required high temperature could only be reached through heating techniques for the confined plasma. Heating techniques are discussed in the following three subsections.

1.2.1 Ohmic Heating: An Inductive Current-Drive Plasma Heating

In a tokamak, the first available mean for plasma heating is the ohmic heating created by the plasma current — introduced before — and is responsible for plasma heating due to plasma resistivity. The energy associated with the plasma current is dissipated as heat through particle collisions. Therefore, the advantages of ohmic heating are two-fold: *i*) it is a plasma confinement requirement for tokamak-type devices, *ii*) and it provides the first mean for plasma heating.

The plasma resistivity is proportional to $T^{-3/2}$ (T being the plasma temperature, assumed to be homogeneous in the plasma’s volume). This proportionality says that the ohmic power decreases with increasing plasma temperature. Consequently, the ohmic heating effect becomes less pronounced as the plasma temperature increases. Therefore, it has been shown that for the typical tokamak’s parameters, the maximum achievable temperature by the ohmic heating process is a few keV. This temperature is insufficient for the alpha power to dominate the fusion power expression. Therefore, there is a requirement for some external auxiliary heating system(s) to complement the ohmic heating process.

1.2.2 Non-Inductive Current-Drive Plasma Heating

We must sustain a constant plasma current to operate a tokamak-type device in a steady-state regime. Nevertheless, as illustrated in Figure 1.6, inducing constant current in the plasma (secondary winding) requires a linearly variable current in the central solenoid (primary winding). A linearly variable current cannot be maintained indefinitely, as the magnetic flux available at the central solenoid’s coil limits the primary-winding current duration. Hence, the plasma-induced-current-duration is also limited.

An intrinsic consequence of this is that tokamak devices are pulsed-type machines. Therefore, to operate a tokamak in a steady state, plasma-induced current must be sustained by other non-inductive means.

1.2.3 Additional Heating and Current Drive Systems

The following systems are currently used as available auxiliary systems in nuclear fusion devices for either heating and/or inducing current in the plasma:

7: We won’t further discuss stellarators in this manuscript.

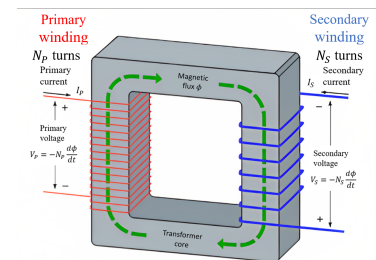


Figure 1.6: Illustration of the tokamak transformer effect, where the primary winding is the central solenoid and the secondary winding is the plasma.

8: Neutral particles are chosen to be injected into the plasma as the presence of the magnetic field prohibits the injection of charged particles. Indeed, they would be deflected by the magnetic field lines as suggested by the Lorentz force.

- ▶ Neutral beam injection heating (NBI), where high-energy beams of neutral atoms are injected into the plasma⁸. Most of these particles deposit their power due to ionisation by collisions with background plasma particles.
- ▶ High-power radio frequency waves, in particular:
 - Ion cyclotron resonance heating (ICRH) radio-frequency systems operating in the frequency range [30 – 120] MHz;
 - Lower hybrid current-drive (LHCD) radio-frequency heating systems operating in the frequency range [1 – 10] GHz;
 - Electron cyclotron resonance heating (ECRH) radio-frequency systems operating in the frequency range [50 – 200] GHz.

Despite their operation at different frequencies, all the radio-frequency (RF) heating and current-drive systems share the following principal requirements:

1. High-power RF generators responsible for transforming electrical power into electromagnetic power;
2. Transmission lines to transport the electromagnetic power to the plasma-facing antennas;
3. Antennas to couple the electromagnetic power to the plasma waves that propagate to the plasma core;
4. Wave-particle resonances leading to the plasma-wave energy transfer to resonant particles.

In this manuscript, we focus on ICRH systems, precisely the ICRH system of the tokamak WEST, to address a problem limiting the operation of the antenna system. An introduction to a generic ICRH system is given in the following section.

1.3 Ion Cyclotron Resonance Heating (ICRH) Systems

As discussed in Section 1.2.1, the ion temperature should be raised to the required values to reach the plasma burning state via auxiliary heating systems. We detail herein the ion cyclotron resonance heating (ICRH) system.

ICRH system is a bulk plasma heating method based on the resonance principle between the cyclotron motion of an ion in a static magnetic field and the electromagnetic wave having the same frequency. Therefore, the ICRH system consists in launching RF waves with frequencies equal to the cyclotron⁹ frequency of one of the ion species of the plasma — or its harmonics¹⁰. ICRH systems are widely employed on thermonuclear fusion devices and are characterised by a power level of several megawatts (MW) coupled to the plasma.

As discussed earlier in the requirements for an RF heating system, the ICRH system could be divided into two main parts: *i*) the first part deals with the technology responsible for generating the RF power and its transportation via transmission lines to the vacuum vessel of the magnetically confined device, *ii*) the second part deals with wave propagation and absorption mechanisms via wave-particle interactions. Between these two parts comes the antenna interface responsible for

9: The ion cyclotron frequency f_c reads:

$$f_c = \frac{q Z B}{2\pi m}$$

where Z is the ion charge number, q the elementary charge, m the ion mass, and B the static magnetic field.

10: The harmonics of the ion cyclotron frequency can be expressed by:

$$f = p f_c$$

where p is an integer greater than one.

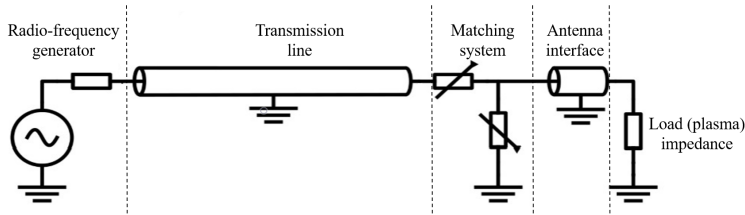


Figure 1.7: A simplified circuit schematic for a generic ICRH system constituted of a radio-frequency generator, transmission lines, matching system, and antenna front interface. The plasma is represented by a load impedance.

coupling the RF power to the plasma waves. Figure 1.7 represents a schematic illustration of the different parts of a generic ICRH system: an RF generator, transmission lines, matching system, and antenna interface. The plasma, which faces the antenna, is the load of the high-power RF system.

1.3.1 High-Power RF Generators

The high-power RF sources ensure the transformation from electrical to electromagnetic power. Typically, they are carried out by a series of amplifiers (Tetrode, Triode) for the ICRH frequency range [30 – 120] MHz. This technology is a derivation from the high-power steady-state broadcast transmitters.

1.3.2 Transmission Lines

We use transmission lines to transmit, split or combine high-power electromagnetic waves from one point to another. In the frequency range of ICRH systems, coaxial transmission lines are a suitable choice to transport the power from the RF sources to the antenna.

For all the ICRH systems, the transmission lines between the generators and the antenna(s) are pressurised with a gas (nitrogen or dry air) to increase the breakdown¹¹ voltage limits. The coaxial transmission lines' dimensions and characteristic impedance Z_0 [Ω] are chosen as a trade-off between power handling and attenuation requirements. The maximum power handling of the transmission line in steady-state operations is expressed by

$$P_{max} = \frac{V_{max}^2}{2Z_0} \quad (1.4)$$

where V_{max} is the breakdown voltage.

ICRH antennas are connected to the vacuum vessel of the device. Hence, parts¹² of the antennas share the vacuum conditions of the torus. Therefore, sealing barriers are required to separate the pressurised parts from the antenna vacuum parts. The sealing barrier is called *RF feed-through* or *RF window*. The RF feed-through of the ICRH systems is usually a coaxial-type feed-through made of a conical piece of ceramic (alumina) brazed or assembled with the inner and outer conductors of the transmission lines coming from the source. Although the RF feed-through ensures the tightness between the pressurised transmission lines and

11: The gas in its normal state is an insulator. Nevertheless, if a voltage is applied between the electrodes and is increased gradually, then there is a threshold value for which the gas will conduct. This gas' transition from an insulator to a conductor state is called "breakdown." The associated voltage for this transition is called the "breakdown voltage."

12: In particular, part of the sealing RF feed-through, the matching system, and the antenna front interface can work under vacuum conditions.

the antenna vacuum regions, it should remain transparent to the RF propagating waves by neither inducing wave reflections nor reducing the voltage stand-off capability.

1.3.3 Matching Systems

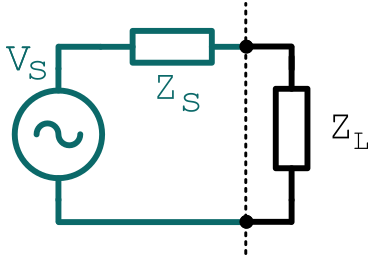


Figure 1.8: Matching a load impedance Z_L to a source of an internal impedance Z_S .

The antenna and the transmission lines' impedance are higher than the plasma-load impedance, leading to an output mismatch that causes noticeable RF power reflection, propagating back to the generators. This power reflection has detrimental effects on the sources: *i*) perturbation of the source impedance and signal's amplitude and phase, *ii*) damage to the RF source, *iii*) an increase in the dissipation losses, *iv*) an increase in the peak voltage on the transmission line causing a voltage breakdown, and *v*) failure of the RF feed-through (vacuum leak risk). Therefore, it is mandatory to use a matching system protecting the high-power RF sources from the reflected power.

However, matching the load impedance to the source impedance is not straightforward, as the load impedance depends on the device setup and the plasma, and it is time-variable. Indeed, the intrinsic plasma instabilities can induce strong and fast load variations. Therefore, the load properties are unpredictable, and in some cases, the system may be, to an extent, intrinsically unmatched. Hence, matching the source to the load impedance is required to maximise the RF power transmission's efficiency to the plasma. Matching systems should be, in many cases, adjustable (tuneable) to ensure some resilience to the plasma load variations [28].

[28] Hillairet (2023)

We recall that to match a given complex load impedance Z_L to an internal source impedance Z_S (Figure 1.8), *conjugate matching* (i.e., $Z_L = Z_S^*$) leads to the maximum power transfer to the load. In contrast, an *impedance matching* (i.e., $Z_L = Z_S$) minimises the reflected power back to the source [29].

[29] Pozar (2011)

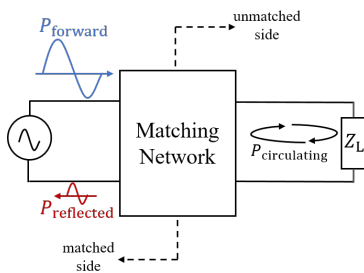


Figure 1.9: Matching network's effect representation.

In our case, the plasma load impedance is complex, and it is, therefore, unfeasible to achieve both matching techniques simultaneously. The matching is optimised in a way meeting the following requirements (Figure 1.9):

- ▶ Maximising the power transfer to the load;
- ▶ Minimising the power reflected toward the generator;
- ▶ Minimising the power losses on the transmission line;
- ▶ Ensuring good control of the signal's amplitude and phase.

The load matching is frequency-dependent for the plasma case, as the load impedance is complex and has a non-zero reactance component. Although perfect impedance matching can be achieved at a single frequency, this is not a big issue for high-power generators having a narrow-band frequency range. Moreover, the matching systems are tuneable as the generator's frequency is also tuneable for the ICRH systems. Therefore, a re-configurable matching network is required to cover the frequency operation range of the ICRH antenna system.

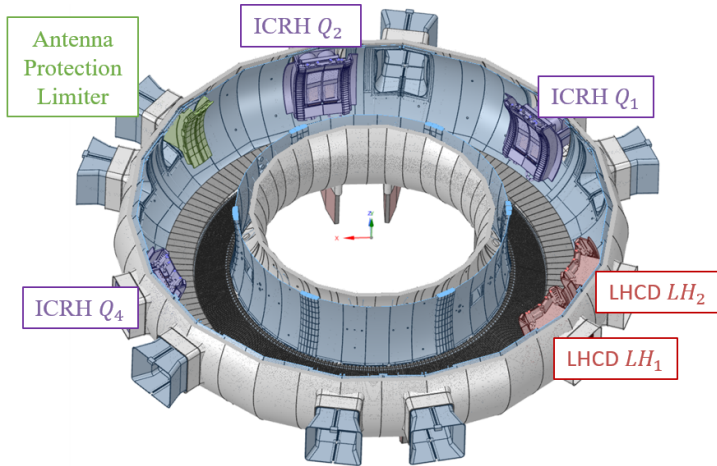


Figure 1.10: An illustration of the vacuum vessel of the tokamak WEST, with the different RF heating systems' employment: in purple three ion cyclotron resonance heating antennas (ICRH), in red two lower hybrid current drive (LHCD) antennas, and in green the moveable antenna protection limiter.

1.3.4 Antennas

The ICRH antennas face the plasma and must, therefore, withstand harsh operating conditions such as:

- ▶ High vacuum compatibility ($< 10^{-4}$ Pa);
- ▶ High temperature (above $200\text{ }^{\circ}\text{C}$);
- ▶ High heat fluxes on plasma facing components (up to few MW/m^2);
- ▶ High RF power (megawatts range);
- ▶ Large electro-mechanical forces (MN).

The large heat fluxes from the plasma and the RF losses impose an active cooling method for the antennas to sustain continuous operations.

In the next section, we describe the WEST RF heating systems, followed by a detailed overview of the ICRH systems of the tokamak WEST.

1.4 Overview of the Tokamak WEST

The tokamak WEST, derived from "tungsten (W) environment in steady-state tokamak," located in Cadarache, France, is an X-point divertor device equipped with actively cooled tungsten plasma-facing units. Among many objectives, its main goal is to test an ITER-like actively cooled tungsten divertor with realistic load-case conditions and heat fluxes of 10 MW m^{-2} for thousands of seconds, and 20 MW m^{-2} for tens of seconds.

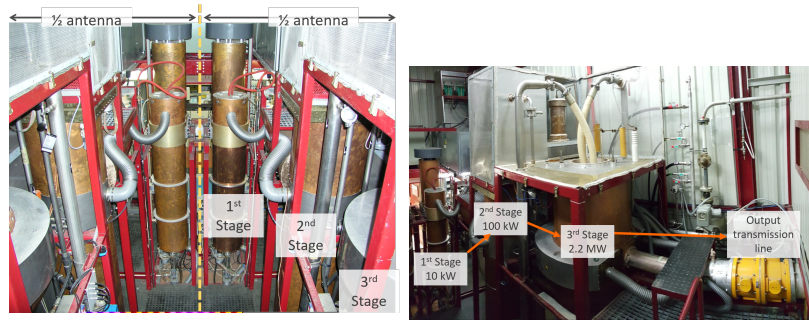
On the tokamak WEST, as of 2023, two RF heating systems are available:

- ▶ Three identical ion cyclotron resonance heating (ICRH) antennas operating in the frequency range $[40 - 78]$ MHz;
- ▶ Two lower hybrid current-drive (LHCD) antennas operating at 3.7 GHz.

An illustration of the vacuum vessel of the tokamak WEST, along with the locations of the different heating systems, is given in Figure 1.10.

In this manuscript, we are only interested in the ICRH antennas of WEST.

Figure 1.11: Pictures of the WEST ICRH plant. The plant consists of six generators (two per antenna), each made of three amplification stages.



1.4.1 WEST ICRH Antennas' Description

The WEST ICRH system is made of three antennas. Each antenna is fed by two generators (one generator per antenna side). The notion of the antenna side is explained at the end of this section.

The six generators are identical, where each consists of a synthesizer, a modulator, a solid-state wide-band amplifier, and a three-stage tetrode amplifier. The plant is operated in the [40 – 78] MHz frequency range, in particular, [46 – 65] MHz to fit the main WEST ICRH scheme consisting of hydrogen-minority in deuterium plasma [30–33]. For a 30 s pulse duration, the power delivered by each generator can reach 1.5 MW. In contrast, for a 1000 s pulse duration, the power is reduced to 500 kW [34]. The WEST ICRH power plant is illustrated in Figure 1.11 with the different amplification stages and powers.

The feeding transmission lines transporting the electromagnetic power consist of Spinner 30 Ω coaxial transmission lines, shown in Figure 1.12, where the inner and outer conductors' diameters are $\phi_i/\phi_o = 140/230$ mm. The inner conductor is made of 2 mm thick copper (Cu), while the outer conductor is of 5 mm thick aluminium (Al). These transmission lines are nitrogen pressurised.

From the generators' side, following the pressurised transmission lines is the sealing RF feed-through barrier, ensuring the tightness between the nitrogen-pressurised transmission lines and the under-vacuum components. On WEST, each sealing barrier is a coaxial feed-through made of a conical ceramic piece, illustrated in Figure 1.13.

Next, we describe the matching system components and the antennas' front faces following the sealing barriers that are, therefore, under the vacuum conditions of the WEST torus. A matching system, one per ICRH antenna side, enables matching the antenna side's impedance to the 30 Ω feeding transmission lines to reduce the reflected power to the generators and increase the coupled power to the plasma. An illustration of the assembled under-vacuum components' geometries — including the RF feed-through windows — for one WEST ICRH antenna is shown in Figure 1.14.

The matching system is a two-stage matching network. The first stage is a passive two-stage quarter-wavelength impedance transformer [1, 30]. The second stage is a tuneable internal conjugate-T [35], composed of tuneable capacitors connected in parallel via a T-junction (referred to as "bridge" herein).

[30] Helou et al. (2015)

[31] Hillairet et al. (2015)

[32] Bernard et al. (2017)

[33] Helou et al. (2020)

[34] Hillairet et al. (2021)



Figure 1.12: Picture of a rigid Spinner coaxial transmission line.



Figure 1.13: Picture of the ceramic's RF feed-through of the WEST ICRH antennas.

[1] Bernard et al. (2019)

[30] Helou et al. (2015)

[35] Bosia (2003)

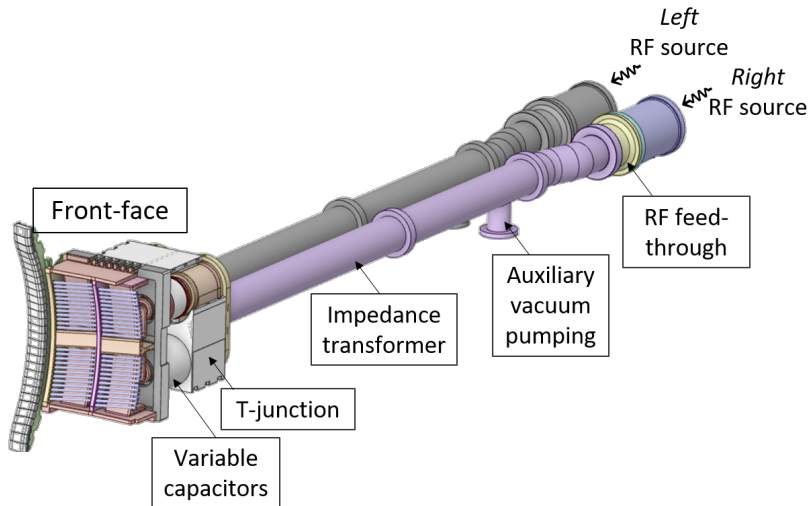


Figure 1.14: An illustration of the different components of one ICRH antenna used on the tokamak WEST. Each side has its own high-power generator.

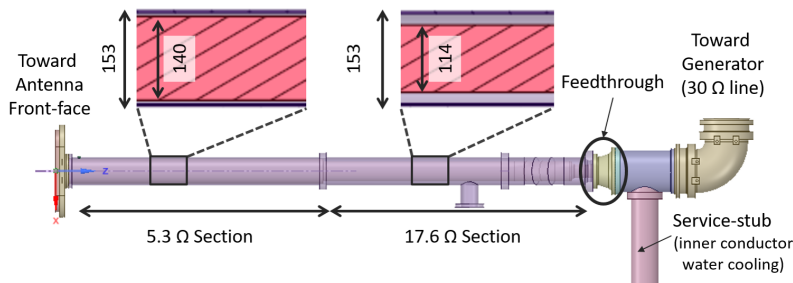


Figure 1.15: An illustration of the two-stage impedance transformer structure showing its dimensions.

The impedance transformer is connected to the $30\ \Omega$ feeding transmission lines via the RF feed-through. It is, therefore, designed to match the impedance of the RF feed-through window to the input port's impedance of the T-junction on a broad range of frequencies.

It is made of two quarter-wavelength stages. The first stage is connected to the RF feed-through and has a $17.4\ \Omega$ characteristic impedance, corresponding to inner and outer conductors of diameters 114 mm, and 153 mm respectively. The second stage of the impedance transformer is connected to the T-junction's input port. It has a $5.5\ \Omega$ characteristic impedance, corresponding to inner and outer conductors of diameters 140 mm, and 153 mm respectively.

The two stages of the impedance transformer are connected via a tapered geometry, ensuring the passage from $17.4\ \Omega$ to $5.5\ \Omega$. Similarly, the impedance of the RF feed-through is not $17.4\ \Omega$. It is, therefore, connected to the first stage of the impedance transformer via transition transmission line geometry. The structure of the two-stage impedance transformer is given in Figure 1.15.

The T-junction, the second stage of the matching network, is a three ports component with the input port connected to the matching network's impedance transformer. The output ports connect, in parallel, two matching capacitors — tuning capacitors. The T-junction inner conductor, vacuum, and outer conductor are shown in Figure 1.16.

The tuneable capacitors are connected to two poloidal straps¹³ from their back end. Once properly tuned, the tuning capacitors make the structure resonant at a particular frequency. The tuneable vacuum capacitors of

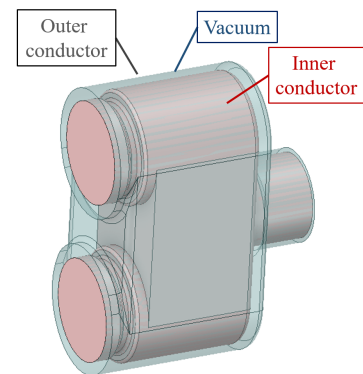
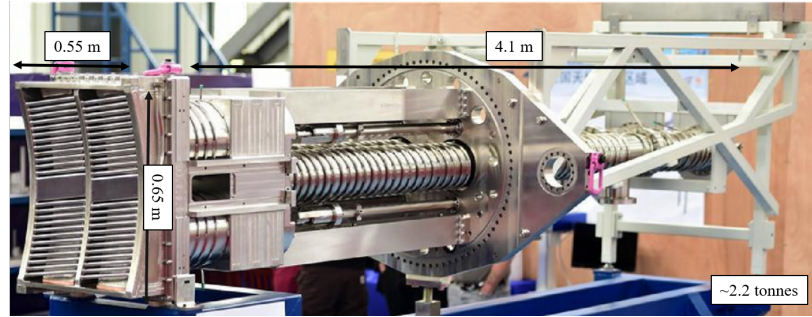


Figure 1.16: An illustration of the T-junction structure showing its inner conductor and outer conductor.

13: The straps are the radiating elements facing the plasma.

Figure 1.17: Picture of one WEST ICRH antenna during its assembly, with its mass and main dimensions.



WEST ICRH antennas are of pF precision, with capacitance ranging from 15 pF to 150 pF.

Each WEST ICRH antenna's front face — connecting the antenna sides — is a phased array of loop radiators, denoted *straps*. Each antenna consists of two resonant-double-loops, as shown in Figure 1.17. The resonant-double-loop scheme was developed in the 1980s [36, 37], where a common feed-point feeds two adjacent straps in the poloidal (vertical) direction. In this configuration, the straps are excited with nearly uniform and in-phase fields.

The straps of each antenna are electrically small, in both poloidal and toroidal directions, with dimensions less than the quarter wavelength. The impedance of each of the straps reads $Z_{\text{strap}} = R_{\text{strap}} + jX_{\text{strap}}$, where R_{strap} is the strap's resistance, which is also known as the *coupling resistance* R_c ¹⁴ and is in the order of few ohms. X_{strap} is the inductance strap's reactance and is of the order of a few tens of ohms.

In addition, the front face of each WEST ICRH antenna is protected by a Faraday screen with a 7° tilt angle, which is close to the total magnetic field lines' angle seen by the antennas.

An illustration of one resonant-double-loop of a WEST ICRH antenna — one antenna side — is given in Figure 1.18. The Faraday screen of the antenna is represented in black, the two adjacent straps of the antenna side are shown in red, and the in-series vacuum matching capacitors connected to each of the straps of the antenna side are illustrated in blue.

Arranging different resonant-double-loops in the toroidal (horizontal) direction creates an antenna array. In the case of WEST ICRH antennas, two resonant-double-loops are toroidally arranged and fed by two different generators to form a single ICRH antenna.

Therefore, each WEST ICRH antenna is a four-straps antenna (2 poloidal × 2 toroidal), composed of two toroidal sides that we will refer to as *left* and *right* sides (as seen from the exterior of the torus), each fed by a high power source, and constituted of one RF feed-through, one impedance transformer, one T-junction, and two parallel tuneable capacitors.

WEST ICRH antennas' surfaces, in particular, the Faraday screens, antenna boxes, straps, and inner and outer conductors, are made of silver-coated stainless steel with 10 μm of nickel (Ni) and around 50 μm of silver (Ag) — more than two times the skin depth within the frequency range of interest.

[36] Owens et al. (1985)

[37] Hoffman et al. (1987)

[28] Hillairet (2023)

14: The *coupling or loading resistance* R_c is a figure of merit used to quantify the coupling and is defined as the ratio of the time-averaged radiated power to the integral, over the strap's arc length, of the radio-frequency current density [28].

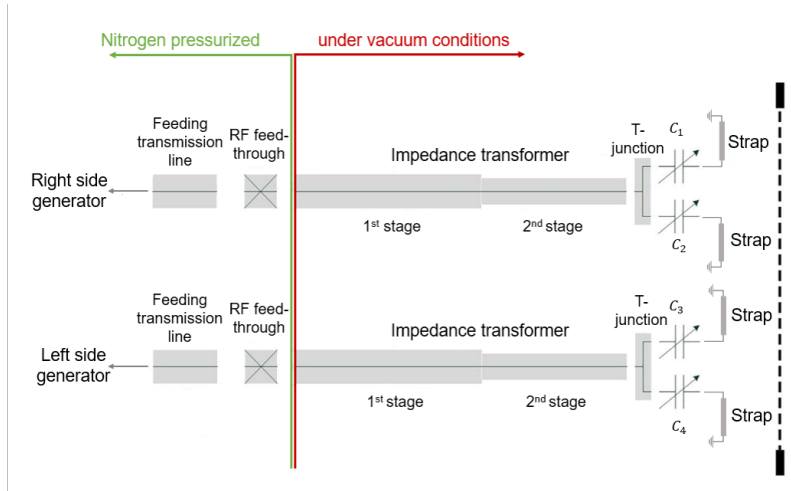


Figure 1.19: A simplified circuit schematic for one WEST ICRH antenna constituted of two sides. Each side is constituted of a radio-frequency generator, feeding transmission lines, RF feed-through, matching system — T-junction, impedance transformer, and two capacitors. The two sides are joint via a Faraday screen — plasma front interface.

A circuitual representation of one WEST ICRH antenna is given in Figure 1.19.

1.4.2 WEST ICRH Main Diagnostic Systems

The rears of the two impedance transformers of one ICRH antenna are connected to one vacuum auxiliary pumping system, which aims to improve the vacuum conditions inside the antenna. Each impedance transformer of one antenna side is equipped with a pressure gauge (two pressure gauges per ICRH antenna) for pressure monitoring during operation. The auxiliary pumping system location is shown in Figure 1.14. Furthermore, the straps' voltages are measured using probes installed between the capacitors and straps.

Several arc detection systems are available to protect the WEST ICRH system. Once an arc is detected, both RF generators feeding an antenna are tripped automatically within a $10 \mu\text{s}$ time scale. The power is re-applied within 30 to 50 ms after the trip, depending on the triggered detection system. The generator is switched off once a predefined number of power trips is registered in a time interval. We list herein the different available arc detection systems [33]:

- ▶ The forward and reflected powers are continuously monitored using bi-directional couplers installed at the rear of the antenna and the generator plant. And to avoid voltage or current overshoots during plasma disruptions, the forward RF power is feedback-controlled — with a fast response time of the order of $10 \mu\text{s}$ — to keep voltages and currents below their maximum safety thresholds [30], set to 28 kV and 915 A respectively, as well as limiting the maximum electric field inside the antenna to less than 2 MV m^{-1} .
- ▶ The sub-harmonic arc detection (SHAD) system [38], in a frequency band lower than the generators' frequency. As the arc is a fast, non-linear transient event, it is a broad-spectrum event with harmonics below and above the generators' frequency. SHAD are pass-band filters monitoring a frequency spectrum below the RF source frequency. This arc detection system is connected to the bi-directional coupler installed at the generator's output and is operated in the frequency range [3 – 35] MHz. Once a detector's measured signal

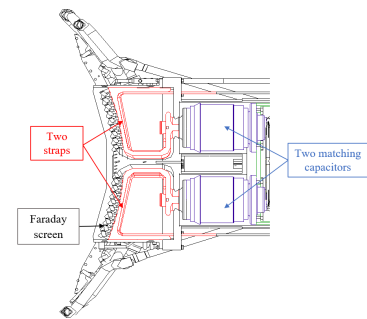


Figure 1.18: A schematic cut illustration of one resonant-double-loop of the WEST ICRH antenna. In black the Faraday screen of the antenna, in red the two poloidally-adjacent straps of the resonant-double-loop, and in blue the in-series matching capacitors connected to each of the straps. Each WEST ICRH antenna is composed of two toroidally-adjacent resonant-double-loops.

[33] Helou et al. (2020)

[30] Helou et al. (2015)

is above a predefined threshold, an order's signal is triggered to shut down the RF high-power source, with a response time of a few microseconds.

[38] Berger-By et al. (2007)

- ▶ The optical arc detection system [31], consisting of six optical fibres per ICRH antenna, protects the low-impedance regions around the T-junctions. This system is operated in the visible spectrum and is associated with fast photo-detectors.

1.4.3 WEST ICRH Operational Conditions

The toroidal phase between the *left* and *right* sides of each antenna is set by the plasma control system, with mainly two configurations: *dipole phasing* for a 180° phase shift between sides (default configuration) and *monopole phasing* for a 0° phase shift between sides. The frequency of the left side generator is the reference, and the right side generator's frequency is modulated using a proportional-integral-derivative (PID) controller while maintaining the requested phase change with a response time of approximately $50 \mu\text{s}$. Furthermore, the ICRH antenna's matching is achieved by tuning its capacitors so that the two parallel branches connecting the capacitors of one side of the antenna have complex conjugate admittance values.

[31] Hillairet et al. (2015)

The WEST ICRH antennas are characterised by a high-power continuous-wave (CW) operation and a load-resilience capability for coupling on H-mode plasma operation with induced edge localised modes (ELMs) while ensuring a voltage standing wave ratio (VSWR) that does not exceed 2:1 at the generators [31]. Moreover, all the ICRH antennas are moveable in the radial direction of the vacuum vessel for power-coupling and thermal load-handling optimisation.

[31] Hillairet et al. (2015)

While the load-tolerance property of the antennas is achieved by the previously detailed design itself, the CW operation requires actively water-cooling all the antenna's components, using two distinct water loops [32, 34].

The first one is the standard WEST high temperature/high-pressure loop ($70^\circ\text{C}/30\text{ bar}$ during plasma operation) used to cool the Faraday screens, housing boxes, and the outer conductors. However, a second loop is required, as the capacitors' maximum rating temperature is 70°C . The latter is a low temperature/low-pressure ($20^\circ\text{C}/7\text{ bar}$) loop used for the straps, capacitors, and inner conductors.

As a first phase before any experimental campaign, the tokamak WEST and its associated heating systems are subject to a baking phase. The high-temperature cooling loop's temperature is increased to the WEST baking temperature (200°C) for a few days. However, the low-temperature cooling loop is kept unchanged to account for the capacitors' temperature limit.

Before using the ICRH system on plasma, a preliminary under-vacuum RF conditioning phase is performed during the tokamak commissioning. During RF conditioning under vacuum, each side of the antenna is powered separately on short pulses up to 20 ms until reaching the antenna voltage limit ($< 28\text{ kV}$). It should be noted that a low power ranging between $[5 - 20]\text{ kW}$ is sufficient to raise the voltages and currents to

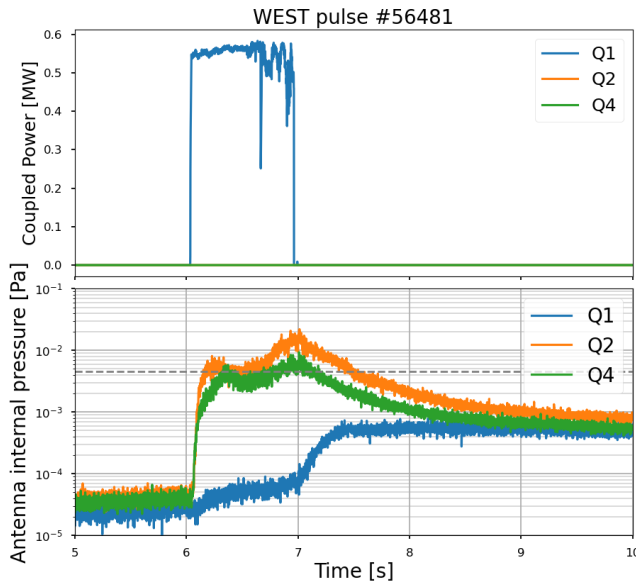


Figure 1.20: An example demonstrating the pressure rise in the off-mode antennas (Q_2 and Q_4) on plasma when only one antenna is on (Q_1 , operating with 0.55 MW). In the top figure, the antennas' coupled powers are plotted versus time. In the bottom figure, the antennas' internal pressure is plotted versus time, and the dashed gray line represents the pressure rise limit (p_{th}) beyond which the (re-)application of RF power is prohibited for security reasons.

their maximum safety thresholds due to the low coupling of the antenna on vacuum loading (no plasma).

Once the nominal voltage is reached, both sides are powered simultaneously. During this phase, the vacuum pressure is monitored for antenna-outgassing tracking. It is observed that pulse after pulse, the outgassing decreases, indicating that the RF surfaces are supposed to become cleaner [1]. The pulse duration is, therefore, progressively increased until reaching a pulse duration of 5 s of uninterrupted forward power at 28 kV. The antennas are then ready to be operated on plasma experiments.

At this stage, it is worth mentioning that a cross-talk exists between both sides of one ICRH antenna and also between the different antennas, depending on the experimental conditions.

1.5 Pressure Rise Problematic Observation on WEST ICRH Antennas

Although the three WEST ICRH antennas are operated at slightly different frequencies, cross-talk between antennas is evidenced, as shown herein. During the experimental campaigns on WEST, the following observation has been made on all three ICRH antennas: if one ICRH antenna is powered with the remaining ICRH antennas being off, a pressure increase is observed in the non-powered antennas. If the pressure exceeds the predefined safety threshold $p_{th} = 4.5 \times 10^{-3}$ Pa [1], a safety interlock prohibits the (re-)application of the RF power to avoid generating and sustaining an RF-induced plasma inside the antennas, which affects the operation of the ICRH system. Therefore, this phenomenon can complicate or even stop the antennas' nominal operations. A pressure rise example is shown in Figure 1.20, where a single ICRH antenna is operated (Q_1), and the remaining two are off (Q_2 and Q_4). When the antenna Q_1 couples its power to the plasma, the pressure increases inside

[32] Bernard et al. (2017)

[34] Hillairet et al. (2021)

[1] Bernard et al. (2019)

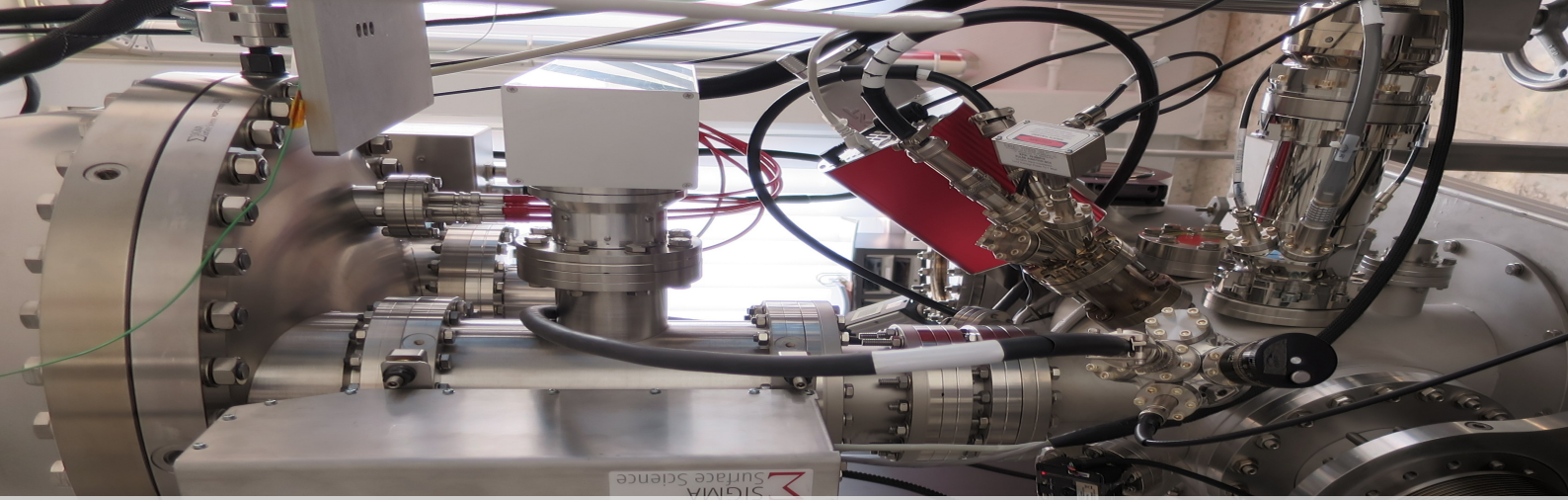
the two powered-off antennas (Q_2 and Q_4). This pressure is sufficient to prohibit Q_2 and Q_4 's use, as it is above the predefined security threshold p_{th} .

[1] Bernard et al. (2019)

One possible cause explaining these observations is the multipactor phenomenon, a resonant RF vacuum discharge [2], induced by antenna cross-talking. A possible worst-case consequence is the metallisation of the capacitors' ceramics or the RF feed-through window if multipactor-induced plasma is sustained in its vicinity. The work objective is to determine whether multipactor is an explanation for the pressure rise occurrence.

1.6 Chapter Summary

After introducing the reader to the geometrical aspects and characteristics of the antenna type of interest in the framework of plasma heating, we illustrated the pressure rise problem observed during the experimental campaigns. This observation could be associated with a phenomenon called "multipactor." As we will see in the following chapters, the multipactor phenomenon highly depends on material properties. Therefore, before explaining the phenomenon, along with its conditions and consequences, the characterisation of the material properties of the antenna is crucial.



2 Material Electron Emission Characterisation

A truth is to be known always, and to be uttered sometimes.

Gibran Khalil Gibran

In this chapter, we provide the basic concepts of the techniques used for the surface characterisation of the WEST ICRH representative samples under its nominal operational conditions: electron emission spectrum's measurements (Section 2.1), total electron emission yield (TEEY) measurements (Section 2.2), and X-ray-induced photoelectron spectroscopy (XPS) technique (Section 2.3). Then, we describe the experimental facility available at the ONERA/DPHY laboratory, which provides the needed surface characterisation techniques, before detailing our experiment's approach for sample preparation, baking, and conditioning procedures and discussing the obtained results (Section 2.4).

2.1 Electron Emission

Bombarding a surface with an electron flux triggers a cascade of phenomena at its surface, eventually leading to the emission of electrons. The interactions between the electrons and the material are various and result in several types of emitted electrons, which are distinguishable by their energy distribution [39].

When an incident electron beam, generally referred to as primary electrons (PEs), impinges on a surface, the emission of electrons may be observed. Under certain circumstances, the number of emitted electrons exceeds the number of incident electrons, indicating that electrons' bombardment liberates electrons from the solid [40].

Three types of emitted electrons [41, 42], distinguished according to the mechanism of energy transfer from the incident electrons, are identified: elastic back-scattered electrons (EBEs), inelastic back-scattered electrons (IBEs), and secondary electrons (SEs).

EBEs are primary electrons that have not lost energy and are reflected elastically. The remainder of the primary electrons penetrate the solid. IBEs are primary electrons that have penetrated the sample and partially

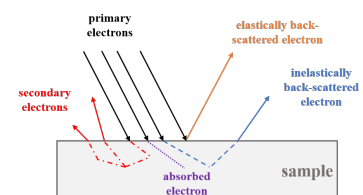


Figure 2.1: Possible emission mechanisms observed when impacting a sample with primary electron flow.

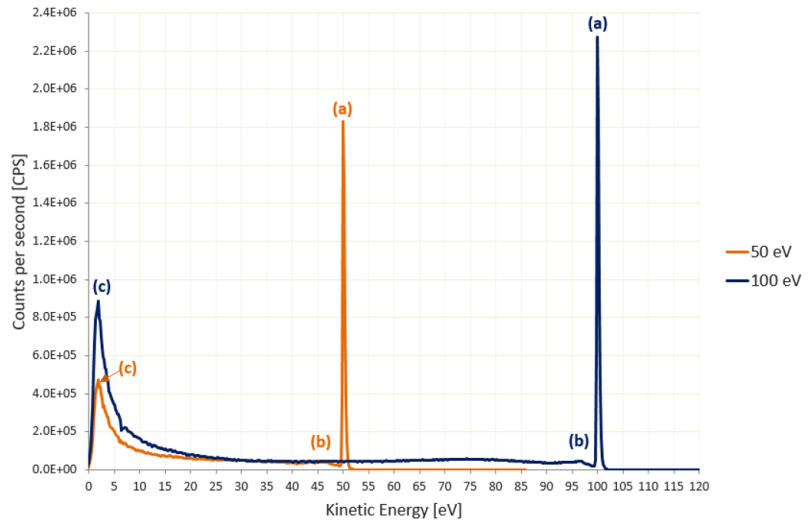
[39] Rudberg (1936)

[40] Bruining (1954)

[41] Dekker (1958)

[42] Dekker (1981)

Figure 2.2: Energy distribution of emitted electrons for a stainless steel silver-coated sample, maintained at 70 °C and baked at 200 °C for three days, subjected to incident electron flows of energy 50 eV, and 100 eV, represented respectively in orange and blue. The y -coordinate corresponds to the number of electrons per second [Counts Per Second]. The peaks (a), (b), and (c) correspond respectively to elastically reflected electrons, in-elastically re-diffused electrons, and the most probable energy of secondaries. These measurements are realised in the framework of this thesis at ONERA/D-PHY.



lost their energy inside the material before escaping from the surface by *Rutherford* scattering. Other primary electrons that have entered the solid lose their energy by lattice electrons' excitement into higher energy levels. The excited electrons that move toward the surface and escape from the material are called "true secondary electrons" (SEs) [11, 42]. Furthermore, there is a possibility for the electrons to be absorbed by the material without causing any emission.

[11] Sounas (2015)

[42] Dekker (1981)

It is common to refer to all the electrons emitted by electrons' beam surface bombardment by "secondary electrons." The various emission mechanisms are represented in Figure 2.1.

[43] Simon et al. (1968)

[44] Kanaya et al. (1972)

[45] Farnsworth (1925)

[46] Willis et al. (1973)

[47] Koshikawa et al. (1974)

[48] Ding et al. (2001)

[49] Lin et al. (2005)

[39] Rudberg (1936)

[50] Chung et al. (1974)

This phenomenon has been studied theoretically [43, 44], experimentally [45, 46], and numerically [47–49]. It depends on the electron impact energy, the angle of incidence, the surface material properties and conditions, and the presence (or not) of a magnetic field.

2.1.1 Energy Distribution of Emitted Electrons

The energy distribution of the emitted electrons should be known to characterise the electron emission. This characteristic distribution function has been investigated both experimentally [39] and theoretically [50].

Experimentally, the emitted electrons' energy distribution could be measured for a fixed incident energy. Figure 2.2 illustrates the energy distribution for a WEST ICRH representative stainless-steel silver coated sample, maintained at 70 °C after being baked at 200 °C for approximately three days to mimic the WEST operational conditions. The primaries' incident energies, for which the measurements are made at normal incidence, are 50 eV, and 100 eV represented respectively in orange and blue.

The energy distribution can be analysed as composed of three main types of electrons. The first peak (a) corresponds to the elastic back-scattered electrons, being reflected primary electrons without energy loss. These electrons have a kinetic energy equal to the incident energy of primary electrons. Therefore, they are observed at 50 eV and 100 eV for the orange and blue curves, respectively. The second peak (b) represents the

inelastic back-scattered electrons, which are reflected primary electrons with kinetic energy slightly less than that of primary electrons. The third peak (*c*) is that of low-energy secondary electrons emitted from the sample at energies less than the conventional energy barrier of 50 eV. Usually, this convention separates the secondary electrons from the inelastic back-scattered electrons, as it is impossible to distinguish sharply between them. Furthermore, the conventional energy barrier is correct for high incident energies, as for low incident energies, the different emission mechanisms' contributions tend to overlap, leading to difficulties distinguishing the various mechanisms [51].

Furthermore, it should be mentioned that the energy distribution of the secondary electrons is independent of the primary electrons' beam energy [42], leading to the possibility of being formulated independently. Two energy distribution models are discussed next: *Chung and Everhart*, and *Maxwell-Boltzmann's* distribution.

2.1.1.1 Chung and Everhart's energy distribution

Chung and Everhart have proposed a simple analytical and physical equation, modelling the energy distribution of low-energy — below 50 eV — secondary electrons emitted from a surface by electron bombardment [50]. They used an analytical expression for the energy-dependent mean free path of the excited electrons, which leads to good agreement with experimentally obtained energy distributions. This distribution, represented in Figure 2.3, is independent of primary electrons' energy and is a function of the effective work function. It is defined as follows

$$f(E_{\text{sec}}) \approx \frac{E_{\text{sec}}}{(E_{\text{sec}} + \Phi)^4} \quad (2.1)$$

where E_{sec} is the secondary emitted electrons' energy, and Φ is the effective material's work function. For metals, $\Phi = W_f$, where W_f is the metal's *work function*, which is the minimum energy that an electron at rest must be provided to be emitted into the vacuum, expressed in [eV]. This value is, in general, between 3 eV and 5 eV for most metals. For dielectrics, $\Phi = \chi + E_g$, where χ is the electron affinity, and E_g is the band gap energy. For most dielectrics, $\chi \approx 1$ eV and E_g is within the range [1 – 10] eV.

The function, $f(E_{\text{sec}})$ of (2.1), has a maximum at an emitted energy of $\Phi/3$ (the most probable energy), and a mathematical expectation $\mathbb{E}[f(E_{\text{sec}})] = 2\Phi$.

2.1.1.2 Maxwell-Boltzmann's energy distribution

The *Maxwell-Boltzmann* distribution can be used to model the energy distribution of the secondary emitted electrons. This distribution is referred to as Maxwellian distribution. It is defined by the following expression [39]

$$f(E_{\text{sec}}, T_e) = \frac{2}{\sqrt{\pi}} \sqrt{\frac{E_{\text{sec}}}{T_e}} e^{-\frac{E_{\text{sec}}}{T_e}} \quad (2.2)$$

[51] Gineste et al. (2014)

[42] Dekker (1981)

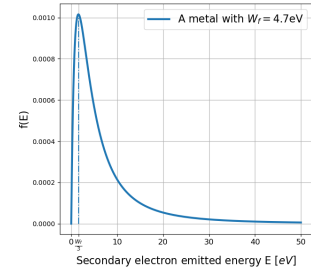


Figure 2.3: Energy distribution for secondary emitted electrons, for a metal sample having a work function of $W_f = 4.7$ eV using the *Chung and Everhart's* proposed model.

[50] Chung et al. (1974)

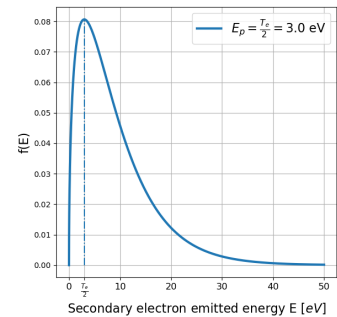


Figure 2.4: Energy distribution for secondary emitted electrons, for a metal sample using the *Maxwell-Boltzmann's* model for a most probable energy $E_p = 3.0$ eV.

[39] Rudberg (1936)

where E_{sec} is the energy of emitted secondary electrons expressed in [eV], and T_e is the electronic temperature expressed in [eV] by $T_e = k_B T$, k_B being the Boltzmann constant, and T the temperature. This distribution, illustrated in Figure 2.4, has a most probable energy $E_p = T_e/2$.

2.1.2 Angle Distribution of Emitted Electrons

2.1.2.1 Angle distribution of secondary electrons

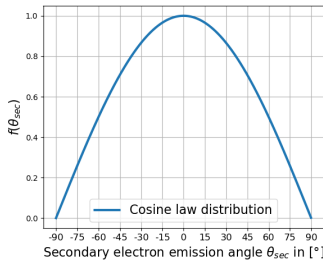


Figure 2.5: The cosine angular distribution function of the secondary emitted electrons.

[40] Bruining (1954)

[52] Jonker (1951)

Secondary electrons are emitted with a spread in angle relative to the normal of the surface. Thus, an electron with 0° emission angle is emitted normally to the surface. It has been shown that the low-energy electrons are emitted with an angular distribution which can be approximated by *Lambert's cosine law* for polycrystalline or amorphous materials, also known as the cosine emission law [40, 52]. This angle distribution, shown in Figure 2.5, is independent of the incidence angle of the primary electrons and is expressed as

$$f(\theta_{\text{sec}}) = \cos(\theta_{\text{sec}}). \quad (2.3)$$

This distribution implies that the secondary electrons are emitted most probably with an angle normal to the surface and almost impossibly emitted at grazing angles.

2.1.2.2 Angle distribution of back-scattered electrons

The elastically and in-elastically reflected electrons can be emitted in all directions but with an angular distribution that depends on the impact angle. Contrary to secondary electrons, their angular distribution is more complicated to model and is generally taken as a mirror reflection direction [40, 52].

[40] Bruining (1954)

[52] Jonker (1951)

2.2 Electron Emission Yield

2.2.1 Definition

The total electron emission yield (TEEY) coefficient, referred to as σ , is defined as the average number of back-scattered and secondary electrons over the number of incident electrons on a material surface. This electron emission yield is represented in a curve as a function of the primary electron impact energy. This curve, of a general shape depicted in Figure 2.7, is generated for one angle of incidence of primary electrons. This qualitative shape is valid for most metals and dielectrics. In general, dielectrics have higher yields than metallic surfaces.

The emission phenomenon is described by the results of the following three steps: *i)* excitation of secondary electrons within the material via energy transfer from primary electrons, *ii)* their transport to the surface attenuated by collisions, and *iii)* those with enough energy escape to the vacuum¹ by overcoming the vacuum barrier being the work function for metals, and the sum of the band gap and electron affinity for insulators.

1: The escaping electrons are of much lower energy than primary electrons.

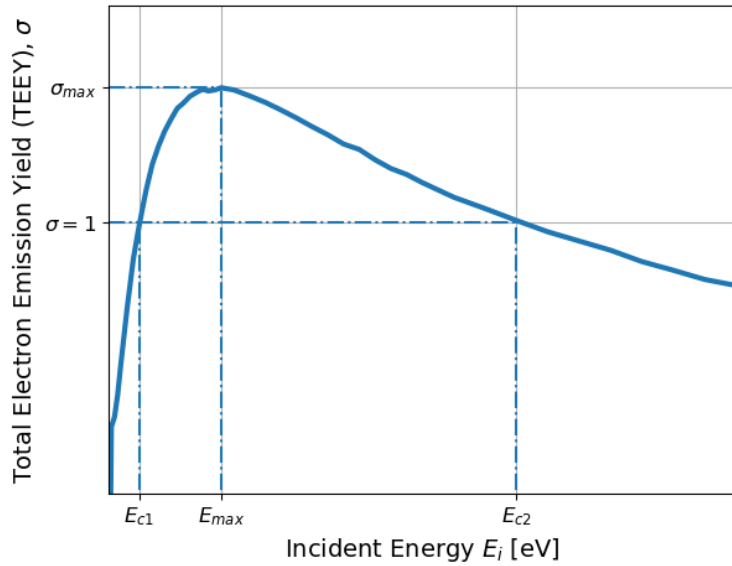


Figure 2.7: The total electron emission yield's general shape (TEEY, σ) as a function of the incident primary energy.

Moreover, the electron emission yield is related to the bulk material properties, surface properties such as surface barrier potential, material density, and conductivity, as well as the surface state and history like the presence or not of contaminants, adsorbed atoms, or surface oxidation.

In addition, the electron emission yield was found to be dependent on the surface morphology, such as its smoothness or roughness. Indeed, an electron escaping from a smooth surface is released directly into the vacuum. However, an electron escaping from a rough surface may be subject to recollection by surrounding obstacles. Therefore, surface roughness tends to decrease the electron emission mechanisms by increasing the probability of electron re-absorption because of neighbouring peaks on the surface (Figure 2.6). If the surface roughness is high enough, most electrons, emitted with a cosine distribution, are scattered within surface peaks and, therefore, will be re-absorbed.

For each TEEY curve, the two energies corresponding to a TEEY value equal to one — of particular interest for our studies — should be well defined. These energies are called the first E_{c1} , and second E_{c2} crossover energies. At E_{c1} and E_{c2} , the number of emitted electrons is equal to that of incident electrons, whereas between them, the yield is greater than one, *i.e.*, the mean number of emitted electrons is larger than the number of primary electrons.

At impact energies lower than E_{c1} , the electrons penetrate the sample and do not have sufficient energy to excite the emission of secondary electrons. There is an absorption process, and the TEEY is less than one. However, continuously increasing the primary electrons' energy increases the number of emitted secondary electrons while simultaneously increasing the depth at which secondary electrons are released.

After the first crossover energy, continuously increasing the primary electrons' beam energy increases the TEEY as electrons transfer energy to secondary electrons that are excited and released by their turn until reaching a maximum value σ_{max} corresponding to the incident energy

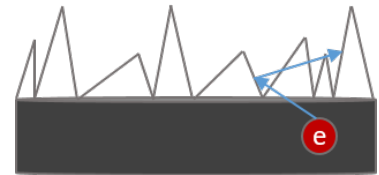


Figure 2.6: Electron re-collection by a neighbouring peak in the case of a rough surface.

[40] Bruining (1954)

[41] Dekker (1958)

[53] Vaughan (1989)

[44] Kanaya et al. (1972)

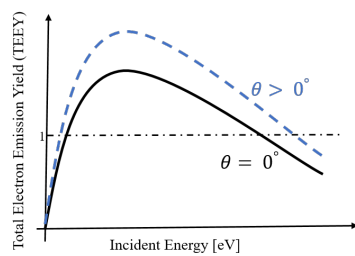


Figure 2.8: Illustration of the total electron emission yield (TEEY) curves for different angle of incidence for primary electrons.

[45] Farnsworth (1925)

[54] Bruining (1936)

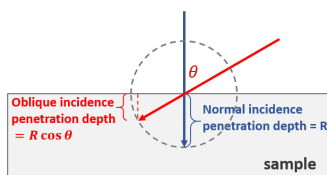


Figure 2.9: The penetration depth R of a normal incident electron, and the penetration depth $R \cos \theta$ of an oblique incident electron with an angle θ with respect to the normal to the surface.

[21] Becerra (2007)

E_{\max} , where we have the maximal release of electrons. Beyond E_{\max} , the primary electrons penetrate more deeply into the material, which increases the probability of loss by absorption [40]. Consequently, the likelihood of having more excited secondaries not close enough to the surface to escape from it increases. This results in a monotonous decrease in the TEEY.

Due to the universal shape of TEEY curves, the emission properties of any materials are usually described in the literature by the values of E_{c1} , E_{c2} , E_{\max} , and σ_{\max} .

For electron multiplication to be possible, the electron emission yield must be greater than one for a significant number of impacts. Therefore, its associated impact energy must lie between the two cross-over energies.

TEEY curves like the one represented in Figure 2.7 have been obtained experimentally [41], and derived empirically [53] and analytically [44] with the aid of different available analytical models.

2.2.2 TEEY Incident Angle Dependence

It has been observed that the TEEY increases when varying the angle of incidence of primary electrons onto the surface from normal angle incidence to grazing angle, especially at high impact energies. This effect is illustrated in Figure 2.8. For the oblique incidence case, the TEEY increase can be explained by a smaller electron penetration depth. Indeed, for oblique incidence, the penetration depth is $R \cos \theta$, while for the normal to the surface incidence case, the penetration depth is R . The smaller electron penetration depth, illustrated in Figure 2.9, allows the penetrated electrons to interact with the electrons closer to the surface and release more electrons. This dependence was observed both experimentally [45] and theoretically [54].

The latter observation corresponds to a material sample of a smooth surface, as the angle of incidence is not well defined for a rough surface such that the effect of changing the angle of incidence is hardly noticeable.

In external magnetic fields' presence, the likelihood of an oblique primary incidence increases [21]. Therefore, the oblique incidence should be accounted for in such cases.

2.2.3 TEEY Measurements Techniques

Two measurements techniques for TEEY have been widely used in laboratories: *i*) the *collector system method* which is a one-step TEEY measurement technique represented in Figure 2.10, and *ii*) the *sample bias method* which is a two-steps TEEY measurement technique, illustrated in Figure 2.11.

In the *collector system method*, the sample is negatively biased and impacted by a primary electron flow having a current I_p . The surface's emitted electrons are repelled and then collected by the positively-biased collector. In this scheme, the emitted electrons' current I_e and the sample to ground current I_{sg} are measured simultaneously for a given incident energy of primaries E_i .

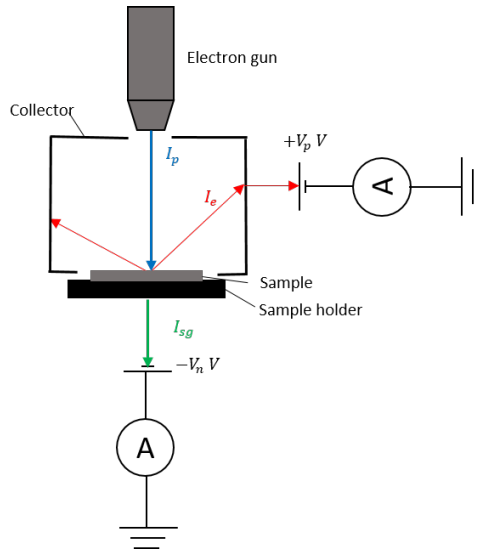


Figure 2.10: The TEEY measurement principle using the collector system. $+V_p$ refers to the positive bias, and $-V_n$ refers to the negative bias.

The primary current I_p , is calculated directly from *Kirchhoff's* current law

$$I_p = I_e + I_{sg}, \quad (2.4)$$

and the TEEY for the impact energy E_i is given by the expression

$$\sigma(E_i) = \frac{I_e(E_i)}{I_e(E_i) + I_{sg}(E_i)}. \quad (2.5)$$

In the *sample bias method*, first, the sample is positively biased so that the emitted electrons are trapped. Thus, the measured current, corresponding to the primary incident energy E_i , is the primary current I_p . In the second step, the sample polarity is switched to a negative bias voltage while keeping the same primaries' incident energy, and the measured current corresponds to I_{sg} . Hence, the emitted electrons' current is given by the difference of the measured currents of the two steps ($I_e = I_p - I_{sg}$, from Equation 2.4). The electron emission yield evaluated for the incident energy E_i is expressed, in terms of measured currents, as

$$\sigma(E_i) = \frac{I_p(E_i) - I_{sg}(E_i)}{I_p(E_i)} = 1 - \frac{I_{sg}(E_i)}{I_p(E_i)}. \quad (2.6)$$

2.2.4 Vaughan's Empirical TEEY Expressions

Numerous analytical expressions have been developed to model TEEY curves for different materials. One simple and widely used empirical approach — agreeing with experiments — is that of *Vaughan* [53, 55].

[53] Vaughan (1989)

In the modified version of the empirical model² proposed by *Vaughan* in 1989, for an incidence angle θ to the normal, the TEEY σ corresponding to incident energy E_i for impacting electrons is expressed as

[55] Vaughan (1993)

2: This model was followed by some improvement works, such as Ludwick2018.

$$\sigma = \begin{cases} \sigma_{\max}(\theta) (ve^{(1-\nu)})^k & \text{for } \nu \leq 3.6 \\ \sigma_{\max}(\theta) \frac{1.125}{\nu^{0.35}} & \text{for } \nu > 3.6 \end{cases} \quad (2.7)$$

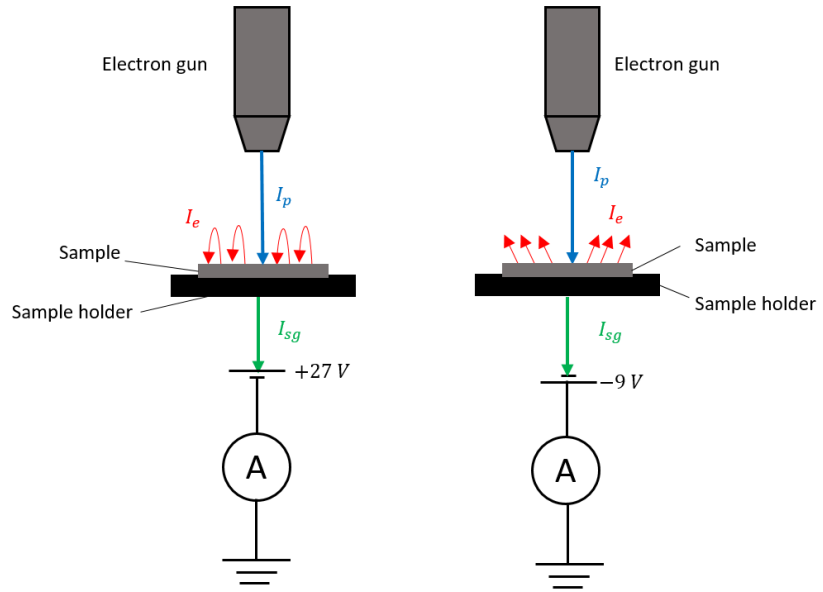


Figure 2.11: Two steps sample bias TEEY measurement technique: in the first step the sample is positively biased with +27 V so that emitted electrons are collected back by the sample, and in the second step the sample is negatively biased with -9 V for emitted electrons to be escaped.

with

$$\nu = \frac{E_i - E_0}{E_{\max}(\theta) - E_0} \quad (2.8)$$

and

$$k = \begin{cases} 0.56 & \text{for } \nu \leq 1 \\ 0.25 & \text{for } 1 < \nu \leq 3.6 \end{cases} \quad (2.9)$$

where E_0 is the minimum impact energy for which secondary electrons can be generated and E_{\max} is the impact energy corresponding to the maximum TEEY, σ_{\max} for an incidence angle θ relative to the surface's normal.

$E_{\max}(\theta)$, and $\sigma_{\max}(\theta)$ can be expressed as a function of their values for normal incidence and the angle of incidence θ — expressed in radians — by the following expressions

$$E_{\max}(\theta) = E_{\max}(0^\circ) \left(1 + \frac{k_{se}\theta^2}{\pi} \right) \quad (2.10)$$

and,

$$\sigma_{\max}(\theta) = \sigma_{\max}(0^\circ) \left(1 + \frac{k_s\theta^2}{2\pi} \right) \quad (2.11)$$

where k_{se} and k_s are surface smoothness factors, for E_{\max} and σ_{\max} respectively, ranging from 0 to 2. For dull surfaces, their default value is 1.0. For roughened surfaces, lower values are appropriate down to zero for textured carbon, and for smooth, clean, and oxide-free surfaces, higher values, up to about 2.0, are appropriate.

2.3 X-ray-induced Photoelectron Spectroscopy (XPS)

Electron spectroscopy is a technique to determine the material surface properties at a depth of a few nanometers. The electron spectroscopy-

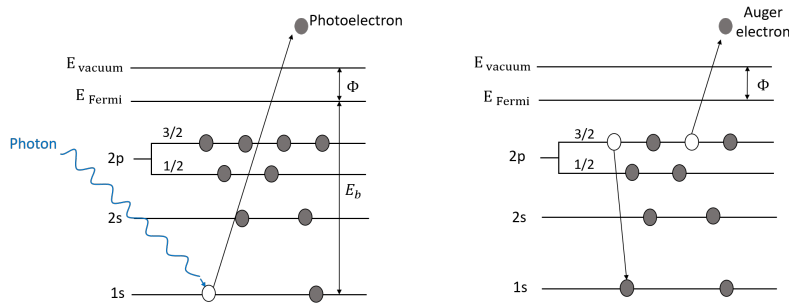


Figure 2.12: X-ray-induced photoelectron spectroscopy (XPS) possible processes. Left — Photoemission process: an incident photon excites a core's electron, that is emitted from the material to the vacuum. Right — Auger electron's emission process: to relax the ionised state, an outer shell's electron fills the inner vacancy, and an Auger electron is emitted from the material with the excess of energy.

based chemical analysis for solid materials relies on the energy analysis of secondary electrons that are emitted due to photons', electrons', ions', or neutrals' excitation [56].

The main common features of the electron spectroscopy techniques are the following:

- ▶ Chemical elements' detection, except for hydrogen and helium;
- ▶ Chemical bonding states' detection;
- ▶ Chemical information in the first few nanometers' depth.

[56] Hofmann (2013)

X-ray-induced photoelectron spectroscopy (XPS) is one of these surface chemical analysis techniques.

In XPS, the sample's surface under characterisation is irradiated with photons, having a known characteristic energy. These photons will directly interact with the core electrons of the sample's atoms, resulting in the creation of ionised states, which may lead to the emission of photoelectrons due to the photoelectric effect principle. Moreover, as different electron orbitals of the targeted atoms could be ionised, electrons from other shells can fill up the ionised states — an outer electron falls into the inner orbital vacancy. The energy released by this process may be transmitted to an electron in an outer orbital level, which will, in turn, be emitted simultaneously from the atom as the so-called Auger electron. Therefore, the excess energy is dissipated in two possible ways: *i*) photoelectron emission, and *ii*) Auger electron emission from an outer shell. These two XPS processes are illustrated in Figure 2.12.

Therefore, the X-ray photoelectron emission can be summarised by the following three steps:

- ▶ Photons of the X-ray beam interact with the atoms' electrons, resulting in photoelectrons and Auger electrons;
- ▶ Part of these electrons move to the surface and are subject to scattering processes;
- ▶ Electrons reaching the surface are emitted in the vacuum after surmounting the work function threshold of the sample's material.

The kinetic energy, E_{kin} , of the released photoelectrons in vacuum is given by [57]

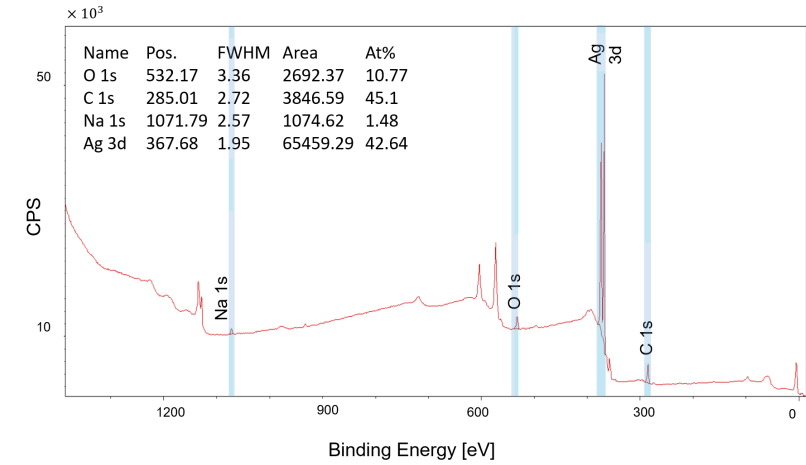
$$E_{kin} = h\nu - E_b - \Phi \quad (2.12)$$

[57] Moulder et al. (1979)

where $h\nu$ is the characteristic energy of the photons' impinging beam (h Planck's constant, and ν the frequency), E_b is the binding energy³ of the core's electron hosting the energy transfer with the beam's photon (with respect to the Fermi level's energy), and Φ is the work function of the sample.

3: The electron binding energy is the minimum energy that is required to remove an electron from an atom.

Figure 2.13: X-ray-induced photoelectron spectroscopy (XPS) spectrum example. The y - (respectively x -) coordinate represents the elements' intensity (respectively binding energy) in counts per second [CPS] (respectively [eV]). The light blue shaded regions from right to left are respectively for: carbon (C - 1s), silver (Ag - 3d), oxygen (O - 1s), and sodium (Na - 1s). The analysis' results on the upper left corner are the: *i*) constituents' name, *ii*) binding energy's position expressed in [eV], *iii*) full width at half maximum (FWHM) of the intensities' peaks, *iv*) area under the intensities' peaks, and *v*) atomic concentration in percent.



XPS can be used to identify and determine the concentration of the elements on the sample's surface since each chemical element has a unique set of binding energies. The latter could be done by evaluating the binding energies of the emitted electrons from their measured kinetic energies. Moreover, the chemical shifts — variations in the elemental binding energies — could be used to identify the chemical state of the analysed materials.

Each analysis results in an energy XPS spectrum giving the intensity (counts per second [CPS]) as a function of the binding energy and permitting the identification of the constituent elements. The binding energy scale is plotted with increasing energy from right to left, as the binding energy has a different sign than the measured kinetic energy. The spectrum peaks are produced by the electrons emitted from the surface without an energy loss. Therefore, they are the electrons originating from the last tens of angstroms of the sample's surface. Consequently, XPS is known to be a surface-sensitive technique.

An example illustrating an XPS spectrum for a WEST ICRH stainless-steel silver coated sample, baked for three days 200 °C and maintained at a temperature of 70 °C, is given in Figure 2.13. The light blue shaded regions appearing from right to left are respectively for the following constituents' elements of the sample: carbon (C - 1s), silver (Ag - 3d), oxygen (O - 1s), and sodium (Na - 1s). These elements are chosen as they correspond to the highest intensities of the XPS spectrum. The analysis of XPS spectra could be done using dedicated software such as CASAXPS, and an example of the results obtained is shown in the upper left corner of Figure 2.13. In particular, the five columns correspond respectively to the following:

- ▶ Constituents' name of the shaded light blue regions;
- ▶ Binding energy's position of the elements;
- ▶ Full width at half maximum (FWHM)⁴ corresponding to the intensity peak of each of the constituents' elements;
- ▶ Area of the surface under the curve of the intensities' peaks;
- ▶ Atomic fractional concentration in per cent for the constituents' elements.

The illustrated example indicates that the sample is contaminated, along

4: The full width at half maximum (FWHM) is the width of a line shape at half of its maximum amplitude (illustrated in Figure 2.14).

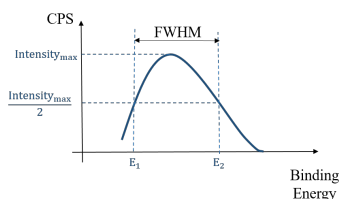


Figure 2.14: Illustration of the full width at half maximum (FWHM).

with the existence of adsorbates of hydrocarbon molecules and hydroxides.

The atomic fractional concentration C_x of any constituent x in a sample is obtained from the area below its intensity peak at its binding energy, weighted by its respective sensitivity factor S_x and normalised over all the detected elements on the sample's surface [58]

$$C_x = \frac{I_x/S_x}{\sum_i I_i/S_i}. \quad (2.13)$$

In this manuscript, the XPS spectrum is calibrated using the carbon peak, commonly present on all the samples exposed to air. Furthermore, additional sweeps are performed in narrow energy regions to obtain high energy-resolution spectra for the main constituent elements of the sample.

[58] Petit (2020)

2.4 Surface Characterisation Means

We are interested in characterising the surface properties of representative samples of the WEST ICRH antennas while accounting for surface treatments of the WEST-tokamak case. Indeed, the tokamak WEST relies on preliminary baking and RF conditioning phases before operating to improve the machine vacuum and cleanliness conditions. The latter commissioning phases are known to modify the electron emission properties of the surfaces [59] and are widely used in the tokamak and particle accelerator communities.

[59] Baglin et al. (2000)

In this study, we mimicked the RF conditioning by *in-situ* electron bombardment treatment — conditioning treatment — to monitor the surface properties. The conditioning treatment of the samples, also known as the dose effect, is a surface treatment method based on impacting the surfaces with an electron beam of specific intensity for a given time [12].

[12] Petit et al. (2019)

The total electron emission yield (TEEY) for the coating material constituting the ICRH antennas used on WEST is measured — using *sample bias method* — in various relevant operational conditions such as baking and temperature, and the surface properties are studied in terms of the desorbed species during conditioning.

2.4.1 Experimental Setup Description

All the experiments presented in this manuscript were performed on the ALCHIMIE⁵ experimental facility located at ONERA/DPHY in Toulouse, France.

5: Standing for "Analyse chimique et mesure de l'émission électronique."

ALCHIMIE is the association of an ultra-high vacuum (UHV) chamber (10^{-9} to 10^{-10} mbar) and an airlock for the sample's introduction and preparation under high vacuum (10^{-8} mbar). In the airlock, the sample could be heated for degassing purposes. This experimental facility is intended for the following:

- ▶ Electron emission's study under electrons or photons' impact;

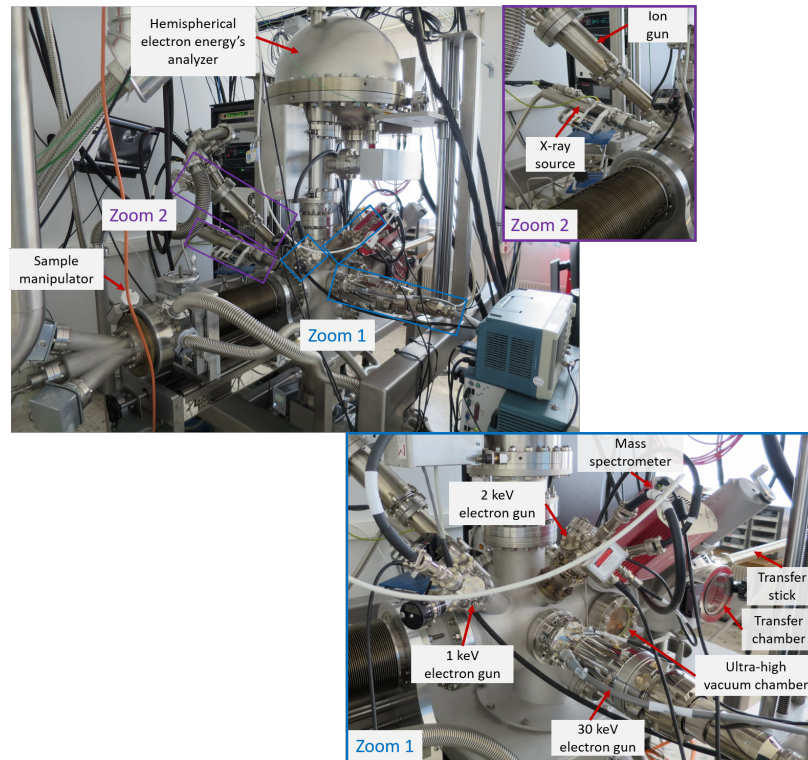


Figure 2.15: The various equipment of the ALCHIMIE experimental facility at ONERA/DPHY.

- ▶ Surface analysis' under ion impact;
- ▶ Surface thickness' probing;
- ▶ Surface analysis by Auger electron spectroscopy (AES);
- ▶ Surface analysis by X-ray photoelectron spectroscopy (XPS);
- ▶ Mass spectroscopy analysis;
- ▶ Understanding other surface phenomena for applications such as ageing, erosion, contamination, *etc.*.

ALCHIMIE is equipped with a 128 channels' hemispherical analyser of a micro-channel plate (MCP) type, an ion source — which could be used in the ultra-high vacuum chamber thanks to the existence of a differential pumping system —, an X-ray source, and three electron guns of maximum energy 1 keV (non-focused gun), 2 keV and 30 keV. The sample holder can be thermo-regulated in a range from $-180\text{ }^{\circ}\text{C}$ to $450\text{ }^{\circ}\text{C}$. The sample is transferred from the airlock to the ultra-high vacuum using a transfer stick and could be rotated in all directions by a manual manipulator — for the sample's surface to be, partially or totally, focused under one gun. The different parts of the installation are illustrated in Figure 2.15.

2.4.2 Experimental Approach

Various installation devices are used for the experiments performed on the ICRH representative sample. The following illustrates the different equipment and their use cases.

- ▶ Airlock and ultra-high vacuum chamber: putting the samples under ultra-high vacuum and sample degassing.
- ▶ Thermal regulator: heating of the sample holder to $70\text{ }^{\circ}\text{C}$.
- ▶ 1 keV electron gun: sample surface's conditioning.

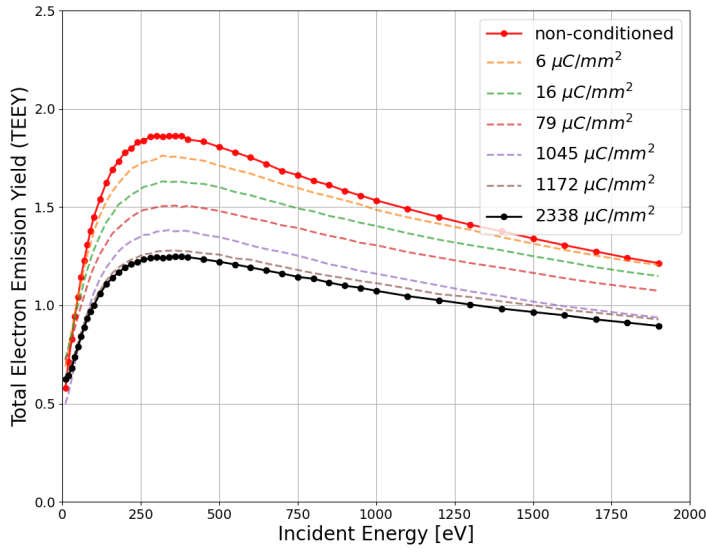


Figure 2.16: TEEY measurements for a baked silver-coated stainless steel sample, maintained at 70 °C, before conditioning, and after impacting its surface by the following cumulative electron doses (from top to bottom): 6 $\mu\text{C mm}^{-2}$, 16 $\mu\text{C mm}^{-2}$, 79 $\mu\text{C mm}^{-2}$, 1045 $\mu\text{C mm}^{-2}$, 1172 $\mu\text{C mm}^{-2}$, and 2338 $\mu\text{C mm}^{-2}$.

- ▶ 2 keV electron gun: electron emission yield's measurements.
- ▶ Mass spectrometer: surface analysis by mass spectroscopy.
- ▶ X-ray source: XPS measurements.

For the treatments to be representative of the WEST-tokamak case, the sample was baked in the airlock at 200 °C for three days — to mimic the tokamak baking phase — and then transferred to the ultra-high vacuum chamber, where it was maintained at a temperature of 70 °C. We measured the TEEY and then started the surface's conditioning with an electron bombardment to mimic the RF conditioning phase. After each conditioning phase, we measured the evolution of the TEEY. Moreover, we analysed the mass spectroscopy of the UHV chamber to identify the various volatile species present.

Then, the sample was subjected to six cumulative electron doses to simulate the RF conditioning effect, and after each dose, the TEEY was measured, along with an XPS measurement.

2.4.3 Results and Discussions

The TEEY measurements for different cumulative electron doses are represented in Figure 2.16, and their associated values of maximum TEEY and first crossover energy are given in Table 2.1. The zero cumulative dose refers to the *non-conditioned* TEEY measurement case represented in red while the cumulative dose of 2338 $\mu\text{C mm}^{-2}$ refers to the *fully-conditioned* case for a reason identified later.

The measurements clearly show the effect of the baking and electron dose conditioning on the TEEY properties. Indeed, the maximum TEEY is reduced from a value of 1.86 to a value of 1.25. And the first crossover energy increases from a value of 46 eV for the *non-conditioned* case to 100 eV for the *fully-conditioned* case.

Table 2.1: TEEY parameters for the seven curves of Figure 2.16.

Cumulative Dose [$\mu\text{C mm}^{-2}$]	σ_{max}	E_{c1} [eV]
0	1.86	46
6	1.76	45
16	1.63	50
79	1.51	60
1045	1.38	88
1172	1.28	94
2338	1.25	100

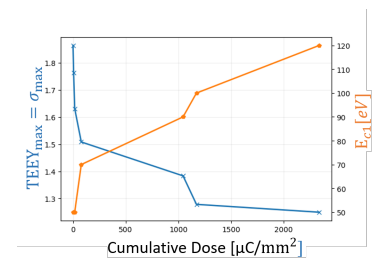


Figure 2.17: The variation of the maximum TEEY (σ_{max}) and the first crossover energy (E_{c1}) versus the cumulative dose of electron bombardment.

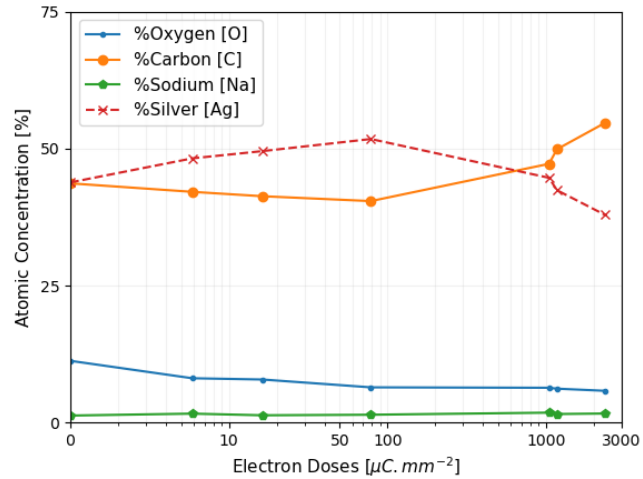


Figure 2.18: Surface atomic concentration for the different elements, found on the surface of the baked silver-coated stainless steel sample at each conditioning phase.

Figure 2.17 represents the variation of the maximum TEEY and first crossover energy versus the cumulative dose. Moreover, the results show the saturation of the TEEY measurements properties when the sample is subject to an electron dose greater than $1172 \mu\text{C} \cdot \text{mm}^{-2}$. Indeed, when the dose is increased from $1172 \mu\text{C} \cdot \text{mm}^{-2}$ to $2338 \mu\text{C} \cdot \text{mm}^{-2}$ (almost doubled), the first crossover and the maximum TEEY change only slightly (with a relative difference of $\sim 2\%$ for the maximum TEEY, and $\sim 6\%$ for the first crossover energy). Therefore, once the surface state reaches the TEEY properties of the curve corresponding to the electron dose of $2338 \mu\text{C} \cdot \text{mm}^{-2}$, the conditioning effects become negligible.

As during the experimental campaigns on WEST, the RF conditioning of the ICRH antennas is done *in-situ* under vacuum, and the surface is not re-exposed to air, the antennas' surface won't be severely re-contaminated. Therefore, the *non-conditioned* case characterises the surface characteristics of the antennas at the beginning of the RF conditioning phase and can be considered the worst surface situation. The *fully-conditioned* case characterises the antennas' surface properties mimicking the end of the RF conditioning phase and can be considered the best surface situation.

The contaminants' desorption was evidenced by monitoring the chemical surface modifications of the sample after each conditioning phase using XPS. The XPS spectra, acquired *in situ* at the conditioning phases, show the presence of carbon and oxygen contaminants added to the core material constituent — silver. The atomic concentration of these different elements for various electron doses is represented in Figure 2.18. For the first three electron doses $6 \mu\text{C} \cdot \text{mm}^{-2}$, $16 \mu\text{C} \cdot \text{mm}^{-2}$, and $79 \mu\text{C} \cdot \text{mm}^{-2}$ a decrease in the concentration of both oxygen and carbon is noticed, indicating hence the desorption of the hydroxides, hydrocarbons, and contaminants from the sample surface. Above the third electron dose, the oxygen's concentration continues to decrease while a re-increase in the concentration of carbon is observed. The latter leads to an eventual decrease in silver atomic concentration.

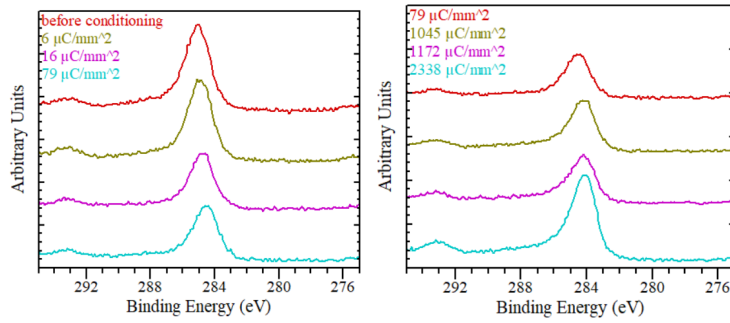


Figure 2.19: C 1s XPS spectra. Left — The C spectra corresponding to the electron cumulative doses of $0 \mu\text{C mm}^{-2}$, $6 \mu\text{C mm}^{-2}$, $16 \mu\text{C mm}^{-2}$, and $79 \mu\text{C mm}^{-2}$. Right — The C spectra corresponding to the electron cumulative doses $79 \mu\text{C mm}^{-2}$, $1045 \mu\text{C mm}^{-2}$, $1172 \mu\text{C mm}^{-2}$, and $2338 \mu\text{C mm}^{-2}$.

Figure 2.19 shows the C 1s XPS spectra at the different conditioning phases. In particular, the figure on the left represents a decrease in the intensity of the carbon peak corresponding to the electron doses $0 \mu\text{C mm}^{-2}$, $6 \mu\text{C mm}^{-2}$, $16 \mu\text{C mm}^{-2}$, and $79 \mu\text{C mm}^{-2}$. The figure on the right shows an increase in the intensity of the C 1s peak corresponding to the electron doses $79 \mu\text{C mm}^{-2}$, $1045 \mu\text{C mm}^{-2}$, $1172 \mu\text{C mm}^{-2}$, and $2338 \mu\text{C mm}^{-2}$. These results are in accordance with the carbon's atomic concentration variation observed in Figure 2.18.

Furthermore, the best-fit results of the C 1s XPS spectra indicate that, for the *non-conditioned* case, the C 1s spectrum has a main peak at a binding energy of 285 eV, which is attributed to sp^3 hybridised C atoms in C—C and C—H bonds. The conditioning effect slowly shifts the C 1s peak to lower binding energies to end up with a peak around 284.1 eV — corresponding to graphitic components — being the main fitting peak of the C 1s spectrum in the *fully-conditioned* case. This shift demonstrated an sp^3 – sp^2 conversion and the chemical state modification by a graphitisation of the adventitious carbon layer. The latter result is in accordance with previous study cases.

The phenomenon of carbon's atomic concentration increase has been observed [60–63] and interpreted [12] before, and is attributed to the electron gun used for conditioning, which becomes a source of contamination due to evacuated molecular fragments containing the carbon element. Indeed, the carbon's intensity growth observed after $79 \mu\text{C mm}^{-2}$ originates from the CO and CO_2 released by the hot electron beam filament. The released carbon atoms adsorb on the sample's surface, bond to each other to form the graphitic-like layer, and are seen in the XPS analysis by an intensity increase. In addition, oxygen atoms are desorbed by conditioning. The latter is evidenced by a continuous decrease in the oxygen peak intensity as observed in Figure 2.20.

Subsequently, we can conclude that baking and conditioning phases are required to reduce the hydroxide and hydrocarbon elements, as well as adsorbed oxides on the surface of the ICRH antennas, and lead to the reduction of the TEEY. Nevertheless, if the conditioning time exceeds $(D_s \times S) / I$, no effect on the surface properties will be noticed (where D_s is the electron dose above which no variation in the TEEY properties is observed, S is the conditioned antenna surface, and I being the conditioning current).

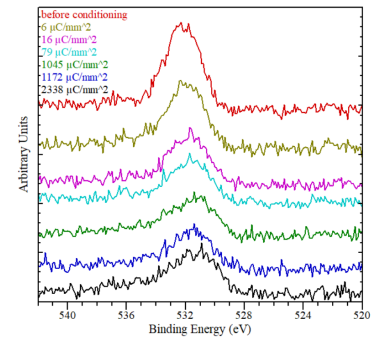


Figure 2.20: The oxygen spectrum corresponding to the electron cumulative doses of $0 \mu\text{C mm}^{-2}$, $6 \mu\text{C mm}^{-2}$, $16 \mu\text{C mm}^{-2}$, $79 \mu\text{C mm}^{-2}$, $1045 \mu\text{C mm}^{-2}$, $1172 \mu\text{C mm}^{-2}$, and $2338 \mu\text{C mm}^{-2}$.

[60] Scheuerlein et al. (2002)

[61] Nishiwaki et al. (2009)

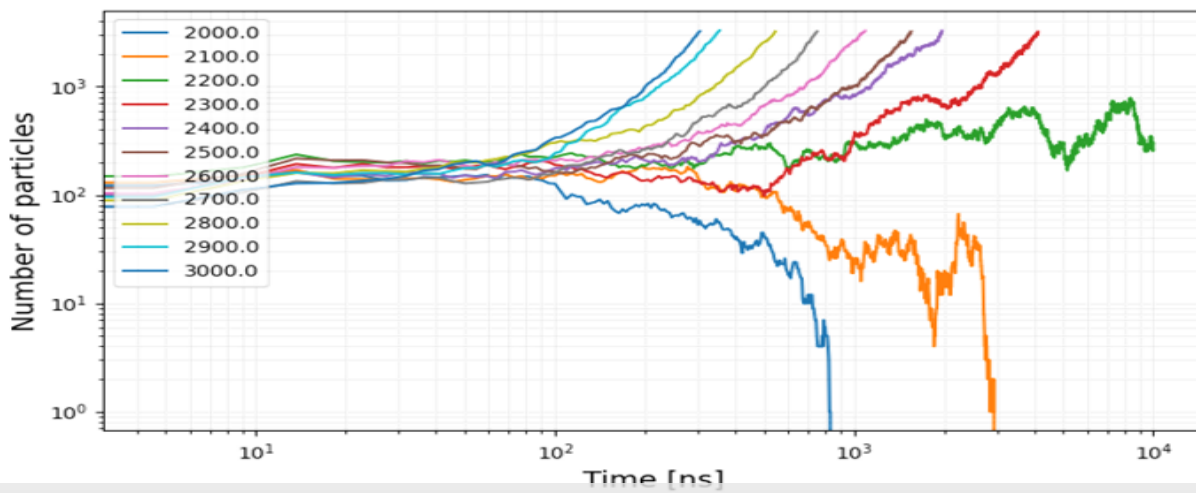
[62] Cimino et al. (2012)

[63] Larciprete et al. (2013)

[12] Petit et al. (2019)

2.5 Chapter Summary and Perspectives

In this chapter, we characterised the material properties of the WEST ICRH antennas' surfaces in the nominal operating conditions of the system. We studied the effect of the baking and simulated the RF conditioning phase by a dose effect to conclude the consequences of these procedures on the material properties. Our observations revealed a reduction in the maximum TEEY and an increase in the first crossover energy. Moreover, we analysed the different chemical components present on the last few nanometers of the surfaces before and after the baking and conditioning phases and evidenced the contaminants' desorption. Although we observed the elimination of the surface contaminants, the maximum TEEY remains above unity, and therefore the surfaces can remain problematic for the electrons' multiplication phenomenon known as "multipactor." In the next chapter, we will introduce the reader to the multipactor mechanism.



3 Multipactor Phenomenon

Sometimes, abundance is in the few, not the many... — And do not lean on your ignorance.

Ali Ibn Abi Taleb

The present chapter builds on the previous chapter, consisting of a foundation for understanding the phenomenon and reviews theories and experimental observations on multipactor in the literature. First, we define multipactor (Section 3.1), then we overview the historical advances in the subject (Section 3.2). Later, we elaborate multipactor conditions (Section 3.3), consequences (Section 3.4), saturation mechanisms (Section 3.5), detection methods (Section 3.6), and mitigation techniques (Section 3.7). The second part of the chapter considers the findings on the canonical geometry of interest in our study, which is the cylindrical coaxial transmission line subject to various wave patterns: travelling wave, mixed wave, and standing wave (Section 3.8).

3.1 Multipactor Definition

Multipactor is a vacuum discharge observed in microwave structures at sufficiently low pressures when the electron mean free path becomes longer than the electrodes' separation distance so that electrons travel between electrodes without undergoing collisions with gas molecules. The multipactor mechanism sustains itself by the secondary electron emission resulting from electrons' impact on the RF device's surfaces with sufficient kinetic energy to release, on average, more secondary electrons than the number of impinging electrons — so that more electrons are generated than removed¹. The secondary electron emission could come from either a metallic or dielectric surface.

¹: Multipactor is independent of the gas in which the discharge takes place (Woo).

In this mechanism, some primary electrons are accelerated by the RF electric field and then impact a surface with enough energy to release additional secondary electrons. The electric field may accelerate the released electrons in their turns until a surface collision occurs, followed by a release of even more secondary electrons, and the process continues. Therefore, an exponential increase in the electron population is observed

when this phenomenon is launched in RF components under vacuum conditions until a discharge characterised by an electron avalanche occurs.

Multipactor can be triggered in various geometries and for a wide range of frequencies from MHz range up to tens of GHz. Multipactor can be observed in low pressure/vacuum RF applications such as RF satellites payloads [3], cyclotrons [4], accelerating cavities [5], experimental tokamak RF components [6, 7]: antennas, transmission lines, and RF windows [8–10]; microwave vacuum tubes such as klystrons [8, 11] or particle accelerator structures [12].

Multipactor can be classified into two types:

- ▶ Two-surface multipactor, involving electrons bouncing between two surfaces and known as "double-sided multipactor²."
- ▶ One-surface multipactor, involving electrons bouncing on one surface and known as a "single-sided multipactor."

For all-conductor devices studied in the literature, the RF electric field is normal to the surface — mostly parallel plates geometry and cylindrical coaxial transmission lines. In such a case, the resonance between the electrons' flight time and the RF field's cycle is responsible for the multipactor development. In particular, for the double-sided multipactor, the one-way electron's flight time — the time between two successive impacts — must be an odd integer number of half the RF period T ($(2n - 1)\frac{T}{2}$, with $n = 1, 2, 3, \dots$). In contrast, for the single-sided multipactor, the one-way transit time must be an even integer number of half the RF period, *i.e.*, an integer of the RF period ($2n\frac{T}{2}$, with $n = 1, 2, 3, \dots$). Each integer n refers to a multipactor *order*, or *mode*.

However, this resonance condition is not necessarily required in the presence of dielectrics. For example, in [18], a dielectric geometry was found to be prone to a single-sided multipactor without resonance condition on the electrons' transit time. In this reference, a dielectric is subjected to two fields: *i*) a normal-to-the-surface DC electric field which bends back the electrons' trajectories to the dielectric surface without imparting energy to the electrons, and *ii*) a tangential RF electric field³ — parallel to the dielectric — responsible for the electrons' energy gain and acceleration.

In this manuscript, unless explicitly stated, the multipactor findings and analysis are for all-conductor RF components.

3.2 Historical Background on Multipactor

Research on multipactor dates back to the twentieth century, when *J.J. Thomson* observed the acceleration of the electrons emitted from a cathode in a vacuum by a high-voltage electric field and then the collision with nearby electrodes, resulting in the emission of secondary electrons.

In the same period, *C. Gutton and H. Gutton* observed for the first time the multipactor, known in this era as the breakdown field strength in gas at low pressures and high frequencies. They found that the breakdown field increases with increasing frequency, and they discovered the existence of

[3] De Lara et al. (2006)

[4] Woo et al. (1967)

[5] Shemelin et al. (2020)

[6] Graves et al. (2006)

[7] Goniche et al. (2014)

[8] Preist et al. (1961)

[9] Hillairet et al. (2017)

[10] Jang et al. (2020)

[8] Preist et al. (1961)

[11] Sounas (2015)

[12] Petit et al. (2019)

2: It consists of a sheet-like electron cloud oscillating between the two electrodes.

[18] Kishek et al. (1998)

3: Usually the case near the transmission RF feed-through windows.

a low cut-off frequency below which breakdown does not occur at all or requires a very high field strength [65, 66].

The systematic study of multipactor began a decade later when researchers investigated the phenomenon in detail.

In 1934, *Fransworth* recognised the damage caused by the potential of the resonant secondary emission-based discharge. But, he took advantage of it as a promising signals' amplification mechanism via an electron multiplication, based on directing an electron stream against a surface capable of emitting secondary electrons [67].

Furthermore, he highlighted that the peaks of the electrons' clouds' current occur when the electrons' average flight time is an odd number of half the cycle of the oscillating voltage. Using this phenomenon, he constructed electron tubes called "Multipactor"⁴.

Following *Fransworth's* findings, the researchers started focusing on developing theoretical models to describe the conditions under which multipactor occurs and the associated electron energy distribution.

In 1936, *Henneburg et al.* developed a theory based on the 1930s gaseous breakdown experiments where multipactor was observed. Among their findings, they derived the emitted electron's transit time resonance condition for zero initial velocity and identified the single particle's *phase focusing* and multipactor stability [18]. Phase focusing is an inherent self-adjustment for the electrons' transit time so that nearly synchronous electrons are pulled toward the synchronous condition. It is a stability requirement for the resonance condition to hold over multiple cycles. It has been shown that the resonance is maintained stable — allowing continuous electron multiplication — as long as the system parameters belong to a resonance zone(s). However, the electrons' population growth is counteracted by space charge force effects tending to disperse the electrons, velocity spread of the emitted electrons, and collisions with gas molecules, among other disturbing mechanisms. Saturation can be expected to occur when these opposing forces come into balance.

Later in 1948, while investigating gas discharges in the high-frequency range at low pressure, *Gill and Von Engel* outlined the first theoretical and experimental study on the susceptible regions for multipactor discharge [68]. They worked on the lowest multipactor electric field thresholds' evaluation for a parallel plates-like geometry represented in Figure 3.1.

Experimentally, they measured the lowest multipactor electric field for flat-ended cylindrical tubes and identified a cut-off frequency below which no multipactor occurs and above which the multipactor electric field thresholds increase with the frequency. Figure 3.2 represents the measured electric field thresholds for flat-ended cylindrical tubes separated by respectively 3 cm and 6 cm and made of glass. The cut-off frequency is the lowest frequency of the curves and corresponds to an infinity multipactor breakdown threshold.

They also developed a theory on the secondary electrons' resonance mechanism with a cut-off law relating the cut-off frequency to the electrodes' separation distance. Furthermore, they checked the sensitivity of the solution to a non-zero emission velocity of secondary electrons, where they avoided using a random distribution for emission velocities by

[65] Gutton et al. (1923)

[66] Gutton (1930)

[67] Fransworth (1934)

4: Derived from "AC Electron Multiplier."

[18] Kishek et al. (1998)

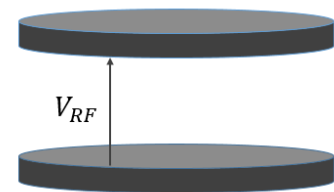


Figure 3.1: The geometrical representation of the two-parallel electrodes analysed by (Gill et al. (1948)) and (Hatch et al. (1954)).

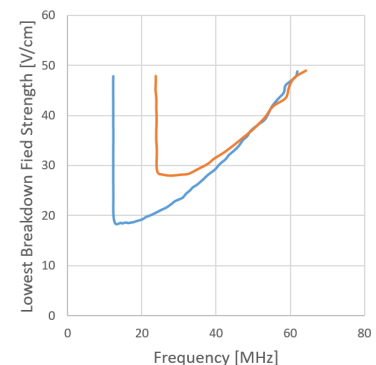


Figure 3.2: The measured lowest multipactor electric field thresholds for flat-ended cylindrical tubes of 3 cm and 6 cm separation distance. Data are extracted from (Gill et al. (1948)).

[68] Gill et al. (1948)

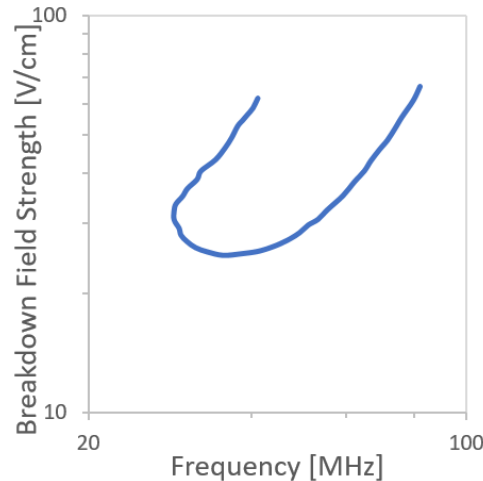


Figure 3.3: The measured lower and upper multipactor electric field thresholds of two silver-copper electrodes. The electrodes' diameter and separation distance are respectively 6.5 cm and 3 cm. The breakdown region is the region between the blue lines. Data are extracted from (Hatch et al. (1954)).

introducing an ad-hoc assumption. This assumption consists of defining a non-physical parameter k that is equal to the ratio of the impact velocity to the emission velocity and considering it as a constant parameter. They argued that these two velocities remain approximately constant. Therefore, their ratio is also constant-valued.

At that time, there was no complete agreement between the developed theory and the experimental results, which opened the door to many investigations — theoretically and experimentally — to refine the conditions of multipactor occurrence.

5: For the first time since the beginning of multipactor study.

6: A parallel plates-like geometry (see Figure 3.1).

[69] Hatch et al. (1954)

In 1954, *Hatch and Williams* measured the lowest and highest⁵ multipactor breakdown electric fields thresholds for two flat metal circular electrodes⁶ to form a multipactor closed breakdown region — bounded by the lowest and highest multipactor thresholds — representing the multipactor electric fields' amplitude for various RF frequencies [69].

For the lowest multipactor thresholds' measurements, they slowly increased the voltage between the plates until multipactor breakdown occurrence accompanied by a blue glow's observation between the electrodes. In contrast, for the highest multipactor thresholds' measurements, they proceeded with the "jumping technique," consisting of suddenly applying the full supply potential and, then, slowly lowering the supply potential until the breakdown occurrence — revealed by a rapid decrease in the voltmeter reading and a blue glow between the plates. They also studied the high sensitivity of the multipactor thresholds to the changing electrodes' surface conditions near the cut-off region.

The measured lowest and highest multipactor electric field thresholds bounding the multipactor region for two silver-copper electrodes separated by 3 cm are shown in Figure 3.3.

In addition to that, they reformulated *Gill and Von Engel's* theory while retaining the constant- k assumption to explain the experimental results. It became known as the "constant- k " theory and was used to construct susceptibility curves — parameterised by the multipactor breakdown voltage (or electric field), frequency, and inter-electrodes' separation distance. This theory remained, for decades, the classical theory of multipactor due to its usefulness in the construction of universal curves, serving as a tool for predicting multipactor occurrence.

In 1958, *Hatch and Williams* generalised the theory of higher order multipactor modes made by preceding researchers and represented by an electron transit time of $(2n - 1)\frac{T}{2}$ with $n = 1, 2, 3, \dots$, and T the RF period. Theoretically, they found that each mode is represented by a bounded domain, and they observed an increasing domain's overlap with order modes' increase. Moreover, the multipactor voltage thresholds follow an $(fd)^2$ scaling for the first order mode — f the frequency and d the electrodes' separation distance. This dependence becomes (fd) for the third order mode — associated with mode overlapping [70].

[70] Hatch et al. (1958)

In 1988, *Vaughan* developed a theory based on a more realistic assumption based on a mono-energetic non-zero initial velocity. He worked on a simple two parallel plates geometry separated by a distance d and driven by an RF voltage at frequency f [2]. He found that the lower and the upper multipactor voltages, bounding the region where multipactor can occur within the geometry, are proportional to $(fd)^2$. Moreover, he highlighted that high multipactor modes are associated with high RF power levels and have a restricted range for operation.

[2] Vaughan (1988)

His work was based on that of *Henneburg* and was considered as an alternative to the "constant- k " theory. Since then, many researchers have adopted *Vaughan's* theory while trying to extend it to generate multipactor susceptibility curves.

Almost all the upper-mentioned analyses were magnetic field-free discussion cases until 1995 when *Riyopoulos et al.* extended *Vaughan's* work on the cross-magnetic-field effect and studied the case of two parallel plates subject to a time-varying electric field and constant magnetic field [71].

[71] Riyopoulos et al. (1995)

The cross-magnetic-field effect refers to the case where electrons impact the surface with an oblique incidence — caused by a transversal DC magnetic field, transverse to RF electric field⁷. The incidence angle increase causes an increase in the electrons' emission yield and the second cross-over energy such that the TEEY remains larger than one for a wide range of impact energies. Subsequently, the cross-magnetic-field multipactor may be potentially more dangerous than its field-free counterpart. Moreover, the magnetic field can give rise to a single-surface multipactor by bending the electrons back to the emission surface.

7: Occurring when the RF frequency is equal to the cyclotron frequency (Vaughan (1988)).

Furthermore, *Riyopoulos et al.* studied the effect of random emission velocity and found that, for sufficiently small emission velocities compared to the oscillating voltage, the multipactor existence follows the criteria for a zero-emission velocity case [71]. The latter reduces the multipactor parameter space to RF electric field and DC magnetic field for the two-surface multipactor. The multipactor parameter space is only the DC magnetic field for the single-surface multipactor.

[71] Riyopoulos et al. (1995)

In 1998, *Kishek et al.* relied on numerical simulations to construct multipactor susceptibility curves while accounting for the interaction with the RF structure and the materials properties of the surface for two main types: double-sided multipactor between two metallic surfaces and single-sided multipactor on a dielectric surface. Furthermore, they stated that for both discharge cases, the multipactor is found to saturate with impact energy in the vicinity of the first cross-over energy of the material [18]. *Kishek et al.'s* results are in good agreement with all the preceding

[18] Kishek et al. (1998)

experimental observations.

Despite the enormous work on multipactor development, all the presented experimental and analytical investigations have mainly focused on simple geometries, such as the two parallel plates. Solely simple geometries have been discussed because the closed-form analytical solutions for the equations governing the electrons' motion in a vacuum are only possible for very few simple cases. Thus, multipactor appearance is not described analytically for complex RF geometries.

Experimental assessments of the multipactor occurrence on realistic geometries are thus still needed but require high-cost campaigns for testing components. The efforts to develop reliable numerical simulations have increased in the last decade. However, while some software tools can model this phenomenon, their predictions are sometimes questionable for complex geometries.

Hence, nowadays, there is no definitive model to predict the multipactor thresholds for complex geometries and different materials, and modelling the multipactor in various RF components with various structures remains challenging.

3.3 Multipactor Conditions

For multipactor to occur in all conductor RF devices, two conditions must be simultaneously fulfilled:

1. One necessary but not sufficient condition that the impact energy of electrons colliding with an electrode must be sufficient to emit more electrons from the surface than the impinging electrons. In electron emission terminology, this condition means that the electrons' impact energy should exceed the first cross-over energy of the material while remaining below the second cross-over energy so that the total electron emission yield (TEEY) of the electrodes' surface is greater than one, for secondary electrons to be released.
2. The second condition is the resonance condition, for the electron's motion to be synchronised with the phase change of the RF electric field.

The multipactor occurrence and thresholds are known to be very dependent on the material characteristics [2, 69, 72]. Consequently, the multipactor thresholds are very sensitive to the electron emission yield, and therefore, the knowledge of the material TEEY is essential for accurate multipactor predictions. Indeed, *Fil et al.* have shown that the lowest multipactor thresholds' amplitude heavily depends on the shape of the TEEY curve, particularly between the first cross-over energy E_{c1} , and the highest electron emission yield σ_{\max} [73–75].

3.4 Multipactor Consequences

The electron multiplication triggered by multipactor was used for some signal amplification applications [67]. However, for most other domains,

[2] Vaughan (1988)

[69] Hatch et al. (1954)

[72] Woo (1968)

[73] Fil et al. (2016)

[74] Fil (2017)

[75] Lin et al. (2023)

[67] Fransworth (1934)

it remains undesirable and should be mitigated, as in experimental fusion reactors' heating systems [6, 7].

In such applications, multipactor-initiated discharges are problematic and have detrimental effects on devices' nominal operation, and can: dissipate an amount of the energy fed into microwave cavities by electrons' electromagnetic energy absorption, load the RF cavity with a built-up electron cloud [13, 14], detune the RF cavity and consequently increase its bandwidth [2], lead to the appearance of abrupt discontinuities in the RF transmission for vacuum tubes [2], raise the system noise level and the return loss that lead to signal degradation [15].

Furthermore, multipactor sustained discharges can cause outgassing [14], a rise in the local temperature of the device which may damage internal components [2, 16, 17], erosion for metallic structures, perforation of the vacuum walls [18], and generation of undesirable integer harmonics [2, 19].

For nuclear fusion devices, multipactor affects or limits the heating antennas' performance, reduces the reliability of the radio-frequency heating and current-drive systems, and limits the maximum power coupled to the plasma [6, 7]. Furthermore, the multipactor can induce a gas breakdown at lower gas pressures than expected by a regular *RF Paschen* breakdown⁸, especially in the case of high DC magnetic fields [20, 21].

In addition, multipactor electrons' cloud can induce reflected power (detuning) to the generators, damaging the high-power sources (klystrons or tetrodes). If not stopped, the temperature rise, and the subsequent increase of pressure due to particles' desorption, caused by multipactor, can lead to RF components' damage, such as the vacuum feed-through ceramics, by excess heat production or its metallisation by arc-induced sputtering [22] up to causing a puncture or a fracture that can lead to a vacuum break event.

Subsequently, a sustained multipactor event can trigger a corona discharge leading to components' partial or total destruction [14, 23]. Indeed, some damaging gas discharges are initiated by the increased outgassing triggered by the multipactor and the local pressure rise [24].

Other manifestations of multipactor are the observation of both light emission — blue-white light — and X-rays emission as reported in [2]. The emitted light is not a direct consequence of multipactor but rather due to collisions-based gas molecules' excitation.

In this work, we are interested in the applications where multipactor effects are deleterious and harmful, particularly the ion cyclotron resonance heating (ICRH) system of the experimental fusion tokamak WEST.

3.5 Multipactor Saturation Mechanisms

Once the multipactor conditions are satisfied, and the electron avalanche takes place, the number of electrons cannot grow indefinitely and is, therefore, limited by some so-called "saturation mechanisms"⁹, acting against the multipactor and preventing its infinite growth.

[6] Graves et al. (2006)

[7] Goniche et al. (2014)

[13] Udiljak et al. (2007)

[14] Sorolla (2012)

[2] Vaughan (1988)

[2] Vaughan (1988)

[15] Semenov et al. (2014)

[14] Sorolla (2012)

[2] Vaughan (1988)

[16] Woode et al. (1990)

[17] Ang et al. (1998)

[18] Kishek et al. (1998)

[2] Vaughan (1988)

[19] Udiljak et al. (2003)

[6] Graves et al. (2006)

[7] Goniche et al. (2014)

8: Details can be found later in Section 3.8.3.3.

[20] Graves (2006)

[21] Becerra (2007)

[22] Kim et al. (2007)

[14] Sorolla (2012)

[23] Höhn et al. (1997)

[24] Yu (2007)

[2] Vaughan (1988)

9: Acts like feedback in a control system, and keeps the electrons' population almost constant in its saturation level.

We distinguish two main electrons' population's saturating processes:

[2] Vaughan (1988)

- ▶ Space charge forces [2, 71];
- ▶ RF loading and detuning of resonant cavities [18].

[71] Riyopoulos et al. (1995)

[18] Kishkek et al. (1998)

The space charge effect refers to the phenomenon occurring when a large number of electrons accumulate in a region. Space charge effects involve two mechanisms affecting the electrons' motion: *i*) the mutual repulsion between the electrons due to Coulomb's force, and *ii*) the electrons' interaction with the induced charges on the device's walls ("image charges") [11].

[11] Sounas (2015)

Early researchers, in particular *Vaughan*, found that de-bunching due to the space charge forces is one multipactor saturation mechanism. The space charge forces are responsible for de-focusing the electrons by accelerating them ahead and behind the focused sheet until the population reaches an equilibrium steady state.

At an early stage of the multipactor occurrence, the number of electrons and the electron density are low. Moreover, the resultant of Coulomb's forces, repelling the electrons when approaching each other, is smaller than the applied RF electric field. Hence, the repulsion effect does not affect the multipactor process. However, once the population increases, the mutual electrons' repulsion becomes dominant over the applied field affecting the electrons' dynamics. The second mechanism of induced charges tends to attract the electrons toward the device's walls.

Consequently, because of the space charge forces, the electrons acquire a phase error that causes them to fall outside the allowed phase range of the resonance region. Therefore, the electrons impact the surfaces with insufficient energy for electron emission and are absorbed by the surface.

In 1988, *Vaughan* estimated the saturation level analytically by evaluating the space charge's phase-dispersion effect. He found that the maximum charge density (J_{max}) of the thin electron sheet oscillating between two parallel plates separated by a distance d and subject to an RF voltage at an angular frequency ω is expressed by $J_{max} = 1.684 \times 10^{-24} \omega^2 d$. This leads to a current $I = \frac{\omega}{2\pi} J_{max} A (2N - 1)$ (A being the electrode's area, and N referring to the double-sided multipactor order) on each electrode [2].

[2] Vaughan (1988)

[76] Kishkek et al. (1996)

10: In a cavity resonator of high Q -factor, the electric field's amplitude is high and the likelihood of multipactor is high.

Later, *Kishkek et al.* [76] proposed the RF loading and detuning — especially for cavity resonators¹⁰ with high-quality factor (Q -factor) — as a second saturation mechanism. The multipactor electrons induce a wall current, which loads the cavity. The cavity, in turn, is detuned, causing a decrease in the electric field strength. Hence, the multipactor self-extinguishes, and the electrons' population saturates. *Kishkek et al.* reported that for high Q -factors, the RF loading and detuning's saturation effect is more noticeable than the space charge forces' effect. Furthermore, he studied this mechanism for resonators with various quality factors and determined a typical multipactor saturation time of 100 to 200 RF periods.

However, when analysing the multipactor on a dielectric, *Kishkek et al.* stated that dielectrics are less sensitive to loading and the primary saturation mechanism is the space charge forces [18].

[18] Kishkek et al. (1998)

Method	Physical parameter(s)
LM1 & LM3 & GM5	quantity of free electrons (electron current)
LM2	ultra-violet (UV) light
GM2 & GM7	RF noise signal
GM1 & GM3 & GM6	RF signal at the fundamental frequency
GM4	RF signal at harmonic frequency(ies)

Table 3.1: Detection methods classification based on the type of measured physical parameter(s).

3.6 Multipactor Detection Methods

Multipactor detection methods are grouped into two classes based on the range of detection: *i)* global methods *ii)* local methods. Global methods are diagnostics used to determine whether or not the overall system is suffering from multipactor discharge. But, these methods cannot pinpoint the exact location of the electron growth within the system. In contrast, the local methods installed in the critical multipactor region's vicinity can pinpoint the location of the electron growth within the structure. The critical region (or gap) is defined as the region of the structure where the multipactor takes place at the lowest RF power.

The global detection methods are:

- GM1** Transmitted/reflected power monitoring via *Schottky* diodes/crystal detectors;
- GM2** Close-to-carrier noise;
- GM3** Phase nulling;
- GM4** Harmonic noise (3rd harmonic detection).
- GM5** Electrons' current monitoring in the inner conductor proposed as an alternative to the biased probe local detection method [77].
- GM6** In-phase and quadrature signals-based detection technique proposed as an alternative to the phase nulling technique [78].
- GM7** Amplitude modulation-based detection method [19].

[77] Chaplin et al. (2017)

[78] Moneris-Belda et al. (2021)

[19] Udiljak et al. (2003)

The local detection methods are:

- LM1** Positively biased probe for electron current density measurements.
- LM2** Optical methods like the photo-multiplier tube (PMT) used for UV light detection. The UV light is a result of a discharge.
- LM3** Electron multiplier tube (EMT) proposed as an alternative to the positively biased probe [79, 80].

[79] Shaw et al. (2019)

[80] Shaw et al. (2020)

[81] ECSS (2020)

It should be noted that the methods listed in the ECSS standards [81] on multipactor design and test are **GM1**, **GM2**, **GM3**, **GM4**, **LM1** and **LM2**. The remaining methods are found in literature as alternatives to the main detection techniques found in the ECSS standards.

In space applications, the global methods are of preference because the goal is to avoid the multipactor trigger, without any concern about the location of its occurrence, within the RF structure. Moreover, as these methods are known to be fast and sensitive, there is a better chance to cope with short and weak multipactor events that result from multi-carrier signals. But, in other cases, where the device is in the hardware development state and redesigning is possible, the local methods are used to determine the multipactor location.

These methods could be classified with respect to the type of the measured physical parameters as shown in Table 3.1.

11: Affected by the quality factor of the device.

12: The sensitivity becomes even worth when the device is prone to multipactor filtering out the third harmonic.

[81] ECSS (2020)

[82] Graves (2014)

Multipactor test beds rely on some of these local and global detection methods and pressure and temperature monitoring in the test environment.

Some of these methods such as **LM1**, **LM2**, **LM3**, **GM3**¹¹, **GM5**, **GM6**, and **GM7** are very sensitive and able to detect the discharges causing a small change in their output parameters, while others are less sensitive such as **GM1**, **GM2**, **GM4**¹² [81, 82].

3.7 Multipactor Mitigation Techniques

In many applications, preventing or suppressing multipactor is the main reason behind studying it. There are four main approaches for mitigating the multipactor occurrence in an RF device:

- ▶ Surface treatments: surface conditioning by controlled discharge events, changing the surfaces' roughness, coating the surfaces;
- ▶ Pre-design and post-design geometrical modifications;
- ▶ DC electric field biasing;
- ▶ DC magnetic field.

The surface treatments aim to modify the material's electron emission properties so that when a beam of electrons impinges on the surface, no electrons are emitted to prevent the multipactor occurrence. However, the main drawback of it is its degradation over time.

Surface conditioning is a long-time and periodic surface treatment based on controlled RF-based discharge events responsible for cleaning and conditioning the surfaces via contaminants and hydroxides' desorption to increase their voltage handling capabilities. Indeed, we showed in the previous chapter that simulating short low-power RF pulses' application by a dose effect reduces the maximum TEEY while increasing the first cross-over energy of the surfaces' material. Consequently, the likelihood of multipactor occurrence is reduced. Nevertheless, the main disadvantage of this process is, once re-exposed to air, the surface degradation over time due to surface contamination. Another possible alternative for the RF-based discharges is the surface impact with an electron beam, such as in particle accelerators' applications [59].

[59] Baglin et al. (2000)

[83] Nishimura et al. (1994)

Changing the surface roughness [83] reduces the electron emission from the surfaces by decreasing the solid angle allowing electrons to escape from the surface to the vacuum without further surface interactions. Changing the surface roughness can be produced by a chemical reaction with the sample or by depositing a strongly dendritic layer on the surface [84, 85].

[84] Curren et al. (1990)

[85] Baglin (1997)

Surface roughening has also been shown to suppress the multipactor while maintaining high-voltage handling properties for nuclear fusion application devices. In particular, for Alcator C-Mod, *Graves* proposed and tested a treatment consisting of sandblasting the copper electrodes of a parallel plates geometry with 50 μm of aluminium oxide bead. He showed that after a glow discharge cleaning process of a few minutes, the sandblasting prevents the multipactor appearance on the frequency range of interest, and proposed it for implementation for the transmission lines section of Alcator C-Mod [20]. However, following *Graves*, *Becerra*

[20] Graves (2006)

tested the sandblasting technique for the coaxial transmission lines and reported that it did not succeed in suppressing multipactor due to the following possible reasons:

- ▶ The low vacuum conductance of the coaxial sections making the glow discharge cleaning¹³ unsuccessful;
- ▶ Some non-pumped impurities — originating from teflon gas barriers — deposited on the coaxial surfaces and preventing a further reduction in the TEEY [21].

Surface coating refers to processing the surface by applying a thin layer of material onto the multipactor-prone components' surfaces to enhance their emission properties by reducing the TEEY. This technique has been shown to reduce the TEEY and hence could prevent the multipactor occurrence.

As it has been shown that the deposition of an ultra-thin film on metals' surfaces could modify the work function [86], *Plaçais et al.* studied the effect of the deposition of perfluorinated alkanethiol onto silver metal, on the lowest multipactor electric field threshold for a parallel plates geometry with a dielectric slab covering the bottom plate, and partially the vacuum gap between the plates. They found that the increase in the work function, from 4.3 eV for the silver case to 5.8 eV for the coated silver, induces a tremendous TEEY reduction. Therefore, they observed a rise in the lowest multipactor electric field threshold of about 40% to 60% [87].

Other possible surface treatments are: *i)* bake-out under vacuum mainly to remove the hydroxides and hydrocarbons adsorbed on the surface and *ii)* argon ion glow discharge to reduce the oxides' layer — its effect is degraded rapidly after air exposure [59]. Therefore, to avoid surfaces' severe contamination, these treatments are done *in-situ* under vacuum, and the treated devices are not re-exposed to air.

Pre-design geometrical modifications consist in designing RF systems such that multipactor is avoided in the designed geometry — by changing the material, frequency, or dimensions. However, the geometry is not always changeable due to design or operational constraints.

Post-design modifications can alter the electrons' trajectories to eliminate multipactor. Usually, this technique is applied for RF feed-through by moving its location with respect to the electric and magnetic fields' peaks and nodes. In [10], the authors have developed a multipactor-free RF vacuum feed-through capable of withstanding the power of 1 MW. The design focused on reducing the total RF electric field to reduce the possibility of arcing and nulling the axial electric field to minimise the multipactor occurrence in a vacuum. The latter was achieved by removing the conductors' grooves for alumina insertion. Moreover, they maintained a low and uniform electric field on the vacuum side by inserting a single series transmission line on the pressurised side to act as an impedance transformer matching the main transmission line to the impedance at the alumina position. Via multipactor simulations, they proved that groove-less conductors and coating alumina and coaxial copper conductors with a titanium nitride (TiN) thin layer reduce the multipactor probability majorly. Indeed, a further reduction in the electron emission yield is remarked in the case of groove-less conductors with the coating when

13: The glow discharge cleaning was mandatory as rough surfaces retain more impurities than flat surfaces.

[21] Becerra (2007)

[86] Cazaux (2010)

[87] Plaçais et al. (2018)

[59] Baglin et al. (2000)

[10] Jang et al. (2020)

compared to the following, *i*) grooved conductors without coating, and *ii*) groove-less conductors without coating.

It is also possible to suppress the electron motion by adding a large-DC electric field bias between the RF electrodes, which are prone to multipactor. The applied DC bias prevents the RF field's electrons' acceleration and eliminates any multipactor trigger. Nevertheless, the main disadvantage of this approach is the DC-biasing constraints that many systems have.

Simulations and experimental results have shown that, for rectangular waveguide geometries, the multipactor could be suppressed in the presence of a constant magnetic field. For example, in [88, 89], Geng *et al.* have shown that although the presence of a magnetic field transverse to the direction of propagation and the alternating electric field enhances the multipactor, the presence of a DC magnetic field along the wave propagation direction nearly eliminates multipactor.

[88] Geng *et al.* (1999)

[89] Geng *et al.* (2002)

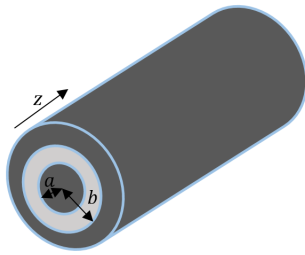


Figure 3.4: Cylindrical coaxial transmission line geometry. The light grey represents the vacuum and the dark grey the conductors. The inner and outer conductors are respectively of radius a and b .

3.8 Coaxial Transmission Lines

3.8.1 Geometry's Main RF Properties

A coaxial transmission line is made of two cylindrical conductors, where its inner conductor is of radius a , the outer of radius b , and encapsulated one inside the other. $d = b - a$ is the gap spacing between the electrodes — inter-electrodes' distance. An illustration of the geometry is given in Figure 3.4.

For high-power applications, inner and outer conductors are generally made of rigid metal with or without coating. The space between the conductors is filled with a dielectric that could be Teflon, dry-air, pressurised nitrogen, or vacuum. In this manuscript, for all multipactor analysis studies, the vacuum is the dielectric between the conductors.

In a coaxial line structure, the fundamental mode is the *transverse electromagnetic* (TEM) mode, where the electric and magnetic fields are transverse to the propagation direction.

The expressions of the electric and magnetic fields inside the coaxial transmission line for a wave propagating in the z -direction are illustrated in Figure 3.5 and are given by:

$$\mathbf{E}(r) = \frac{V}{r \ln(b/a)} \hat{\mathbf{e}}_r \quad (3.1a)$$

$$\mathbf{H}(r) = \frac{I}{2\pi r} \hat{\mathbf{e}}_\phi \quad (3.1b)$$

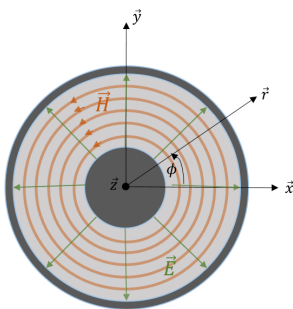


Figure 3.5: Transverse electromagnetic (TEM) mode representation for a coaxial line at high frequencies.

valid for $a \leq r \leq b$. Here $V = V_0^+ e^{-\gamma z} + V_0^- e^{+\gamma z}$ is the voltage between the conductors expressed as the sum of forward (wave propagating in the $+z$ direction) and reflected voltages (wave propagating in the $-z$ direction), and $I = I_0^+ e^{-\gamma z} - I_0^- e^{+\gamma z}$, is the current flowing on each conductor. $\gamma = \alpha + j\beta$ (in $[\text{m}^{-1}]$) being the lossy propagation constant, where α is the attenuation constant expressed in $[\text{Np/m}]$ and β the phase

constant in [rad/m]. For a lossless transmission line, the attenuation constant vanishes.

The reflection coefficient $\Gamma = Re^{j\psi}$ of the coaxial transmission line is defined as the ratio of the reflected to forward voltage (or current)¹⁴. Two extreme cases are possible:

- ▶ Travelling-wave case inducing no reflection on the coaxial transmission line: $|\Gamma| = 0$.
- ▶ Standing-wave case inducing a total reflection on the coaxial transmission line: $|\Gamma| = 1$.

The characteristic impedance Z_0 [Ω] of the coaxial transmission line is given by [29, 90]:

$$Z_0 = \frac{1}{2\pi} \sqrt{\frac{\mu}{\epsilon}} \ln \frac{b}{a} \quad (3.3)$$

where ϵ and μ are, respectively, the permittivity and permeability of the filling material between the inner and outer conductors, which is the vacuum in our study case ($\epsilon = \epsilon_0$, $\mu = \mu_0$; ϵ_0 , and μ_0 being respectively the vacuum permittivity and the vacuum permeability).

From Equation (3.1a), the electric field is inhomogeneous and inversely proportional to the radial distance from the centre of the inner conductor to the outer conductor. Its maximum value is reached on the inner conductor, and the maximum associated voltage and power are respectively given by:

$$V_{\max} = a \ln(b/a) E(r = a) \quad (3.4)$$

$$P_{\max} = \frac{V_{\max}^2}{2 Z_0 \text{SWR}} \quad (3.5)$$

where $E(r = a)$ and SWR are the electric field's magnitude at the centre conductor and the standing wave ratio, respectively.

3.8.2 Geometry's Main Multipactor Properties

As the electric field expression is non-uniform in a cylindrical coaxial transmission line, an exact analytical solution providing the electrons' trajectory is impossible.

For a coaxial cable, two different types of multipactor can occur [11, 13]: double-sided multipactor, a discharge between the inner and outer conductors, and single-sided multipactor on the outer conductor.

Moreover, as for the parallel plate geometry, *hybrid-modes* exist in cylindrical coaxial transmission lines. A hybrid multipactor mode is a double-sided and single-sided multipactor combination where both coexist and interact. The latter could be explained by the velocity spread of the secondary electrons and their non-zero initial velocity, making the double-sided and single-sided multipactor separation difficult and leading to a vacuum discharge being a mixture of both.

In this geometry, a ponderomotive force, also known as the Gaponov-Miller force (or simply Miller force) [11], tends to push the electrons toward the outer region of lower electric field amplitude. Consequently, upon the multipactor conditions' fulfilment, a single-sided multipactor

14: The *standing wave ratio* (SWR) is expressed as:

$$\text{SWR} = \frac{1 + |\Gamma|}{1 - |\Gamma|}. \quad (3.2)$$

[29] Pozar (2011)

[90] Rizzi (1988)

[11] Sounas (2015)

[13] Udiljak et al. (2007)

[11] Sounas (2015)

on the outer conductor is possible. In most cases, this force also leads to a shorter transit time when travelling from the inner conductor to the outer one than the other way around transit time. For resonance to occur, the sum of the two-way transit times should be equal to an integer number of RF cycles [13].

[13] Udiljak et al. (2007)

The multipactor problem for a cylindrical coaxial transmission line can be studied as a one-dimensional problem. It is, therefore, similar to the multipactor analysis for a parallel plate geometry [13]. The latter assumption is valid, provided that the effect of the magnetic field is neglected compared to the electric field.

[13] Udiljak et al. (2007)

3.8.3 Multipactor Analysis' State of the Art

3.8.3.1 Travelling wave case

Many authors have investigated the multipactor thresholds expressed as voltage, electric field, or power for a cylindrical coaxial transmission line geometry analytically [4, 13], numerically [91–94] and experimentally [64, 72], for which main findings are recalled here.

[4] Woo et al. (1967)

[13] Udiljak et al. (2007)

The first and easiest way to predict the multipactor thresholds is the critical gap voltage method, based on the use of the formula relating the multipactor power threshold to the multipactor peak voltage threshold:

[91] Sakamoto et al. (1989)

[92] Somersalo E. et al. (1995)

$$P_{th} = 1 \text{ W} \left(\frac{V_{th}}{V_{1W}} \right)^2$$

[93] Somersalo et al. (1998)

[94] Chojnacki (2000)

where V_{1W} is the critical gap peak voltage corresponding to an input power of 1 W obtained either analytically for simple geometries or through electromagnetic simulation, V_{th} is the predicted multipactor peak voltage obtained from charts or reported experimental data, like the multipactor limit of the ECSS European standard [81], or the Aerospace US standard charts [82] based on a parallel plates topology. This method lacks accuracy, especially in the multipactor peak voltage threshold estimation, and requires the structure's complete design to estimate V_{1W} . However, it could serve as a first approximation method.

[64] Woo (1970)

[72] Woo (1968)

[81] ECSS (2020)

[82] Graves (2014)

In 1967, *Woo and Ishimaru* extended the work done by *Hatch and Williams* to geometries different from the parallel plates to simplify the multipactor prediction for non-uniform electric field's geometries such as the coaxial transmission lines. They accomplished this objective by introducing a "similarity principle." The similarity principle relies on developing multipactor scaling laws obtained by studying the Lorentz force equation. It says that if multipactor occurs for a set of parameters: voltage V , magnetic flux density B , frequency f , separation distance d , impact velocity v_i , emission velocity v_e , then, as long as $V/(fd)^2$, B/f , $v_i/(fd)$, and $v_e/(fd)$ are constant, the electrons will have the same phase relationship with the fields and the same kinetic energy, and therefore, the multipactor is maintained. Furthermore, the similarity principle explains the constant- k assumption's success, as the secondary electrons satisfying the multipactor phase conditions and participating in the breakdown are those with constant $v_i/(fd)$ and $v_e/(fd)$ so that the ratio v_e/v_i must remain constant [4].

[4] Woo et al. (1967)

In subsequent works [64, 72], Woo measured experimentally the lowest and highest multipactor voltage thresholds for a coaxial transmission line having a characteristic impedance ranging from $50\ \Omega$ to $175\ \Omega$. Woo stated that the similarity principle leads to two scaling relations for the coaxial cables. In the first one, for various products $f \times d$, the multipactor breakdown voltages are proportional to $(fd)^2$, in agreement with Vaughan's analytical studies [2], but provided that there is no change in the multipactor mode. Moreover, he revealed that the highest multipactor voltage thresholds follow this law remarkably well for all b/a . For the lowest multipactor voltage thresholds, he found that the $(fd)^2$ is only valid for a high¹⁵ b/a ratio, and the exponent is less than 2 otherwise, where the breakdown voltage is more sensitive to surface conditions. In particular, before surfaces' outgassing, the exponent is less than 2 and increases to 2 once outgassing occurs. In the second law, for constant product $f \times d$, two coaxial cables of different dimensions but with the same characteristic impedance, *i.e.*, ratio b/a , exhibit the same breakdown voltages.

Furthermore, a shift to higher values for breakdown voltages of the multipactor region has been observed with increased characteristic impedance, or equivalently the ratio b/a . Woo explained it by the multipactor's occurrence-probability decrease because of the increased electric field's gradient for increasing b/a .

Woo found that surfaces' outgassing effect is to shrink down the multipactor region while keeping the overall shape the same.

In [13], the authors were interested in studying the non-uniform electric field's effect on the multipactor initiation's properties. To this end, they derived an approximated analytical solution — providing the expressions of the electrons' position and velocity — for the non-linear differential electrons' motion equation in cylindrical coaxial transmission lines. The latter is based on dividing the electron position into a fast oscillating motion and a slow varying motion being the time-averaged position.

They proved that when the inner radius is of the order of the outer one, that is, for low characteristic impedance, the multipactor analysis for the coaxial is similar to that of a parallel plates geometry, and therefore, the double-sided multipactor is dominant. However, in the case when the inner radius is smaller than a determined threshold equal to 58% of the outer radius, that is, for high characteristic impedance, higher-order double-sided multipactor are no longer possible and only single-sided multipactor is present, provided that the initial velocity is low and fast oscillating motions of the electron's position are small.

For single-sided multipactor, Udiljak *et al.* found that it exhibits a $(fb)^2 Z_0$ voltage dependence. This result is in agreement with numerical calculations done by Somersalo *et al.* [92] and later by Pérez *et al.* [95].

For the double-sided multipactor, they derived a multipactor voltage scaling law given by $(fd)^2$. This law is valid for the first order resonance, for all values of the characteristic impedance, whereas for higher order resonances, it is valid only for low characteristic impedance [13]. In agreement with the results found by Woo [72], their analysis showed that an increase in the line's characteristic impedance leads to increasing

[64] Woo (1970)

[72] Woo (1968)

[2] Vaughan (1988)

15: For high b/a , the non-uniformity of the electric field increases, and the existence of higher-order multipactor modes decreases.[13] Udiljak *et al.* (2007)[92] Somersalo E. *et al.* (1995)[95] Pérez *et al.* (2009)[13] Udiljak *et al.* (2007)

[72] Woo (1968)

the multipactor thresholds and a narrower region for the first-order multipactor.

However, the range of validity of their work is restrained to the GHz range of frequencies because the division of the electron position into fast and slow motions is valid as long as the oscillations are much smaller than the average position. In this case, the latter parameter can be considered constant on the fast time scale. Moreover, the taken assumption that $\Lambda \ll (\omega R)^2$, where $\Lambda = eE_0 b/m$ is the normalised electric field, E_0 the electric field on the outer conductor, e and m respectively the charge and mass of one electron, and R the time-averaged position of the electron, is valid for GHz frequencies [21].

[21] Becerra (2007)

Hence, in the MHz range of frequencies used in this work, the presented analytical method could not be applied and an alternative should be found.

Somersalo et al. developed a computational method to analyse the multipactor phenomenon in different RF structures to determine the multipactor power, type (single-sided or double-sided), order, phase space's range responsible for the process, and multipactor electrons' trajectories. In their formulation, the electron trajectories are described by a discrete dynamical system in an appropriate phase space for the multipactor occurrence. The latter corresponds to the fixed and n -periodic points of the defined phase space [96].

[96] Somersalo et al. (1994)

To study the multipactor, the authors defined a *Poincaré* or *first return map*, where they introduce the concept of "fixed point" and " n -periodic point" for the electron returning to its initial position in the phase space respectively after one and n impacts. These electrons are the ones contributing to the multipactor. They divided, therefore, the phase space into two sets: *i*) a bright set corresponding to the electrons emitted in the vacuum, and contributing, hence, to the multipactor, and *ii*) the shadow set corresponding to the electrons captured by the walls of the structure.

To search for the fixed points in the phase space, *i.e.*, contributing to multipactor and belonging, hence, to the bright set, they defined a distance function telling how far the electron trajectory is from its initial point after n -impacts. For a high number of impacts, if the distance function is small, then the electron is considered a contributor to the multipactor occurrence [92].

[92] Somersalo E. et al. (1995)

Furthermore, to account for the electron emission yield of the walls, *Somersalo et al.* defined a multiplicity function telling how many secondary electrons are emitted upon walls' collisions of each initial electron of the phase space. The described formulation allows them to track the electrons in the simulated domain.

To determine if a given power triggers the multipactor in the structure, they count the number of electrons remaining in the bright set after a given number of iterations while accounting for the electron emission yield. If the latter, the so-called "enhanced electron function," is relatively large, the tested power is considered a multipactor-triggering power [97].

[97] Yla-Oijala (1997)

Somersalo *et al.* analysed the multipactor in a coaxial transmission line and extracted from the results four scaling laws: *i*) the single-sided multipactor voltage, for a coaxial cable of fixed characteristic impedance, follows $(fd)^2/(n+1)$, n being the multipactor order, *ii*) a scaling law for the double-sided multipactor voltage, with respect to the frequency and dimensions, that agrees with Woo's experimental laws $(fd)^2$, and *iii*) for varying line impedance, the single-sided, and double-sided multipactor voltages follow respectively $(fd)^2 Z_0$ and $(fd)^2 Z_0^{3/2}$ [93]. Furthermore, the authors found that the average impact energy of the electrons obeys roughly an $(fd)^2$ law, and the multipactor voltage thresholds are inversely proportional to the multipactor order.

[93] Somersalo et al. (1998)

In [98], the authors simulated the minimum voltage thresholds on a wide range of $f \times d$ products for the onset of multipactor, using the commercial software CST Particle Studio and compared the results with Woo's published experiments [72]. They concluded that the level of agreement depends on the secondary electron emission yield model.

[98] Langelloti et al. (2020)

[72] Woo (1968)

Most of these studies focused on predicting the minimum breakdown voltage for multipactor onset. However, for magnetic confinement-based fusion reactors' applications — where high power (MW range) antennas are used — we are also interested in predicting the maximal breakdown voltage triggering the multipactor phenomenon, for which little literature exists.

3.8.3.2 Mixed and standing wave cases

In [93, 97], the authors applied the computational method described in Section 3.8.3.1 on a quarter-wavelength coaxial transmission line operating under travelling (TW), mixed (MW), and standing waves (SW). The coaxial is excited only from one side by applying a voltage source between the inner and outer conductor. Hence, the multipactor power threshold is defined as incident power. Following the electron trajectories in the structure, they used their developed method to determine multipactor features: incident powers, type, and order.

[93] Somersalo et al. (1998)

[97] Yla-Oijala (1997)

For the SW case, the authors start the analysis with initial electrons seeded on both conductors. They found that, for SW, the surviving trajectories, being the electrons causing multipactor, are the ones that appear near the maximum of the electric field. Moreover, they stated that the contribution of the surviving electrons far from the electric field's maximum appeared at high incident powers, and the non-phase focusing electrons far from the electric field's maximum drift toward the minimum of the electric field. They deduced that, within their power-incident range, the multipactor for coaxial lines operating in SW is due to the electric field. For the single and double-sided multipactor types of SW cases, they plotted a chart giving the various power multipactor bands as a function of the frequency, coaxial characteristic impedance, and dimensions.

In addition, they found similar processes type but different multipactor electron trajectories for SW and TW. Indeed, for the TW case, the multipactor electrons travel along the same direction of the wave propagation but in a slow movement compared to the radial direction — the ratio of the axial to radial direction is 1/10 for a coaxial transmission line. Furthermore, the authors proposed a scaling law relating the multipactor

powers of the TW case to those of the SW case. This scaling law is given by $P_{TW} = 4P_{SW}$ since the peak voltage of the SW is twice that of the TW in such a case.

For the MW case, they found that when the reflection coefficient is higher than zero (TW case), the multipactor resonance regime splits into two distinct modes. The first set of resonance modes will coincide with the *electric* multipactor mode of the SW case. The second set of resonance modes shifts exponentially to very high incident powers and is caused by the magnetic field. The multipactor caused by the magnetic field is known as the *magnetic* multipactor mode. A scaling law exists between the electric multipactor powers of the MW case and the TW multipactor powers and is given by $P_{MW} \sim \frac{1}{(1+R)^2} P_{TW}$.

They summarised that the multipactor for the TW case is of a mixed nature, where both the electric and magnetic fields contribute to the multipactor. But as the reflection coefficient increases, the multipactor processes are dissociated into electric and magnetic multipactor processes. In contrast, for the pure SW case, the multipactor resonance mode appears close to the maximum of the electric field, and no multipactor is maintained at the electric field nodes. *Somersalo et al.* indicate that the *magnetic* multipactor process does not exist for this case since it requires infinite incident power to be sustained. However, some multipactor processes have not been considered due to numerical limitations, and the scanned incident power range is limited to hundreds of kW.

[95] Pérez et al. (2009)

In [95], the authors developed a numerical model — similar to the one developed by *Somersalo et al.* — to predict the multipactor thresholds in transverse electromagnetic (TEM) mode, for cylindrical coaxial transmission lines of infinite length in the propagation direction (z). They excited the coaxial from both ports so that the resultant wave is a superposition of two waves propagating in opposite directions. In their paper, three types of RF signals of different reflection coefficient $\Gamma = Re^{j\psi}$ (where R and ψ are respectively the magnitude and the phase) are studied: *i*) travelling wave (TW) corresponding to a null reflection, where $R = 0$. *ii*) Mixed wave (MW) is defined by a reflection coefficient of magnitude $0 < R < 1$ and phase $\psi = \pi$. *iii*) Standing wave (SW) corresponding to $R = 1$, and $\psi = \pi$.

Their model was based on the computation of effective electrons' trajectories that are perturbed by the electromagnetic fields and the inter-electron interactions to account for the space charge effect due to Coulombian repulsion. Their simulation tool allows determining the number of electrons released after each collision based on the TEEY data of the tested material.

They focused only on the lower voltage multipactor thresholds and found that the voltage multipactor thresholds remain the same for the TW, MW, and SW cases for all $f \times d$ (where f is the frequency, and d is the distance separating the inner conductor from the outer one) products lower than a threshold. Moreover, they found that above $700 \text{ MHz} \cdot \text{cm}$, the lower voltage multipactor thresholds are higher for the SW than the case of a TW, and independently of the choice of f and d , the characteristic impedance, and the chosen material.

They attributed this to the null electric field regions in the wave propagation direction (SW nodes), absorbing the electrons before the multipactor phenomenon ignition. Indeed, when the frequency increases, the distance between adjacent electric field nodes is reduced, and therefore, the travel time of an electron to the next node is shorter. The latter mitigates the multipactor occurrence, as for high-order multipactor, more impacts are needed before additional electron release. Consequently, in the SW case, a higher multipactor voltage is needed for the multipactor to take place.

In addition to that, *Pérez et al.* analysed the axial drift produced by the axial component of the acceleration vector, and they found the following:

- ▶ For the TW case, in the double-sided and single-sided multipactor, a net force drives the electrons toward $z > 0$;
- ▶ For the SW case, in the double-sided multipactor, on average, there is an axial drift toward $z < 0$ until the electron reaches an electric-field node, where it starts oscillating around it;
- ▶ For the SW case, in the single-sided multipactor, there is a net force that drives the electrons toward $z < 0$.

In [99, 100], the author performed simulations of multipactor discharge using CST Particle Studio for a coaxial transmission line subject to SW. The findings of [95] were confirmed to come from the ponderomotive force, which pushes electrons toward the low electric field region and contributes to mitigating multipactor. In addition, three multipactor zones have been identified in the SW mode: *i)* the low electric field zones showing the similarity between the multipactor for SW and that for TW, where the ponderomotive force has no effect. *ii)* A medium electric field zone where this force gains strength and secondary electrons are more concentrated in the electric field nodes. *iii)* The high electric field zones where the concentration of electrons is denser on a small volume located in the electric field nodes.

The results from *Romanov's* work disagreed with the analysis done by *Somersalo et al.* for the SW case since their simulations have shown multipactor near the nodes of the electric field, and, therefore, that the existence of the ponderomotive force has a qualitative and quantitative effect on the multipactor results.

3.8.3.3 Other interesting findings

Graves [20] has provided the multipactor energy distribution functions for two parallel plates and coaxial transmission lines at a range of very high frequencies using two methods that have shown a good agreement: *i)* an experiment-based method using a multipactor test-bed relying on retarding potential analysers (RPAs) to measure the current-voltage characteristics, and *ii)* a simulation-based Monte Carlo method using a 1-D particle tracking simulator.

We summarise, herein, his main findings for the 50Ω coaxial transmission line geometry [20]. He observed that the multipactor discharges give a maximum electron current density of the order of 1 A m^{-2} , that increases with the TEEY increase and that absorbs 10% to 15% of the RF power.

[99] Romanov (2011)

[100] Romanov (2011)

[95] Pérez et al. (2009)

[20] Graves (2006)

[20] Graves (2006)

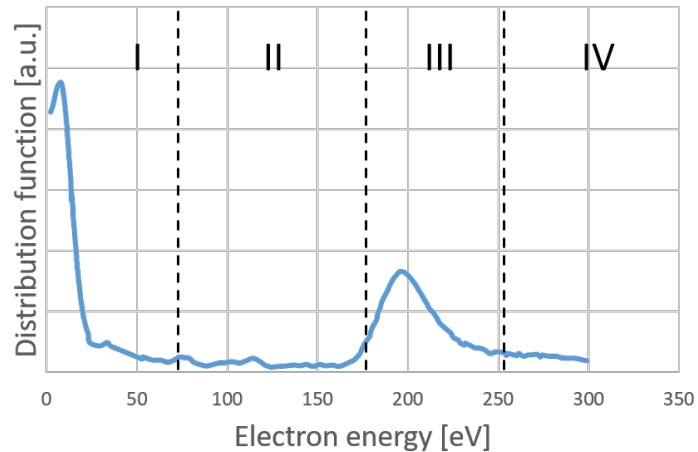


Figure 3.6: Distribution function for the multipactor electrons in a coaxial transmission line at a frequency of 70 MHz, and an RF voltage of 250 V. The distribution is divided into four different regions. Data are extracted from (Graves (2006)).

Furthermore, the multipactor electrons' energy distributions for frequencies between 55 MHz and 150 MHz are constituted of two main populations: *i)* a high energy population — resulting from the multipactor resonance conditions and the electric field's radial dependence — seen at 80% of the multipactor voltage threshold, and responsible for sustaining the multipactor. *ii)* A low energy population from 0 to 75 eV resulting from the space charge effects — de-focused electrons and secondary electrons emitted from the RPA entrance grid.

In addition, he showed that there is a high energy tail resulting from the electrons starting and impacting at the outer conductor, and hence, suggesting the outer-conductor multipactor occurrence — single-sided multipactor — for the coaxial transmission line.

An example of the energy distribution of the electrons contributing to the multipactor for the coaxial transmission line is represented in Figure 3.6. The illustrated energy distribution corresponds to an RF voltage of 250 V at a frequency of 70 MHz and is divided into four regions. Region I corresponds to the low energy population resulting from the space charge effects and the entrance grid's electron emission, causing the electrons to fall outside the resonant phase. The latter defocusing results in low energy electrons' impact. Region II corresponds to the unfavourable range of energy for resonance. Region III corresponds to the high energy population fulfilling the resonance conditions, with a peak located at 200 eV, being the 80% of the 250 V RF voltage. Region IV is the tail region corresponding to the electrons starting and impacting at the outer conductor, responsible for the multipactor occurrence at the outer conductor.

Moreover, *Graves'* work identified the multipactor-induced glow discharge as the main cause for the neutral pressure limitations¹⁶ observed on Alcator C-Mod, and constraining its operation. Indeed, the development of the gas breakdown is affected by the electron population's increase and the gas density increase by molecules' desorption from the surfaces. The latter increases the rate of gas ionisation by electron impact. To solve this problem, he proposed a surface treatment of 50 μm aluminium oxide sandblast on the copper electrodes to prevent the multipactor occurrence.

16: An example of the pressure increase is given in Figure 3.7.

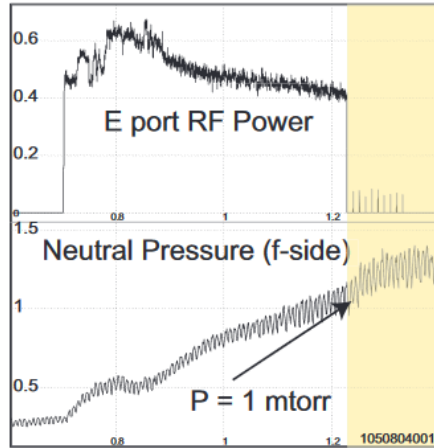


Figure 3.7: Neutral pressure limit observed on Alcator C-Mod ICRH antenna at port E. The yellow region shows short RF pulses signalling the failure of the antenna's restart at a pressure beyond the limit 0.133 Pa. The results are taken during typical operation of the tokamak with a 5.4 T magnetic field at the centre of the torus. Data source (Graves (2006)).

Becerra analysed experimentally and numerically the multipactor in a $50\ \Omega$ cylindrical coaxial transmission line in the presence of a constant and uniform magnetic field transverse to the electromagnetic wave propagation to approximate the Alcator C-Mod tokamak magnetic field lines as measured in the vacuum sections of the transmission lines of an ICRH antenna [21].

Experimentally, he showed that the presence of the DC magnetic field decreases the degree to which the multipactor detunes the RF system¹⁷, as the reflection coefficient measured at the source is higher when the multipactor occurs in an unmagnetised case than that of a multipactor occurrence in a magnetised case. Although this means that the multipactor is less likely to damage the high-power generators, it becomes more difficult to detect the discharge in such cases. *Becerra* explained the reduction in the detuning by the slight change in the impedance of the line as the electrons are confined around the magnetic field lines, leading to a decrease in the likelihood of an opposite-electrode impact [21].

Furthermore, he showed that accounting for the DC magnetic field decreases the lowest voltage thresholds triggering a glow discharge and the minimum pressure at which it occurs — compared to the unmagnetised case.

Although his simulations showed that the DC magnetic field highly affects the electron trajectories, the experimental observation was not explained by the conducted simulations, as the obtained results did not show a higher electron population growth nor a higher averaged electrons' emission yield for the case of a high magnetic field when compared to the unmagnetised case. The latter could be accounted for by the limitations of the simulations, such as the simulation duration of five RF periods and the absence of the space charge effects.

3.9 Chapter Summary and Perspectives

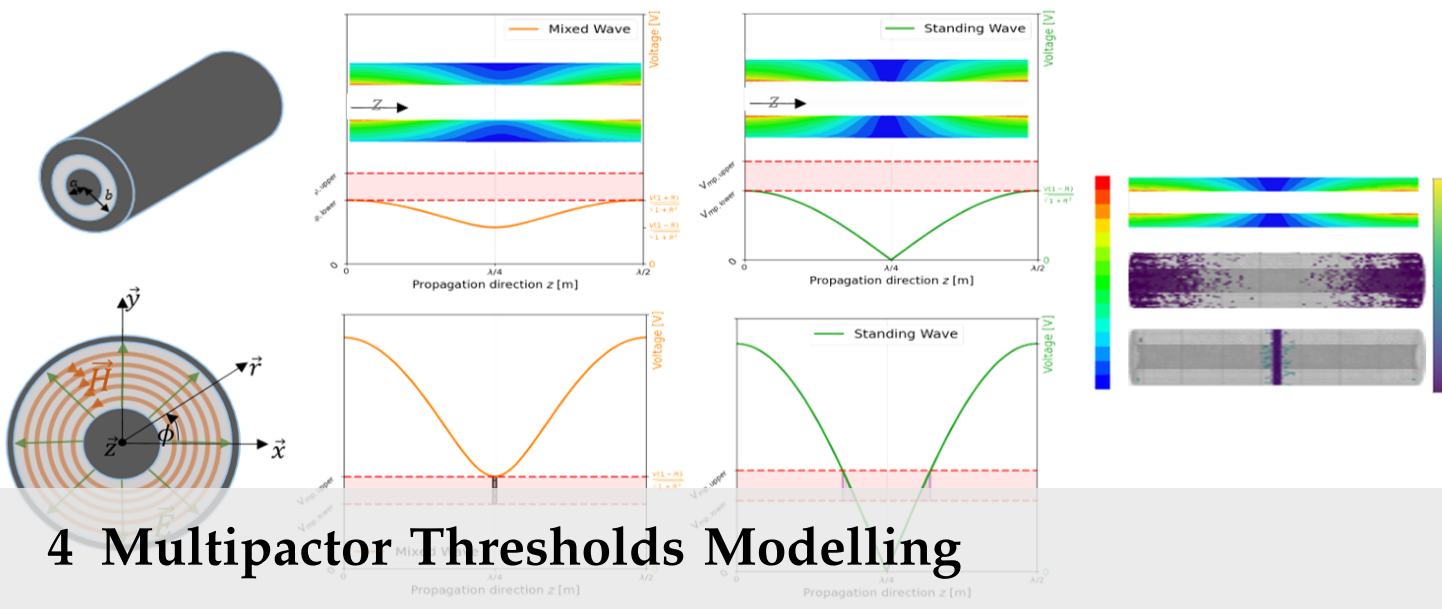
In this chapter, we reviewed all the findings and scaling laws on multipactor for the parallel plates geometry and the cylindrical coaxial transmission lines. The latter is interesting, as the WEST ICRH antennas

[21] Becerra (2007)

17: Multipactor discharges are known to detune the system by changing the transmission lines' impedance.

[21] Becerra (2007)

are composed mainly of various coaxial sections. In the next chapter, we will evaluate the multipactor thresholds for a cylindrical coaxial transmission line subjected to different wave patterns.



4 Multipactor Thresholds Modelling

Knowledge is better than wealth... Wealth decreases with spending, but the more you make use of knowledge, more it increases... Those who acquire knowledge will live, by virtue of their knowledge & wisdom, even after their death.

Nahjul Balagha — The peak of Eloquence

As multipactor experiments are expensive to realise, especially with complex components of big dimensions such as the one used as ion cyclotron resonance heating (ICRH) systems for fusion reactors, using numerical tools for multipactor prediction is valuable. In this manuscript, we rely, therefore, on particle simulators to predict the lowest and highest multipactor thresholds.

However, as evidenced in the previous chapters, the multipactor thresholds are highly dependent on the RF device geometry, frequency of operation, and material properties. Added to these dependences are the configuration issues of the simulators to carry out realistic multipactor analysis.

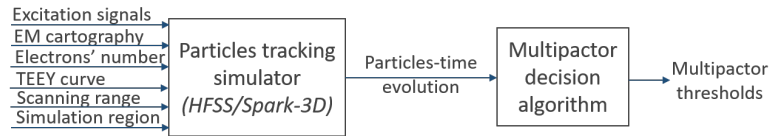
In this chapter, we describe the multipactor software tools used in this manuscript (Section 4.1). Then, we discuss our multipactor decision algorithm used for both software tools (Section 4.2). Furthermore, we investigate the multipactor thresholds' determination in the case of standing waves patterns (Section 4.3) before illustrating the results on the cylindrical coaxial transmission lines (Section 4.4).

4.1 Numerical Multipactor Software Details

We use numerical simulations to determine the multipactor thresholds for any RF three-dimensional (3D) structure. In particular, we use commercial-available particle simulators on the electromagnetic (EM) component's model to predict the multipactor thresholds. This type of multipactor thresholds' prediction is among the most precise methods provided that we have good meshing¹, and parameters' configuration.

1: The meshing refers to the decomposition of the structure in polyhedra so that the EM fields are computed at the vertices of each polyhedron.

Figure 4.1: A generic block diagram for a multipactor thresholds' prediction using a particles' tracking simulator like Spark-3D or Ansys-HFSS.



The particles' tracking algorithm requires the knowledge of the electric and magnetic field cartography for the multipactor-prone device, which could be cumbersome and resources demanding in terms of CPU time and memory for complex geometries, especially if a high meshing density is needed. Moreover, the simulation set-up, the configuration parameters, and the results' interpretation highly affect the multipactor predicted results. Hence, numerical simulations require particular attention.

Few commercial particle simulators have been used in the last decade for multipactor analysis. Among these commercial software are:

- ▶ Spark-3D from Dassault Systems;
- ▶ CST Particle Studio (CST-PS)²;
- ▶ Ansys-HFSS Multipaction³.

In this manuscript, the software products Spark-3D* [101] and ANSYS-HFSS Multipaction[†] are used.

We describe, first, the generic block diagram for a multipactor thresholds' prediction simulation, given in Figure 4.1. A particle tracking simulator — Spark-3D or Ansys-HFSS — requires as input the following:

- ▶ Ports' excitation signals⁴ — responsible for varying the reflection coefficient of the structure;
- ▶ EM fields' cartography of the RF device depending on the chosen ports' excitation;
- ▶ Electron seeding characteristics: the number of electrons, the initial distribution of the seeded electrons, and the emitted electrons' energy distribution⁵;
- ▶ TEEY curve(s) for the different surfaces involved in the multipactor simulation;
- ▶ Scaling factors' scanning range;
- ▶ Multipactor simulation region(s).

A multipactor simulation consists of seeding electrons in the user-defined multipactor region. In the latter, the electrons are accelerated by the EM fields. The electrons' trajectories are perturbed by the EM fields and dynamically computed in time. Once an electron collides with one of the surfaces, for which we have assigned a TEEY data curve, the TEEY value defining the number of released electrons due to the electron-surface collision is evaluated. This particle-tracking results in an electron population evolution with time, being the only required entry for predicting the multipactor thresholds.

The EM fields' cartography affects the accuracy of the multipactor simulation, as the meshing should be suited to the structure's geometrical details and the regions subject to very high EM fields, such as the sharp edges. Consequently, the meshing should be dense enough in the multipactor simulation region to obtain a good representation of the EM fields for

2: CST-PS is not described herein.

3: Starting 2020.

[101] Vicente (2017)

4: The ports' excitation are the mean incident powers on the activated ports of the RF structure.

5: For both Spark-3D and Ansys-HFSS, the user has no choice to change the emitted electrons' energy distribution, yet it affects the simulation results.

* Version 1.6.3.

† Version 2023R2.

the electrons' trajectories computation to be accurate. In most cases, the meshing needed to converge in terms of multipactor predicted results is denser than the one required to get S-parameters convergence. Therefore, we perform a convergence study of the multipactor prediction results versus the tetrahedral meshing size before choosing the mesh properties of any studied structure.

The number of seeded electrons is also relevant for accurate multipactor prediction and depends on the simulation region's dimensions. Therefore, there is a minimum required electron density for the multipactor simulation results to be convergent, determined before any multipactor prediction simulation by performing an analysis for the multipactor thresholds' variation with respect to the number of seeded electrons in the simulation region.

The TEEY data for the different surfaces of the structure under study remains the most relevant parameters to conduct accurate multipactor simulations, as most of the discrepancies between the measured and simulated multipactor thresholds are explained by the uncertainties on the TEEY data curve⁶. Therefore, we prioritise TEEY data curves obtained through measurement campaigns for representative samples of the devices' material and operational conditions.

6: The TEEY data curve used in simulations is not representative of the TEEY characteristics of the measured device's material.

The scanning range is a user-defined range of scaling factors over which we check for multipactor vulnerability. Spark-3D and Ansys-HFSS have an option for an automatic scaling factors sweep to search for the lowest multipactor threshold. However, as we are interested in both the lowest and highest multipactor thresholds' prediction, we have developed a Python-based algorithm for scaling factors' sweep to search for the multipactor triggering input powers up to a certain user-defined precision. This algorithm allows a user-defined scanning range of scaling factors as input. The latter could help reduce the simulation time if the user has an *a priori* knowledge of the first multipactor guess range. However, it could also be automatically defined without initial guessing.

A scaling factor is a multiplying factor by which the initial ports' excitation — incident ports' power — are scaled to check for the occurrence or not of the multipactor phenomenon. Assume that we want to check the multipactor thresholds for an RF structure having N -activated ports, where each port i has an initial incident power P_i , $i = 1, \dots, N$; then, for each tested scaling factor f the following steps are done:

- ▶ The ports are scaled by f such that the ports' excitation powers become $f \times P_i$, $i = 1, \dots, N$.
- ▶ The electrons' trajectories are computed in the new EM field cartography.
- ▶ For each scaling factor f , the software calculates the temporal evolution of the number of electrons.
- ▶ Based on the number of particles versus time data, the multipactor occurrence decision is made.

Spark-3D and Ansys-HFSS have their own multipactor decision criteria⁷, based on the electrons' population evolution, to decide whether or not a multipactor discharge takes place for a given scaling factor. However, we have developed a common multipactor criterion to evaluate if a multipactor is triggered in a particular geometry. The developed multipactor

7: The available detection criteria of Spark-3D and Ansys-HFSS are not described herein.

decision criterion is based on the electron-population-time-evolution and is two-fold:

- ▶ It enables a direct and meaningful comparison of the multipactor predicted thresholds for a particular geometry between Spark-3D and Ansys-HFSS.
- ▶ Once associated with the automatic scanning sweep developed algorithm, it enables predicting the lowest and highest multipactor thresholds causing multipactor.

The developed multipactor criterion is detailed in Section 4.2.

In the following subsections, we describe the particle tracking simulators' properties, considered herein: Spark-3D and Ansys-HFSS Multipaction.

4.1.1 Spark-3D from Dassault Systems

Spark-3D is a full 3D particle tracking simulator employing a leap-frog-based algorithm for electrons' path integration.

Spark-3D is convenient for conducting multipactor and corona discharge simulations. To use Spark-3D, the cartography of the electromagnetic fields of any geometry must be imported before running the multipactor calculation. The steady-state EM fields should be computed using one of the external compatible frequency domain electromagnetic solvers: FEST-3D, CST Microwave Studio, or Ansys-HFSS. In this manuscript, ANSYS-HFSS is used for solving the electromagnetic fields of the geometries in the frequency domain.

Once fed into Spark-3D, the software performs an internal interpolation to compute the fields at each mesh location of the region under analysis. Spark-3D allows the user to analyse multipactor in the whole structure or to define a multipactor analysis region: a parallelepiped box defined to bound the region where multipactor analysis is performed⁸. By default, the multipactor region is the complete imported structure.

8: The electrons impacting surfaces of the multipactor analysis region corresponding to vacuum conditions are automatically absorbed.

Defining multipactor analysis region(s) is highly recommended as it reduces the computational resources' need and achieves higher seeded electrons' density than the whole structure's analysis with the same number of electrons. Besides improvements in the computational and statistical performance of the simulation, defining multipactor analysis regions for big-dimensional RF structures, such as the ones discussed in this manuscript, allows for determining the multipactor critical area(s) of the device under study.

As mentioned before, the initial number of seeded electrons is a user-defined value, and these electrons are seeded only once at the beginning of the simulation run. By default in Spark-3D, the initial seeded electrons are non-uniformly distributed in the multipactor simulation region while favouring high field regions, as they are multipactor-prone regions. However, the user can choose a uniform distribution for the initial seeded electrons within the multipactor region volume.

The non-uniform distribution could be problematic when exploiting the highest multipactor threshold for a multipactor region and the complex structures with standing wave patterns. These cases are tricky since it was observed that the multipactor occurrence is no more restricted to

high electric field regions. Consequently, in our simulations, the uniform electron distribution is prioritised.

Spark-3D is a particle-in-cell (PIC) code and is, therefore, based on macro-particles assumption while ensuring enough statistical quality for the problem. Each macro-particle is equivalent to an integer number of electrons. The latter is upgraded automatically at each time step, depending on the number of existing electrons and their distribution among all macro-particles. Furthermore, electrons and macro-particles may coexist while having different sizes. When a macro-particle composed of N electrons impacts a surface mesh having a TEEY > 1 , the released macro-particle will be composed of $N \times \text{TEEY}$ electrons. This macro-particle may split, as well, into smaller macro-particles and/or single electrons.

For a given geometry to be analysed, TEEY boundary conditions must be defined for the structure's surfaces. However, Spark-3D in its used version does not allow the user to assign multiple TEEY data describing the presence of multi-material structure⁹.

Spark-3D provides three different options for TEEY surface assignment:

- ▶ Import TEEY data curve in ASCII code format — for example, obtained from TEEY measurement campaigns. A linear piece-wise interpolation is used to determine the TEEY between two imported data points, and outside the imported range of incident energies, the TEEY is considered zero.
- ▶ Choose a TEEY data curve from predefined curves for a range of widely used typical materials (copper, silver, aluminium, *etc.*). These software-integrated curves are based on the modified Vaughan model.
- ▶ Define the TEEY parameters: E_1 (the first cross-over energy), E_{\max} (electrons' incident energy at the highest electron emission yield), TEEY_{\max} (maximum total electron emission yield), and TEEY_{low} (electron emission yield for incident energies below the first cross-over — for the elastically back-scattered electrons). Then, the TEEY data curve is generated automatically from Vaughan's modified model.

The energy distribution of the emitted electrons is a Maxwell-Boltzmann distribution [39] with the most probable energy of 4 eV. The angular distribution for secondary electrons is a cosine law.

[39] Rudberg (1936)

For our version of Spark-3D, only Continuous Wave (CW) single-carrier operation is supported and defining a DC bias field is allowed. Moreover, space charge effects are not taken into consideration.

Finally, we will introduce the statistical post-simulation data provided by Spark-3D and used for the multipactor location's determination — multipactor susceptible zone. Spark-3D gives four types of statistical data averaged over the simulation time. Each statistical data is given for each surface mesh of the structure. Let k be the index of the surface mesh of surface s_k for which the following statistical data are associated:

- ▶ Average secondary emission yield (SEY): δ_k referring to the average secondary emission yield of the material at mesh k ;

9: From the 2021 version onward, multi-material structures are allowed for multipactor simulations.

Table 4.1: Main features' comparison between Spark-3D and Ansys-HFSS.

Feature	Spark-3D	Ansys-HFSS
EM fields' computation	Imported in frequency domain from: FEST-3D, CST, or Ansys-HFSS	Computed directly in frequency domain
TEEY data	Modified Vaughan or imported data	Modified Vaughan or imported data
TEEY extrapolation	Zero	Constant value
Electrons' seeding	Uniform or non-uniform distribution without re-seeding	Uniform distribution without re-seeding
Simulation region	Whole structure or user defined	Whole structure or user defined
Macro-particles	Automatic electrons and macro-particles' grouping and ungrouping	Macro-particles and electrons coexistence
Sapce charge effects	Not included	Included

- ▶ Impact density: ρ_k^i referring to the electrons impact density [e/m^2] at mesh k ;
- ▶ Average impact energy: E_k^i referring to the average impact energy of electrons impacting surface mesh k [eV];
- ▶ Emission density: ρ_k^e referring to the electron emission density [e/m^2] for mesh k , and it represents the number of emitted electrons minus the number of absorbed electrons per unit surface.

Using these data, we can evaluate the average TEEY and the average electrons' impact energy [eV] given by the following:

$$\delta_{\text{avg}} = \frac{\sum_{\Omega} \rho_k^i s_k \delta_k}{\sum_{\Omega} \rho_k^i s_k} \quad (4.1)$$

$$E_{\text{avg}} = \frac{\sum_{\Omega} \rho_k^i s_k E_k}{\sum_{\Omega} \rho_k^i s_k} \quad (4.2)$$

where Ω is the set or subset of the simulated region's surface meshes.

4.1.2 Ansys-HFSS Multipaction

Ansys-HFSS Multipaction package is a full particle-in-cell (PIC) simulator providing a finite element approach to simulate multipactor in vacuum devices and employing a leap-frog-based algorithm for electrons' path integration.

Conducting HFSS multipactor simulations requires time-harmonic fields to be solved. Furthermore, it requires defining a multipactor analysis region consisting of one or multiple objects.

In Ansys-HFSS, the initial number and velocity of electrons are user-defined values. The electrons are seeded uniformly in the multipactor simulation's region and only once at the beginning of the simulation run.

For a given geometry to be analysed, TEEY boundary conditions must be applied to vacuum-material interfaces, as electrons will be absorbed by surfaces in contact with vacuum but not covered by TEEY boundaries — such as port faces allowing the electrons to leave the simulation domain. Ansys-HFSS permits the user to assign multiple TEEY data for the same structure — a multi-material structure, which is an advantage over Spark-3D.

In Ansys-HFSS, the user must specify if a surface is a dielectric to allow the accumulation of positive surface charges after secondary electrons' release or negative surface charges after primary electrons' absorption.

Ansys-HFSS provides two different options for TEEY surface assignment:

- ▶ Import TEEY data curve in ASCII code format — for example, obtained from TEEY measurement campaigns. A linear piece-wise interpolation determines the TEEY between two imported data points. Outside the imported range of incident energies, the TEEY is considered a constant equal to the TEEY entry of the lowest (respectively highest) impact energy in the tabulated data.
- ▶ Define the TEEY parameters: E_1 and E_2 (the first and second cross-over energy), E_{\max} (electrons' incident energy at the highest electron emission yield), TEEY_{\max} (maximum total electron emission yield), E_0 and TEEY_0 (electron emission yield for incident energies between zero and E_0). Then, the TEEY data curve is generated automatically from non-classical¹⁰ Vaughan's modified model.

10: In Ansys-HFSS, there is a built-in optimisation for Vaughan's modified model.

The energy distribution of the emitted electrons is a *Chung and Everhart's* distribution [50], for which the work function is a user-defined value. The angular distribution for secondary electrons is a cosine law. Moreover, the elastic and inelastic scattering are accounted for in Ansys-HFSS.

[50] Chung et al. (1974)

For Ansys-HFSS, multiple-carrier operation and uniform DC biasing are supported. Moreover, space charge effects are taken into consideration.

Table 4.1 summarises the main features of each of the described multipactor tools.

4.2 Multipactor Decision Algorithm

In this section, we discuss the derived multipactor criterion that we applied in Spark-3D and Ansys-HFSS. Once we have admitted a multipactor criterion, we developed a multipactor decision algorithm, which takes, as a single input, the electron population time evolution generated by any particle tracking simulator. As an output, it gives a binary value indicating whether or not a multipactor discharge occurs for each tested scaling factor — the second block in the generic multipactor simulation's block diagram of Figure 4.1.

First, we mention two widely used multipactor criteria in the literature. Then, we describe the chosen criterion and show some results validating its preference.

Two multipactor criteria derived from the electron population time evolution are found in the literature to estimate if multipactor discharge is likely to occur. In the following, we briefly describe each criterion:

► **The threshold criterion — final number of electrons**

At the end of the simulation time, the remaining number of electrons is checked, and if it exceeds a certain threshold, a multipactor discharge is assumed. The predefined threshold depends on the number of electrons seeded at the beginning of the simulation and is expressed as $k \times N_{e,0}$; where k is an integer number, and $N_{e,0}$ is the initial number of electrons [102]. *Plaçais et al.* chose $k = 2$ in their simulations, which mainly tested multipactor in parallel plates geometries and rectangular waveguides¹¹.

► **The growth rate criterion**

In this case, the multipactor threshold is determined based on the calculated growth rate of the electron population. In [103], the authors defined an exponential coefficient a to predict an increase of the electron population in the case of multipactor, given by:

$$a = \frac{\log_{10} N_{e,f} - \log_{10} N_{e,0}}{t_f - t_0} \quad (4.3)$$

where $N_{e,f}$, $N_{e,0}$ are the number of electrons at t_f , a pre-selected time, and the number of electrons at the initial time t_0 , respectively. The multipactor criterion depends on a : if $a > 0$, a multipactor discharge is assumed. Otherwise, there is no multipactor.

We have tested both criteria to choose the one that corresponds more to the type of geometries we are interested in checking its vulnerability to multipactor, *i.e.*, geometries with a non-uniform electric field, such as cylindrical coaxial transmission lines. However, for the second criterion, we calculated the coefficient a such as it expresses the rate of growth or decrease of electron population over the last N periods, where N is a predefined number dependent on the geometry, and the software used for generating the particle-time evolution data.

The tests correspond to a measured TEEY data curve of a stainless-steel silver-coated sample representative of the ICRH antennas. First, the sample was subjected to a baking phase for two hours at 190 °C. Then, the TEEY data were measured at normal incidence using the sample bias method detailed in Chapter 2. These measurements were done in the framework of *A. Plaçais'* thesis [102] at ONERA/DPHY, and are represented in blue in Figure 4.2. The tested geometry is a cylindrical coaxial transmission line of characteristic impedance $Z_0 = 50 \Omega$ — corresponding to $b/a = 2.3$, and an inter-electrode separation distance of 4 cm. The frequency ranges from 10 to 150 MHz for a travelling wave pattern case. The number of seeded electrons is 2000, and the predefined threshold of the first criterion is 4000, two times the initial electron number.

Figure 4.3 illustrates the multipactor voltage thresholds, obtained for each tested criterion, as a function of the $f \times d$ product, where f refers to the frequency and d to the inter-electrodes distance. Ten consecutive similar runs are done for each tested case to avoid statistical errors. The results corresponding to the threshold and growth rate criteria are represented as green cross points and blue plain curves, respectively. The

[102] Plaçais (2021)

11: Geometries with non-uniform electric field were not tested in this work.

[103] Souнас et al. (2011)

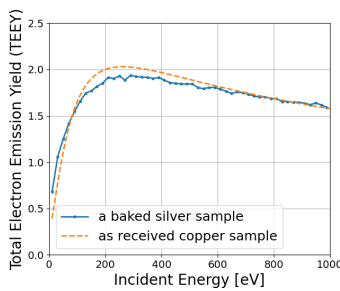


Figure 4.2: In blue, the measured TEEY data at normal incidence for a silver-coated stainless-steel sample, baked at 190 °C for two hours. In orange, the measured TEEY data at normal incidence for an as-received copper sample. Both measurements are done at ONERA/DPHY.

[102] Plaçais (2021)

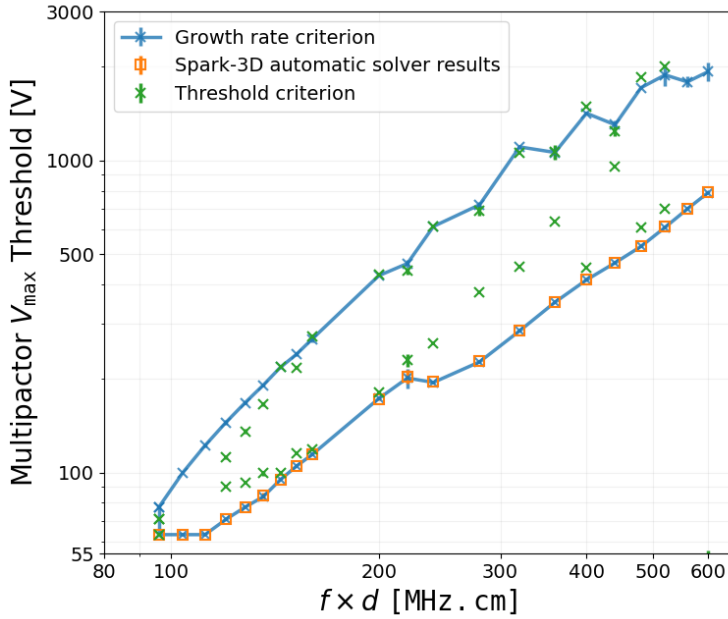


Figure 4.3: Simulated susceptibility data for a coaxial transmission line of characteristic impedance $Z_0 = 50 \Omega$, and inter-electrode distance $d = 4$ cm. The frequency of operation is varied in the range $[10 - 150]$ MHz. The plots are obtained for the TEEY measured data of a silver-coated stainless steel sample, illustrated in blue in Figure 4.2. The multipactor decision is made using three different criteria: *i*) the threshold criterion represented as green cross points, *ii*) the growth rate criterion represented in plain blue line, and *iii*) the Spark-3D automatic solver's estimated lowest multipactor thresholds represented as orange square points. The time-particle evolution data are obtained using Spark-3D.

orange squares correspond to the lowest multipactor voltage thresholds obtained by the automatic multipactor decision algorithm implemented in Spark-3D.

The built-in multipactor criteria in Spark-3D¹² and Ansys-HFSS are based on an exponential fitting for the electron population evolution in time to check whether there is a positive or negative growth of the electron number in time. Therefore, they are a software-property implementation of the growth rate criterion.

First, we conclude on the good agreement between the multipactor predictions obtained by the growth rate-based algorithm and that of the automatic Spark-3D multipactor-decision implementation. The observed agreement validated, hence, the validity of our developed algorithm. Second, the growth rate criterion is more reliable than the threshold criterion, especially at low and high $f \times d$ products. Indeed, no multipactor is found for the second, third, and last two tested frequencies when using the criterion based on the fixed number of electrons. The absence of multipactor detection could be related to the slow electrons' increase with respect to the simulation time and predefined threshold since, for the first few RF periods, a drop in the number of particles is observed due to the loss of the out-of-phase electrons. Therefore, the simulation ends before the electrons reach the predefined threshold.

We suggest two simple solutions to minimise the disparity between the results obtained using the threshold criterion and those obtained using the growth rate criterion:

- ▶ Increase the simulation duration to ensure that the simulation duration is sufficient for the electron growth to reach the predefined threshold $k \times N_{e,0}$, in case of multipactor occurrence. However, this could be time- and resource-consuming.

12: In Spark-3D, there are various built-in multipactor decision criteria suitable for different types of signals, but they are not described in this manuscript.

- Reduce the predefined threshold, which could increase the probability of false positive multipactor detection, particularly in mixed wave patterns. In these cases, we observed an initial increase in the electron population during the first few RF periods, followed by a subsequent reduction and extinction. This phenomenon is primarily due to the force that attracts electrons towards regions of low electric field, known as the ponderomotive force. This effect has also been documented in previous studies [95, 99, 100].

[95] Pérez et al. (2009)

[99] Romanov (2011)

[100] Romanov (2011)

Therefore, to avoid false positive and cumbersome simulations' additional requirements, we stick to the growth rate criterion for the multipactor decision-based algorithm searching for the lowest and highest multipactor thresholds.

4.3 Multipactor Thresholds under Standing Waves

High-power RF systems, such as RF plasma heating antennas, can be subject to standing waves. Indeed, as discussed in Section 1.3.3 of Chapter 1, the ICRH system employed on a tokamak may be intrinsically unmatched due to the frequency-dependent matching system and the plasma impedance variation. In such a situation, the electromagnetic fields' amplitude is no longer longitudinally homogeneous, and the electric field gradient affects the electron trajectories in non-linear ways.

For these reasons, predicting multipactor is more challenging for standing waves than travelling wave cases. Indeed, there is an interest in developing the lowest and highest multipactor thresholds that would not be affected by the brutal change of the reflection coefficient within the various antennas' components. This interest is explained by our aim of predicting the generators' forward powers responsible for triggering the multipactor phenomenon in the ICRH antennas, regardless of the plasma properties and, hence, the induced reflected wave caused by its instabilities' events.

In the following subsections, first, we propose a methodology based on which we extracted two criteria for providing multipactor thresholds that remain constant regardless of the variability of the reflection coefficient within the frequency range of the ICRH antennas. However, the developed methodology is valid, provided the frequency is low enough for electrons' trajectories to be less affected by the ponderomotive force. Then, we describe how this methodology is implemented within our multipactor decision algorithm.

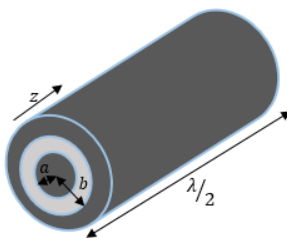


Figure 4.4: Cylindrical coaxial transmission line geometry of length $\lambda/2$ in the wave propagation direction. λ corresponds to the wavelength at the frequency of operation of the transmission line.

4.3.1 Methodology

To develop two criteria respectively for *i)* the ignition and *ii)* extinction of the multipactor phenomenon, regardless of the value of the reflection coefficient, we investigate the case of a coaxial transmission line for its simplicity. Let us consider a coaxial transmission line, for which we suppose that the multipactor conditions are simultaneously fulfilled at a given frequency so that the multipactor voltage thresholds $V_{mp,lower}$ and $V_{mp,upper}$ are known, as represented in Figure 4.5. The multipactor

region — bounded by the dashed red lines of Figure 4.5 being the lowest ($V_{mp,lower}$) and highest ($V_{mp,upper}$) voltage multipactor thresholds — is constant regardless the wave pattern and is dependent solely on the frequency, and geometry's dimensions and material.

This coaxial geometry will be subjected to different wave patterns for identifying relevant physical quantities for the lowest and highest multipactor thresholds and the multipactor location from its ignition phase to its extinction phase. Figure 4.5 represents different voltage magnitudes for different wave patterns as a function of the position along the wave propagation direction z of the coaxial geometry represented in Figure 4.4. Three wave patterns are considered:

1. Travelling wave (TW), *i.e.* $R = 0$ illustrated in Figure 4.5a to Figure 4.5c. The blue horizontal line represents the constant voltage V .
2. Mixed wave (MW) illustrated in Figure 4.5d to Figure 4.5f. The orange curve represents the voltage pattern of a coaxial line subject to MW with $R = 0.5$, and $\psi = 0^\circ$ (The voltage standing wave ratio quantifying the reflected power is defined as $VSWR = \frac{V_{max}}{V_{min}} = \frac{1+R}{1-R} = 3$), so that the voltage's minimum is $\frac{V(1-R)}{\sqrt{1+R^2}}$, and the voltage maximum is $\frac{V(1+R)}{\sqrt{1+R^2}}$.
3. Standing wave (SW) illustrated in Figure 4.5g to Figure 4.5i. The green curve represents the voltage in a coaxial transmission line subject to a SW with $R = 1$, and $\psi = 0^\circ$ ($VSWR = \infty$), so that the voltage's minimum is zero, and the voltage's maximum is $\sqrt{2}V$. V is progressively increased when going from (Figure 4.5a to Figure 4.5c), (Figure 4.5d to Figure 4.5f), and (Figure 4.5g to Figure 4.5i).

For the TW case, when $V < V_{mp,lower}$, no multipactor occurs. When $V_{mp,lower} \leq V \leq V_{mp,upper}$, the multipactor can take place along the coaxial, as represented in Figure 4.5a to Figure 4.5c. For the MW and SW cases, we can observe that once the peaks of the orange and green curves reach the value $V_{mp,lower}$ (respectively in Figure 4.5d and Figure 4.5g), the multipactor can take place in the vicinity of the maximal voltages location only. The latter reveals that multipactor ignition is controlled by the peak voltage on the line (*i.e.* peak electric field), regardless of the wave pattern, and is localised in the maximal voltage's vicinity.

Moreover, for the MW and SW cases, once the multipactor region intersects the voltage pattern seen across the line (illustrated respectively in Figure 4.5e and Figure 4.5h), the multipactor will be triggered in the zones where the voltage is within the multipactor region. These zones are dotted and hatched for the MW and SW cases and correspond to the geometry's parts where the multipactor conditions are fulfilled simultaneously. The latter reveals that for both MW and SW, as the voltage V increases, a displacement in the location of the sustained-multipactor phenomenon is observed. Therefore, the multipactor drifts from the maximal voltage's vicinity toward the minimal voltage on the line. Moreover, one can remark that for such cases, the maximal voltage observed on the line is no more the relevant physical quantity, in terms of location and value, for the developed multipactor.

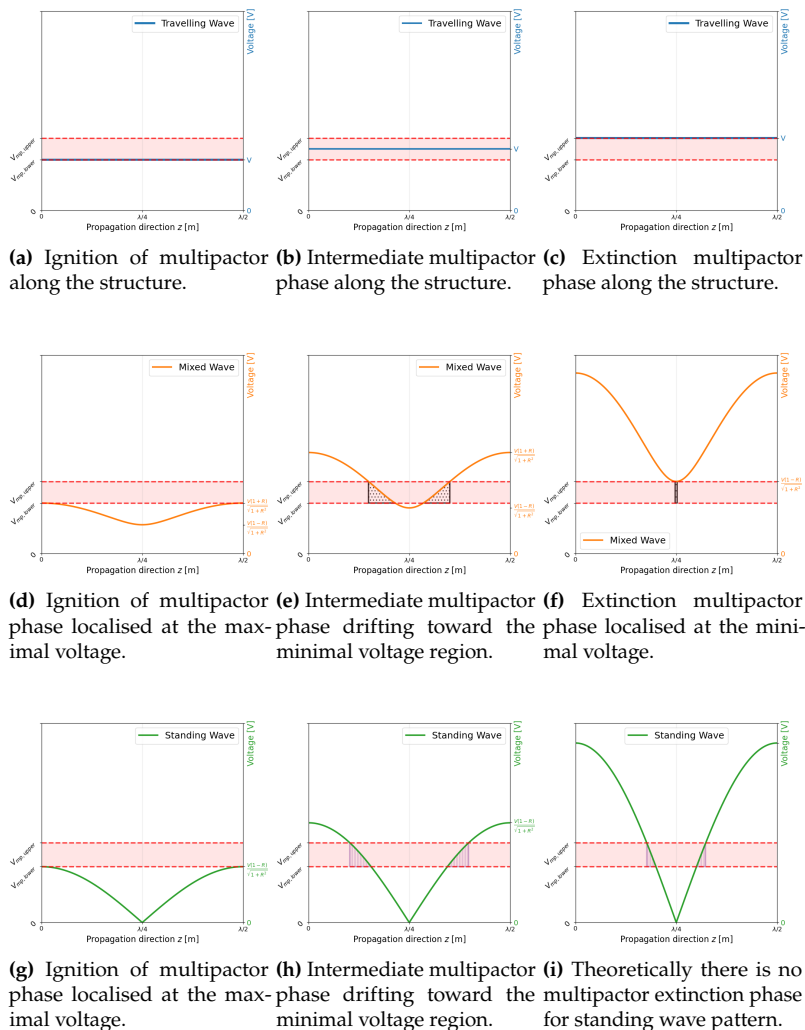


Figure 4.5: Different multipactor phases for a given coaxial transmission line experiencing three different wave patterns: a travelling waveform: (4.5a to 4.5c); a mixed waveform: (4.5d to 4.5f); and a standing waveform: (4.5g to 4.5i).

[104] Sorolla et al. (2015)

[105] Chen (2016)

Theoretically, for the MW case, the multipactor extinction takes place when the minimum voltage across the line reaches a value higher than $V_{mp,upper}$, as illustrated in Figure 4.5f. Therefore, the multipactor is localised in the minimum voltage’s vicinity before extinction. Nevertheless, there is always a null voltage across the line for the pure SW case. The latter means that, in theory, the multipactor could always be sustained close to the voltage nodes for SW cases. It should be noted that, in reality, due to the space charge effects [104], non-linear effects such as ponderomotive force [105], and the surface conditioning effects (reduction of TEEY), the multipactor is no more sustained above a certain threshold, even for the pure SW case.

As for generic and multi-ports complex geometries, it is sometimes not possible to define a voltage unequivocally, and as the electric field is the gradient of the voltage ($\vec{E} = -\nabla V$), these criteria are expressed as multipactor electric field thresholds rather than voltage thresholds.

Motivated by the coaxial transmission line analysis, we expect that the maximal multipactor electric field’s magnitude of the multipactor susceptible zone corresponds to the ignition of the multipactor and remains almost the same for the three wave patterns (TW, MW, or SW).

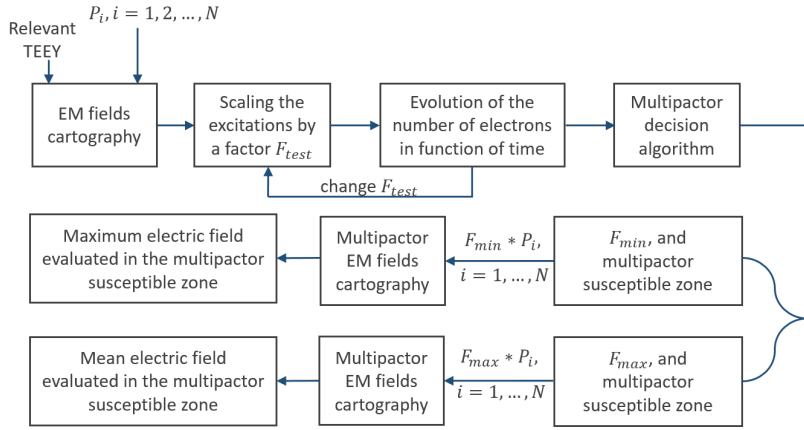


Figure 4.6: The steps summarising the applied methodology for the determination of the multipactor electric field thresholds, which are constant regardless of the standing wave ratio, for each defined multipactor region.

Moreover, we expect that the mean (average) multipactor electric field's magnitude, calculated in the multipactor susceptible zone, corresponds to the extinction of the multipactor and remains almost the same for the three wave patterns. The multipactor susceptible zone corresponds to the geometry's part where the multipactor conditions are fulfilled simultaneously. We expect that this principle is also true when working with complex 3D geometries.

4.3.2 Implementation

For an imported geometry into Spark-3D, the total initial incident power on all the ports of the geometry must be equal to 1 W. If the imported geometry has one activated port, then the software will give, as output, the multipactor incident power(s). Otherwise, if the imported geometry has N -activated ports, where each port i has an initial incident power P_i , $i = 1, \dots, N$ and such that the total initial incident power is one watt, i.e., $\sum_{i=1}^N P_i = 1$ W; the software's output is a scaling factor F , which, once multiplied by each port's incident power (P_i), gives the ports' incident powers triggering multipactor in the analysed geometry. In other terms, to obtain the multipactor electric field in the geometry, each port will have an incident power equal to $P_i \times F$, $i = 1, \dots, N$. Note that if the geometry has two multipactor thresholds, then the output of the multipactor decision algorithm is two scaling factors, F_{\min} and F_{\max} , for the ignition and extinction of the multipactor, respectively. As we deal with coaxial transmission lines having two thresholds, we stick to F_{\min} and F_{\max} .

As varying the reflection coefficient can be obtained by changing the initial incident power on the different geometry's ports, the scaling factors F_{\min} and F_{\max} obtained by the multipactor software will vary as well. And therefore, for each port and each reflection coefficient, we associate an incident multipactor power, which is not practical, especially with multi-port geometries of variable reflection coefficients. Therefore, defining the multipactor thresholds as multipactor electric field thresholds rather than multipactor incident power thresholds is crucial.

The proposed methodology is implemented as illustrated in Figure 4.6. In the first step, the electromagnetic (EM) field cartography is calculated by an electromagnetic solver. After choosing the initial power ports' excitation and the appropriate TEEY curve, the electromagnetic field

Table 4.2: Comparison between the measured multipactor power thresholds and the simulated power thresholds for a 50 Ω coaxial transmission made of copper.

Freq [MHz]	Lowest multipactor power [W]		Highest multipactor power [W]	
	Measurements	Simulations	Measurements	Simulations
100	64	55	180	161
120	74	73	414	383
140	119	117	619	681

is imported into the multipactor solver. In the second step, the scaling factor F_{test} is iteratively changed for decision-making on the existence of a multipactor based on the number of electrons' evolution in time. The output of this step is the determination of F_{min} and F_{max} , as well as the multipactor susceptible zones where the multipactor conditions are simultaneously fulfilled (detailed in the next paragraph). After that, the excitations of the ports are scaled with the multipactor scaling factors to generate the multipactor electromagnetic field cartography. The final step is the multipactor criteria evaluation proposed in Section 4.3.1.

The multipactor susceptible zone is the zone of the simulated region where multipactor takes place for the lowest and highest multipactor thresholds and, therefore, where the multipactor conditions are fulfilled simultaneously. The multipactor susceptible zone is determined by analysing the statistical data generated by Spark-3D. In particular, the average TEEY and the average impact energy for each surface mesh in the model are interesting statistical quantities for defining the susceptible zone. The two conditions simultaneously imposed on a surface mesh to be considered in the multipactor susceptible zone are the following: *i*) the average TEEY of the surface mesh should be greater than or equal to one. *ii*) The average impact energy E_i should satisfy $E_{c,1} \leq E_i \leq E_{c,2}$, where $E_{c,1}$ and $E_{c,2}$ are respectively the first and second crossover energies of the TEEY imported data.

4.4 Coaxial Transmission Line's Results

4.4.1 Comparison with Experimental Data

In this section, we validate the growth rate multipactor decision criterion and the associated algorithms determining the lowest and highest multipactor thresholds. This validation is done by comparing measured multipactor power thresholds to Spark-3D-based multipactor simulation results.

[106] Martinez et al. (2021)

In [106], a detailed description of a multipactor test-bed facility dedicated to cylindrical coaxial transmission lines' multipactor measurements is provided. The lowest and highest multipactor power thresholds for a 50 Ω copper coaxial line and an inter-electrode separation distance $d \approx 1.1$ cm are given in Table 4.2 at the frequencies 100 MHz, 120 MHz, and 140 MHz. The coaxial line was subjected to a travelling wave pattern.

To accurately simulate the multipactor power thresholds, electron emission characterisation is needed. For this reason, the TEEY of an as-received representative sample of the coaxial transmission line was measured at normal incidence at ONERA/DPHY and is represented as a dashed orange curve in Figure 4.2. Then, the electron population evolution was obtained for the same geometry using Spark-3D at the three tested

frequencies. The growth rate criterion was applied to deduce the lowest and highest multipactor power thresholds, given in Table 4.2.

A good agreement between the measured and simulated multipactor power thresholds is evidenced. Indeed, the difference between the simulation results obtained by averaging the multipactor predicted thresholds from ten similar runs and the measured thresholds did not exceed 15 %, validating hence the validity of the growth rate criterion and the developed algorithms scanning the scaling factors to determine the lowest and highest multipactor thresholds.

4.4.2 Scaling Laws' Validation

This section aims to verify the two scaling laws predicted by *Woo* for the cylindrical coaxial transmission lines and developed in Section 3.8.3.1 of Chapter 3.

The measured TEEY data for the silver-coated stainless-steel representative sample of the WEST ICRH antennas are used for the simulations discussed here. The TEEY data curve is illustrated in blue in Figure 4.2 and is imported into Spark-3D for the electron population versus time evolution's evaluation. In all the simulations, the vacuum region of a 50Ω cylindrical coaxial transmission line is initially seeded with 2000 electrons, and the developed algorithm relying on the electrons' growth rate is applied.

We note that no DC magnetic field is applied during multipactor simulations. There is no reflection in the coaxial transmission line — matched situation, where only one port of the geometry is excited. The thresholds are given in voltage rather than power as further studies will focus on unmatched configurations — where multi-ports are excited — for which voltage, or equivalently electric field, is more meaningful than incident powers on the different powered ports.

As the travelling wave pattern is studied, the length of the cylindrical coaxial transmission line in the wave propagation direction does not affect the multipactor results. The latter is explained by the constant voltage along the propagation direction since there is no electric field variation in the axial direction — being the z -direction in our case. An illustration of the travelling wave pattern is given in Figure 4.7.

Figure 4.8 represents the lowest and highest multipactor thresholds versus the $f \times d$ product. Each multipactor threshold is expressed as the maximal voltage seen on the line. For these simulations, the frequency is varied between 10 MHz and 150 MHz for a 50Ω coaxial transmission line of two different separation distances. The black dotted curve corresponds to the voltage multipactor thresholds and error bars for a coaxial transmission line of separation distance $d = 2$ cm. The orange dashed curve corresponds to the average voltage multipactor thresholds and the error bars for a coaxial transmission having a separation distance d of 4 cm. Each marker, being one multipactor threshold, results from ten consecutive simulations to avoid possible minor statistical errors — seen as error bars on the figure.

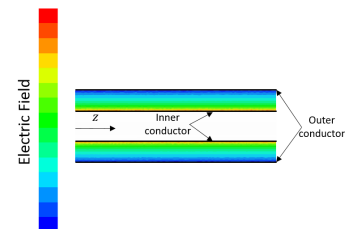
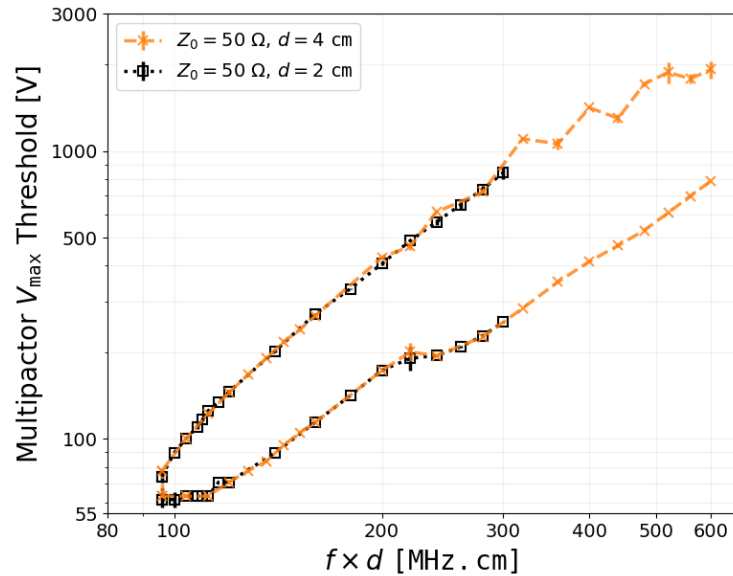


Figure 4.7: A cut-view of a cylindrical coaxial transmission line subject to a travelling wave pattern propagating in the z -direction.

Figure 4.8: Simulated susceptibility data for a cylindrical coaxial transmission line of characteristic impedance $Z_0 = 50 \Omega$ subjected to a travelling wave pattern, and inter-electrode distance $d = 4 \text{ cm}$ (orange) and $d = 2 \text{ cm}$ (black), while varying the frequency in the range $[10 - 150] \text{ MHz}$. The plots are obtained for the TEEY curve of the silver-coated material in Figure 4.2 (blue curve), using the multipactor prediction algorithm based on the growth rate applied on the time-particle evolution results of Spark-3D.



Inside the region bordered by the multipactor threshold points, the multipactor is triggered for this geometry. On the contrary, outside of it, no multipactor can take place.

The results — obtained for the multipactor prediction algorithm based on the rate of growth of electrons — have a shape similar to the ones found by Woo. Nevertheless, the multipactor thresholds obtained by numerical simulations are not quantitatively comparable to the measured multipactor thresholds, given in [64, 72]. Indeed, their measured multipactor thresholds are those of a copper coaxial of undetermined TEEY, whereas our simulations correspond to a silver-coated coaxial. Only the global shape of the multipactor thresholds versus the $f \times d$ product is comparable.

[64] Woo (1970)

[72] Woo (1968)

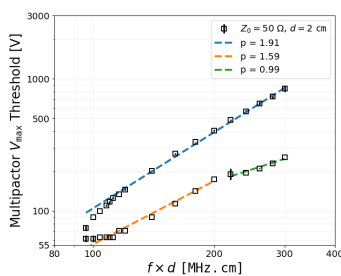


Figure 4.9: $(fd)^p$ fitting for the multipactor voltage thresholds of the 50Ω coaxial transmission line of $d = 2 \text{ cm}$. The black markers are from Figure 4.8. In blue, the fitting of the highest multipactor voltage thresholds. In orange and green the fitting of the lowest multipactor thresholds.

[64] Woo (1970)

Furthermore, it can be observed that varying the inter-electrode separation distance d while keeping the $f \times d$ product constant does not affect the predicted multipactor thresholds. Indeed, the lowest and highest multipactor thresholds for $d = 2 \text{ cm}$ overlap with those for $d = 4 \text{ cm}$. The latter validates that two coaxial cables of different dimensions and fixed characteristic impedance exhibit the same multipactor thresholds at a fixed $f \times d$ product.

Now, we want to confirm the dependence stated by Woo and further authors: for the highest multipactor voltage thresholds, the dependence law is $(fd)^2$, whereas, for the lowest multipactor voltage thresholds, the law is proportional to $(fd)^p$, where p is a fitting parameter, ranging between 1 and 2, and determined for each multipactor mode. For that, we fitted with a power law $(fd)^p$ the multipactor voltage thresholds for the results corresponding to $d = 2 \text{ cm}$, and $d = 4 \text{ cm}$. The data are fitted separately for the highest multipactor voltage thresholds, and for each mode of the lowest multipactor voltage thresholds — the passage to higher multipactor order is indicated by a discontinuity in the curve, as observed by Woo [64]. The results are illustrated in Figure 4.9 and Figure 4.10, from which we can conclude that the fitting parameter p

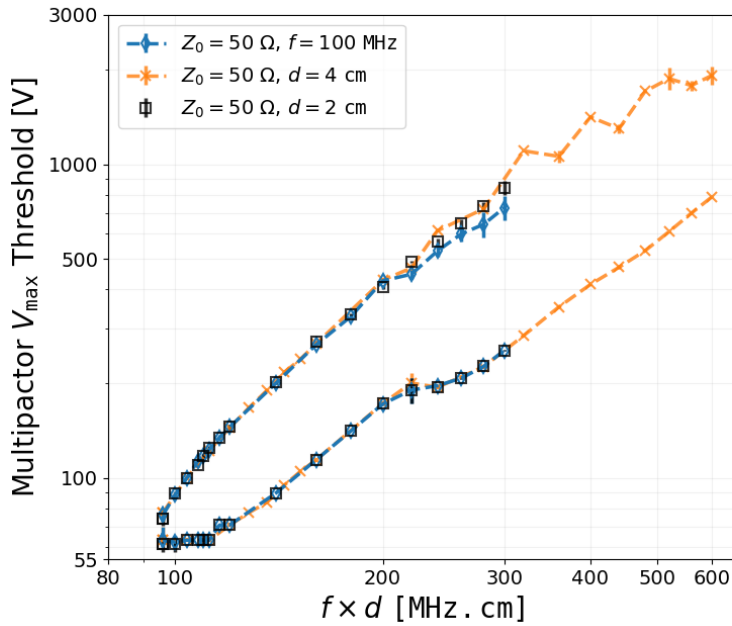


Figure 4.11: In orange and black, the simulated susceptibility data were obtained by varying the frequency, and fixing the separation distance d . The curve in blue corresponds to the simulated susceptibility data when the separation distance d is varied in the range $[0.4 - 3]$ cm, and the frequency is fixed to 100 MHz. Plots are obtained for the TEEY curve, of the silver-coated sample (Figure 4.2), for a coaxial transmission line of characteristic impedance $Z_0 = 50 \Omega$.

ranges between 1 and 2, for all the voltage multipactor thresholds.

According to the second scaling law proposed by Woo [64], for a coaxial transmission line of fixed characteristic impedance, the multipactor thresholds should be the same for a given $f \times d$, independently of the choice of the frequency and the inter-electrode distance. To prove that this is indeed the case for the simulated multipactor thresholds independently of the scanned parameter (f or d), the maximum multipactor voltage thresholds obtained for a 50Ω coaxial transmission line of variable separation distance d and operating at a fixed frequency of 100 MHz, are represented in blue in Figure 4.11 (the orange and black data points of Figure 4.8 are re-plotted here for comparison purpose). The results show that, in the $f \times d$ product range $[20 - 600]$ MHz \cdot cm, the multipactor voltage thresholds for the 50Ω coaxial of fixed distance d and variable frequency are in good correspondence with the multipactor voltage thresholds obtained for a 50Ω coaxial of variable distance and fixed frequency.

4.4.3 Conditioning Effect on Multipactor Thresholds

In this section, we investigate the effect of the WEST-relevant conditioning phase on the multipactor voltage thresholds for a coaxial transmission line geometry of characteristic impedance 50Ω , and 30Ω . The operational conditioning effects are studied by carrying out simulations using two extreme TEEY measurements' curves represented in Figure 4.12: before impacting the surface with an electron beam — *non-conditioned*, and after an impact with a cumulative electron dose of $2338 \mu\text{C mm}^{-2}$ — *fully-conditioned*. The considered TEEY measurements are those of a silver-coated stainless-steel sample representative of the WEST ICRH antennas — discussed in Section 2.4.3 of Chapter 2. We recall that the

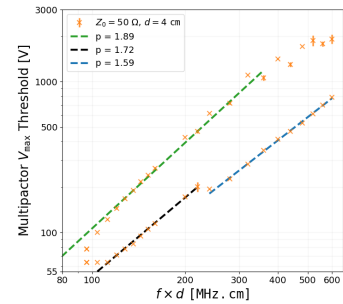
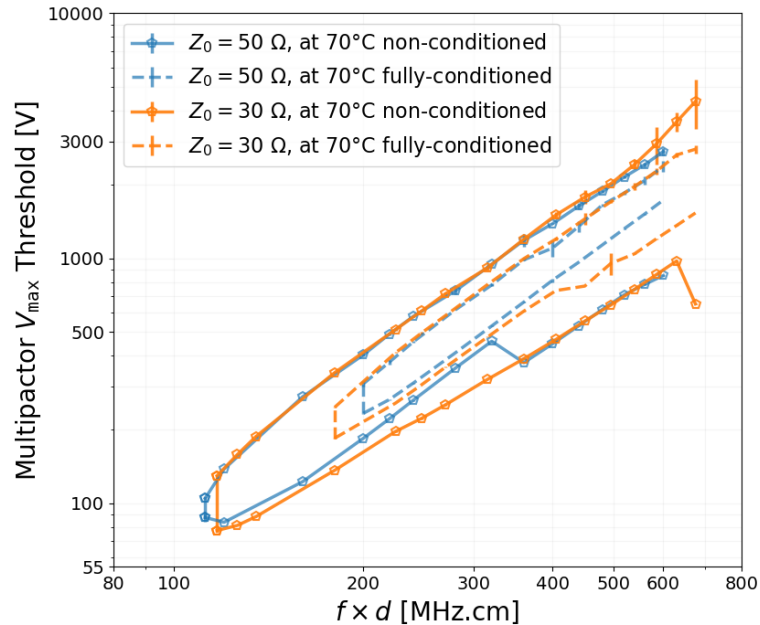


Figure 4.10: $(fd)^p$ fitting for the multipactor voltage thresholds of the 50Ω coaxial transmission line of $d = 4$ cm. The orange markers are from Figure 4.8. In green, the fitting of the highest multipactor voltage thresholds. In black and blue the fitting of the lowest multipactor thresholds.

[64] Woo (1970)

Figure 4.13: The blue (respectively orange) plots are the simulated susceptibility voltage multipactor data for a coaxial transmission line of characteristic impedance $Z_0 = 50 \Omega$ (respectively $Z_0 = 30 \Omega$), and inter-electrode distance $d = 4$ cm (respectively $d = 4.5$ cm), while varying the frequency in the range [10 – 150] MHz. Plots are obtained for the TEEY curves represented in Figure 4.12, corresponding to the *non-conditioned* case, and the *fully-conditioned* case, after impacting the sample with a cumulative electron dose of $2338 \mu\text{C mm}^{-2}$.



sample was, first, baked at 200°C for three days and then maintained at a temperature of 70°C during TEEY measurements.

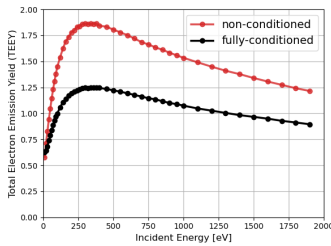


Figure 4.12: TEEY measurements for a baked WEST ICRH representative silver-coated sample, maintained at 70°C . In red, the TEEY data are measured before any conditioning treatment; and in black, the TEEY data are measured after a full conditioning treatment of the surface (with a cumulative electron dose of $2338 \mu\text{C mm}^{-2}$).

In Figure 4.13, the simulated lowest and highest maximal multipactor voltage thresholds and the error bars, evaluated from 3 consecutive runs, for a matched coaxial transmission line of characteristic impedance 50Ω and a separation distance d of 4 cm, are plotted in blue. Similarly, the simulated multipactor voltage thresholds and the error bars for a coaxial transmission line of characteristic impedance 30Ω and a separation distance d of 4.5 cm are plotted in orange. The maximum multipactor voltages are plotted as a function of the $f \times d$ product, for the TEEY curves corresponding to the *non-conditioned* and the *fully-conditioned* measurements, are represented in Figure 4.13 in plain and dashed lines respectively. The frequency is scanned in the range [20 – 150] MHz. It is found that the conditioning both increases the lowest multipactor thresholds and decreases the highest multipactor thresholds. The latter decreases the overall region area where the multipactor is expected to be triggered in the coaxial transmission line. Moreover, the conditioning suppresses the multipactor occurrence at low $f \times d$ products, as shown in Figure 4.13. These effects could be explained by the increase in the first crossover energy and the decrease in the maximum TEEY values.

Owing to the ICRH high voltage operational conditions, the multipactor region should be bypassed by achieving an RF rise time less than the multipactor rise time. This jump in the RF voltage is known as "multipactor push-through," as the multipactor is not sustained in the antenna since there is no sufficient time for it to be developed. Therefore, reducing the multipactor region affects the reduction of the efforts needed to achieve the push-through.

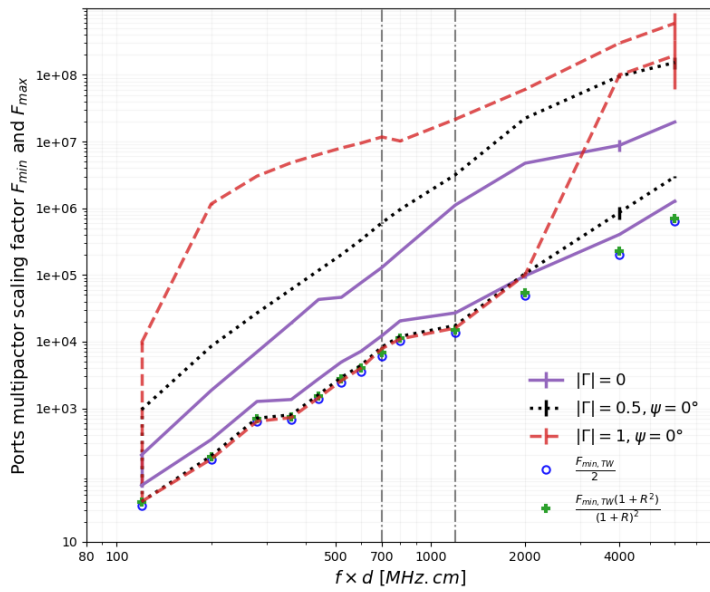


Figure 4.14: The lowest and highest multipactor scaling factor F_{min} and F_{max} ; obtained by Spark-3D for the three wave patterns: travelling wave (TW), mixed wave (MW), and standing wave (SW) represented in plain purple, dotted black, and dashed red respectively. The green crosses and blue circles correspond to the scaling laws proposed by Somersalo et al. [93] respectively for the MW case and the SW case.

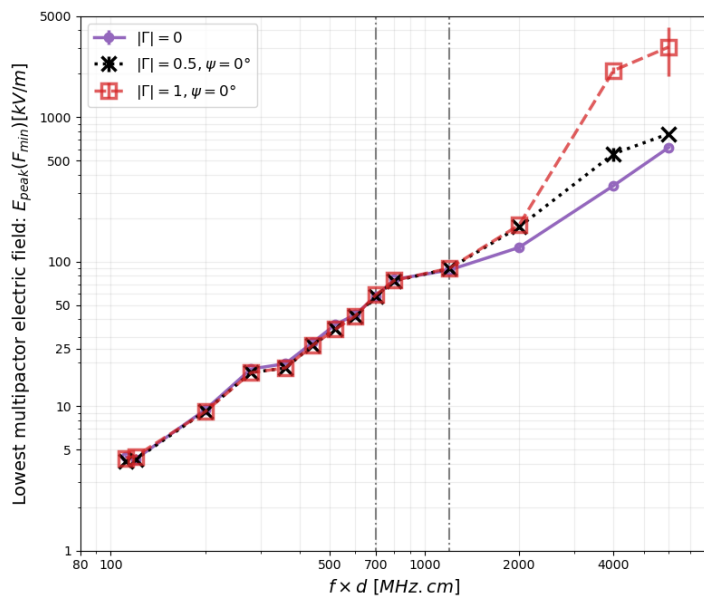


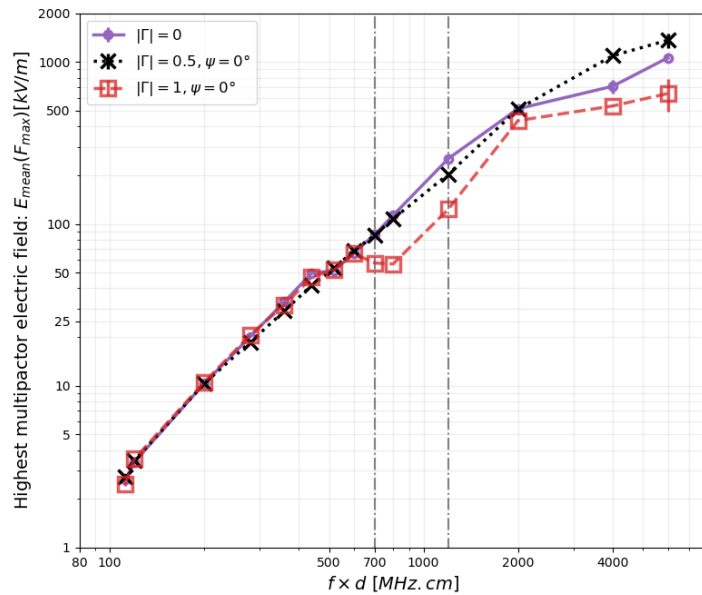
Figure 4.15: The relevant physical quantity for the multipactor's ignition which is the maximum electric field's magnitude evaluated in the multipactor susceptible zone of the coaxial line, when the initial ports' excitation are scaled by the multipactor scaling factor F_{min} . The lowest multipactor electric field thresholds are evaluated for the three wave patterns travelling wave (TW), mixed wave (MW), and standing wave (SW) and are represented in plain purple, dotted black, and dashed red respectively.

4.4.4 MW and SW Results

First, we want to look at the scaling factors given by the Spark-3D software for a 50Ω coaxial transmission line to check its variability with the reflection coefficient, *i.e.*, its dependence on the ports' excitation. Figure 4.14 represents the lowest and highest scaling factors F_{min} and F_{max} obtained for the different wave patterns: TW (plain violet curve), MW (black dotted curve), and SW (dashed red curve) in the frequency range [25 – 1500] MHz.

Moreover, the scaling laws of [93], mentioned in Section 3.8.3.2 of

Figure 4.16: The relevant physical quantity for the multipactor's extinction which is the mean electric field's magnitude evaluated in the multipactor susceptible zone of the coaxial line, when the initial ports' excitation are scaled by the multipactor scaling factor F_{\max} . The highest multipactor electric field thresholds are evaluated for the three wave patterns travelling wave (TW), mixed wave (MW), and standing wave (SW) and are represented in plain purple, dotted black, and dashed red respectively.



Chapter 3, for the MW and the SW cases as a function of the multipactor input power obtained for a TW case are represented respectively in blue circles and green crosses. The scaling laws are proposed for the lowest multipactor thresholds.

[93] Somersalo et al. (1998)

The first dashed-dotted grey vertical line represents the threshold (700 MHz · cm) suggested by Pérez *et al.* [95]. In this manuscript, above this threshold, we found that the ponderomotive force affects only the highest multipactor thresholds' results. Moreover, we found a second threshold at 1200 MHz · cm, higher than the first one, above which the non-linear force affects the lowest multipactor thresholds' results. The latter is motivated by observing that the multipactor initiates near the maximal electric field corresponding to a null ponderomotive force's magnitude. As the multipactor threshold increases, a displacement toward the electric field's node is observed, correlated with an increase in the ponderomotive force — details are given in Appendix A. Therefore, intuitively, the effect of the ponderomotive force should be observed first for the highest and then the lowest multipactor thresholds.

[95] Pérez et al. (2009)

Figure 4.14 shows that the scaling factors F_{\min} and F_{\max} , corresponding to the ignition and extinction of multipactor, vary with the variability of the reflection coefficient. In addition to that, we remark that: *i*) below the second threshold (1200 MHz · cm), the F_{\min} for the MW and SW cases (the lowest branch respectively for the black dotted curve, and the dashed red curve), show a good agreement with the proposed scaling laws by Somersalo *et al.* [93] (respectively the green crosses, and the blue circles). *i*) Above the second threshold, the proposed laws are no longer in good agreement with their corresponding simulated scaling factors. The latter is explained by the ponderomotive force's effect.

Second, the methodology explained in Section 4.3.1 is applied for the three wave patterns to prove that, below a certain frequency, the developed

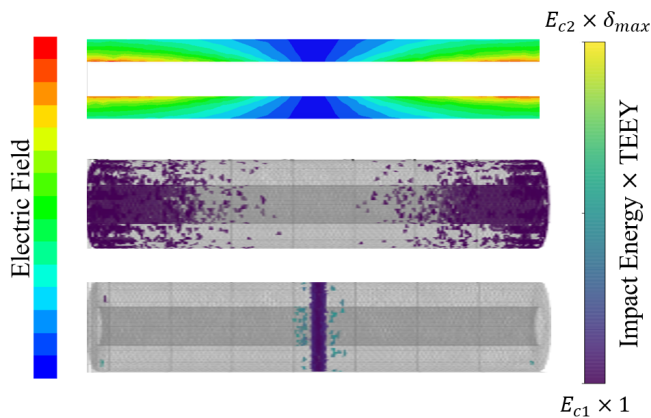


Figure 4.17: Top Figure — Electric field representation (corresponding to the colour map on the left) for a standing wave propagating in the coaxial transmission line. Middle (Bottom) Figure — Multipactor susceptible zone located near the maximal (minimal) electric field for the lowest (highest) multipactor threshold. The colour map of the susceptible zones is represented on the right side.

multipactor electric field criteria are constant regardless of the variability of the reflection coefficient.

The relevant physical quantity for the ignition (respectively extinction) of multipactor, corresponding to the lowest (respectively highest) scaling factor F_{\min} (respectively F_{\max}), for the TW, MW, and SW is represented in Figure 4.15 (respectively Figure 4.16). As suggested in Section 4.3.1, this criterion is the maximum (respectively mean) electric field's magnitude evaluated in the multipactor susceptible zone after scaling the ports' excitation by F_{\min} (respectively F_{\max}).

Below $700 \text{ MHz} \cdot \text{cm}$ (respectively $1200 \text{ MHz} \cdot \text{cm}$), the results show that the obtained highest (respectively lowest) multipactor electric field thresholds are constant for the different tested reflection coefficients, proving that the proposed methodology is valid below $700 \text{ MHz} \cdot \text{cm}$. Consequently, the ponderomotive force does not affect the electrons' dynamics below $700 \text{ MHz} \cdot \text{cm}$.

Nevertheless, the non-linearity effect of the ponderomotive force is more pronounced above $700 \text{ MHz} \cdot \text{cm}$ for the highest multipactor thresholds as we remark that the multipactor electric field responsible for the extinction of multipactor in the SW case is smaller than that of the TW case, as the extinction takes place easier when there is a significant force pushing the electrons toward the nodes of a null electric field. Moreover, above $1200 \text{ MHz} \cdot \text{cm}$, it affects the lowest multipactor thresholds, where we notice that the multipactor electric field responsible for the ignition of multipactor in the SW case is higher than that of the TW case, as more power is needed to trigger multipactor since the ponderomotive force is attracting the electrons toward the electric field nodes without having enough energy to maintain a multipactor in the nodes' vicinity.

Our results agree with Pérez *et al.* [95], except for having two non-linearity-triggering thresholds for the highest, then the lowest multipactor thresholds. The non-linearity-triggering $f \times d$ product for the highest multipactor thresholds is lower than that of the lowest ones.

It should be noted that the results of Figure 4.15 and Figure 4.16 cannot be quantitatively compared as they refer to different quantities evaluated in different susceptible zones.

[93] Somersalo *et al.* (1998)

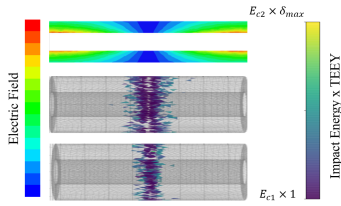


Figure 4.18: Top Figure — Electric field representation (corresponding to the colour map on the left) for a standing wave (SW) propagating in the coaxial transmission line, for an $f \times d$ product above $4000 \text{ MHz} \cdot \text{cm}$. Middle (Bottom) Figure — Multipactor susceptible zone located near the minimal electric field for the lowest (highest) multipactor threshold. The colour map of the susceptible zones is represented on the right side.

Below $4000 \text{ MHz} \cdot \text{cm}$, the multipactor’s susceptible zone, for the lowest (respectively highest) multipactor thresholds, is in the vicinity of the maximal (respectively minimal) electric field on the line as expected for the coaxial transmission line as represented in Figure 4.17.

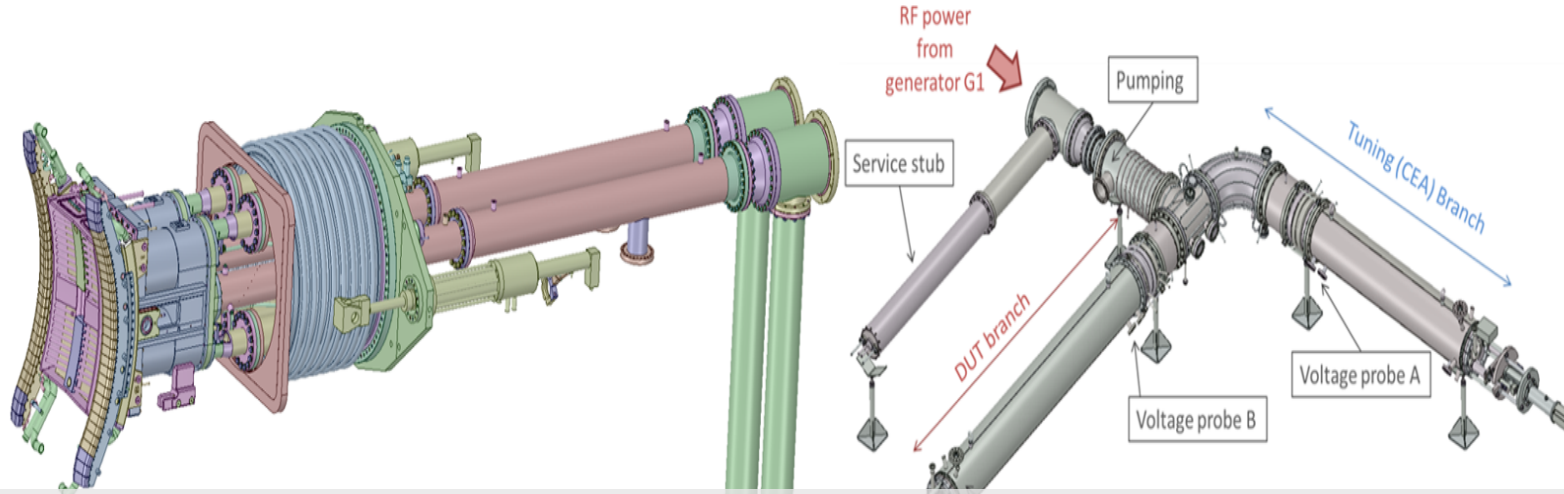
Nevertheless, above $4000 \text{ MHz} \cdot \text{cm}$, the ponderomotive force in the axial direction outperforms that in the radial direction over a wide range of the coaxial — as the distance between the maximum of the electric field and its node is reduced — so that the electrons are pushed to the direction of the electric field node before initiating any multipactor process. Subsequently, the ignition and extinction of the multipactor are in the electric field’s nodes’ vicinity, as illustrated in Figure 4.18. The latter could explain the low difference between the lowest and highest multipactor scaling factors — where the lowest scaling factor tends to overlap with the highest scaling factor triggering the multipactor in the geometry — for the $f \times d$ products of $4000 \text{ MHz} \cdot \text{cm}$ and $6000 \text{ MHz} \cdot \text{cm}$ seen in Figure 4.14.

4.5 Chapter Summary and Perspectives

In this chapter, we proposed a multipactor detection algorithm to determine the lowest and highest multipactor voltage thresholds bounding the range of voltages where the multipactor is triggered in any coaxial transmission line. We compared the multipactor power thresholds obtained by our decision-making algorithm to the multipactor measured experimental results obtained for a 50Ω coaxial line made of copper. In addition, we validated the scaling laws proposed for this type of geometry. Moreover, we studied the effect of the TEEY properties’ variations resulting from the conditioning on the multipactor thresholds. In particular, we used two different TEEY curves for the representative material of the ICRH antennas: before conditioning the sample and after conditioning it with a cumulative electron dose of $2338 \mu\text{C mm}^{-2}$. We showed that the baking and the dose-effect reduce the $f \times d$ product range over which the multipactor is triggered inside the geometry and reduce the multipactor’s zone for each $f \times d$ product.

On the other hand, to account for the standing wave patterns, we proposed two multipactor electric field-based criteria for the ignition and extinction of multipactor regardless of the wave patterns, *i.e.* reflection coefficients. We found that regardless of the ports’ number and excitation, the lowest multipactor threshold depends on the maximum electric field, and the highest multipactor threshold depends on the mean electric field. The proposed criteria were validated for a 50Ω coaxial transmission line below $700 \text{ MHz} \cdot \text{cm}$. The obtained results agree with the proposed scaling laws of previous findings for the lowest multipactor voltage thresholds and the sustainability of the multipactor near the nodes of the SW pattern before its extinction.

In the following chapter, we will apply the methodologies for the multipactor analysis of complex structures such as the ion cyclotron resonance heating (ICRH) antennas of the experimental tokamak WEST, operating in the frequency range $[46 - 65] \text{ MHz}$ which are subject to standing waves.



5 Multipactor in Complex Geometries

When you learn, learn with a mind that desires to nourish its knowledge, & not a mind that merely desires to pass it a long... For many are the conveyors, but rare are the nourishers.

Ali Ibn Abi Taleb

In this chapter, we describe the generic methodology applied to determine the generators' forward powers triggering multipactor in the various components of the WEST ICRH antennas (Section 5.1). Then, we evaluate the multipactor electric field thresholds in the RF structures of the WEST ICRH antennas (Section 5.2) and the generators' forward powers responsible for triggering multipactor in one ICRH antenna during its RF conditioning phase (Section 5.3) and during the WEST ICRH system's operation during plasma scenarios (Section 5.4). The last part is dedicated to the multipactor analysis of a complex double-branch resonator (Section 5.5).

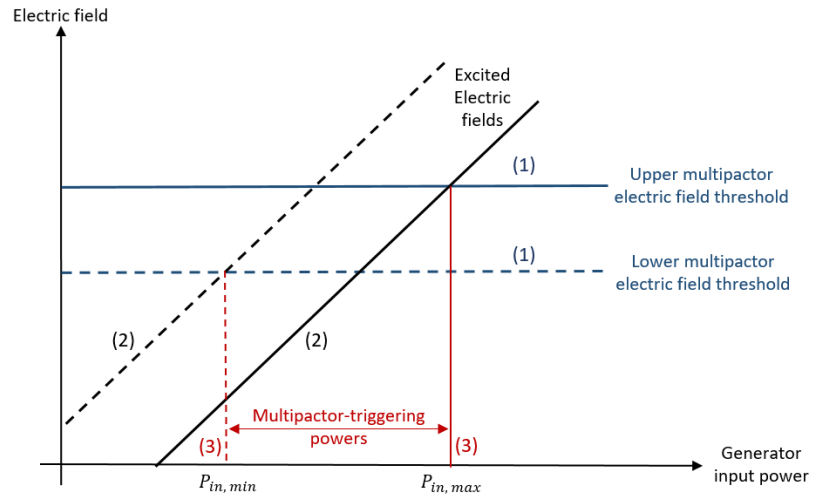
5.1 Methodology Description

During the WEST ICRH antennas' operation, the operator has to make the following decisions:

- ▶ Choosing the number of active antennas;
- ▶ Choosing the frequency at which each operating antenna is matched, *i.e.*, at which the circuit is resonant;
- ▶ Choosing the forward power of each activated generator;
- ▶ Tuning the capacitors of the antenna(s) — or each side of the antenna — at its (their) frequency(ies) of interest. Two main situations are found: *i)* the capacitors are tuned to match the antenna — or one antenna side — and are called *tuned capacitors*. *ii)* The capacitance of each capacitor is set to 120 pF — highest capacitance value — and they are called *detuned capacitors*, as the antenna (or antenna side) is no more resonant.

During RF conditioning, the ICRH operators control the total forward power per antenna side and the phase shift between the sides of one

Figure 5.1: Illustration of the main three steps used to solve the problem for a given frequency. The blue lines correspond to the multipactor electric field thresholds, the black lines correspond to the excited electric fields, and the red lines correspond to the resultant generators' forward powers triggering multipactor inside the geometry.



antenna, usually in dipole mode with 180° . During plasma operations, power and phase are controlled by the plasma control system in real time.

During plasma operations, when an antenna is powered, both sides are powered, and the four capacitors of the antenna are tuned to make it resonant at the frequency of interest. In contrast, we are interested in powering only one side of an antenna during its RF conditioning phase, where matching the capacitors amounts to tuning the two capacitors of the side.

In this chapter, our goal is to *i)* determine the generators' forward powers and capacitor states that can trigger multipactor inside the different sides and components of the antennas at each frequency of interest; *ii)* deduce the best strategies to reduce or avoid multipactor in different operational scenarios. In this case, the operator could choose the setup parameters — generators' forward powers and capacitors' state — avoiding the multipactor causing operational problems.

To achieve our goals, we divided the problem's analysis into three main parts, illustrated schematically in Figure 5.1 for a given frequency:

1. Determining the electric fields responsible for triggering multipactor inside the different components of the antenna (blue lines in Figure 5.1). The multipactor electric fields are determined according to our methodology, detailed in Chapter 4. We applied it to the main components of the WEST ICRH antennas: T-junction, impedance transformer, and the RF feed-through in the frequency range [46 – 65] MHz. These thresholds are called the *multipactor electric fields thresholds* and are determined while considering the measured ICRH-relevant operational material secondary emission properties.
2. Solving for the electric field in the antenna sections, using a full-wave and a circuit solver (ANSYS Electronics). The latter accounts self-consistently for the generator powers, the capacitor states, and the coupling between both sides (between antennas) for vacuum (plasma conditions). Thus, this step leads to the determination of the *excited electric fields* in all components of the antenna (black lines in Figure 5.1).

3. Comparing the *multipactor electric fields thresholds* to the *excited electric fields*. It leads to the determination of the forward generators' powers — lower and upper thresholds, triggering multipactor inside the different components of the antenna (red points in Figure 5.1).

In the following section, we elaborate on the first step in detail.

5.2 Multipactor Electric Fields Thresholds' Determination

To accurately determine the multipactor thresholds in the T-junction, impedance transformer, and RF feed-through components, which are complex 3D geometries, we have split each into separate multipactor analysis regions. The multipactor regions are chosen such that the electromagnetic fields and/or the geometry are as much as possible homogeneous.

The WEST ICRH antennas are resonant antennas and, hence, are subject to standing wave patterns. In standing wave conditions, it is relevant to determine the multipactor thresholds in terms of the electric fields, following the methodology detailed in Chapter 4. For each of the defined regions, we have determined two multipactor electric field thresholds: the *lowest multipactor electric field threshold*, responsible for the ignition of the multipactor regime in the region, and the *highest multipactor electric field threshold* above which the multipactor extinguishes in the region.

5.2.1 T-junction and Impedance Transformer

The geometry of the T-junction (represented in Figure 5.2) is divided into three regions: *Region A* being close to a parallel-plates-like geometry, *Region B* a coaxial geometry of elliptical cross-section and *Region C* being the two regions connected to the capacitors, joined by a parallel-plates-like geometry. The geometry of the impedance transformer (represented in Figure 5.3) is split into four regions: two circular coaxial transmission lines of characteristic impedance 5.5Ω (*Section 1*) and 17.4Ω (*Section 2*), and two complex tapered transition geometries called *Transition 1* and *Transition 2*.

For these two components, the multipactor thresholds are evaluated for two TEEY curves corresponding to the *non-conditioned* and the *fully-conditioned* measurements — two extreme cases for the material properties under relevant WEST ICRH operational conditions, represented in Figure 5.4.

Figure 5.5 and Figure 5.6 represent, for each tested TEEY, the lowest and highest multipactor electric field thresholds for the multipactor analysis regions of the T-junction and impedance transformer respectively. The DC magnetic field of the tokamak WEST is not accounted for. The results correspond to the average of various reflection coefficients — different ports' excitation. Indeed, we have found that our methodology is valid in the frequency range of the ICRH antennas. The maximal electric field (respectively average) evaluated in the multipactor susceptible zone

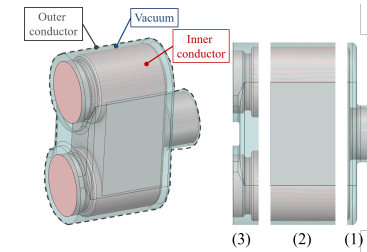


Figure 5.2: Left — The design of the T-junction, where in red the inner conductor is represented, in blue the vacuum volume, and in dashed black the outer conductor. Right — The cut view representation of each of the T-junction multipactor regions. The T-junction is divided into three different multipactor regions: (1) — *Region A*, (2) — *Region B*, and (3) — *Region C*.

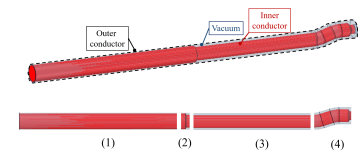


Figure 5.3: Top — The design of the impedance transformer, where in red the inner conductor is represented, in blue the vacuum volume, and in dashed black the outer conductor. Bottom — The cut view representation of each of the impedance transformer multipactor regions. The impedance transformer is divided into four different multipactor regions: (1) — *Section 1*, (2) — *Transition 1*, (3) — *Section 2*, and (4) — *Transition 2*.

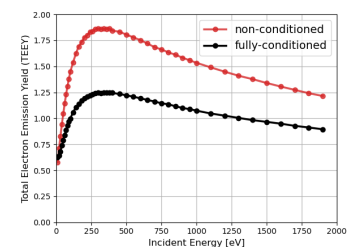


Figure 5.4: TEEY measurements for a baked WEST ICRH representative silver-coated sample, maintained at 70°C . In red, the TEEY data are measured before any conditioning treatment; and in black, the TEEY data are measured after a full conditioning treatment of the surface (with a cumulative electron dose of $2338 \mu\text{C mm}^{-2}$).

Figure 5.5: The multipactor electric field thresholds for the three multipactor analysis regions of the T-junction: *Region A*, *Region B*, and *Region C* represented in blue, orange, and green respectively. The lowest and highest multipactor electric field thresholds are determined for the *non-conditioned* (plain lines) and *fully-conditioned* (dotted lines) TEEY curves. The DC magnetic field is not accounted for.

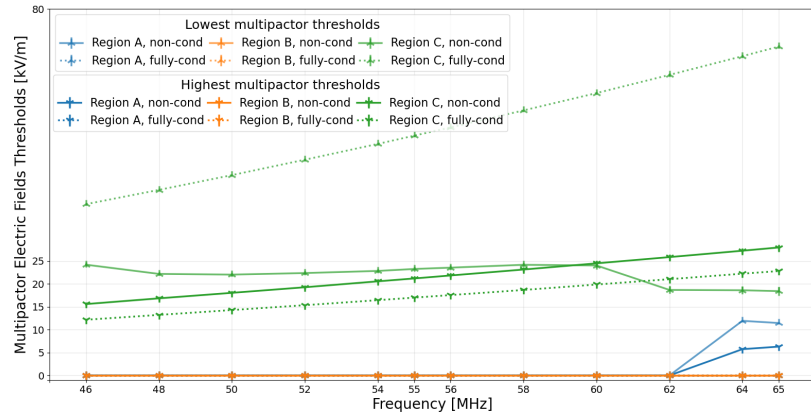
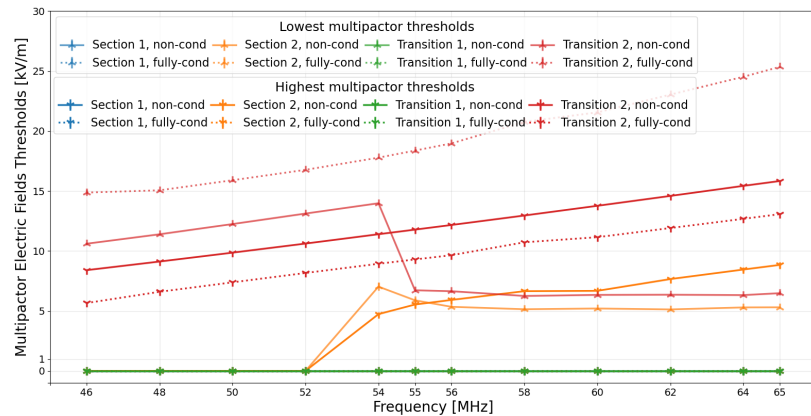


Figure 5.6: The multipactor electric field thresholds for the four multipactor analysis regions of the impedance transformer: *Section 1*, *Section 2*, *Transition 1*, and *Transition 2* represented in blue, orange, green, and red respectively. The lowest and highest multipactor electric field thresholds are determined for the *non-conditioned* (plain lines) and *fully-conditioned* (dotted lines) TEEY curves. The DC magnetic field is not accounted for.



is a relevant criterion for the lowest (respectively highest) multipactor threshold, remaining constant regardless of the variability of the reflection coefficient.

The figures show that, for the T-junction, *Region A* — only in the frequency range [64 – 65] MHz — and *Region C* of the T-junction are prone to multipactor for the *non-conditioned* TEEY case. In contrast, only the *Region C* is prone to multipactor when using the *fully-conditioned* TEEY case. For the impedance transformer, the regions *Section 2* and *Transition 2* are problematic when using the *non-conditioned* TEEY, and only the *Transition 2* remains problematic when it comes to the *fully-conditioned* TEEY.

Furthermore, we can remark that for 3D complex geometries, the conditioning effect on the multipactor electric field thresholds is the same as observed for a cylindrical coaxial transmission line in Chapter 4. In particular, a reduction in the multipactor electric field range is observed when the surface is conditioned: *i)* the *lowest multipactor electric field threshold* is higher for the *fully-conditioned* case than that for the *non-conditioned* case. *ii)* The *highest multipactor electric field threshold* is lower for the *fully-conditioned* case, than that for the *non-conditioned* case.

1: *Region A* of the T-junction and *Section 2* of the impedance transformer are not analysed in detail. Indeed, *Region A* is a parallel-plates-like geometry with a uniform electric field. And *Section 2* is a cylindrical coaxial transmission line subject to a standing wave pattern. Therefore, once the multipactor conditions are fulfilled, the multipactor ignition (respectively extinction) is in the vicinity of the high (respectively low) electric field zone.

Now, we are interested in investigating the multipactor susceptible zones for the *non-conditioned* and *fully-conditioned* TEEY data in two of the multipactor analysis regions¹. In particular:

- *Region C* of the T-junction. Figure 5.7 illustrates the various multipactor susceptible zones for the lowest and highest multipactor thresholds of each tested TEEY data curve, in the WEST ICRH

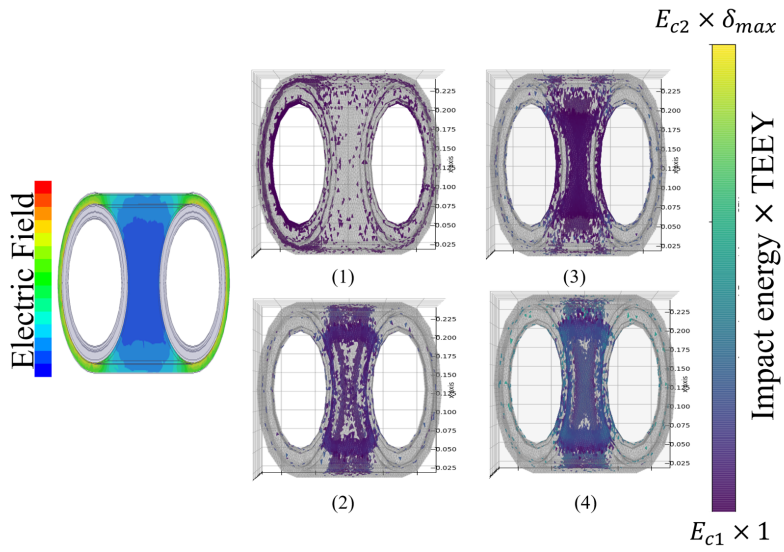


Figure 5.7: (1) (respectively (2)) — The multipactor susceptible zone corresponding to the lowest (respectively highest) multipactor threshold when the *non-conditioned* TEEY is used. This zone remains the same in the frequency range [46 – 65] MHz. (3) (respectively (4)) — The multipactor susceptible zone corresponding to the lowest (respectively highest) multipactor threshold when the *fully-conditioned* TEEY is used. This zone remains the same in the frequency range [46 – 65] MHz.

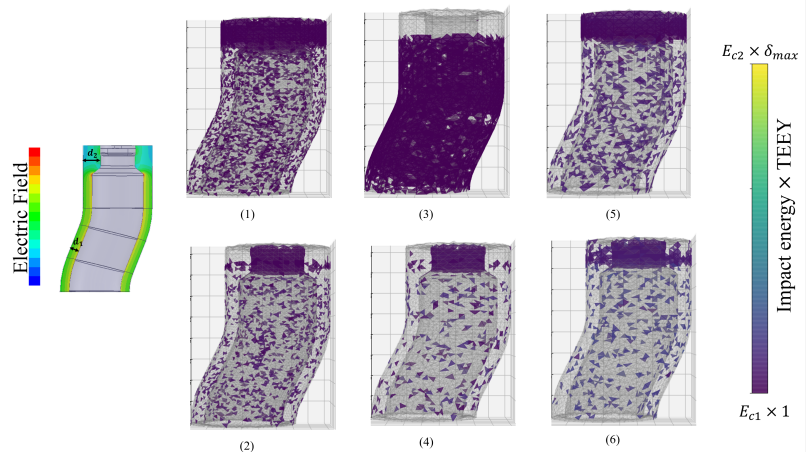
frequency range [46 – 65] MHz. For the *non-conditioned* case, we remark that the ignition of multipactor takes place in the vicinity of the maximal electric field zone — the coaxial-like zones connected to the capacitors of the antenna —, while its extinction is near the minimal — the parallel-plates-like geometry — electric field zone (Sub-figures (1) and (2)). For the *fully-conditioned* case, the multipactor conditions are no more satisfied² near the coaxial zone of the region. Therefore, the ignition and extinction of the multipactor take place near the parallel-plates-like zone (Sub-figures (3) and (4)).

- *Transition 2* of the impedance transformer. Figure 5.8 illustrates the various multipactor susceptible zones for the lowest and highest multipactor thresholds of each tested TEEY data curve in the WEST ICRH frequency range [46 – 65] MHz. The discontinuity in the plain red curve representing the lowest multipactor electric fields thresholds for the *non-conditioned* TEEY data observed in Figure 5.6 is explained herein. As *Transition 2* is made of two different inter-electrode separation distances d_1 ($d_1 = 19.5$ mm) and d_2 ($d_2 = 37.8$ mm) — $d_1 < d_2$, we found that in the frequency range [46 – 54] MHz the $f \times d_1$ product is too small for the multipactor occurrence and the multipactor ignition and extinction take place near the d_2 zone for the *non-conditioned* case (Sub-figures (1) and (2)). However, in the frequency range [55 – 65] MHz the $f \times d_1$ product was sufficient for sustaining multipactor, and the multipactor ignition is near the d_1 zone, while its extinction is near the d_2 zone for the *non-conditioned* case (Sub-figures (3) and (4)). For the *fully-conditioned* case, the multipactor conditions are not fulfilled in the d_1 zone, and the multipactor ignition and extinction are in the vicinity of the d_2 zone (Sub-figures (5) and (6)).

Therefore, it is worth mentioning that the lowest and highest multipactor electric field thresholds of Figure 5.5 and Figure 5.6 cannot be quantitatively compared as they refer to different quantities evaluated in different susceptible zones.

2: This could be explained by the increase of the first crossover energy and the reduction of the maximum TEEY.

Figure 5.8: (1) (respectively (2)) — The multipactor susceptible zone corresponding to the lowest (respectively highest) multipactor threshold when the *non-conditioned* TEEY is used. This zone remains the same in the frequency range [46 – 54] MHz. (3) (respectively (4)) — The multipactor susceptible zone corresponding to the lowest (respectively highest) multipactor threshold when the *non-conditioned* TEEY is used. This zone remains the same in the frequency range [55 – 65] MHz. (5) (respectively (6)) — The multipactor susceptible zone corresponding to the lowest (respectively highest) multipactor threshold when the *fully-conditioned* TEEY is used. This zone remains the same in the frequency range [46 – 65] MHz.



5.2.2 RF feed-through

The geometry of the RF feed-through, illustrated in Figure 5.9, is split into two regions: a conical silver-coated transmission line region (*Pre-Window*) and a multi-material region composed of a silver-coated conductor and the alumina ceramic (*Window*). The analysis has shown that the *Pre-Window* region is not prone to multipactor for the *non-conditioned* and the *fully-conditioned* TEEY data curves of a silver-coated stainless steel representative sample of the ICRH antenna (red and black curves of Figure 5.4).

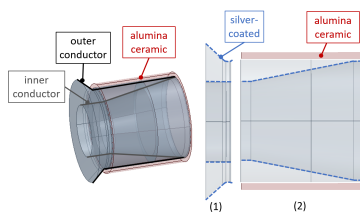


Figure 5.9: Left — The design of the RF feed-through, where in red the alumina ceramic is represented, in grey the inner conductor, and in black the outer conductor. Right — The cut view representation of each of the RF feed-through multipactor regions. The RF feed-through is divided into two different multipactor regions: (1) — *Pre-Window* of silver-coated stainless steel material, (2) — *Window* of multi-material structure (alumina and silver-coated stainless steel).

As the *Window* region is a multi-material region, we determined the multipactor electric field thresholds using the Spark-3D software while assigning a single TEEY data curve at a time for all the surfaces constituting the region:

1. The *non-conditioned* TEEY data of a WEST representative silver-coated stainless steel sample — red curve of Figure 5.4.
2. The *fully-conditioned* TEEY data of a WEST representative silver-coated stainless steel sample — black curve of Figure 5.4.
3. An as-received alumina's TEEY data — blue curve of Figure 5.10.
4. A conditioned TEEY data of an alumina sample — orange curve of Figure 5.10.

The multipactor simulations have shown that when the TEEY data curves (2) and (4) are assigned to the surfaces, no multipactor is triggered. Therefore, only the results of (1) and (3) are represented in blue and orange, respectively, on Figure 5.11.

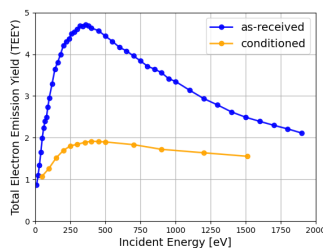


Figure 5.10: In blue, the TEEY data for an as-received alumina sample (measured at ONERA/DPHY). In orange, the TEEY data for a conditioned alumina sample. The conditioned TEEY data are extracted from (Bira (2021)).

In Figure 5.11, the Spark-3D results show that the as-received alumina TEEY assignment (3) triggers multipactor over the WEST ICRH frequency range, while the *non-conditioned* silver TEEY assignment (1) triggers multipactor for frequencies above 60 MHz. The same surface material assignments are tested at 55 MHz using Ansys-HFSS and have shown different results. In particular, (1) shows the presence of multipactor (bold blue markers), and (3) shows a wider range of multipactor than the Spark-3D case (bold orange markers). The difference between Spark-3D and Ansys-HFSS results could be attributed to the particle tracking implementation and the difference in the electron emission distribution function. Nevertheless, it is not possible to conclude on the

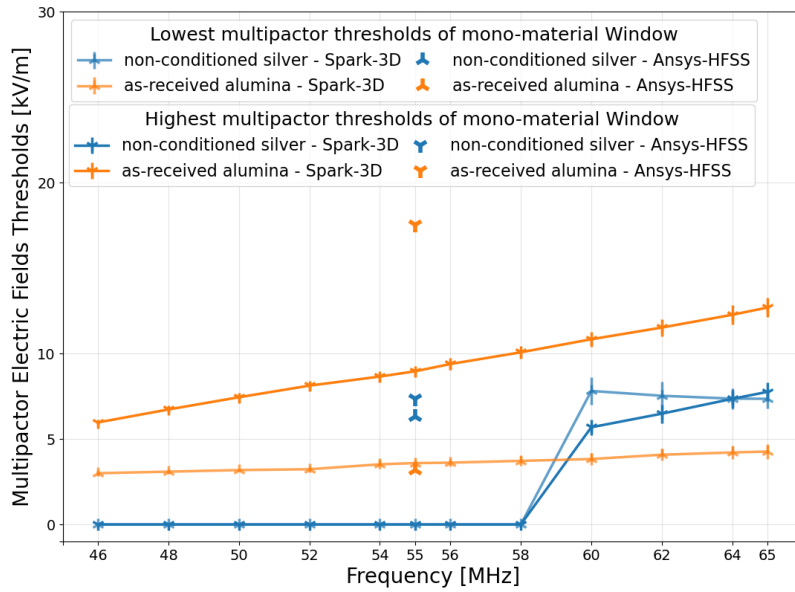


Figure 5.11: The multipactor electric field thresholds for the *Window* multipactor analysis region of the RF feed-through: The blue (respectively orange) plain lines correspond to the lowest and highest multipactor electric field thresholds obtained by Spark-3D when the *non-conditioned* TEEY corresponding to the silver-coated WEST ICRH representative sample (respectively the TEEY of an as-received alumina sample) is assigned. The bold blue (respectively orange) markers correspond to the lowest and highest multipactor electric field thresholds obtained by Ansys-HFSS at 55 MHz for the same TEEY assignment of Spark-3D.

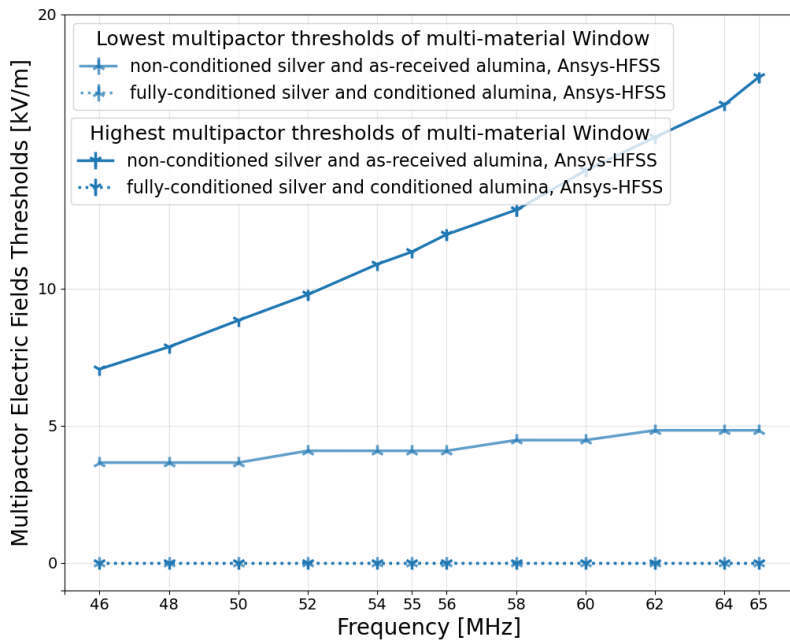


Figure 5.12: The multipactor electric field thresholds for the *Window* multipactor analysis region of the RF feed-through using multi-material TEEY data. For the plain blue lines the *non-conditioned* silver and the as-received alumina are used and for the dotted blue lines the *fully-conditioned* silver and the conditioned alumina are assigned to the region's surfaces.

out-performance of one over the other since there are no benchmark data for comparison.

Moreover, we conducted multi-material simulations using Ansys-HFSS where we assigned first the *non-conditioned* silver data (red curve of Figure 5.4) along with the as-received alumina TEEY data (blue curve of Figure 5.10), and then the *fully-conditioned* silver data (black curve of Figure 5.4) with the conditioned alumina data (orange curve of Figure 5.10). The multipactor electric field thresholds for the first and second cases are shown respectively as plain and dotted blue lines in Figure 5.12. For the conditioned silver and alumina data, there is no multipactor in the region, and the multipactor electric field thresholds are null.

It should be noted that we used the multipactor electric fields obtained

by Ansys-HFSS for the determination of the generators' forward powers triggering multipactor in the RF feed-through of the ICRH antennas. Moreover, the lowest and highest multipactor electric field thresholds are not quantitatively compared as they refer to different quantities.

5.3 Multipactor during WEST ICRH RF Conditioning

[34] Hillairet et al. (2021)

During the RF conditioning step — introduced in Section 1.4.3 of Chapter 1, pressure rises are measured inside the antenna by the vacuum gauges connected to the rear of each impedance transformer. In addition, visible light, RF sub-harmonics, and reflected power are observed [34]. We expect that the multipactor is responsible for some of these observations.

During this RF conditioning phase, there is no plasma in the vacuum vessel, and we will assume that no toroidal magnetic DC field is present. As the antennas face vacuum-loading, they have a very low coupling under these conditions, and only a very small fraction of the generators' power is coupled into the vacuum vessel. The forward power of the generators during this phase is, in practice, limited to the range [5 – 20] kW per antenna side, and applied during 20 ms maximum, to avoid exceeding the voltage and current limits of the variable capacitors.

During the first phase of the antenna's RF conditioning, one antenna side is energised at a time while the other generator remains off. Once the nominal voltage across the capacitors (28 kV) is reached, the same process is repeated for the other side. Once both sides are conditioned independently on short pulses, then both sides are powered in dipole configuration. Once achieving 28 kV on both sides of the antenna on short pulses, the duration of the RF pulse is progressively increased, up to 5 s. As the cross-talk between the two sides of one ICRH antenna can also trigger the multipactor into the non-energised side, we should determine the multipactor-triggering conditions and the locations where the multipactor is initiated on both powered and non-powered sides of one antenna.

During its RF vacuum conditioning phase, operators of the ICRH antennas control, for a given frequency, the RF power of the generators feeding one or both sides of the antenna and the four internal variable capacitors. The three antennas are identical, and the coupling between the antennas is negligible when facing the vacuum. The latter means we can neglect the coupling between antennas during the RF conditioning phase. Nevertheless, the coupling between the sides of one antenna remains significant. Therefore, we studied three operational cases for one ICRH antenna:

Case 1: The generators of both sides of the antenna are on, and the capacitors of both sides are *tuned*. The antenna is operated in dipole — with a 180° phase difference between both sides.

Case 2: The generator of one side of the antenna (*right* or *left*) is on, the generator of the other side is off, and capacitors of both sides are *tuned*.

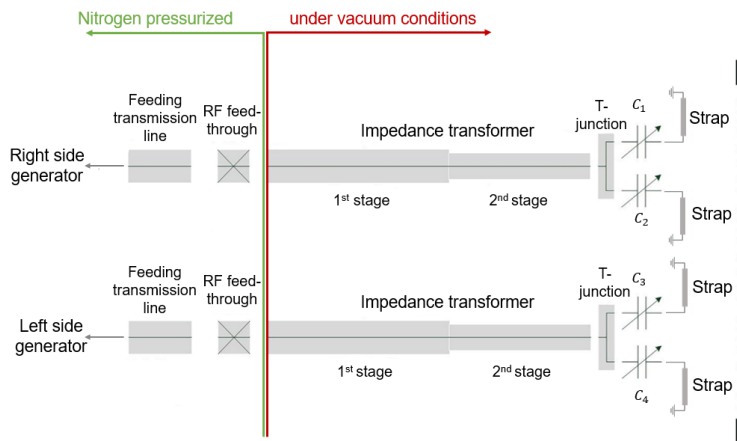


Figure 5.13: Circuit model of one ICRH antenna, during its RF conditioning phase, where both sides of the antenna are modelled to take into account the RF coupling. Each side of the antenna is composed of (1) — one generator that could be in one of two possible states (on or off), (2) — one RF ceramic feed-through window, (3) — one impedance transformer, (4) — one T-junction, (5) — two variable capacitors. Both sides of the ICRH antenna are connected through (6) — one front face. The operator of the antenna could only configure the RF frequency, powers and phases of the generators and the values of the capacitors.

Case 3: The generator of one side of the antenna is on, and that of the other is off. The capacitors of the powered generator are *tuned*, while the capacitors of the off-mode side are *detuned*.

We apply our methodology described in Section 5.1 for each operational case. In particular, for the first step of it, we use the results given in Section 5.2. The second and third steps are elaborated in the following subsections.

5.3.1 Determination of the Antenna Electric Fields

The circuit model of one ICRH antenna during its RF conditioning is represented in Figure 5.13. In this circuit model, all the components (T-junction, impedance transformer, and RF feed-through) of the *left* and *right* sides of the antenna are taken into consideration using their full-wave models in ANSYS Circuit, except for the capacitors that are modelled using an equivalent lumped circuit determined from a fitting of a full-wave model [107]. The series resistor is set to zero (respectively infinity) when a generator is on (respectively off) and the shunt resistor to infinity (respectively zero). The latter is done to mimic the operational situation while accurately modelling the forward impedance seen from the RF window's side when the generator is off.

[107] Hillairet (2020)

At a particular frequency of interest, and for each side: *i*) generator state is chosen — on or off, and the forward power(s) of the on-mode generator(s) is (are) set. *ii*) Capacitors' state is chosen — *tuned* or *detuned* along with the capacitance values for the tuned side(s). Then, solving the self-consistent simulation leads to the determination of the *excited electric fields* in each multipactor region of the T-junction, impedance transformer, and RF feed-through components. The *excited electric fields* are evaluated in two susceptible zones: the susceptible zone corresponding to the *lowest multipactor electric field threshold*, and the one corresponding to the *highest multipactor electric field threshold*, as obtained in Section 5.2.

Figure 5.14: The generators' forward powers, as a function of the ICRH frequency range, responsible for triggering the multipactor in its corresponding antenna side (the figure of the left (respectively right) corresponds to the results of the left (respectively right) side of the antenna). The red (respectively black) curves correspond to the minimal and maximal forward powers triggering multipactor in one antenna side for the *non-conditioned* (respectively *fully-conditioned*) TEEY cases represented in red (respectively black) in Figure 5.4. The dashed grey band corresponds to the nominal RF conditioning operational powers.

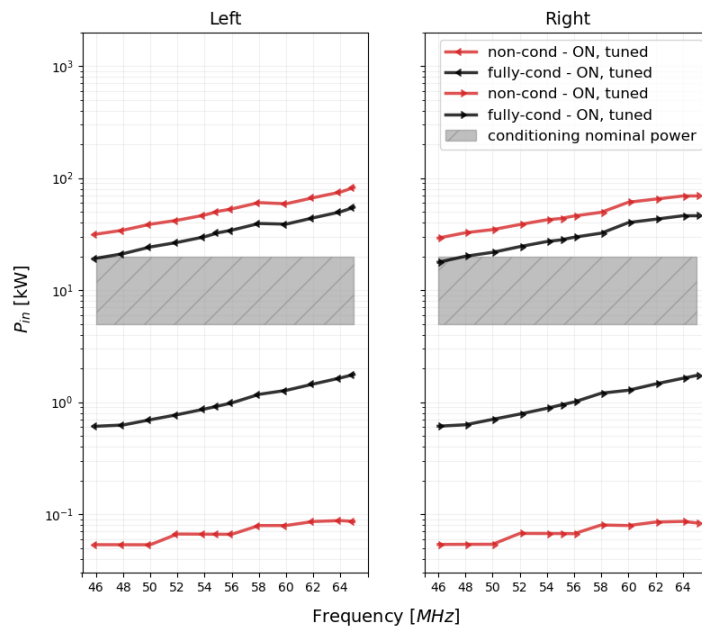
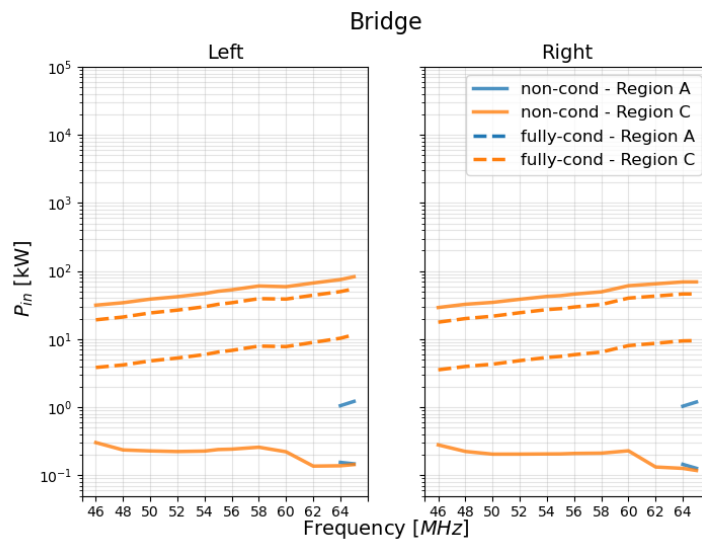


Figure 5.15: Left (respectively Right) — In solid lines, the generators' forward powers, as a function of the ICRH frequency range, responsible for triggering multipactor in the multipactor-prone regions (*Region A* and *Region C*) of the T-junction for the *left* (respectively *right*) side of the antenna. The solid lines are the results for the *non-conditioned* TEEY case. In dashed lines, the generator's forward powers, as a function of the ICRH frequency range, responsible for triggering multipactor in the multipactor-prone region (*Region C*) of the T-junction for the *left* (respectively *right*) side of the antenna. The dashed lines are the results for the *fully-conditioned* TEEY case. *Region A* is not prone to multipactor for the *fully-conditioned* TEEY case (The blue dashed line is zero-valued and is not visible in the logarithmic scale.).



5.3.2 Multipactor-Triggering Generators' Forward Powers

In this section, multipactor regions are bounded by the lower and upper generators' forward powers triggering multipactor on each antenna side as a function of the antenna frequency range. Red curves represent the results of the *non-conditioned* TEEY for the *left* and the *right* sides of the antenna. Black curves represent the results of the *fully-conditioned* TEEY. The nominal generator forward power range during RF conditioning is represented as a grey band.

We note that, when examining the generators' forward powers triggering multipactor in various regions, such as the T-junction, impedance transformer, and RF feed-through, the zero-valued multipactor electric field

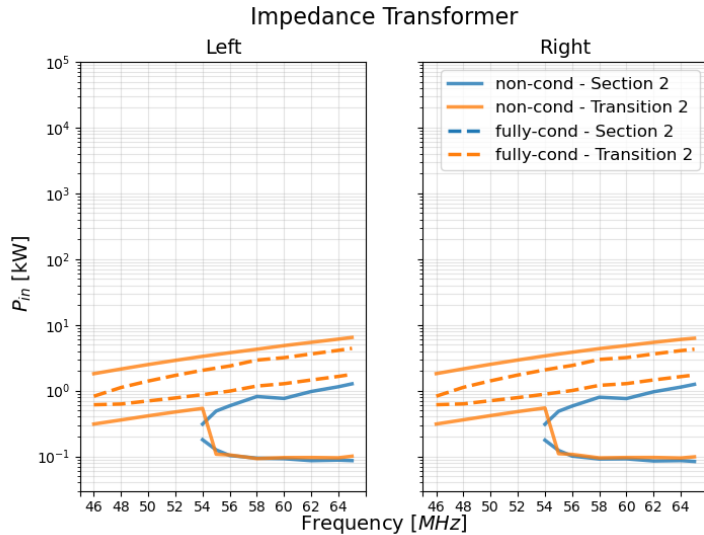


Figure 5.16: Left (respectively Right) — In solid lines, the generators' forward powers, as a function of the ICRH frequency range, responsible for triggering multipactor in the multipactor-prone regions (*Section 2* and *Transition 2*) of the impedance transformer for the *left* (*right*) side of the antenna. The solid lines are the results for the *non-conditioned* TEEY data curve. In dashed lines, the generator's forward powers, as a function of the ICRH frequency range, responsible for triggering multipactor in the multipactor-prone region (*Transition 2*) of the impedance transformer for the *left* (*right*) side of the antenna. The dashed lines are the results for the *fully-conditioned* TEEY data curve. *Section 2* is not prone to multipactor for the *fully-conditioned* TEEY case (The blue dashed line is zero-valued and is not visible in the logarithmic scale.).

thresholds shown in Figure 5.5, Figure 5.6, and Figure 5.12 will not be visible. This is because we will represent the generators' forward powers triggering multipactor on a logarithmic scale for readability.

5.3.2.1 Results — Case 1

In this first case, both generators are powered with the same forward power, and both capacitors' sides are *tuned*. Because of the antenna symmetry and vacuum loading (isotropic), it is expected to obtain similar multipactor power thresholds on both sides. The thresholds illustrated in Figure 5.14 confirm this expectation as, for both TEEY cases, *left* generator's forward powers triggering multipactor on its side are the same as for the *right* side.

Surface conditioning reduces the generators' forward power multipactor thresholds, as for the multipactor electric field thresholds in Section 5.2. In particular, it tends to increase the lower generators' forward power thresholds and decrease the upper generators' ones, thus reducing the multipactor domain.

The regions where multipactor takes place are deduced by looking at the generators' forward powers responsible for triggering multipactor in each component. The T-junction's, impedance transformer's, and RF feed-through's different multipactor regions, corresponding to the *right* and *left* sides of the antenna, are represented in Figure 5.15, Figure 5.16, and Figure 5.17 respectively. The solid lines correspond to the results for the *non-conditioned* case (red curve of Figure 5.4), while the dashed lines correspond to the *fully-conditioned* case (black curve of Figure 5.4). Results of the *left* side of the antenna are identical to those of the *right* side. In addition, the multipactor zone is reduced within the *Region C* of the T-junction and the *Transition 2* of the impedance transformer for the *fully-conditioned* case.

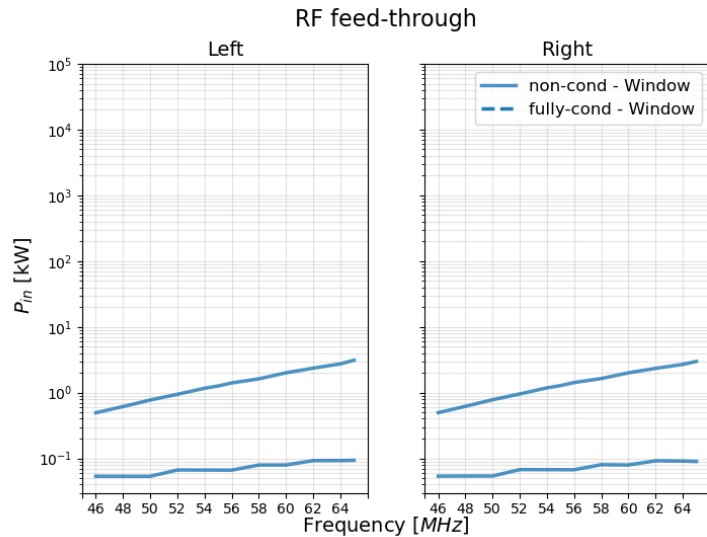


Figure 5.17: Left (respectively Right) — In solid lines, the generators’ forward powers, as a function of the ICRH frequency range, responsible for triggering multipactor in the multipactor-prone region (*Window* of the RF feed-through) for the *left* (respectively *right*) side of the antenna. The solid lines are the results for the *non-conditioned* TEEY data curve. *Window* is not prone to multipactor for the *fully-conditioned* TEEY case (The blue dashed line is zero-valued and is not visible in the logarithmic scale).

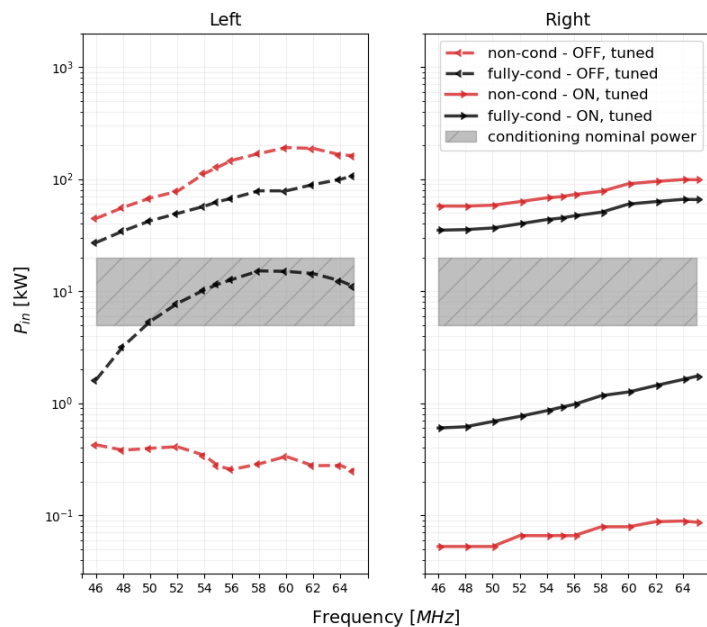


Figure 5.18: The *right*-side generator’s forward powers, as a function of the ICRH frequency range, responsible for triggering the multipactor in the different antenna sides (the figure of the left (respectively right) corresponds to the results of the *left* (respectively *right*) side of the antenna). The red (respectively black) curves correspond to the minimal and maximal forward powers of the on-mode generator, triggering multipactor in one antenna side for the *non-conditioned* (respectively *fully-conditioned*) TEEY data curve represented in red (respectively black) in Figure 5.4. The dashed grey band corresponds to the nominal RF conditioning operational powers.

5.3.2.2 Results — Case 2

In the second case, only the generator of the *right* side is energised. Hence, multipactor-triggering powers correspond to the *right* side generator’s forward powers. In other terms, we are interested in determining the forward powers for the *right* generator triggering multipactor in both the powered side (*right*) and the non-powered side (*left*), the latter being caused by the cross-talk between antenna sides.

Figure 5.18 represents the minimal and maximal forward powers, triggering multipactor in the *left* and the *right* sides of the RF-conditioned antenna, for the *non-conditioned* TEEY in red, and the *fully-conditioned* TEEY in black. This figure reveals that, in the RF-conditioning nominal power range and within the ICRH frequency range, leaving the off-mode side’s capacitors *tuned* leads to the trigger of multipactor in both sides of

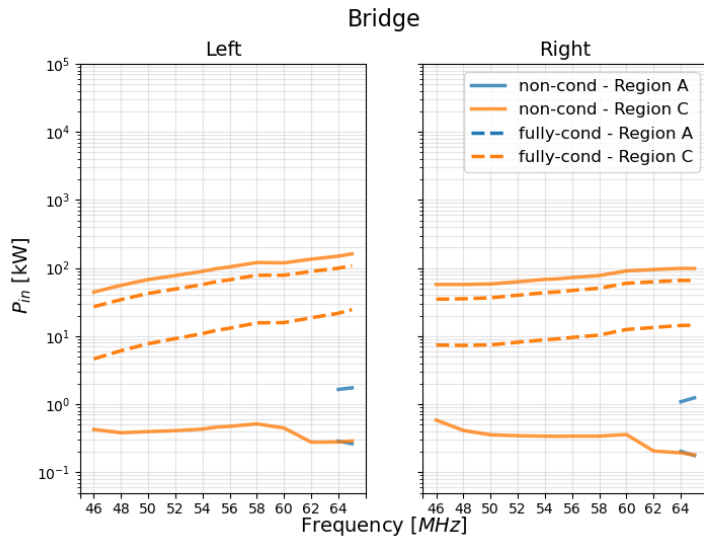


Figure 5.19: Left (respectively Right) — In solid lines, the on-mode generator’s forward powers, as a function of the ICRH frequency range, responsible for triggering the multipactor in the multipactor-prone regions (*Region A* and *Region C*) of the T-junction for the *left* (respectively *right*) side of the antenna. The solid lines are the results for the *non-conditioned* TEEY data curve. In dashed lines, the on-mode generator’s forward powers, as a function of the ICRH frequency range, responsible for triggering multipactor in the multipactor-prone region (*Region C*) of the T-junction for the *left* (*right*) side of the antenna. The dashed lines are the results for the *fully-conditioned* TEEY data curve. *Region A* is not prone to multipactor for the *fully-conditioned* TEEY case (The blue dashed line is zero-valued and is not visible in the logarithmic scale.).

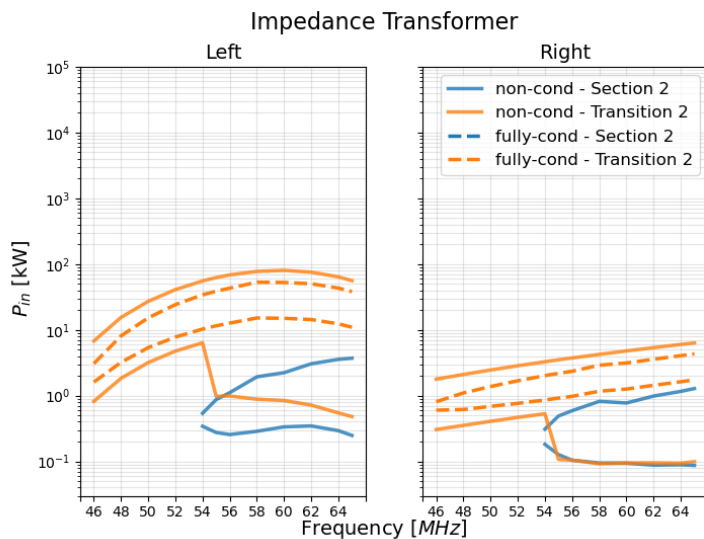


Figure 5.20: Left (respectively Right) — In solid lines, the on-mode generator’s forward powers, as a function of the ICRH frequency range, responsible for triggering the multipactor in the multipactor-prone regions (*Section 2* and *Transition 2*) of the impedance transformer for the *left* (respectively *right*) side of the antenna. The solid lines are the results for the *non-conditioned* TEEY data curve. In dashed lines, the on-mode generator’s forward powers, as a function of the ICRH frequency range, responsible for triggering multipactor in the multipactor-prone region (*Transition 2*) of the impedance transformer for the *left* (*right*) side of the antenna. The dashed lines are the results for the *fully-conditioned* TEEY data curve. *Section 2* is not prone to multipactor for the *fully-conditioned* TEEY case (The blue dashed line is zero-valued and is not visible in the logarithmic scale.).

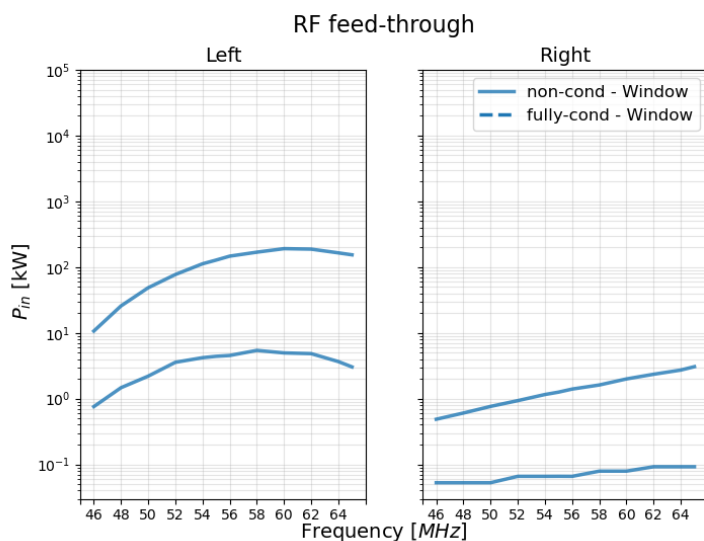


Figure 5.21: Left (respectively Right) — In solid lines, the on-mode generator’s forward powers, as a function of the ICRH frequency range, responsible for triggering the multipactor in the multipactor-prone region (*Window* of the RF feed-through) for the *left* (respectively *right*) side of the antenna. The solid lines are the results for the *non-conditioned* TEEY data curve. *Window* is not prone to multipactor for the *fully-conditioned* TEEY case (The blue dashed line is zero-valued and is not visible in the logarithmic scale.).

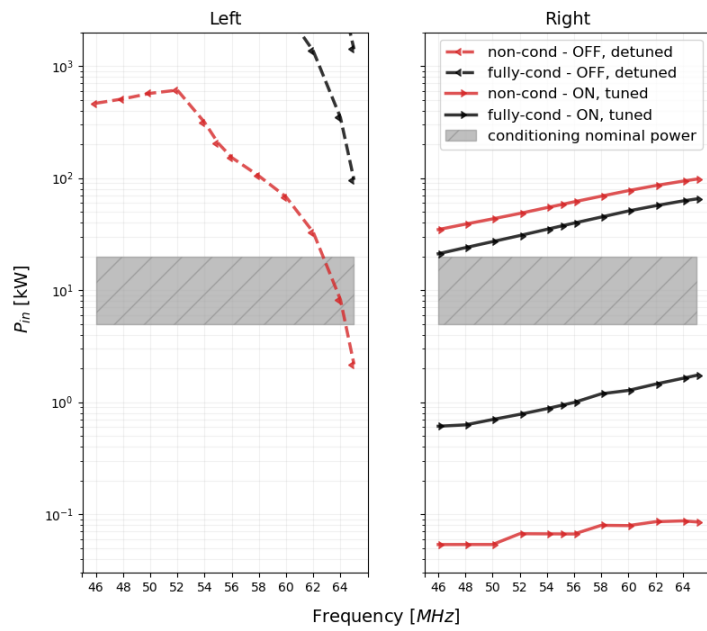


Figure 5.22: CASE DESCRIPTION. Same caption as Figure 5.18 but for Case 3. The non-visible lines have values higher than the maximum value readable on the y -axis coordinate.

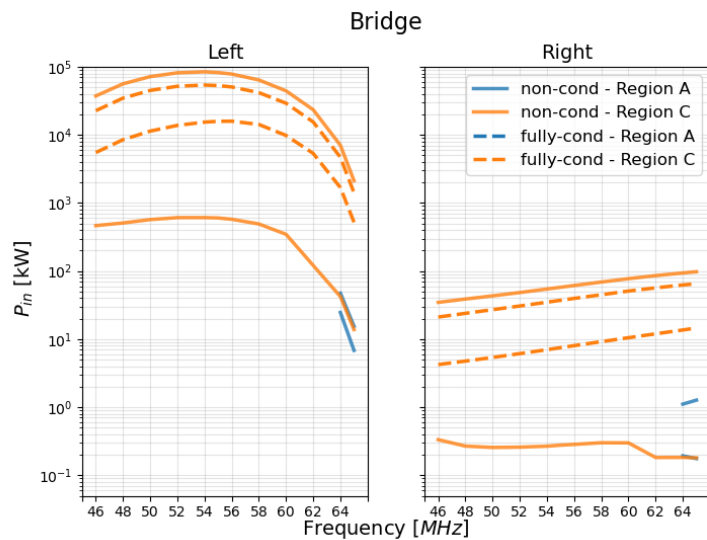


Figure 5.23: CASE DESCRIPTION. Same caption as Figure 5.19 but for Case 3.

the antenna, for the *non-conditioned* TEEY measurements. Nevertheless, the probability of triggering the multipactor on the non-powered side is reduced when the surface of the antenna is fully conditioned.

Therefore, the very remarkable similarity between **Case 1** and **Case 2**, especially for the *non-conditioned* TEEY curve, is explained by the state of the capacitors. In particular, for the TEEY measurements before any conditioning, the multipactor-triggering generator’s powers for the T-junction of the *right* (on) and *left* (off) sides of the antenna (represented in Figure 5.19) are very comparable even though one of the sides is not even powered. When the capacitors of the off-mode side are *tuned*, the power is coupled to the off-mode side and is responsible for triggering the multipactor in the T-junction, the nearest component to the front face, due to the sides’ cross-talk. Nevertheless, this is not the case for the impedance transformer and the RF feed-through, as shown in Figure 5.20

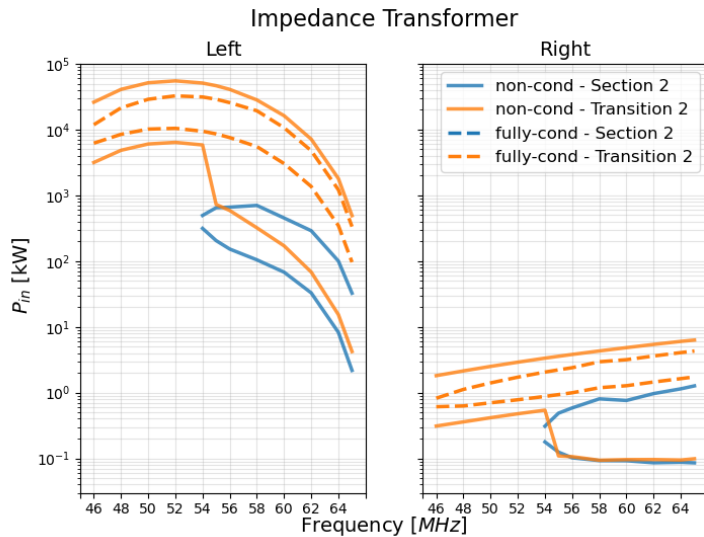


Figure 5.24: CASE DESCRIPTION. Same caption as Figure 5.20 but for Case 3.

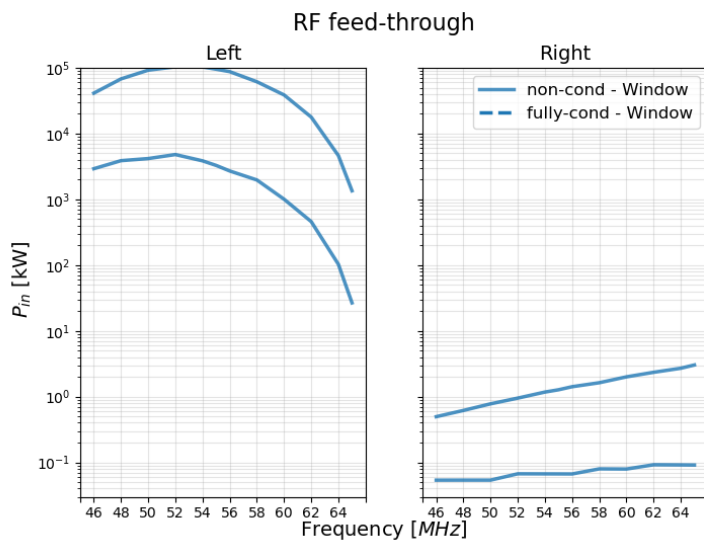


Figure 5.25: CASE DESCRIPTION. Same caption as Figure 5.21 but for Case 3.

and Figure 5.21 respectively. At a given frequency, the forward power needed to trigger the multipactor inside the impedance transformer of the off-mode side (*left*) is higher than for the on-mode side (*right*) as the impedance transformer and the RF feed-through are farther from the capacitors than the T-junction.

5.3.2.3 Results — Case 3

In this last case, the capacitors of the off-mode (*left*) side are *detuned* while the capacitors of the on-mode (*right*) side are *tuned*. On-mode generator's forward powers, responsible for triggering multipactor, are illustrated in Figure 5.22. This figure shows that, for the *non-conditioned* case, in the nominal power range for RF-conditioning, and within the frequency range [46 – 63] MHz, multipactor can be triggered only in the on-mode side and not the off-mode side. Nevertheless, within [63 – 65] MHz, multipactor can still be triggered inside the components of both sides of the antenna. Moreover, for the *fully-conditioned* case, within the ICRH

frequency range, the multipactor is only triggered on the on-mode side, while the off-mode side is not prone to multipactor.

The differences between Figure 5.22 and Figure 5.18 are attributed to the capacitors' states of the off-mode side, which are respectively *detuned*, and *tuned*. This result reveals the necessity of having *detuned* capacitors to avoid or reduce multipactor on the non-powered side. This conclusion is particularly relevant to operation, as safety interlocks do not depend on the off-mode side during RF conditioning on a single side.

For **Case 3**, the forward powers needed to trigger multipactor inside the T-junction, impedance transformer, and RF feed-through (shown in Figure 5.23, Figure 5.24, and Figure 5.25) of the non-powered side are higher than those seen in **Case 2**, as the cross-talk to the off-mode side is reduced when the capacitors are *detuned*.

5.3.3 Conclusion on the Results

The results indicate the best strategy for the RF operators to follow to minimise risks associated with multipactor during the RF conditioning phase. The latter is to detune the capacitors of the off-mode side of the ICRH antenna when only one side is active. In addition, the TEEY's reduction associated with the surface conditioning reduces the multipactor power domain or even totally suppresses it. The latter could be related to the experimental observation of the pressure rise level decrease after many RF conditioning shots.

5.4 Multipactor during WEST ICRH Plasma Scenarios

In this section, we want to investigate the multipactor's responsibility for the pressure rise measured in the non-powered ICRH antennas when only one antenna is powered — detailed in Section 1.5 of Chapter 1.

In such scenarios, the antennas facing plasma have a high coupling depending on the plasma properties, and a noticeable fraction of the generators' power is coupled to the plasma. The forward generators' power during plasma scenarios is within the [100 kW – 1.5 MW] range per antenna side, and applied during a few seconds. During plasma scenarios, when an ICRH antenna is powered, both sides are powered — with the same power — in dipole configuration.

During plasma operation, operators of the ICRH antenna system control, for a given frequency, the RF power of the generators feeding both sides and the four internal variable capacitors of all three ICRH antennas. We studied the following two operational cases:

Case 1: One ICRH antenna is on — the generators of both sides are powered — and the four capacitors are *tuned* at 55 MHz. The antenna is operated in dipole — with a 180° phase difference between both sides. The remaining two antennas are off, and their capacitors are *tuned* at 55 MHz.

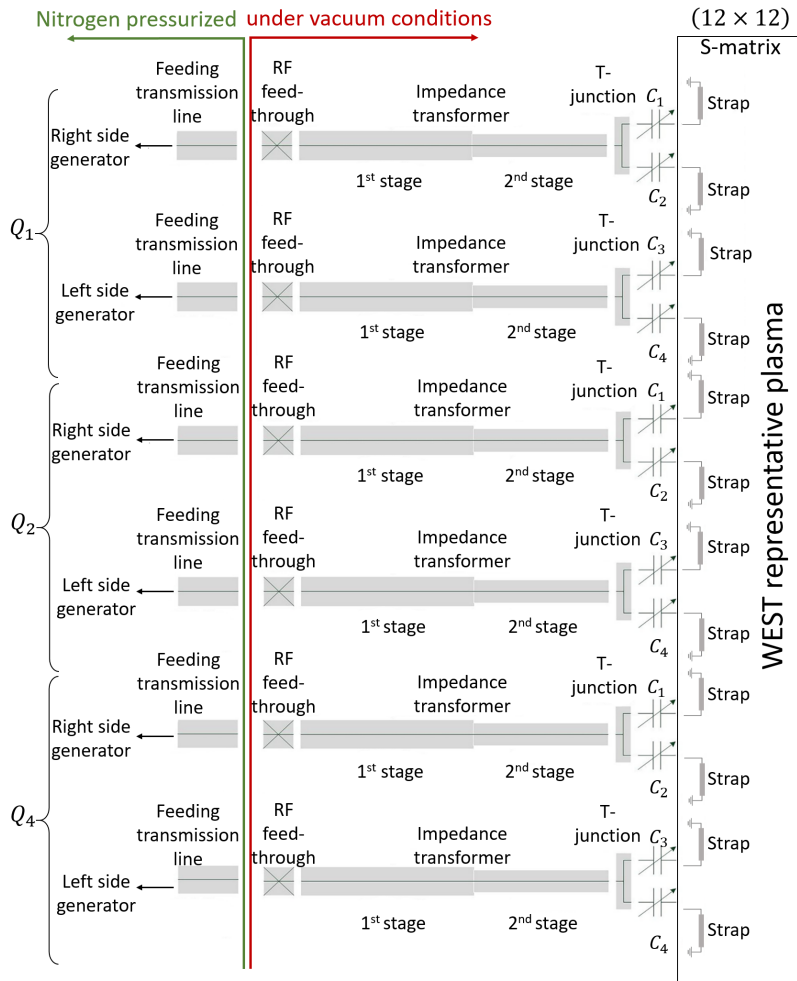


Figure 5.26: Circuit model of the three WEST ICRH antennas facing plasma, where both sides of each antenna are modelled. The WEST representative plasma scenario is represented by a (12×12) S-matrix to take into account the RF coupling between the ICRH antennas.

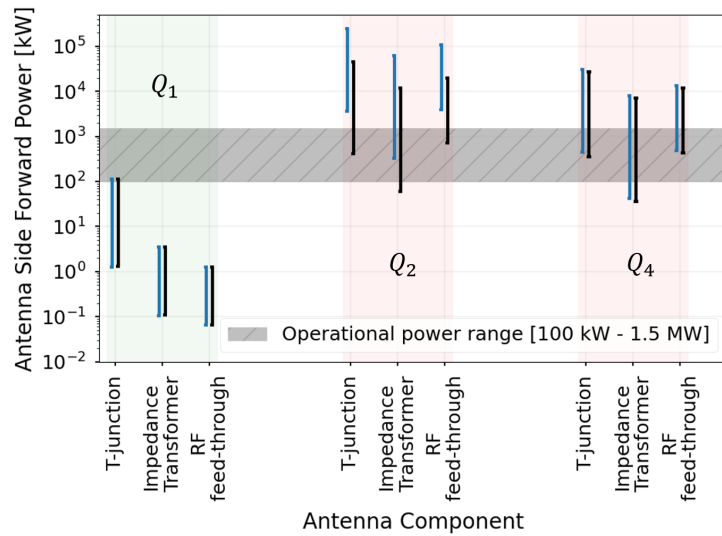
Case 2: One ICRH antenna is on — the generators of both sides are powered — and the four capacitors are *tuned* at 55 MHz. The antenna is operated in dipole — with a 180° phase difference between both sides. The remaining two antennas are off, and their capacitors are *detuned*.

5.4.1 Determination of the Antennas Electric Fields

The circuit model of three ICRH antennas during plasma scenarios is represented in Figure 5.26. Similarly to Section 5.3.1, each antenna side’s components are modelled. Moreover, an S-matrix representative of a WEST plasma scenario is obtained by a full wave model of the WEST torus with the three ICRH front faces. Therefore, this matrix is of dimension (12×12) as each antenna front face is a four-port passive component.

As in Section 5.3.1, at the frequency of interest the operators choose *i)* the generators’ state of each antenna and the forward power of the on-mode generators — the same power is applied for the *left* and *right* side generators, and *ii)* the four capacitors’ state of each ICRH antenna — *tuned* at a given frequency (could be different from the frequency of the on-mode generators) or *detuned*. Then, solving self-consistently the

Figure 5.27: The forward powers of one generator triggering the multipactor in the T-junction, impedance transformer and RF feed-through of each antenna Q_1 , Q_2 , and Q_4 . The blue (respectively black) vertical lines correspond to the forward powers triggering multipactor in the components of the *left* (respectively *right*) side of each antenna. The grey hatched region corresponds to the nominal operational power range of one powered generator. The results correspond to **Case 1**.



simulation leads to the determination of the *excited electric fields* in all the WEST ICRH antennas.

5.4.2 Multipactor-Triggering Generators' Forward Powers

In this section, we determine for each component of each antenna side the lower and upper one side generator forward powers triggering the multipactor at the frequency of 55 MHz.

5.4.2.1 Results — Case 1

In this first case, both generators of the antenna Q_1 are powered with the same forward power, and the four capacitors are *tuned* for the antenna to resonate at 55 MHz. Q_2 and Q_4 are non-powered with their capacitors *tuned* at 55 MHz.

First, we considered the *non-conditioned* TEEY data curve (red curve of Figure 5.4) of the silver-coated components and the as-received TEEY data curve of the alumina ceramic (blue curve of Figure 5.10). The results are illustrated in Figure 5.27 where we represented the range of forward generator's power³ triggering the multipactor in each antenna component — T-junction, impedance transformer and the RF feed-through. The blue (respectively black) vertical lines correspond to the forward powers triggering multipactor in the components of the *left* (respectively *right*) side of each antenna. The grey hatched region corresponds to the operational nominal power range of one powered generator [100 kW – 1.5 MW].

It is seen that within the operational range of one generator of WEST ICRH antennas, the multipactor is triggered in all the components of the non-powered antennas (Q_2 and Q_4) except for the T-junction and RF feed-through of the *left* side of the Q_2 antenna as the electric field observed in their multipactor regions, within the [100 kW – 1.5 MW] power range, is not enough for the multipactor to be triggered in these components.

3: The forward power of the generator of one side of the powered antenna.

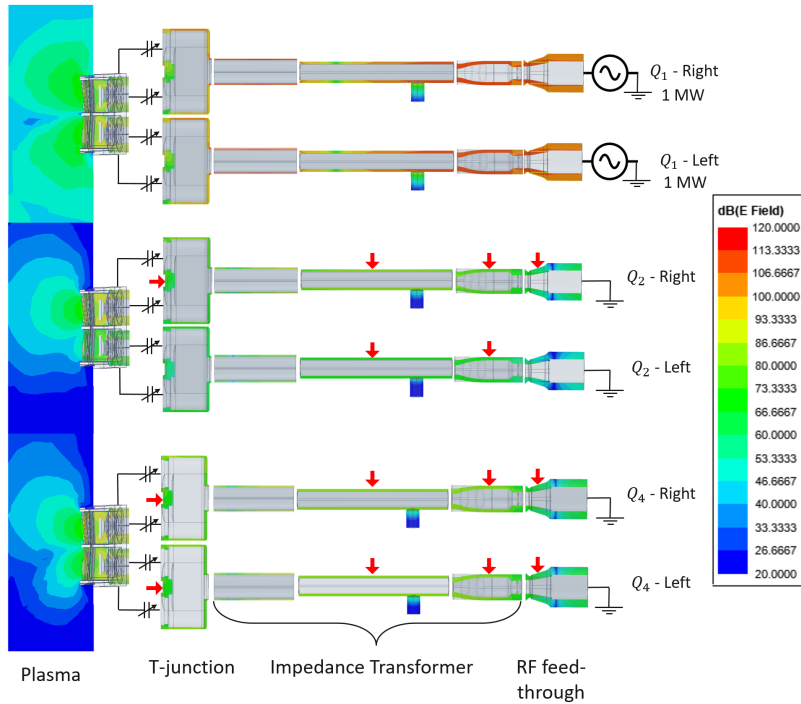


Figure 5.28: The electric field cartography in the various components of the three WEST ICRH antennas. Only Q_1 is powered with a forward power of 1 MW per antenna side. The components where the multipactor is triggered are indicated with red arrows.

The latter could be attributed to the anisotropic characteristics of the non-symmetrical S-matrix of the simulated plasma.

As an illustrative example, Figure 5.28 represents the electric field cartography in the WEST ICRH antennas for a forward power of 1 MW for both generators of the antenna Q_1 . In this figure, the red arrows refer to the components where the multipactor is triggered.

Second, we considered the *fully-conditioned* TEEY data curve (black curve of Figure 5.4) of the silver-coated components and the conditioned TEEY data curve of the alumina ceramic (orange curve of Figure 5.10). The results are illustrated in Figure 5.29. There is no forward power range for which the multipactor is triggered in the RF feed-through component since there is no multipactor in this component for the conditioned TEEY data.

Figure 5.29 shows that the conditioning reduces the multipactor range in the various components of the WEST ICRH antennas and that within the [100 kW – 1.5 MW] forward power range, there is almost no multipactor-trigger in the non-powered antennas when compared to the results of Figure 5.27 except for the impedance transformer of Q_4 when the forward power is approximately equal to 1.5 MW.

5.4.2.2 Results — Case 2

In this second case, both generators of the antenna Q_1 are powered with the same forward power, and the four capacitors are tuned for the antenna to resonate at 55 MHz. Q_2 and Q_4 are non-powered with their capacitors *detuned*. The results corresponding to the non-conditioned TEEY data curves are represented in Figure 5.30. The latter shows that, due to the capacitors detuning⁴, there is almost no multipactor-trigger in the non-powered antennas when compared to the results of Figure 5.27

4: The reduction of the multipactor range when the capacitors are detuned was also observed in the RF conditioning phase of one ICRH antenna.

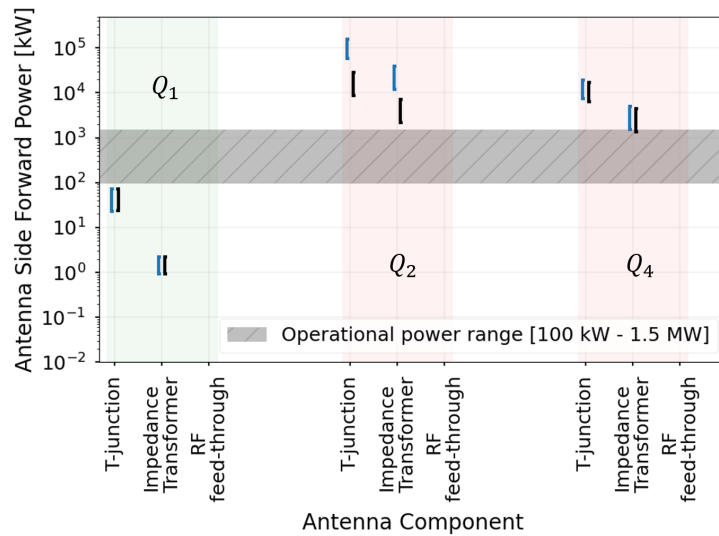


Figure 5.29: Same caption as Figure 5.27 but for *fully-conditioned* TEEY data for silver-coated and alumina surfaces.

except for the impedance transformer of the Q_4 's left side when the forward power is approximately equal to 1.5 MW. The multipactor is completely non-triggered when the conditioned TEEY data are used.

5.4.3 Conclusion on the Results

The results indicate that when only one antenna of the WEST ICRH system is powered, while the remaining two are off, the multipactor is triggered in the various components — T-junction, impedance transformer, and RF feed-through — of the non-powered antennas due to the inter-antennas coupling. The latter indicates that the multipactor-trigger could be the internal pressure rise's cause, which was observed experimentally in the non-powered antennas. Furthermore, the results show that the multipactor range is reduced when the surfaces are conditioned, and the capacitors of the off-mode antennas are detuned. The latter finding was evidenced during the RF conditioning phase and under plasma operation.

5.5 Multipactor on TITAN's Resonator

[108] Bernard et al. (2011)

TITAN [108] is a test-bed facility devoted to ion cyclotron resonance heating (ICRH) sub-assembly testing, built at CEA-Cadarache in France. Within this test-bed facility, the under-test component is connected to a high-power RF generator, delivering up to 2 MW in the frequency range 46 to 65 MHz. An RF resonator was used to reach relevant RF performance in vacuum, *i.e.*, a voltage in the order of a few tens of kilo-volts and current in the range of thousands of amperes. This resonator was made of two coaxial transmission lines fed with a T-junction. One of these branches is connected to the device under test, followed by a variable-matching short circuit. The other one is also connected to a variable-matching short circuit. For a given generator's frequency, the matching point is achieved by optimising the electric lengths of the coaxial transmission lines, being

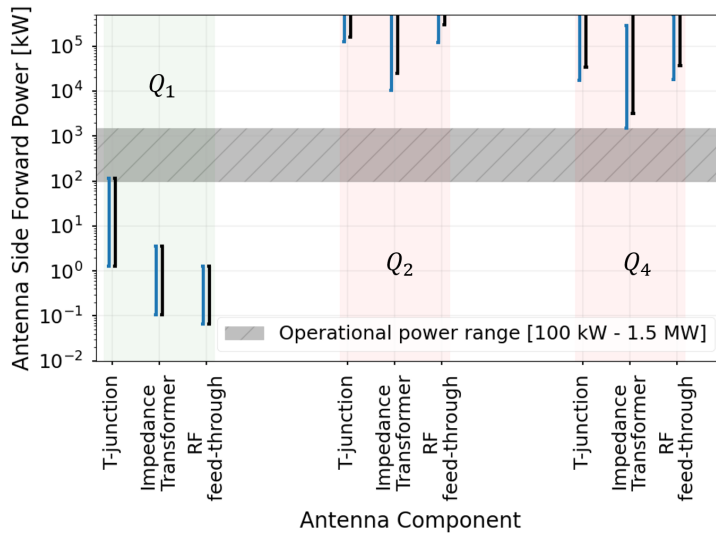


Figure 5.30: Same caption as Figure 5.27 but for Case 2.

the two variable-matching components. This resonator operated at levels up to (50 kV - 3 kA) to mimic the operating voltage and current of the devices under test (for a single frequency) [31]. The resonator is fed by an RF generator with a 30 Ω coaxial transmission line. As an under-vacuum device, it is therefore prone to multipactor.

[31] Hillairet et al. (2015)

The main specificity of the double-branch resonator is its operation with a high standing waves ratio (SWR). The benefit of the resonators' operation under standing waves is that we can achieve high voltages or currents at specific target locations within the resonator branches with relatively low input power. Nevertheless, the remaining components of the resonator are subject to low voltages or currents.

In TITAN, RF components are tested at high voltage (or current) densities in ranges possibly above the highest multipactor thresholds. Therefore, in practice, the multipactor power bands of the different parts of the resonator are bypassed during operation. However, it requires ramping up the RF power sufficiently fast to minimise the time spent in the multipactor regions to avoid multipactor to develop and detune the RF system [6]. Therefore, it is necessary to determine the lowest and the highest multipactor thresholds for all the resonator's parts.

[6] Graves et al. (2006)

5.5.1 TITAN's Resonator Description

The resonator is a 3-port passive RF geometry, constituted of two coaxial branches as illustrated in Figure 5.31. *Port 1* is the input port of the geometry and is connected to the RF generator. *Port 2* and *Port 3* are connected to two short circuits of variable lengths and resistance, adjusted for a standing wave pattern to be created. On the left side of Figure 5.31, the inner (bottom figure) and outer (top figure) conductors of the resonating loop are shown. Different colours refer to various materials: green for silver-coated conductors, light red for copper-coated conductors, and violet for stainless steel conductors.

Figure 5.31: Left — Resonator inner (bottom) and outer (top) conductors materials. Green refers to silver, light red to copper, and light violet to stainless steel. The numbers refer to the different multipactor sections. The underlined red sections' number refer to the sections that are found to be prone to multipactor. Right — The resonator's electric field plot, where the ports' excitation corresponds to the one obtained from the circuit analysis, leading to a standing wave with a minimised reflected power on the RF generator port (*Port 1*).

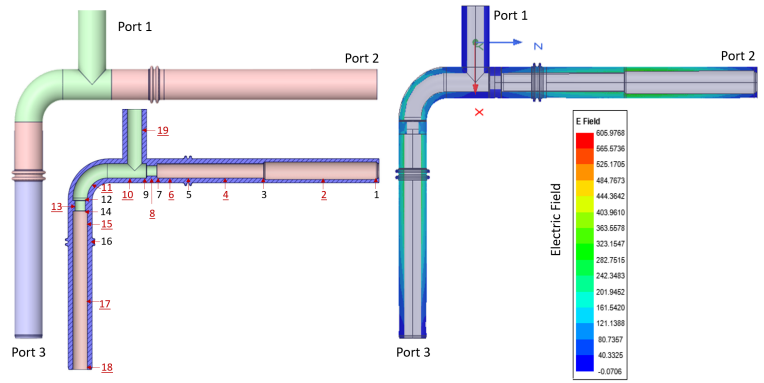


Figure 5.33: The resonator circuit used to minimise the reflected power back to *Port 1* at the frequency of interest, while the other two ports are short-circuited to create a standing wave pattern. The variable parameters are d_{DUT} and d_{CEA} being the physical length of the variable coaxial terminations.

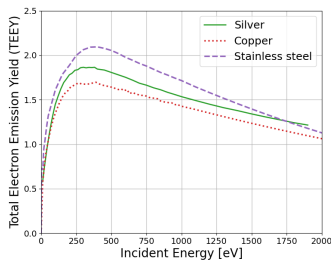
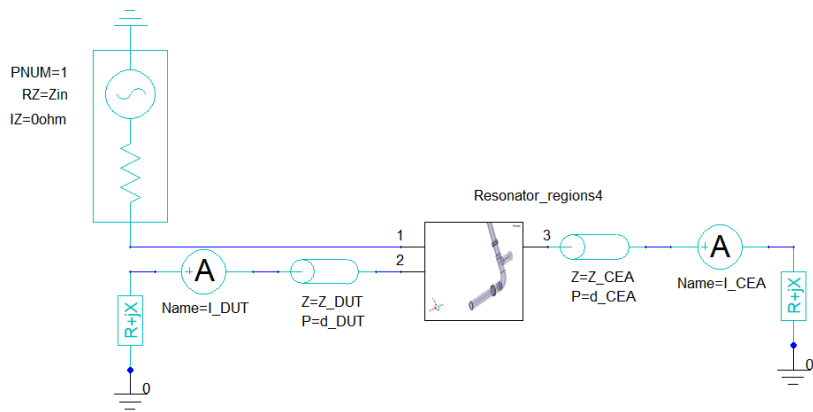


Figure 5.32: The TEEY data for a silver-coated, copper and stainless steel samples.

The total electron emission yields (TEEY) used for the different materials are measured at ONERA/DPHY and are given in Figure 5.32. As Spark-3D's version only supports a single TEEY, the sections having multiple TEEY will be analysed for each TEEY, composing the section separately.

Herein, the resonator's frequency of interest is 63 MHz. Therefore, to minimise the reflected power back to the RF generator (S_{11} parameter at *Port 1*) at the frequency of interest, the physical length of the two variable-matching coaxial transmission lines connected to *Port 2* and *Port 3* is optimised. To do so, we use ANSYS Electronics as shown in Figure 5.33, where two resistors are added to *Port 2* and *Port 3* to model the connected resistive shorts. Once the lengths minimising the reflected power at *Port 1* are determined, the electric field pattern in the resonator is similar to the plot on the right of Figure 5.31, where it is seen that the wave is a standing wave consisting of a resultant from an incident and reflected waves.

To perform multipactor analysis for such configurations, we create numerous multipactor sections of homogeneous geometry and/or electric field. For the resonator, 19 sections are chosen, whose location of each is indicated with numbered arrows in Figure 5.31. Details on each section's type and material are given in Table 5.1.

5.5.2 Multipactor Resonator Results

The methodology developed in Chapter 4 is applied to find the maximal (respectively mean) multipactor electric field evaluated in the susceptible

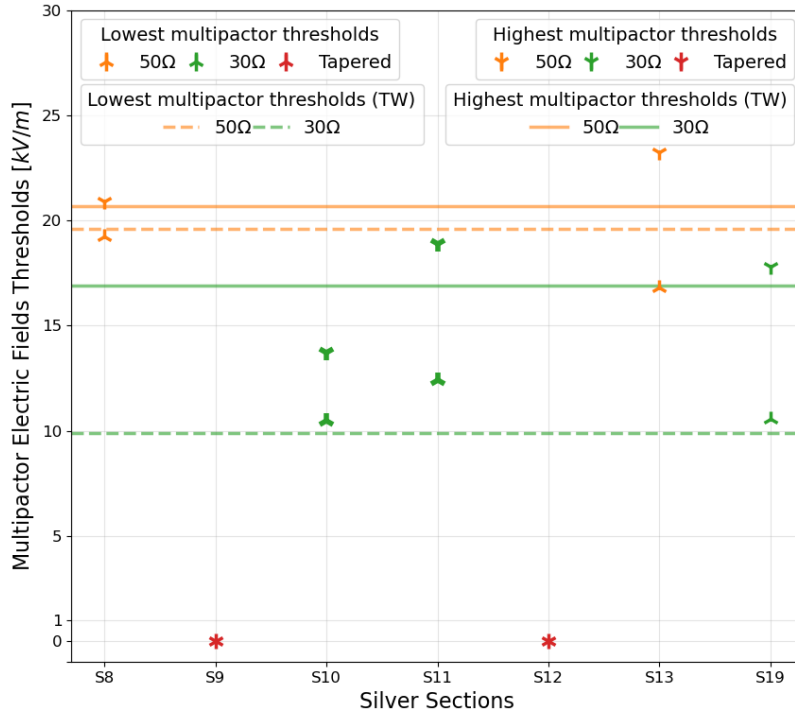


Figure 5.34: The relevant physical quantities for the multipactor's ignition and extinction when the initial ports' excitation are scaled by the multipactor scaling factor F_{min} and F_{max} . The horizontal lines are the physical quantities obtained for a TW in coaxial transmission lines of different characteristic impedance. Silver material sections are considered.

region corresponding to the ignition (respectively extinction) of multipactor in each resonator's section. The analysis is performed for each material type separately. The sections having the same geometries and materials but different electric fields (as illustrated in Figure 5.31) are comparable. Moreover, the coaxial transmission lines' sections' results are compared to the reference TW case results.

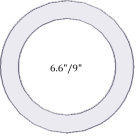



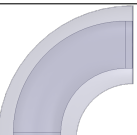




Figure 5.34, Figure 5.35 and Figure 5.36 represent respectively the lowest and highest multipactor electric field thresholds obtained by our methodology for the silver, copper, and stainless steel material sections. Each point of the figures is the averaged result obtained by three simulations run.

As represented in Figure 5.34, the silver-coated tapered geometries S9 and S12 are not prone to multipactor (red markers). The lowest and highest multipactor electric field thresholds of 50 Ω coaxial transmission line geometries S8 and S13 (orange markers) are within at most 15 % of the ones obtained for the same geometry subject to TW (orange plain and dashed horizontal lines). The same is observed for the 30 Ω coaxial transmission line S19 (green). The electric field thresholds of S10 and S11 are represented as bold green markers since the geometries are not typical 30 Ω coaxial transmission lines, yet their thresholds are comparable to the ones of a typical 30 Ω coaxial transmission line.

Similarly as illustrated in Figure 5.35, the copper-coated tapered geometries (S1, S3, S7, S12, S14, and S18) are not prone to multipactor. The lowest and highest multipactor electric field thresholds for the 18.74 Ω (S2), 30 Ω (S4, S6, S15, and S17), and 50 Ω (S8 and S13) coaxial transmission lines are at most within 15 % of the multipactor thresholds obtained for the same geometry subject to a TW pattern. The outer conductor bellows 30 Ω (S5 and S16) are not prone to multipactor (bold green markers).

The same conclusion is applied to the stainless steel 30 Ω coaxial trans-

Table 5.1: The different multipactor-analysis sections of the resonator structure. The type of the geometry, section's name, inner and outer conductors surface material, and the in-plane vacuum illustration are given.

Geometry	Section(s)	Inner conductor	Outer conductor	Vacuum Illustration
~18.74 Ω coaxial geometry	S2	Copper	Copper	
50 Ω coaxial geometry	S8 & S13	Silver	Copper	
30 Ω coaxial geometry	S4, S6 & S15	Copper	Copper	
	S17	Copper	Inox	
	S19	Silver	Silver	
Tee-junction 30 Ω coaxial geometry	S10	Silver	Silver	
Bend 30 Ω coaxial geometry	S11	Silver	Silver	
Helical (bellows) 30 Ω coaxial geometry	S5 & S16	Copper	Copper	
Tapered geometry (50 Ω - 30 Ω)	S7	Copper	Copper	
	S12	Silver	Copper	
	S9	Silver	Silver	
	S14	Copper	Copper	
Tapered geometry (30 Ω - ~18.74 Ω)	S1	Copper	Copper	
	S3	Copper	Copper	
Tapered geometry (30 Ω - 26 Ω)	S18	Copper	Inox	

mission line (S17) as shown in Figure 5.36. It was found that the stainless steel material tapered geometry S18 is prone to multipactor, and its multipactor thresholds are determined.

It should be noted that the lowest and highest multipactor electric field thresholds of Figure 5.34, Figure 5.35, and Figure 5.36 cannot be

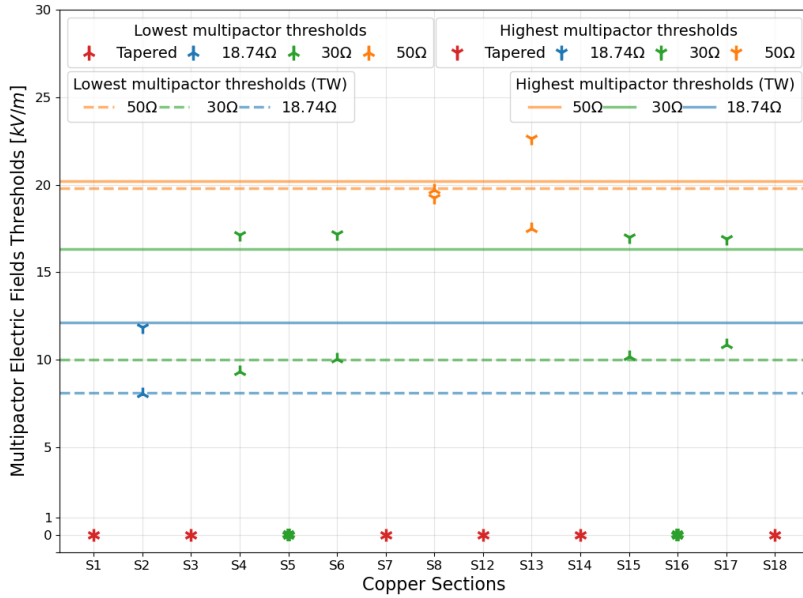


Figure 5.35: Same caption as Figure 5.34. Copper material sections are considered.

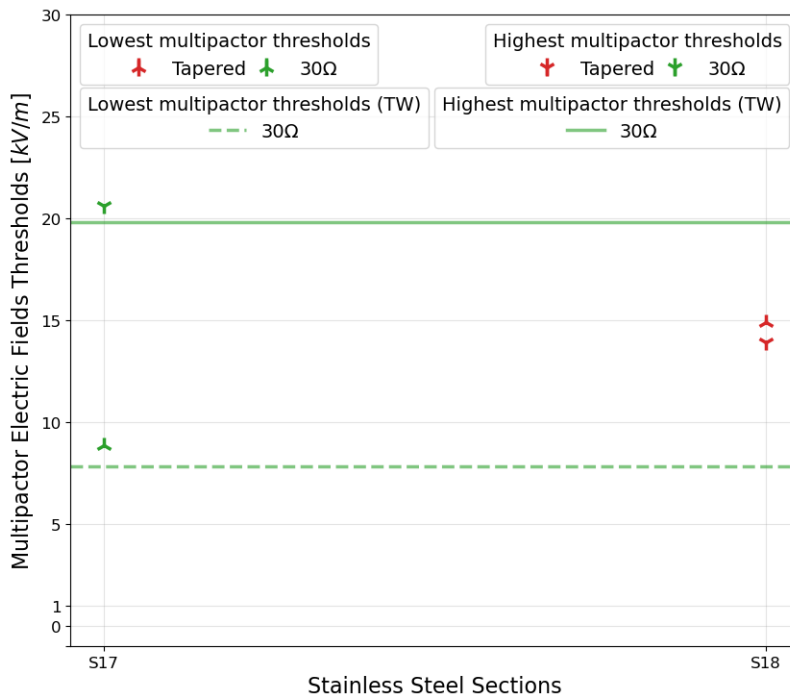


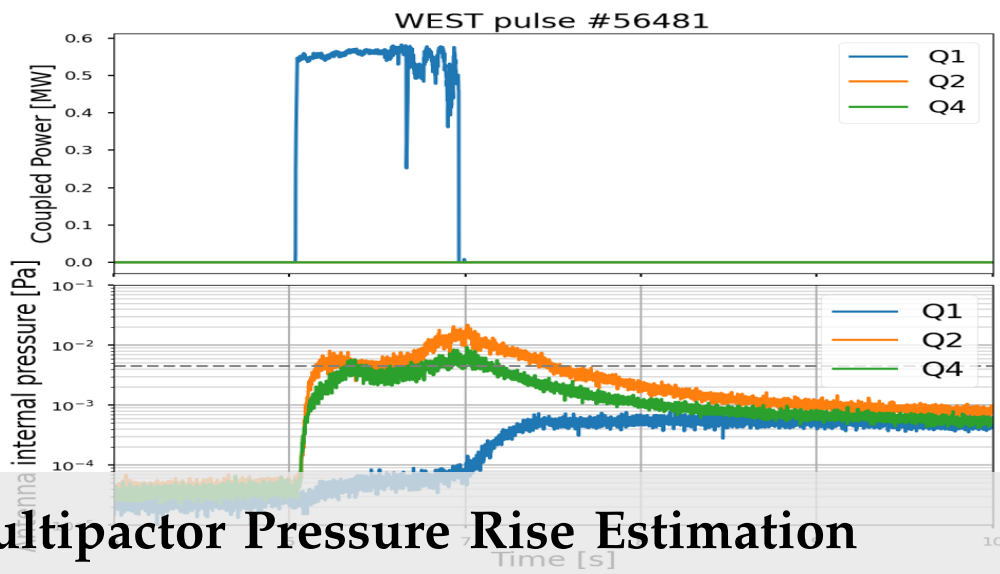
Figure 5.36: Same caption as Figure 5.34. Stainless Steel material sections are considered.

quantitatively compared as they refer to different quantities evaluated in different susceptible zones.

These results show that our methodology is also valid for the resonator's complex structure operating at 63 MHz as the multipactor of the sections having the same geometries are almost similar regardless of the wave pattern. Once the multipactor conditions are met for the analysed sections, the ignition (respectively extinction) of the multipactor is in the vicinity of the high (respectively low) electric field magnitude seen on the section. The sections that are prone to multipactor are marked with underlined red numbers in Figure 5.31.

5.6 Chapter Summary and Perspectives

In this chapter, we detailed the methodology used to determine the generator's forward power range triggering the multipactor in the various components of one ICRH antenna during its RF conditioning phase in three different operational cases. Moreover, we applied the same methodology to determine the generator's forward power range triggering multipactor in the WEST ICRH system during plasma scenarios when only one antenna is powered, where we have seen that the pressure rise could be attributed to the multipactor triggered in the non-powered antennas. Consequently, we showed that detuning the capacitors and conditioning the surfaces reduce the multipactor range in all operational cases — under vacuum and facing a plasma. We should note that the multipactor electric field thresholds of the ICRH antennas' complex components are determined without accounting for the existence of a DC magnetic field responsible for altering the trajectories of the electrons when analysing the multipactor occurrence.



6 Multipactor Pressure Rise Estimation

Settle for nothing but the stars, if you venture for a noble aim. — Whether a great or a trifling death, the bitter cup tastes the same.

Al-Mutanabbi — Arabic Poetry

The goal is to estimate the pressure rise caused by the multipactor avalanche whenever it takes place in the ICRH antennas' system of WEST. The estimated pressure rise will be compared to that observed during the experimental campaign on the tokamak WEST.

We start by formulating the pressure rise problem (Section 6.1), and then we estimate the pressure rise caused by the multipactor phenomenon (Section 6.2). Later, the experimental pressure rise observations are summarised (Section 6.3) to conclude with a comparison between the evaluated pressure rise caused by the multipactor and the experimental observations (Section 6.4).

6.1 Problem Formulation

6.1.1 Formulation 1 — Steady State Assumption

We assume that the steady state is reached when a pressure rise is observed on an ICRH antenna since the time needed for the pressure to rise on the system is much greater than the rebounding time of the desorbed particles. Indeed, in such a case, it is possible to establish a balance equation between the rate of desorption and the rate of pumping — Rate of desorption = Rate of pumping, resulting in a constant pressure of the desorbed molecules in the system — comparable to the one observed experimentally.

Consequently, the molecular desorption balance equation is given by

$$+R - \phi \cdot S_p = 0 \quad (6.1)$$

where

- ▶ R is the surfaces' molecular desorbed rate (caused by multipactor) expressed in $[(\text{\#molecules}) / \text{s}]$.
- ▶ ϕ is the pump-impinging molecular flux defined as the number of molecules crossing a surface-unit during a time-unit, and expressed in $[(\text{\#molecules}) / (\text{m}^2 \text{s})]$.
- ▶ S_p is the pumping effective surface $[\text{m}^2]$, depending on the pump system design.

Therefore, we have to evaluate R — using the multipactor simulation results — and ϕ .

6.1.1.1 Pump-impinging molecular flux evaluation ϕ

Knowing that the molecular distribution is spatially uniform and non-uniform in the velocity space, the molecular flux can be expressed as — details about the formula's derivation could be found in Appendix B:

$$\phi = \frac{1}{4} n \langle v \rangle \quad (6.2)$$

where, n is the molecular volume density and $\langle v \rangle$ is the gas molecules' mean speed.

We assume we are dealing with a rarified gas to evaluate the molecular volume density. Consequently, the thermodynamics properties are governed by the ideal gas state equation: $pV = Nk_B T$, where p is the gas pressure, V is the gas volume, N is the total number of molecules, k_B is the Boltzmann constant, and T is the gas temperature. The molecular volume density is then

$$n = \frac{N}{V} = \frac{p}{k_B T}. \quad (6.3)$$

The mean speed of gas molecules $\langle v \rangle$ is calculated by the Maxwell–Boltzmann distribution and is given by

$$\langle v \rangle = \sqrt{\frac{8k_B T}{\pi m}} \quad (6.4)$$

where m is the mass of the desorbed molecules.

Putting Equations (6.3) and (6.4) in Equation (6.2), we obtain

$$\phi = p \sqrt{\frac{1}{2\pi m k_B T}}. \quad (6.5)$$

6.1.1.2 Surfaces' molecular desorbed rate R

In Chapter 2, we simulated the RF surface conditioning phase of the WEST ICRH antennas by an *in-situ* electron bombardment for a representative sample of the antenna surfaces. Moreover, we monitored the constituent elements of the components' surface using XPS. Therefore, we relied on these data and related them to the multipactor simulation results to estimate the molecular desorbed rate R .

We stick to the carbon-based molecular desorbed rate evaluation, as the carbon atom is one of the chemical atoms detected by XPS. Furthermore,

as in general, the volatile molecules are the most desorbed molecules during electron beam bombardment, we consider only the methane-desorbed molecules.

The evaluation of R , relying on the XPS experimental data and the multipactor simulations, results from six steps summarised in the following:

1. Exploitation of the XPS data obtained after each *in-situ* conditioning phase to calculate the percentage of desorbed carbon atoms per electron dose. The evaluated quantity is denoted m_C and is expressed in $[\%Carbon/(C\ m^{-2})]$.
2. Evaluation of the electron dose caused by the multipactor discharge. The latter is denoted d and is expressed in $[C\ m^{-2}]$. The multipactor electron dose quantity is evaluated from the Spark-3D statistical data, giving the average multipactor electrons' impact density i expressed in $[e/m^2]$. d is related to i through the elementary electron's charge $|q| = 1.6 \times 10^{-19}\ C$, where $d = i \times q$.
3. Evaluation of the desorbed carbon atoms' percentage caused by multipactor, obtained by multiplying the percentage of desorbed carbon atoms per electron dose m_C by the electron dose caused by the multipactor d . The quantity is denoted $p_C = m_C \times d$ and is expressed in $[\%Carbon]$.
4. Calculation of the number of carbon $\#Carbon_{S_{MP}}$ present on the surface contributing to the multipactor avalanche. The surface contributing in multipactor is evaluated from Spark-3D, and is denoted as $S_{MP}\ [m^{-2}]$.
5. Calculation of the number of desorbed carbon due to multipactor:

$$\#\text{desorbed(Carbon)}_{S_{MP}} = \#Carbon_{S_{MP}} \times p_C.$$

6. Evaluation of the molecular desorbed rate:

$$R = \frac{\#\text{desorbed(Carbon)}_{S_{MP}}}{t}$$

where t is the time needed for the desorption to take place that we will consider equal to the multipactor simulation time — the time for the multipactor discharge to be sustained.

Now that the pump-impinging molecular flux ϕ and the molecular desorbed rate R are evaluated, we get back to the balance equation and express the pressure rise (in [Pa]) caused by multipactor by the following

$$p = \frac{R\sqrt{2\pi mk_B T}}{S_p}. \quad (6.6)$$

A representative example of the pressure rise estimation in the WEST ICRH antennas is presented in Section 6.2.

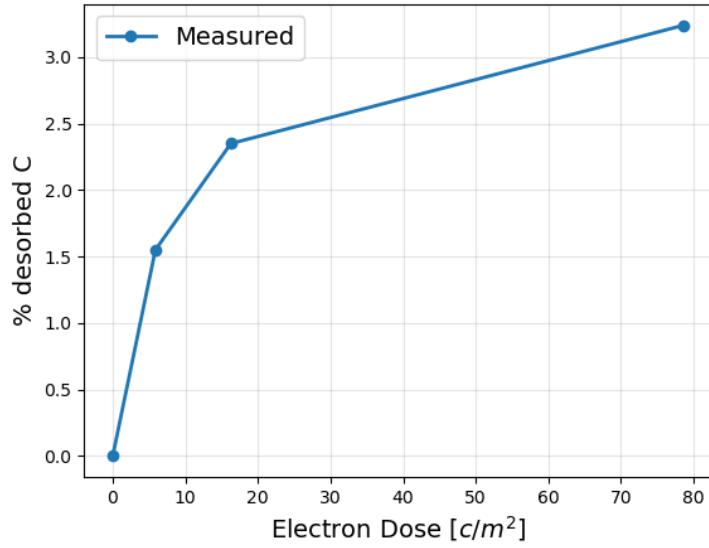


Figure 6.1: The percentage of desorbed carbon per cumulative electron dose received by the WEST ICRH representative sample.

6.1.2 Formulation 2 — Transient State Assumption

We suppose that the steady state assumption does not hold. Therefore, the pressure and the number of molecules are time-dependent. In this case, the molecular desorption flow equation is given by:

$$+R(t) - p(t) \frac{1}{\sqrt{2\pi m k_B T}} S_p = \frac{dN(t)}{dt} \quad (6.7)$$

As the thermodynamic properties are governed by the ideal gas state equation $p(t)V = N(t)k_B T$, the time variation of the total number of molecules is expressed by

$$\frac{dN(t)}{dt} = \frac{V}{k_B T} \frac{dp(t)}{dt}$$

Equation (6.7) becomes

$$\frac{k_B T}{V} R(t) - \frac{S_p}{V} p(t) \sqrt{\frac{k_B T}{2\pi m}} = \frac{dp(t)}{dt}. \quad (6.8)$$

Therefore, in this formulation, the pressure rise is estimated by solving this first-order differential equation with a second member.

The transient state formulation might offer improved accuracy, but it introduces a challenge because the molecular desorption rate R on the surfaces needs to be time-dependent. However, the statistical results obtained from Spark-3D are based on averaged statistical data throughout the simulation time, and detailed data at each time step is unavailable.

6.2 Multipactor Pressure Rise Estimation

We start by estimating the surface molecular desorbed rate R by following the steps summarised in Section 6.1.1.2.

1. Estimation of m_C — We exploited the contaminants' desorption in Chapter 2 by monitoring the chemical surface modifications of the studied representative sample of the WEST ICRH antennas. Indeed, the XPS spectra, acquired at the different conditioning phases, showed the presence of contaminants such as carbon and oxygen. In particular, from the concentration of carbon at each electron dose received by the sample (Figure 2.18 of Chapter 2), we can extract the corresponding percentage of desorbed carbon elements. These data are given in Figure 6.1 and are limited to the electron doses for which we notice a decrease in the concentration of carbon.

We estimate m_C , the percentage of desorbed carbon atoms per electron dose, by linearly interpolating¹ the first two percentages of desorbed carbon:

$$m_C = \frac{\Delta\%C}{\Delta dose} = 0.264\%. \quad (6.9)$$

2. Multipactor electrons' impact density i — We are interested in evaluating the multipactor electrons' impact density i . As one of Spark-3D simulations' outputs is the statistical data averaged over the simulation time, we define the average electrons' impact density as the relevant quantity needed for the pressure rise evaluation. Nevertheless, i should be estimated after the saturation of the multipactor phenomenon, *i.e.*, the development of the electron cloud caused by the multipactor in the antennas' components. The latter is a limitation of the Spark-3D tool since it does not take into account the saturation mechanisms. Yet, if the simulation is forced for a long time, it could reach that time with a numerical plateau region in the number of electrons. Or even stops once the number of electrons reaches a maximum threshold — simulator internal parameter as the simulations are resource-demanding. Consequently, Spark-3D is not the best tool for evaluating such a quantity.

For example, simulating the T-junction of the WEST ICRH antenna at 55 MHz for 10 000 ns, with the *non-conditioned* TEEY data curve leads to a numerical saturation. The average multipactor electrons' impact density² evaluated in this case is: $i = 1.284 \times 10^{14} \text{ e/m}^2$. Consequently, the multipactor dose is $d = 2.05 \times 10^{-5} \text{ C m}^{-2}$.

3. The desorbed carbon atoms' percentage is: $p = 0.5412 \times 10^{-5} \%$.
4. As we are considering methane molecules, we can assume that one carbon atom exists per 10^{-20} m^2 . The number of carbon can be expressed as: $\#\text{Carbon}_{S_{MP}} = S_{MP} \times 10^{20}$. S_{MP} for the T-junction component is $\sim 0.85 \text{ m}^2$. Therefore, $\#\text{Carbon}_{S_{MP}} = 0.85 \times 10^{20}$.
5. The number of desorbed carbon by the multipactor effect is $\#\text{desorbed}(\text{Carbon})_{S_{MP}} = 0.46 \times 10^{13}$.
6. Using the simulation time, the surfaces' molecular desorbed rate is estimated as $R = 4.6 \times 10^{17} \text{ (\#molecules) /s}$.

Now, we can evaluate the pressure rise caused by the multipactor avalanche triggered in the T-junction of a WEST ICRH antenna us-

1: We have chosen to linearly interpolate the first two data points as the electron dose estimated by the multipactor simulations lies within this range of values.

2: By averaging over the surface meshes satisfying a TEEY > 1 and impact energy lying between the first and second cross-over energies.

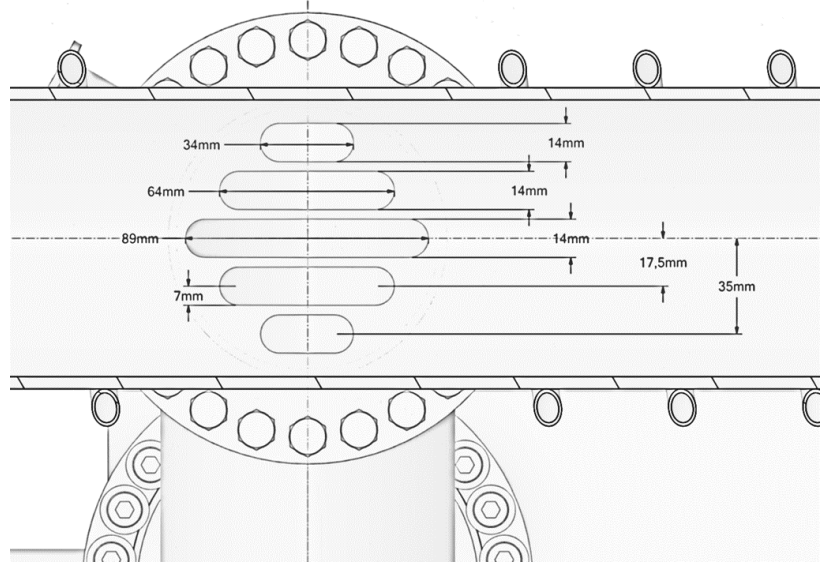


Figure 6.2: The effective pump surface of one side of the WEST ICRH antennas.

ing Equation (6.6). For this, the temperature is taken equal to that of the antenna during its operation, 70 °C or 343 K. The mass m is that of the methane molecules. As we will account for methane fragments and methane molecules with oxygen elements, the molar mass of methane is then: $10 \text{ g mol}^{-1} \leq M \leq 50 \text{ g mol}^{-1}$, and the methane mass is bounded by $1.67 \times 10^{-26} \text{ kg} \leq m \leq 8.34 \times 10^{-26} \text{ kg}$.

The pumping surface of one side of the WEST ICRH antenna is illustrated in Figure 6.2, and the total effective pump surface of one ICRH antenna is $S_p = 7560 \text{ mm}^2$.

Therefore, the pressure rise (calculated from Equation (6.6)) caused by the multipactor triggered in the T-junction geometry is

$$1.35 \text{ mPa} \leq p \leq 3 \text{ mPa}.$$

As the Spark-3D does not account for the space charge effects, we have conducted a simulation for the *Transition 2* region of the impedance transformer of the WEST ICRH antenna using a multipactor tool called SPIS that accounts for the space charge effects [109]. The simulation is performed at the frequency of 55 MHz for the *non-conditioned* TEEY data curve of the ICRH representative sample. It was found that the average current density of this geometry at the saturation level is 9 A m^{-2} . Consequently, the evaluated molecular desorbed rate for the region in question is $R = 7.6 \times 10^{17} \text{ (#molecules) / s}$.

Consequently, the pressure rise (calculated from Equation (6.6)) caused by the multipactor triggered in the *Transition 2* of the impedance transformer is

$$2.2 \text{ mPa} \leq p \leq 5 \text{ mPa}.$$

6.3 Experimental Pressure Rise

One possible way to evaluate the surfaces' molecular desorbed rate resulting from the pressure rise observed on the WEST ICRH antenna is

[109] Peysson et al. (2022)

Table 6.1: Data from plasma shots, where only one ICRH antenna is active: shot number, antennas' states (ON/OFF), antennas' frequency, antennas' capacitors' states ([T/D] for [Tuned/Detuned]), pressure rise of the non-activated antennas, and expected molecular desorbed rates.

Shot#	Antenna State			Antenna Frequency [MHz]			Capacitors State			~Pressure Rise [Pa]			~Desorbed Rate [(#molecules) /s]		
	Q_1	Q_2	Q_4	f_{Q_1}	f_{Q_2}	f_{Q_4}	C_{Q_1}	C_{Q_2}	C_{Q_4}	Δp_1	Δp_2	Δp_4	R_{Q_1}	R_{Q_2}	R_{Q_4}
56469	OFF	ON	OFF	55.65	55.8	55.5	D	T	D	10^{-4}	-	10^{-4}	10^{16}	-	10^{16}
56485	OFF	ON	OFF	55.65	55.8	55.5	T	T	T	10^{-3}	-	10^{-3}	10^{18}	-	10^{18}
57658	ON	OFF	OFF	54.225	55.575	57	T	D	T	-	10^{-4}	10^{-3}	-	10^{17}	10^{18}
57694	ON	OFF	OFF	54.225	55.575	57	T	T	T	-	10^{-3}	10^{-4}	-	10^{18}	10^{16}

to fit the pressure rise data by an exponential function to determine its time variation function: $p(t) = ae^{bt} + c$, then evaluate the experimental molecular desorbed rate $R(t)$ using Equation (6.8) of the transient state assumption — Formulation 2. In this equation, the volume V is taken equal to the pumped volume of the WEST ICRH antenna.

We evaluated the pressure rise — according to the fitted pressure data — and the experimental molecular desorbed rate $R(t)$ for four different shots where only one of the antennas is activated. A summary of the most relevant data is given in Table 6.1. In particular, we list the shot number, antennas' states (on or off), antennas' frequency, antennas' capacitors' states — whether the capacitors are tuned or detuned, approximate pressure rise level of the non-activated antennas, and the evaluated experimental molecular desorbed rates for the non-activated antennas.

In particular, we have chosen two groups of shots: *i*) a slight shift in the frequency of operation of the three antennas (56469 and 56485), and *ii*) a higher shift in the frequency of operation of the three antennas (57658 and 57694).

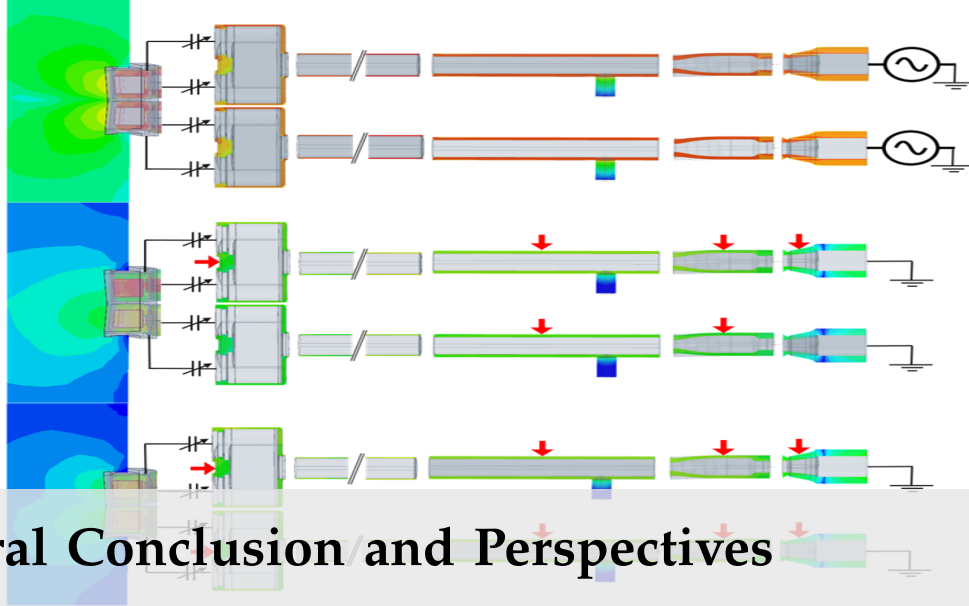
From the data represented in Table 6.1, we notice that on average, the pressure rise of the non-activated antennas ranges between 10^{-4} Pa and 10^{-3} Pa with a lower pressure rise for the case of detuned capacitors. Furthermore, in average the molecular desorbed rate ranges between 10^{16} [(#molecules) /s] and 10^{18} [(#molecules) /s]. It should be noted that the maximal pressure value measured could reach a factor ten times higher than the average value. Therefore, the analysis is approximated to a factor of ten.

6.4 Discussion

At this step, we can compare the experimental pressure rise of Section 6.3 to the multipactor pressure rise evaluated in Section 6.2 by the formulation developed in Section 6.1.1. Although the numerical saturation is not physical for Spark-3D, there is a good agreement between the estimated pressure rise (10^{-3} Pa) obtained via the multipactor simulations and the experimentally measured pressure rise (ranging in the interval $[10^{-3} - 10^{-2}]$ Pa) once fitted to an exponential function. This agreement is also evidenced when a multipactor tool accounting for the space charge effects is used.

Therefore, not only the multipactor is triggered in the non-powered antennas when only one antenna is active (as seen in Section 5.4 of

Chapter 5), but also the pressure rise observed on the ICRH antennas when only one antenna is active could be attributed to the multipactor phenomenon, as it agrees with the estimated multipactor pressure level.



7 General Conclusion and Perspectives

If you fear something, expose yourself to it;
for you suffer more in imagination than in
reality.

Ali Ibn Abi Taleb

7.1 Conclusions

The results from this work lead to several important conclusions about the multipactor analysis in complex multi-ports components that are subject to various wave patterns and its impact on the operation of the ICRH antenna system for auxiliary plasma heating on the tokamak WEST — applicable to other high-power RF systems suffering from multipactor.

We developed a methodology — using available numerical multipactor tools — to determine the lowest and highest multipactor thresholds for any RF component subject to the multipactor phenomenon. It was also extended to account for the variability of the wave pattern within the RF component up to a standing wave with a total reflection. The developed methodology was applied using the Spark-3D software on cylindrical coaxial transmission lines of various characteristic impedance, the impedance transformers, the T-junctions, and the RF feed-through of the WEST ICRH antennas and the T-resonator structure of the TITAN facility at IRFM. Although the methodology was applied using Spark-3D and Ansys-HFSS, it should be noted that any other multipactor software could be used.

Some of the presented results — such as those of the RF feed-through — are preliminary for the following reasons:

1. There are no benchmark cases to validate the simulation results for multi-material structures.
2. The available version of Spark-3D does not account for multi-material assignment and does not recognise dielectric TEEY, which means there is no consideration for the developed DC electric field caused by the multipactor taking place on the dielectric surface of the structure.

1: During this work, we tested Ansys-HFSS [Version 2023 R2] for a cylindrical coaxial transmission line geometry and compared the results to Spark-3D where a good agreement was shown. Moreover, the results were compared to multipactor measurements for a travelling wave case, and a good similarity is shown.

3. Ansys-HFSS has recently included the multipactor tool and is not largely tested¹ nor compared to other available software, especially for multi-material structures.

To account for various wave patterns, we defined the lowest multipactor electric field thresholds (being the maximal electric field's magnitude evaluated in the multipactor zone) corresponding to the ignition of the multipactor and the highest multipactor electric field thresholds (being the mean electric field's magnitude evaluated in the multipactor zone) corresponding to the extinction of it, remaining constant regardless of the variability of the reflection coefficient. The latter developed criteria are valid up to an $f \times d$ product above which the non-linear ponderomotive force — pushing the electrons toward low electric field regions — becomes more noticeable and affects the electrons' trajectories depending on the wave pattern.

The first geometry analysed was the cylindrical coaxial transmission line for which we compared numerically determined multipactor thresholds to experimentally measured data for a travelling wave pattern. Then, we analysed the geometry for mixed and standing wave patterns and validated the electric field criteria. Furthermore, we found that the surface conditioning reduces the multipactor range — increases (respectively decreases) the lowest (respectively highest) multipactor threshold — caused by the higher first cross-over energy and the decrease of the maximum TEEY of the material.

The non-linearity effect was found negligible for the geometries and frequencies under study, and the developed methodology is valid within the ICRH frequency range. Consequently, for each component of the WEST ICRH antennas (T-junctions, impedance transformers and RF feed-throughs), we determined the lowest and highest multipactor electric field thresholds.

As the electric fields are out of monitoring during ICRH operations, we developed a methodology to compare the excited electric fields within the antenna components — obtained by solving the circuit model of the antenna while accounting for the coupling between the sides of one antenna and the coupling between the antennas — to the multipactor electric fields thresholds. The latter comparison leads to the determination of the generator forward power range triggering multipactor in the various components of the antenna.

Consequently, we determined the generator's forward power range triggering multipactor on both sides of one ICRH antenna during its RF conditioning phase. Three cases were studied: *i*) two sides are powered, and the four capacitors are tuned; *ii*) one side is powered, and the four capacitors are tuned, and *iii*) one side is powered, and only its corresponding capacitors are tuned while detuning the capacitors of the non-powered side. We found that the multipactor is triggered on the off-mode side due to the coupling between the sides and that the capacitors should be detuned to reduce the multipactor-trigger. Moreover, we studied the effect of surface conditioning on multipactor reduction.

In addition, we determined the generator's forward power range triggering multipactor in the ICRH antenna system when only one antenna is powered on plasma while the remaining two are non-powered. In such

cases, it was found that the multipactor is triggered in the off-mode antennas due to the inter-antennas' coupling. The latter could be reduced by conditioning the surfaces and/or detuning the capacitors of the off-mode antennas, as in the RF conditioning phase.

Finally, we formulated the pressure rise problem by establishing a balance equation between the pumping rate and the molecular desorbed rate caused by the multipactor phenomenon and found that the multipactor is a high-probability reason behind the internal pressure rise observed experimentally in the off-mode antennas when only one antenna is active. The latter is concluded from the agreement between the experimental pressure rise level and the one resulting from the formulated problem.

7.2 Perspectives and Future Works

Several axes could be elaborated as future works:

- ▶ For the RF conditioning phase's analysis, one future axis is to account for the toroidal magnetic field for the multipactor electric field thresholds' determination of the different components of the ICRH antennas. Indeed the presence of a DC magnetic field transverse to the direction of the wave propagation is known to affect the TEEY properties of the material [74] and alter the electrons' trajectories and the multipactor thresholds. Subsequently, the generator's power range triggering the multipactor in the ICRH antenna during its RF conditioning phase could be re-determined following the developed methodology presented in Chapter 5 of this manuscript.
- ▶ For the plasma case analysis, one future axis is to account for the helical magnetic field — due to the presence of the toroidal and poloidal magnetic fields — when determining the multipactor electric field thresholds. Therefore, the DC magnetic field consideration may alter the results of the forward power range responsible for triggering multipactor in the off-mode antennas.
- ▶ For the analysis presented in this work, we used typical alumina TEEY data when analysing the multipactor in the RF feed-through of the ICRH antenna. Nevertheless, a better way is to measure the TEEY data before and after fully conditioning for an alumina representative sample of the RF feed-through while accounting for the ICRH operational conditions such as baking time and temperature, operation temperature, and RF conditioning phase. The latter is crucial because the TEEY depends on the morphology, surface treatments, and sample conditions, as discussed in this manuscript.
- ▶ The results of this work suggest that the multipactor is problematic in the *Region C* of the T-junction geometry of the WEST ICRH antenna in almost all the studied cases. Being close to the tuneable capacitors of the antenna emphasises the importance of demounting one ICRH antenna and checking the state of the ceramics², whether the multipactor has been causing any metallisation for the ceramics due to a glow discharge induced by the multipactor or any other possible damage. Indeed, the capacitors' temperature is maintained at 20 °C due to the manufacturing constraints of the capacitors, and

[74] Fil (2017)

2: The RF feed-through surface state could be checked as it could suffer from metallisation.

the neighbourhood surfaces are not subject to any baking phase, which could degrade the surface properties in this region.

- ▶ Revisit the RF conditioning phase of the WEST ICRH antennas. This phase aims to condition the surface via RF waves responsible for removing some impurities by wave-material interactions. Nevertheless, we have seen that, in standing wave scenarios, the multipactor — one of the phenomena responsible for cleaning the surfaces during this phase via the associated electrons' bombardment — is not triggered everywhere and is subject to displacement dependent on the applied power. Therefore, one can question whether we are conditioning all the surfaces homogeneously or missing some antenna regions. Moreover, one can investigate whether there is a better way to follow, enhancing the RF conditioning phase's impact on the surfaces' properties of the antennas.
- ▶ Study the effect of the pumping system's performance and characteristics, such as the pumping velocity and pumping effective surface, on the internal pressure rise's reduction. Moreover, to suggest some enhancements if there are any.
- ▶ Extrapolate the same methodologies developed herein to study the multipactor's effect on different antennas used on other nuclear fusion devices, such as the case of the ITER ICRH antennas. Indeed, on the tokamak ITER, two ICRH antennas are supposed to be deployed, each composed of 8 modules. Therefore, once not all the modules are powered, multipactor could be problematic in the non-powered modules of the same antenna, but also on the other antenna due to possible coupling.
- ▶ Conduct an experimental campaign on a multipactor test-bed facility to study the multipactor behaviour for a simple geometry such as the cylindrical coaxial transmission line subjected to various wave patterns. An interesting aspect of such a campaign is the observation of the multipactor displacement from the neighbourhood of the maximal electric field region to the minimal electric field region.

APPENDICES

A

Appendix A

From the expression of the ponderomotive force, it is seen that this force has a component in the radial direction due to the non-homogeneity of the electric field in a coaxial transmission line, and an axial component that exists only if the electric field is non-homogeneous in the wave propagation direction z . Therefore, the axial component of the ponderomotive force is non-zero in the case of a mixed wave (MW) or a standing wave (SW).

We exploit herein the case of a SW, where the electric field can be expressed as

$$\vec{E}(\vec{r}, t) = \frac{\sqrt{2}V}{r \ln\left(\frac{b}{a}\right)} \cos(\omega t) \cos(\beta z) \vec{e}_r = \vec{E}_S(\vec{r}) \cos(\omega t)$$

where $\vec{E}_S(\vec{r})$ is the spatial vector of the electric field.

From the derivation of the ponderomotive force [105], we can find that the averages of the radial and axial components, over one time period, are expressed by

$$\begin{aligned} \vec{F}_r &= \frac{q^2}{m\omega^2} \frac{|\vec{E}_S|^2}{r} \vec{e}_r \\ \vec{F}_z &= \frac{q^2}{m\omega^2} |\vec{E}_S|^2 \frac{\beta \sin(\beta z)}{\cos(\beta z)} \vec{e}_z \end{aligned}$$

[105] Chen (2016)

Figure A.1 to Figure A.4 represent the average radial and axial components of the ponderomotive force averaged over one time period corresponding to the highest multipactor threshold of the coaxial transmission line at the $f \times d$ products

- ▶ 120 MHz cm: an $f \times d$ for which the proposed methodology is valid;
- ▶ 700 MHz cm: an $f \times d$ threshold above which the proposed methodology is non-valid for the highest multipactor threshold;
- ▶ 1200 MHz cm: an $f \times d$ threshold above which the proposed methodology is non-valid for the lowest multipactor threshold;
- ▶ 4000 MHz cm: an $f \times d$ for which the proposed methodology is non-valid for the lowest and the highest multipactor threshold.

For the lowest multipactor thresholds, the two components of the ponderomotive force have the same shape but different values and are not plotted for clarity purposes.

At 120 MHz cm, the radial component's magnitude is larger than that of the axial component, *i.e.*, the force pushing the electrons toward the node of the electric field is negligible with respect to its radial counterpart.

Figure A.1: The magnitude of the axial and radial components of the ponderomotive force versus the wave propagation direction z . The plots correspond to the highest multipactor threshold, but have the same shape for the lowest multipactor threshold with slightly lower values, and therefore are omitted. The plots correspond to 120 MHz cm.

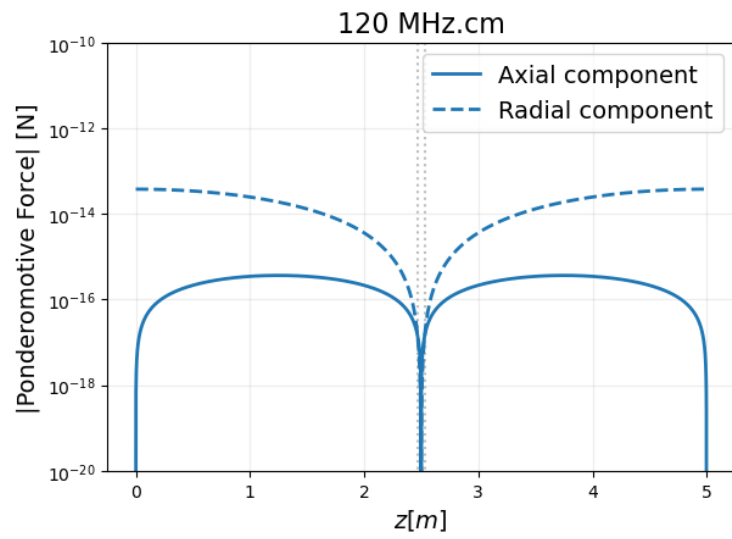


Figure A.2: Same caption as Figure A.1. The plots correspond to 700 MHz cm.

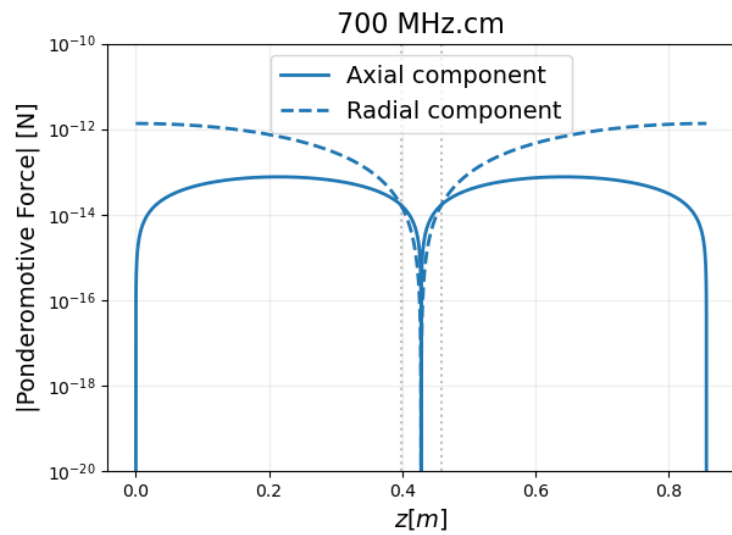
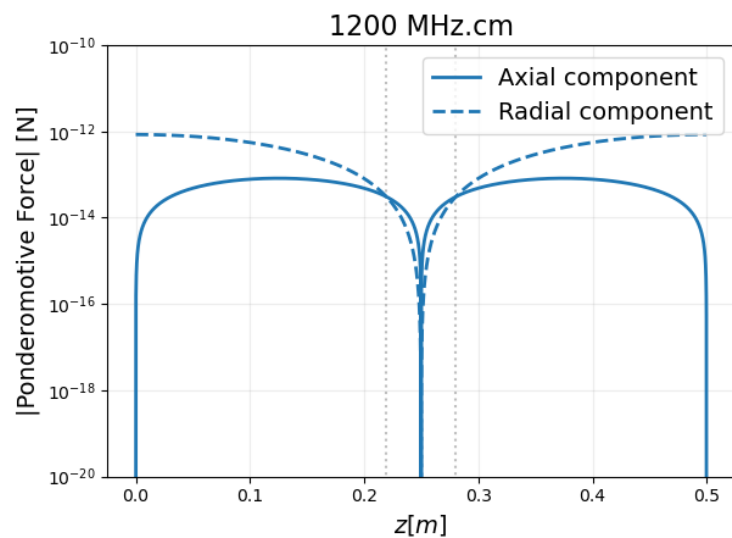


Figure A.3: Same caption as Figure A.1. The plots correspond to 1200 MHz cm



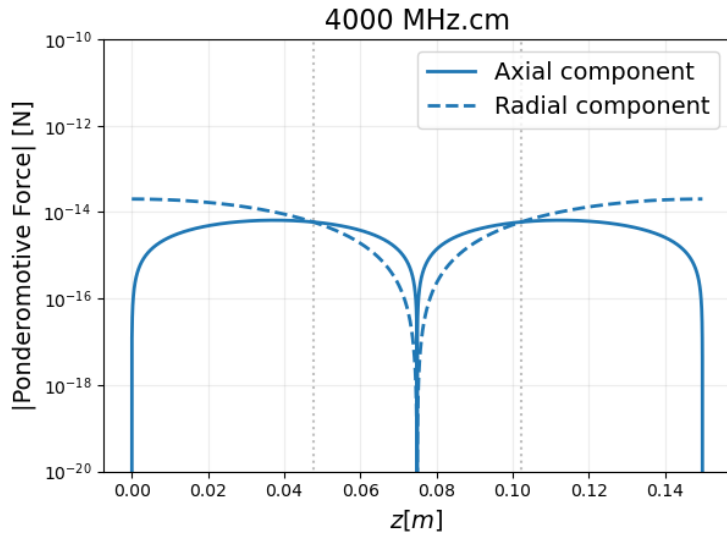


Figure A.4: Same caption as Figure A.1. The plots correspond to 4000 MHz cm.

Hence, there is no effect for this non-linear force at such low frequencies, and the proposed methodology is valid.

At 700 MHz cm, the radial component's magnitude is larger than that of the axial component, except for the region in the vicinity of the electric field node (center of the coaxial transmission line $\sim 7\%$ of the coaxial). Hence, the effect of this non-linear force is more pronounced on the highest multipactor threshold but still insufficient for affecting the lowest multipactor threshold, for which the multipactor is triggered near the maximal electric field. At higher $f \times d$, we observe that the region over which the axial component exceeds the radial one is wider ($\sim 12\%$ of the coaxial at 1200 MHz cm, and $\sim 36\%$ of the coaxial at 4000 MHz cm). Therefore, the non-linear effect will be seen on the lowest and highest multipactor thresholds.

B

Appendix B

The distribution of the molecules is uniform in space, yet this is not the case for their distribution in the velocity space (v_x, v_y, v_z) . Therefore, we introduce the velocity distribution function $G(v_x, v_y, v_z)$ satisfying the normalisation

$$\iiint_{-\infty}^{+\infty} G(v_x, v_y, v_z) dv_x dv_y dv_z = 1.$$

The number of molecules dN with velocities within the elementary volume $dv_x dv_y dv_z = d^3v = d\mathbf{v}$ around the velocity vector (v_x, v_y, v_z) is expressed by:

$$dN = NG(v_x, v_y, v_z) dv_x dv_y dv_z$$

where N is the total number of molecules.

As the directions of the molecular velocities are distributed uniformly, $G(v_x, v_y, v_z)$ depends only on the norm of the velocity, $v = \sqrt{v_x^2 + v_y^2 + v_z^2}$. Therefore, in the spherical coordinate system, the elementary number of molecules is written as

$$dN = NG(v)v^2 dv d\Omega$$

where $d\Omega = \sin\theta d\theta d\varphi$ is the elementary solid angle.

The number of molecules within the spherical shell of width dv is $dN = 4\pi NG(v)v^2 dv$, where 4π is the integral of the solid angle. Let us define the distribution function over molecular speeds as $f(v) = 4\pi G(v)v^2$. Then, the elementary number of molecules is expressed as

$$dN = Nf(v)dv \frac{d\Omega}{4\pi}.$$

The molecular flux is defined as the number of molecules dN crossing a unit surface in one direction during a unit of time, $\phi = dN/(dSdt)$. As the molecules approach the elementary surface dS from all the azimuthal and elevation directions, we should, therefore, consider the number of molecules $dN_{\theta,\varphi}$ coming from a particular direction θ, φ within the solid angle $d\Omega$ around it (as illustrated in Figure B.1).

From these molecules, we take the molecules with speeds in the interval dv , thus obtaining $dN_{v,\theta,\varphi}$. The volume of this cylinder is $dV = dSv \cos\theta dt$, with a total number of molecules in it equal to $dN_V = n dV$. Therefore

$$dN_{v,\theta,\varphi} = dN_V f(v)dv \frac{d\Omega}{4\pi} = n v \cos\theta f(v)dv \frac{\sin\theta d\theta d\varphi}{4\pi}.$$

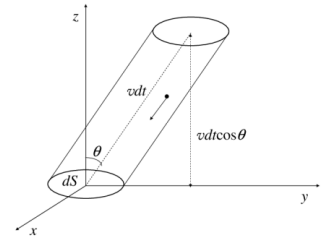


Figure B.1: The elementary volume formed by the molecules approaching an elementary surface.

And the molecular flux is

$$\begin{aligned}\phi &= \int dN_{v,\theta,\varphi} \frac{1}{dS dt} \\ &= \frac{1}{4\pi} n \int_0^\infty v f(v) dv \times \int_0^{\frac{\pi}{2}} \cos \theta \sin \theta d\theta \times \int_0^{2\pi} d\varphi \\ &= \frac{1}{4} n \langle v \rangle.\end{aligned}$$

Bibliography

References are in alphabetical order.

- Ang, L. K. et al. (June 1998). 'Power Deposited on a Dielectric by Multipactor'. In: *IEEE Transactions on Plasma Science* 26.3, pp. 290–295. doi: [10.1109/27.700756](https://doi.org/10.1109/27.700756) (cited on pages xvi, 39).
- Baglin, V. (Mar. 1997). *Mesure de la rugosité de surfaces techniques à l'aide de la méthode B.E.T.* Tech. rep. Geneva: CERN (cited on page 42).
- Baglin, V. et al. (June 2000). 'The secondary electron yield of technical materials and its variation with surface treatments'. In: *Seventh European Particle Accelerator Conference*. Vienna, Austria (cited on pages 27, 42, 43).
- Ball, J. (Sept. 2019). 'Maximizing specific energy by breeding deuterium'. In: *Nuclear Fusion* 59.10, p. 106043. doi: [10.1088/1741-4326/ab394c](https://doi.org/10.1088/1741-4326/ab394c) (cited on page 2).
- Becerra, G. (June 2007). 'Studies of Coaxial Multipactor in the Presence of a Magnetic Field'. PhD thesis. Massachusetts Institute of Technology (cited on pages xvi, 22, 39, 43, 48, 53).
- Berger-By, G. et al. (Oct. 2007). 'Arc security system based on harmonics detection for the Tore Supra ICRH transmitter'. In: *Fusion Engineering and Design* 82.5-14, pp. 716–722. doi: [10.1016/j.fusengdes.2007.06.039](https://doi.org/10.1016/j.fusengdes.2007.06.039) (cited on pages 13, 14).
- Bernard, J. M. et al. (Nov. 2017). 'Design and construction of the first ELM resilient long pulse ICRH antenna for WEST'. In: *Fusion Engineering and Design* 123, pp. 217–222. doi: [10.1016/j.fusengdes.2017.05.024](https://doi.org/10.1016/j.fusengdes.2017.05.024) (cited on pages 10, 14, 15).
- Bernard, J. M. et al. (Sept. 2019). 'Commissioning of the first WEST load-resilient long pulse ICRF launcher in the TITAN testbed and on WEST plasmas'. In: *Fusion Engineering and Design* 146, pp. 1778–1781. doi: [10.1016/j.fusengdes.2019.03.033](https://doi.org/10.1016/j.fusengdes.2019.03.033) (cited on pages xiv, 10, 15, 16).
- Bernard, J.M. et al. (2011). 'New high power CW test facilities for ITER ICRH components testing'. In: *Fusion Engineering and Design* 86.6. Proceedings of the 26th Symposium of Fusion Technology (SOFT-26), pp. 876–879. doi: [10.1016/j.fusengdes.2011.02.100](https://doi.org/10.1016/j.fusengdes.2011.02.100) (cited on page 96).
- Bira, S. (June 2021). 'Conception d'un résonateur quadripolaire pour la caractérisation des propriétés de couches minces supraconductrices en régime radiofréquence pour les cavités accélératrices'. Theses. Université Paris-Saclay (cited on pages xxi, 82).
- Bosia, G. (2003). 'High-Power Density Ion Cyclotron Antennas for Next Step Applications'. In: *Fusion Science and Technology* 43.2, pp. 153–160. doi: [10.13182/FST03-A256](https://doi.org/10.13182/FST03-A256) (cited on page 10).
- Bruining (1954). *Physics and Applications of Secondary Electron Emission*. Pergamon Science Series, Electronics and waves. London, Pergamon Press (cited on pages 17, 20, 22).
- Bruining, H. (1936). 'The depth at which secondary electrons are liberated'. In: *Physica* 3.9, pp. 1046–1052. doi: [10.1016/S0031-8914\(36\)80330-9](https://doi.org/10.1016/S0031-8914(36)80330-9) (cited on page 22).
- Cazaux, J. (2010). 'Calculated influence of work function on SE escape probability and Secondary Electron Emission yield'. In: *Applied Surface Science* 257.3, pp. 1002–1009. doi: [10.1016/j.apsusc.2010.08.007](https://doi.org/10.1016/j.apsusc.2010.08.007) (cited on page 43).
- Chaplin, V. H. et al. (2017). 'Center conductor diagnostic for multipactor detection in inaccessible geometries.' In: *Review of Scientific Instruments* 88, p. 014706. doi: [10.1063/1.4974346](https://doi.org/10.1063/1.4974346) (cited on page 41).
- Chen, F. (2016). *Introduction to Plasma Physics and Controlled Fusion*. 3rd ed. Switzerland, Cham: Springer, pp. 284–285 (cited on pages 66, 117).
- Chojnacki, E. (Mar. 2000). 'Simulations of a multipactor-inhibited waveguide geometry'. In: *Physical Review Special Topics Accelerators and Beams* 3 (3), p. 032001. doi: [10.1103/PhysRevSTAB.3.032001](https://doi.org/10.1103/PhysRevSTAB.3.032001) (cited on page 46).
- Chung, M. S. and T. E. Everhart (Feb. 1974). 'Simple calculation of energy distribution of low-energy secondary electrons emitted from metals under electron bombardment'. In: *Journal of Applied Physics* 45.2, pp. 707–709. doi: [10.1063/1.1663306](https://doi.org/10.1063/1.1663306) (cited on pages 18, 19, 61).

- Cimino, R. et al. (Aug. 2012). 'Nature of the Decrease of the Secondary-Electron Yield by Electron Bombardment and its Energy Dependence'. In: *Physical Review Letters* 109.6, p. 064801. doi: [10.1103/PhysRevLett.109.064801](https://doi.org/10.1103/PhysRevLett.109.064801) (cited on page 31).
- Curren, A. N., K. A. Jensen, and R. F. Roman (Jan. 1990). *Secondary electron emission characteristics of molybdenum-masked, ion-textured OFHC copper*. Tech. rep. NASA (cited on page 42).
- De Lara, J. et al. (Apr. 2006). 'Multipactor Prediction for On-Board Spacecraft RF Equipment with the MEST Software Tool'. In: *IEEE Transactions on Plasma Science* 34.2, pp. 476–484. doi: [10.1109/TPS.2006.872450](https://doi.org/10.1109/TPS.2006.872450) (cited on pages xvi, 34).
- Dekker (1981). 'Secondary Electron Emission'. In: *Solid State Physics*. London: Mac Millan Education UK, pp. 418–445. doi: [10.1007/978-1-349-00784-4_17](https://doi.org/10.1007/978-1-349-00784-4_17) (cited on pages 17–19).
- Dekker, A. J. (1958). 'Secondary Electron Emission'. In: *Advances in Research and Applications*. Ed. by Frederick Seitz and David Turnbull. Vol. 6. Solid State Physics. Academic Press, pp. 251–311. doi: [10.1016/S0081-1947\(08\)60728-6](https://doi.org/10.1016/S0081-1947(08)60728-6) (cited on pages 17, 22).
- Ding, Z. J., X. D. Tang, and R. Shimizu (2001). 'Monte Carlo study of secondary electron emission'. In: *Journal of Applied Physics* 89.1, pp. 718–726 (cited on page 18).
- ECSS (June 2020). *Space Engineering: Multipactor Handbook*. report ECSS-E-HB-20-01A. Noordwijk, The Netherlands: European Cooperation for Space Standardization (cited on pages 41, 42, 46).
- Farnsworth, H. E. (Jan. 1925). 'Electronic Bombardment of Metal Surfaces'. In: *Physical Review* 25.1, pp. 41–57. doi: [10.1103/PhysRev.25.41](https://doi.org/10.1103/PhysRev.25.41) (cited on pages 18, 22).
- Fil, N. (Nov. 2017). 'Caractérisation et modélisation des propriétés d'émission électronique sous champ magnétique pour des systèmes RF hautes puissances sujets à l'effet multipactor.' PhD thesis. Université de Toulouse, Institut Supérieur de l'Aéronautique et de l'Espace (cited on pages 38, 113).
- Fil, N. et al. (Dec. 2016). 'Multipactor Threshold Sensitivity to Total Electron Emission Yield in Small Gap Waveguide Structure and TEEY Models Accuracy'. In: *Physics of Plasmas* 23.12, p. 123118. doi: [10.1063/1.4972571](https://doi.org/10.1063/1.4972571) (cited on page 38).
- Fransworth, P. T. (Oct. 1934). 'Television by electron image scanning'. In: *Journal of the Franklin Institute* 218.4, pp. 411–444. doi: [10.1016/S0016-0032\(34\)90415-4](https://doi.org/10.1016/S0016-0032(34)90415-4) (cited on pages 35, 38).
- Geng, R. L. and H. S. Padamsee (1999). 'Exploring multipacting characteristics of a rectangular waveguide'. In: *Proceedings of the 1999 Particle Accelerator Conference* (cited on page 44).
- Geng, R. L. et al. (2002). 'Experimental Studies of Electron Multipacting in CESR Type Rectangular Waveguide Couplers'. In: *8th European Particle Accelerator Conference* (cited on page 44).
- Gill, E. W. B. and A. Von Engel (Feb. 1948). 'Starting potentials of high-frequency gas discharges at low pressure'. In: *Proceedings of the Royal Society of London, Series A. Mathematical and Physical Sciences* 192.1030, pp. 446–463. doi: [10.1098/rspa.1948.0018](https://doi.org/10.1098/rspa.1948.0018) (cited on page 35).
- Gineste, T. et al. (2014). 'Un nouveau moyen expérimental de mesure de rendement de rétrodiffusion.' In: *9ème conférence de la Société Française d'Electrostatique*. Toulouse, France (cited on page 19).
- Goniche, M. et al. (Jan. 2014). 'Modelling of Power Limit in RF Antenna Waveguides Operated in the Lower Hybrid Range of Frequency'. In: *Nuclear Fusion* 54.1, p. 013003. doi: [10.1088/0029-5515/54/1/013003](https://doi.org/10.1088/0029-5515/54/1/013003) (cited on pages xvi, 34, 39).
- Graves, T. P. (June 2006). 'Experimental Investigation of Electron Multipactor Discharges at Very High Frequency'. PhD thesis. Massachusetts Institute of Technology (cited on pages xvi, 39, 42, 51–53).
- Graves, T. P. et al. (May 2006). 'Effect of Multipactor Discharge on Alcator C-Mod Ion Cyclotron Range of Frequency Heating'. In: *Journal of Vacuum Science & Technology A: Vacuum, Surfaces, and Films* 24.3, pp. 512–516. doi: [10.1116/1.2194937](https://doi.org/10.1116/1.2194937) (cited on pages xvi, 34, 39, 97).
- Graves, Timothy P. (May 28, 2014). *Standard/Handbook for Multipactor Breakdown Prevention in Spacecraft Components*. Tech. rep. American Institute of Aeronautics and Astronautics. doi: [10.2514/4.104602.001](https://doi.org/10.2514/4.104602.001) (cited on pages 42, 46).
- Gutton, G., S. K. Mitra, and V. Yostalo (1923). 'Sur la décharge à haute fréquence dans les gaz raréfiés'. In: *Journal de Physique et le Radium* 4.11, pp. 420–428. doi: [10.1051/jphysrad:01923004011042000](https://doi.org/10.1051/jphysrad:01923004011042000) (cited on page 35).
- Gutton, M. H. (1930). 'Recherches sur les propriétés diélectriques des gaz ionisés et la décharge en haute fréquence'. In: *Annales de Physique* 10.13, pp. 63–130. doi: [10.1051/anphys/193010130063](https://doi.org/10.1051/anphys/193010130063) (cited on page 35).

- Hatch, A. J. and H. B. Williams (Apr. 1954). 'The Secondary Electron Resonance Mechanism of Low-Pressure High-Frequency Gas Breakdown'. In: *Journal of Applied Physics* 25.4, pp. 417–423. doi: 10.1063/1.1721656 (cited on pages 35, 36, 38).
- Hatch, Albert J. and H. B. Williams (Nov. 1958). 'Multipacting Modes of High-Frequency Gaseous Breakdown'. In: *The Physical Review* 112.3, pp. 681–685. doi: 10.1103/PhysRev.112.681 (cited on page 37).
- Helou, W. et al. (Oct. 2015). 'Radio-frequency electrical design of the WEST long pulse and load-resilient ICRH launchers'. In: *Fusion Engineering and Design* 96-97, pp. 473–476. doi: 10.1016/j.fusengdes.2015.01.005 (cited on pages 10, 13).
- Helou, W. et al. (Sept. 2020). 'Characterizations and first plasma operation of the WEST load-resilient actively cooled ICRF launchers'. In: *AIP Conference Proceedings* 2254.1. 030009. doi: 10.1063/5.0013992 (cited on pages 10, 13).
- Hillairet, J. (2020). 'RF network analysis of the WEST ICRH antenna with the open-source python scikit-RF package'. In: *AIP Conference Proceedings* 2254.1, p. 070010. doi: 10.1063/5.0013523 (cited on page 85).
- Hillairet, J. et al. (Dec. 2015). 'Ton cyclotron resonance heating systems upgrade toward high power and CW operations in WEST'. In: *AIP Conference Proceedings* 1689.1, p. 070005. doi: 10.1063/1.4936512 (cited on pages 10, 14, 97).
- Hillairet, J. et al. (Apr. 2017). 'Multipactor in High Power Radio-Frequency Systems for Nuclear Fusion'. In: *MULCOPIM (Multipactor, Corona and Passive Intermodulation)* (cited on pages xvi, 34).
- Hillairet, J. et al. (Sept. 2021). 'WEST actively cooled load resilient ion cyclotron resonance heating system results'. In: *Nuclear Fusion* 61.9, p. 096030. doi: 10.1088/1741-4326/ac1759 (cited on pages 10, 14, 15, 84).
- Hillairet, Julien (Jan. 2023). 'Review on recent progress in ion cyclotron range of frequency systems, experiments and modelling for magnetic confinement fusion'. In: *Reviews of Modern Plasma Physics* 7 (1). doi: 10.1007/s41614-023-00116-5 (cited on pages 8, 12).
- Hoffman, D. et al. (1987). 'The design of high-power ICRF antennas for TFTR and Tore Supra'. In: *AIP Conference Proceedings*. Vol. 159. 1. doi: 10.1063/1.36700 (cited on page 12).
- Hofmann (2013). *Auger- and X-Ray Photoelectron Spectroscopy in Materials Science: A User-Oriented Guide*. Vol. 49. Springer Series in Surface Sciences. Berlin Heidelberg: Springer (cited on page 25).
- Höhn, F. et al. (Apr. 1997). 'The Transition of a Multipactor to a Low-Pressure Gas Discharge'. In: *Physics of Plasmas* 4.4, pp. 940–944. doi: 10.1063/1.872564 (cited on pages xvi, 39).
- Jang, K. H. et al. (Dec. 2020). 'Design of multipactor-suppressed high-power VFT for helicon current drive in KSTAR'. In: *Fusion Engineering and Design* 161, p. 111960. doi: 10.1016/j.fusengdes.2020.111960 (cited on pages xvi, 34, 43).
- Jonker, J. L. H. (1951). 'The angular distribution of the secondary electrons of nickel'. In: *Philips Research Reports* 6.5, pp. 372–387 (cited on page 20).
- Kanaya, K. and H. Kawakatsu (Sept. 1972). 'Secondary electron emission due to primary and backscattered electrons'. In: *Journal of Physics D: Applied Physics* 5.9, p. 1727. doi: 10.1088/0022-3727/5/9/330 (cited on pages 18, 22).
- Kim, H., J. Verboncoeur, and Y. Lau (Aug. 2007). 'Modeling RF Window Breakdown: from Vacuum Multipactor to RF Plasma'. In: *IEEE Transactions on Dielectrics and Electrical Insulation* 14. doi: 10.1109/TDEI.2007.4286505 (cited on pages xvi, 39).
- Kishek, R. A. and Y. Y. Lau (May 1996). 'A novel phase focusing mechanism in multipactor discharge'. In: *Physics of Plasmas* 3.5, pp. 1481–1483. doi: 10.1063/1.872027 (cited on page 40).
- Kishek, R. A. et al. (May 1998). 'Multipactor Discharge on Metals and Dielectrics: Historical Review and Recent Theories'. In: *Physics of Plasmas* 5.5, pp. 2120–2126. doi: 10.1063/1.872883 (cited on pages xvi, 34, 35, 37, 39, 40).
- Koshikawa, T. and R. Shimizu (1974). 'A Monte Carlo calculation of low-energy secondary electron emission from metals'. In: *Journal of Physics D: Applied Physics* 7.9, p. 1303 (cited on page 18).
- Langelotti, S. V. et al. (June 2020). 'CST Particle Studio Simulations of Coaxial Multipactor and Comparison With Experiments'. In: *IEEE Transactions on Plasma Science* 48.6, pp. 1942–1949. doi: 10.1109/TPS.2020.2981257 (cited on page 49).

- Larciprete, R. et al. (Jan. 2013). 'Secondary electron yield of Cu technical surfaces: Dependence on electron irradiation'. In: *Physical Review Special Topics - Accelerators and Beams* 16.1, p. 011002. doi: [10.1103/PhysRevSTAB.16.011002](https://doi.org/10.1103/PhysRevSTAB.16.011002) (cited on page 31).
- Lin, S. et al. (Mar. 2023). 'Quantitative analysis of multipactor threshold sensitivity to secondary emission yield of microwave devices'. In: *Physics of Plasmas* 30.3, p. 033104. doi: [10.1063/5.0138875](https://doi.org/10.1063/5.0138875) (cited on page 38).
- Lin, Y. and D. C. Joy (2005). 'A new examination of secondary electron yield data'. In: *Surface and Interface Analysis* 37.11, pp. 895–900. doi: [10.1002/sia.2107](https://doi.org/10.1002/sia.2107) (cited on page 18).
- Martinez, Y. G. et al. (2021). 'First Measurements on Multipactor Study'. In: *Proceedings of the 12th International Particle Accelerator Conference*. Vol. IPAC2021. Campinas, SP, Brazil: JACoW Publishing, Geneva, Switzerland. doi: [10.18429/JACOW-IPAC2021-WEPAB396](https://doi.org/10.18429/JACOW-IPAC2021-WEPAB396) (cited on page 68).
- Monerris-Belda, O. et al. (Dec. 2021). 'High Power RF Discharge Detection Technique Based on the In-Phase and Quadrature Signals'. In: *IEEE Transactions on Microwave Theory and Techniques* 69.12, pp. 5429–5438. doi: [10.1109/TMTT.2021.3120657](https://doi.org/10.1109/TMTT.2021.3120657) (cited on page 41).
- Moulder, J. F. et al. (1979). *Handbook of X-Ray Photoelectron Spectroscopy*. Eden Prairie, Minnesota 55344, United States of America: Perkin-Elmer Corporation, Physical Electronics Division. 260 pp. (cited on page 25).
- Nishimura, K., T. Itotani, and K. Ohya (Aug. 1994). 'Influence of Surface Roughness on Secondary Electron Emission and Electron Backscattering from Metal Surface'. In: *Japanese Journal of Applied Physics* 33.8R, p. 4727. doi: [10.1143/JJAP.33.4727](https://doi.org/10.1143/JJAP.33.4727) (cited on page 42).
- Nishiwaki, M. and S. Kato (Dec. 2009). 'Graphitization of inner surface of copper beam duct of KEKB positron ring'. In: *Vacuum* 84.5, pp. 743–746. doi: [10.1016/j.vacuum.2009.06.028](https://doi.org/10.1016/j.vacuum.2009.06.028) (cited on page 31).
- Owens, T. L., F. W. Baity, and D. J. Hoffman (1985). 'ICRF antenna and feedthrough development at the Oak Ridge National Laboratory'. In: *AIP Conference Proceedings* 129.1, pp. 95–98. doi: [10.1063/1.35242](https://doi.org/10.1063/1.35242) (cited on page 12).
- Pérez, A. M. et al. (Oct. 2009). 'Prediction of Multipactor Breakdown Thresholds in Coaxial Transmission Lines for Traveling, Standing, and Mixed Waves'. In: *IEEE Transactions on Plasma Science* 37.10, pp. 2031–2040. doi: [10.1109/TPS.2009.2028428](https://doi.org/10.1109/TPS.2009.2028428) (cited on pages 47, 50, 51, 64, 74, 75).
- Petit, V. (Jan. 2020). 'Conditioning of surfaces in particle accelerators'. PhD thesis. Université de Toulouse, Institut Supérieur de l'Aréonautique et de l'Espace (cited on page 27).
- Petit, V. et al. (Aug. 2019). 'Role of the different chemical components in the conditioning process of air exposed copper surfaces'. In: *Physical Review Accelerators and Beams* 22.8, p. 083101. doi: [10.1103/PhysRevAccelBeams.22.083101](https://doi.org/10.1103/PhysRevAccelBeams.22.083101) (cited on pages xvi, 27, 31, 34).
- Peysson, Q. et al. (Oct. 2022). 'New 3D Simulation Tool for Multipactor in Presence of Dielectrics'. In: (cited on page 108).
- Plaçais, A. (2021). 'Modélisation et mesures de l'émission secondaire de diélectriques et des phénomènes multipactor en présence de champ magnétique pour la fusion nucléaire contrôlée et le spatial'. PhD thesis. Université de Toulouse, Institut Supérieur de l'Aréonautique et de l'Espace. doi: [10.13140/RG.2.2.30381.82407](https://doi.org/10.13140/RG.2.2.30381.82407) (cited on page 62).
- Plaçais, A. et al. (2018). 'Influence of work function on the multipactor threshold'. In: *2018 IEEE MTT-S International Conference on Numerical Electromagnetic and Multiphysics Modeling and Optimization (NEMO)*, pp. 1–4. doi: [10.1109/NEMO.2018.8503473](https://doi.org/10.1109/NEMO.2018.8503473) (cited on page 43).
- Pozar, D. M. (2011). *Microwave Engineering, 4th Edition*. River Street, Hoboken, NJ: John Wiley Sons, Inc. (cited on pages 8, 45).
- Preist, D. H. and R. C. Talcott (1961). 'On the heating of output windows of microwave tubes by electron bombardment'. In: *IEEE Transactions on Electron Devices* 8.4, pp. 243–251 (cited on pages xvi, 34).
- Richardson, A. S. (2019). *2019 NRL Plasma Formulary*. Washington, DC 20375: U.S. Naval Research Laboratory (cited on page 3).
- Riyopoulos, S., D. Chernin, and D. Dialetis (Aug. 1995). 'Theory of electron multipactor in crossed fields'. In: *Physics of Plasmas* 2.8, pp. 3194–3213. doi: [10.1063/1.871151](https://doi.org/10.1063/1.871151) (cited on pages 37, 40).
- Rizzi, P. A. (1988). *Microwave Engineering. Passive Circuits*. Upper Saddle River, New Jersey 07458: Prentice-Hall, p. 73 (cited on page 45).

- Romanov, G. (2011a). *Stochastic features of multipactor in coaxial waveguides for travelling and standing waves*. Tech. rep. ERMILAB-PUB-11-003-TD. Fermi National Accelerator Lab.(FNAL), Batavia, IL (United States) (cited on pages 51, 64).
- Romanov, Gennady (2011b). 'Update on Multipactors in Coaxial Waveguides using CST Particle Studio'. In: *Proceedings of 2011 Particle Accelerator Conference*, p. 3 (cited on pages 51, 64).
- Rudberg, E. (July 1936). 'Inelastic scattering of electrons from solids'. In: *Physical Review* 50.2, pp. 139–150. doi: [10.1103/PhysRev.50.138](https://doi.org/10.1103/PhysRev.50.138) (cited on pages 17–19, 59).
- Sakamoto, K., Y. Ikeda, and T. Imai (Dec. 1989). 'Numerical study of RF discharge caused by secondary electron emission'. In: *Journal of Physics D: Applied Physics* 22.12, p. 1840. doi: [10.1088/0022-3727/22/12/007](https://doi.org/10.1088/0022-3727/22/12/007) (cited on page 46).
- Scheuerlein, C. and M. Taborelli (2002). 'Electron stimulated carbon adsorption in ultrahigh vacuum monitored by Auger electron spectroscopy'. In: *Journal Of Vacuum Science & Technology, A-Vacuum Surfaces and Films* 20.1. doi: [10.1116/1.1424273](https://doi.org/10.1116/1.1424273) (cited on page 31).
- Semenov, V. E. et al. (Feb. 2014). 'Simple Model of the Rf Noise Generated by Multipacting Electrons'. In: *Journal of Physics D: Applied Physics* 47.5, p. 055206. doi: [10.1088/0022-3727/47/5/055206](https://doi.org/10.1088/0022-3727/47/5/055206) (cited on pages xvi, 39).
- Shaw, Z. C. et al. (Apr. 2019). 'Direct observation of electrons in microwave vacuum components'. In: *Review of Scientific Instruments* 90, p. 054702. doi: [10.1063/1.5089764](https://doi.org/10.1063/1.5089764) (cited on page 41).
- Shaw, Z. C. et al. (July 2020). 'On the limits of multipactor in rectangular waveguides'. In: *Physics of Plasma* 27, p. 083512. doi: [10.1063/5.0012833](https://doi.org/10.1063/5.0012833) (cited on page 41).
- Shemelin, V. D. and S. A. Belomestnykh (2020). *Multipactor in accelerating cavities*. Particle acceleration and detection. Springer (cited on pages xvi, 34).
- Simon, R. E. and B. F. Williams (1968). 'Secondary-electron emission'. In: *IEEE Transactions on Nuclear Science* 15.3, pp. 167–170 (cited on page 18).
- Somersalo, E., P. Yla-Oijala, and D. Proch (1994). *Electron multipacting in RF structures*. Tech. rep. (cited on page 48).
- Somersalo, E. et al. (Jan. 1998). 'Computational methods for analyzing electron multipacting in RF structures'. In: *Particle Accelerators* 59, pp. 107–141 (cited on pages 46, 49, 72–75).
- Somersalo E., Yla-Oijala P. and Proch D. (May 1995). 'Analysis of Multipacting in Coaxial Lines'. In: *Proceedings Particle Accelerator Conference*. Vol. 3, pp. 1500–1502. doi: [10.1109/PAC.1995.505264](https://doi.org/10.1109/PAC.1995.505264) (cited on pages 46–48).
- Sorolla, E. (2012). 'Contribution to Modeling Multipactor and Corona Discharges in High Power Electromagnetic Fields'. PhD thesis. École Polytechnique Fédérale de Lausanne. doi: [10.5075/epfl-thesis-5542](https://doi.org/10.5075/epfl-thesis-5542) (cited on pages xvi, 39).
- Sorolla, E., A. Sounas, and M. Mattes (Mar. 2015). 'Space Charge Effects for Multipactor in Coaxial Lines'. In: *Physics of Plasmas* 22.3, p. 033512. doi: [10.1063/1.4915130](https://doi.org/10.1063/1.4915130) (cited on page 66).
- Sounas, A. (2015). 'Modeling of Long-Term Multipactor Evolution in Microwave Components Including Dielectric Layers'. PhD thesis. École Polytechnique Fédérale de Lausanne. doi: [10.5075/EPFL-THESIS-6535](https://doi.org/10.5075/EPFL-THESIS-6535) (cited on pages xvi, 18, 34, 40, 45).
- Sounas, A., E. Sorolla, and M. Mattes (2011). 'Analysis of Multipactor Effect in Coaxial Lines'. In: *MULCOPIM 2011*. CONF (cited on page 62).
- Udiljak, R. et al. (2003). 'New Method for Detection of Multipaction'. In: *IEEE Transactions on Plasma Science* 31.3 (cited on pages xvi, 39, 41).
- Udiljak, R. et al. (Mar. 2007). 'Multipactor in a Coaxial Transmission Line. I. Analytical Study'. In: *Physics of Plasmas* 14.3, p. 033508. doi: [10.1063/1.2710464](https://doi.org/10.1063/1.2710464) (cited on pages xvi, 39, 45–47).
- Vaughan, J. R. M. (Sept. 1989). 'A new formula for secondary emission yield'. In: *IEEE Transactions on Electron Devices* 36.9, pp. 1963–1967. doi: [10.1109/16.34278](https://doi.org/10.1109/16.34278) (cited on pages 22, 23).
- Vaughan, R. (July 1988). 'Multipactor'. In: *IEEE Transactions on Electron Devices* 35.7, pp. 1172–1180. doi: [10.1109/16.3387](https://doi.org/10.1109/16.3387) (cited on pages xiv, xvi, 16, 37–40, 47).
- Vaughan, R. M. (Apr. 1993). 'Secondary Emission Formulas'. In: *IEEE Transactions on Electron Devices* 40.4. doi: [10.1109/16.202798](https://doi.org/10.1109/16.202798) (cited on page 23).
- Vicente, C. (Aug. 2017). 'Multipactor and Corona Discharge: Theoretical Fundamentals and Analysis with CST and SPARK3D Software Tools'. In: *2017 IEEE International Symposium on Electromagnetic Compatibility*

- & Signal/Power Integrity (EMCSI)*. Washington, DC, USA: IEEE, pp. 1–48. doi: [10.1109/ISEMC.2017.8078121](https://doi.org/10.1109/ISEMC.2017.8078121) (cited on page 56).
- Willis, R. F. and D. K. Skinner (1973). 'Secondary electron emission yield behaviour of polymers'. In: *Solid State Communications* 13.6, pp. 685–688 (cited on page 18).
- Woo, R. (Feb. 1968). 'Multipacting Discharges between Coaxial Electrodes'. In: *Journal of Applied Physics* 39.3, pp. 1528–1533. doi: [10.1063/1.1656390](https://doi.org/10.1063/1.1656390) (cited on pages 38, 46, 47, 49, 70).
- Woo, R. and A. Ishimaru (Dec. 1967). 'A Similarity Principle for Multipacting Discharges'. In: *Journal of Applied Physics* 38.13, pp. 5240–5244. doi: [10.1063/1.1709307](https://doi.org/10.1063/1.1709307) (cited on pages xvi, 34, 46).
- Woo, Richard (Oct. 1970). *Final Report on RF Voltage Breakdown in Coaxial Transmission Lines*. Tech. rep. 32-1500. National Aeronautics and Space Administration (cited on pages 33, 46, 47, 70, 71).
- Woode, A. and J. Petit (1990). 'Investigations into multipactor breakdown in satellite microwave payloads'. In: *ESA Journal* 14.4, pp. 467–478 (cited on pages xvi, 39).
- Yla-Oijala, P. (Nov. 1997). *Analysis of electron multipacting in coaxial lines with traveling and mixed waves*. Tech. rep. DESY (cited on pages 48, 49).
- Yu, M. (2007). 'Power-handling capability for RF filters'. In: *IEEE Microwave Magazine* 8.5, pp. 88–97. doi: [10.1109/MMM.2007.904712](https://doi.org/10.1109/MMM.2007.904712) (cited on pages xvi, 39).